GASDYNAMIC PHENOMENA AND PROPULSIVE PERFORMANCE OF PULSE DETONATION ENGINES

by

JAMES T. PEACE

Presented to the Faculty of the Graduate School of
The University of Texas at Arlington in Partial Fulfillment
of the Requirements
for the Degree of

DOCTOR OF PHILOSOPHY

THE UNIVERSITY OF TEXAS AT ARLINGTON

May 2019

To my parents,

Jerry and Jacque Peace

ACKNOWLEDGEMENTS

With a deep sense of gratitude, I would like to thank my advisor, Prof. Frank K. Lu, for his guidance, encouragement, and support throughout my undergraduate and doctoral studies. I am honored that he provided me the opportunity to conduct research at the Aerodynamics Research Center, through which I have acquired invaluable knowledge and skills that will have a lasting impact on my life and career. I would like to thank Prof. Luca Maddalena for his many valuable suggestions and discussions that have enhanced the quality of my work, and for allowing me to work as a Graduate Teaching Assistant for the Aerodynamics and Fluids Laboratory. I express my gratitude towards Prof. Donald Wilson, Prof. Zhen Xue Han, and Prof. Habib Ahmari for providing helpful recommendations and serving on my dissertation committee.

I would like to thank all the members of the Aerodynamics Research Center family, notably Vijay Gopal, Rohit Pulimidi, Davide Viganò, David Campbell, Ananth Jayamani, and Umang Dighe for the many thoughtful and inspiring discussions we have had. I wish to extend a special thanks to Dr. Andrew Mizener and Dr. Dibesh Joshi for their friendship and recommendation that I participate in research during my undergraduate studies. I would also like to thank our technician, Mr. David Carter, for his numerous helpful suggestions and practical advice, and Juan Lopez, for his assistance with many experiments.

I am forever indebted to my parents, Jacque and Jerry Peace, who never once stifled my curiosity and without whom none of my success would be possible. Thanks also to my siblings, Jessica and Jeff, for their encouragement and support, and to Bella, for being a quirky companion throughout this endeavor.

Finally, I would like to thank my dear fiancée, Mary, for her continued love, patience, and support.

April 23, 2019

ABSTRACT

GASDYNAMIC PHENOMENA AND PROPULSIVE PERFORMANCE
OF PULSE DETONATION ENGINES

James T. Peace, Ph.D.

The University of Texas at Arlington, 2019

Supervising Professor: Frank K. Lu, Ph.D., P.E.

The pulsed detonation engine (PDE) is an advanced propulsion system that makes use of intermittent detonations to provide thrust. In recent decades, the PDE has been at the center of various propulsion research efforts focused on practical implementation of a reliable detonation-based engine for aerospace propulsion applications. However, many design challenges remain to be solved due to the PDEs unsteady operating characteristics. In particular, the unsteady nature of the thrust chamber flow field inherent to the PDE operation makes the design of nozzles aimed at adequately expanding the burned detonation products especially difficult. In order to address this design challenge, a series of related analytical, numerical, and experimental studies have been conducted, which are focused on investigating the manner in which the PDE propulsive performance is governed by the various gasdynamic processes occurring within the thrust chamber and nozzle flow fields.

In this study, three primary PDE configurations are considered. These configurations include fully- and partially-filled PDEs, and PDEs equipped with diverging nozzles. For each configuration, a comprehensive description of the PDE flow field is provided, whereby details concerning the evolution and interaction of various gasdynamic waves and discontinuities are discussed. Additionally, the dominant gasdynamic processes within the thrust chamber

and nozzle flow fields are identified, as these processes must be appropriately modeled in order to accurately evaluate the propulsive performance.

The collision of a detonation wave with a contact surface separating detonable and non-combustible mixtures is a fundamental gasdynamic interaction process that takes place every cycle in the cyclic operation of the PDE. This interaction can drastically influence the evolving thrust chamber flow field and the subsequent propulsive performance metrics. To improve its understanding, this gasdynamic interaction is investigated analytically in order to predict the resulting transmitted shock wave properties, and the necessary conditions for a shock, Mach, or rarefaction wave to reflect at the contact surface. Concurrently, this interaction is investigated experimentally with the use of a detonation-driven shock tube. The analytical and experimental results indicate that the transmitted shock can either be amplified or attenuated depending on the reflection type at the contact surface, and the ratio of the acoustic impedance across the interface.

A quasi-one-dimensional method of characteristics (MOC) model is developed to evaluate the single-cycle gasdynamic flow field and associated propulsive performance of general PDE configurations. The model incorporates the current detonation-contact surface interaction results in order to accurately treat the one-dimensional collision of a detonation wave with a contact discontinuity. Additionally, the MOC model is developed using a simplified unit process approach with an explicit inverse time marching algorithm in order to readily construct the complex thrust chamber flow field along a predefined grid. A thorough validation of the model is presented over a broad range of operating conditions with existing higher-fidelity numerical and experimental performance data for fully- and partially-filled PDEs, and PDEs equipped with diverging nozzles. This includes PDEs operating with a variety of detonable fuels, non-combustible inert mixtures, fill fractions, blowdown pressure ratios, and nozzle expansion area ratios. Lastly, a detailed discussion of the model limitations is provided, and particular operating conditions that lead to a breakdown of the assumptions used in the development of the model are addressed.

A simplified analytical model is developed based on control volume analysis for evaluating the primary performance metrics of a general fully-filled PDE. The MOC model is used to justify and establish a simplified thrust relation based solely on the flow properties at the exit plane of a fully-filled PDE. A detailed analytical description of the thrust chamber flow field is provided, from which an analytical piecewise expression for thrust is derived based on the exit plane pressure history. This expression is then used to evaluate the specific impulse, total impulse, and time-averaged thrust of a fully-filled PDE. This simplified model is validated against the current MOC model and higher-fidelity numerical and experimental performance data for a variety of detonable fuels, equivalence ratios, and blowdown pressure ratios.

Using the current MOC model, the single-cycle propulsive performance of partially-filled PDEs is investigated. The results of the detonation-contact surface interaction study are used to tailor the acoustic impedance of the non-combustible mixture at a fixed fill fraction in order to demonstrate the sensitivity of the thrust chamber flow field to the non-combustible acoustic impedance. Subsequently, the detonable fill fraction and non-combustible acoustic impedance are varied simultaneously in order to characterize the general partially-filled PDE performance. The partial-filling performance benefit is also investigated by varying the initial pressure and temperature of the non-combustible mixture in order to highlight the advantage of using a cold purge gas during operation, and disadvantage of operating in sub-atmospheric environments. It is demonstrated that the partially-filled specific impulse performance results generated with the MOC model from these various parametric investigations are successfully modeled using a previously developed scaling law, whereby this scaling law is extended in the current work to partially-filled total impulse and time-averaged thrust.

Similarly, the single-cycle propulsive performance of PDEs with diverging nozzles is examined. A parametric investigation is conducted to characterize the combined effects of nozzle expansion area and blowdown pressure ratios on the resulting thrust chamber and

nozzle flow fields. Detailed discussion of the transient nozzle flow field is provided in order to emphasize the influence of non-combustible acoustic impedance on the partial-fill effect in diverging nozzles. Moreover, a comparative study is used to demonstrate the performance advantages of a diverging nozzle in sub-atmospheric environments compared to a straight-extension nozzle. Lastly, a detailed parametric investigation is conducted by simultaneously varying the nozzle length, expansion area ratio, and blowdown pressure ratio in order to determine the optimum nozzle performance characteristics.

An analytical model is formulated to predict the strength and motion of a transmitted shock wave through a general contour diverging nozzle for PDEs. The model is derived on the basis of a two-equation approximation of the generalized CCW (Chester–Chisnell–Whitham) theory for treating general shock dynamics in non-uniform channels. A major feature of the two-equation model is the ability to incorporate non-uniformity in the flow immediately following the shock wave, which turns out to be essential for describing the transmitted shock dynamics in PDE nozzles. This model is then used to demonstrate the effects of thrust chamber length on the magnitude of flow non-uniformity behind the transmitted shock entering the nozzle, and how drastically this can influence the nature of shock attenuation within the nozzle. Further, the shock dynamics model is used in conjunction with the MOC model to demonstrate how different nozzle wall curvature influences the PDE propulsive performance, due to the changes in transmitted shock attenuation and gasdynamic over-expansion in the nozzle flow field during the nozzle starting process.

TABLE OF CONTENTS

LIST OF ILLUSTRATIONS

LIST OF TABLES

NOMENCLATURE

a	sound speed
A	cross-section area
A_0	cross-section area of constant-area PDE thrust chamber
c_p	specific heat at constant pressure
E_a	activation energy
F	single-cycle thrust force
$\bar{F}$	time-averaged single-cycle thrust force
g	standard Earth gravitational acceleration
h	specific enthalpy
h_f°	specific enthalpy of formation
I_t	single-cycle total impulse
I_{sp}	single-cycle propellant based specific impulse
k	reaction rate constant
L	combustion chamber length
L_f	propellant fill length
L_n	nozzle length
L_t	tube length
m	mixture mass
M	Mach number
p	pressure
q	heat added or rejected
Q_n	measure of flow non-uniformity $Q_n = \partial^{n-1}/\partial t \left(\partial p/\partial t + \rho a \partial u/\partial t\right)$
R	specific gas constant
s	specific entropy

t	time coordinate
t_f	blowdown time
T	temperature
u	gas velocity in x direction
v	characteristic exhaust velocity
W	shock or detonation wave velocity
x	axial coordinate
X	mole faction
Y	mass faction
z	acoustic impedance
Z	mass-fraction, $m_d/(m_d + m_i)$, or ratio of acoustic impedance, z_0/z_1
α	fill fraction
α_0	ratio of tube length-to-overall length, L_t/L
α_R	Rayleigh angle
γ	ratio of specific heats
η_{th}	thermal efficiency
η_e	adiabatic expansion efficiency
λ	slope of pathline and Mach lines in x–t space
Λ	normalized single-cycle time-averaged thrust force, $\bar{F}/\bar{F}_{full}$
η	normalized single-cycle specific impulse, $I_{sp}/I_{sp,full}$
Ω	normalized single-cycle total impulse, $I_t/I_{t,full}$
ϕ	equivalence ratio
ψ	blowdown pressure ratio, p_1/p_{amb}
ρ	density
τ	normalized single-cycle blowdown time, $t_f/t_{f,full}$

Subscripts

$+$	right-running characteristic Mach line
$-$	left-running characteristic Mach line
0	pathline or purge state
$0'$	transmitted shock post state
1	unburned detonable mixture state
2	equilibrium Chapman-Jouguet detonation state
$2'$	incident reflected interface post state
3	stagnation state behind Taylor rarefaction wave
4	state tube exit and nozzle entrance
$1/2$	half-reaction zone state
add	added quantity
amb	ambient state
CJ	Chapman-Jouguet detonation property
d	detonable mixture
$full$	performance property associated with fully-filled PDE
i	inert mixture
rej	rejected quantity
s	property on transmitted shock
vN	von Neumann state
w	property at PDE thrust wall

CHAPTER 1

INTRODUCTION

1.1 Fundamentals of Detonations

1.1.1 Qualitative Description

The topics discussed in this dissertation concern the application of detonation combustion for aerospace propulsion systems. Accordingly, it is of importance to give a proper description of what exactly is a detonation, and how it differs from deflagration, namely, the combustion process used in existing chemical rocket and airbreathing engines. In general, there are two types of self-propagating combustion waves, namely, deflagration (subsonic) and detonation (supersonic). Following the ignition of a combustible mixture, a combustion wave forms that propagates away from the ignition source. While propagating, the combustion wave transforms the mixture reactants into burned products. For traditional fuel and oxidizer mixtures used in propulsion systems, such as hydrogen or hydrocarbon fuels with either air or pure oxygen, the combustion process through the wave is exothermic, such that the potential energy stored in the chemical bonds of the reactant molecules is released and converted into internal and kinetic energy of the combustion products. The propagation nature of the combustion wave can yield drastically different burnt product states in regard to the pressure, temperature, and velocity, depending on whether a deflagration or detonation manifests in the reactant mixture. Whether a deflagration or detonation occurs in the combustible mixture is predominantly governed by the initial mixture composition, ignition source, and boundary conditions, i.e., physical confinement. Hence, it is useful to discuss the conditions upon which each combustion wave occurs in practice.

Glassman and Yetter [1] describe the mechanism by which deflagration and detonation propagation occurs through a premixed reactant contained in a long tube with different boundary conditions. If the tube is open at both ends, ignition of the reactants will manifest

in a self-propagating deflagration wave, traveling with a relatively low subsonic velocity with respect to the reactants ahead of the wave. As described by Lee [2], a deflagration is an expansion wave where the pressure drops across the reaction front, and the combustion products are accelerated away from the wave in a direction opposite to its propagation. In general, a deflagration wave propagates into the reactants by means of transport processes, such as heat conduction and diffusion of radicals as a result of the sharp gradients in temperature and chemical species concentration. Consequently, the propagation velocity of a deflagration wave is on the order of 0.2–2 m/s [1], and is proportional to the square root of reactant thermal diffusivity and reaction rate [3–5].

If one of the open-end boundary conditions is instead closed, such that the combustible reactants are now contained in a long tube with one end closed and the other open, ignition at the closed-end will manifest in a self-propagating detonation wave that travels away from the closed-end at a supersonic velocity. However, the onset of a detonation wave is not immediately achieved following ignition. In fact, a deflagration wave is initiated first; however, the addition of physical confinement at the rear boundary allows the deflagration to accelerate until eventually undergoing an abrupt transition into a detonation. Formally, this process is known as deflagration-to-detonation transition (DDT), and is an active area of research in combustion dynamics of reactive systems [6, 7]. The mechanisms by which DDT takes place are not well understood, which results in several competing ideas in the literature [8]. As described by Lee [2], deflagrations are intrinsically unstable and subject to numerous instability mechanisms that render the reaction front turbulent. This includes flame instabilities such as Darrieus–Landau and thermal-diffusive instabilities, as well as those associated with an accelerating density interface such as Rayleigh–Taylor and Richtmyer–Meshkov instabilities. Further, because the confinement of a closed-end boundary condition imposes a zero velocity condition behind the reaction front, compression waves are able to travel into the reactants ahead of the reaction front. Although weak at first, these compression waves disturb the reactants ahead of the reaction front, which simulta-

neously causes an unstable amplification in the burning rate when the disturbed reactants are inducted through the reaction front. Such a process provides a positive feedback mechanism that couples the heat release in the reaction front with disturbed reactants ahead of the front, permitting the rapid acceleration of the deflagration to velocities as high as 1 km/s [8].

As the deflagration front accelerates, compression waves emanating from the reaction front eventually coalesce into a traveling shock wave ahead of the deflagration. This shock wave is commonly referred to as the precursor shock, and leads the accelerating deflagration wave. It has been observed experimentally by Urtiew and Oppenheim [9] that the DDT process requires both the positive feedback mechanism between the accelerating turbulent deflagration reaction front and disturbed reactants, as well as the formation of the precursor shock wave. However, it was shown in [9] and described by Kuo [10] that the physical transition to detonation can take place at the precursor shock front, turbulent deflagration front, or in between these respective fronts. In the event detonation transition occurs at the precursor shock front, adiabatic compression from the shock is substantial enough to dissociate the reactants into radicals in an induction zone immediately behind the shock. These radicals then react in a series of chain branching reactions that rapidly release heat in a reaction zone following the induction zone. The combined induction and reaction zones are coupled to the shock front and typically range from 1–10 mm in length [1]. Additionally, the expansion of burned products through the reaction zone provides the mechanism for a self-propagating detonation.

Alternatively, if detonation initiation occurs at the turbulent deflagration front or between the front and precursor shock, a rapidly expanding detonation bubble forms that propagates and eventually coalesces with the precursor shock forming the detonation wave structure previously mentioned. In either mode of DDT, a self-propagating detonation is formed that travels through the reactants with a very high velocity on the order of 1–4 km/s [1]. The DDT method of detonation initiation above is commonly referred to as self-ignition

and usually requires a weak deposition of activation energy to achieve the initial deflagration wave. Subsequently, the transition to detonation occurs over a distance on the order of a meter for highly reactive fuels such as hydrogen and hydrocarbons [1]. Alternate methods of detonation initiation exist that include shock transmission [11, 12], shock focusing [13], and blast initiation by a strong igniter [14]. These methods generally result in the direct ignition of a detonation wave without requiring the DDT process; however, these are not considered practical for propulsion applications.

The qualitative difference between deflagration and detonation waves are provided in Table 1. In this table, subscripts 1 and 2 correspond to the reactant and product states, respectively. Note that the propagation Mach number of a deflagration relative to the unburned reactants is several orders of magnitude less than that of a detonation. Additionally, because a deflagration wave is a chemically reacting expansion wave sustained by transport processes, a slight pressure drop is observed through the wave. The same is not true for detonations since the detonation wave is headed by a leading shock front sustained by a coupled chemical reaction zone. Hence, the reactant pressure drastically rises from adiabatic compression of the shock front, and subsequently relaxes through the reaction zone to a product pressure that is more than an order-of-magnitude higher than the initial reactant pressure. Similarly, the detonation product temperature is nearly double that achieved by deflagration. These qualitative differences are some of the primary motivations for pursuing detonation combustion in propulsion systems as opposed to deflagration. However, a more thorough assessment of the potential benefits of using detonation in propulsion systems can be addressed by considering the gasdynamic and thermodynamic properties of detonations and deflagrations, which is the goal of the following subsections.

1.1.2 Chapman–Jouguet Theory

It is of interest to mention important works that directly influenced the development of the Chapman–Jouguet (CJ) detonation theory to provide historical context regarding

Table 1.1. Qualitative difference between deflagrations and detonations in gases [1].

Ratio	Deflagration	Detonation
u_1/a_1	0.0001–0.03	5–10
u_2/u_1	4–16	0.4–0.7
p_2/p_1	0.98–0.976	13–55
T_2/T_1	4–16	8–21
ρ_2/ρ_1	0.06–0.25	1.4–2.6

the state of knowledge during its development. Until the late 19th century, the existence of detonation waves had not been conclusively demonstrated. The work of French scientists Berthelot and Vieille [15–18] in the early 1880s provided the first experimental measurements of detonation wave velocities by means of the Boulengé chronograph in a variety of gaseous fuels. Shortly thereafter in 1883, French scientists Mallard and Le Chatelier [3] observed the transition of a deflagration to detonation using a drum streak camera, which definitively proved the existence of two distinct modes of combustion in a given gaseous mixture, namely, deflagration and detonation. As noted by Lee [2], Berthelot and Vieille recognized the supersonic nature of detonation waves and the role of adiabatic shock compression in initiating the chemical reactions behind a detonation. However, at the time of their detonation studies, a formal theory of shock waves had not been fully established. In 1870, the Scottish engineer Rankine [19] made the first major contribution to a thermodynamic formulation of shock waves from the conservation of mass, momentum, and energy. Subsequently, without knowledge of Rankine's work, these equations were later rediscovered in 1887 by the French scientist Hugoniot [20]. Together, these works provided the necessary formulation for appropriately determining the change in thermodynamic state across a shock wave, and have historically been referred to as the Rankine–Hugoniot (RH) relations. It was not until the English chemist Chapman [21] in 1899, and later by the French engineer Jouguet [22, 23] in 1905, that the work of Rankine and Hugoniot on shock

waves was extended to a steadily propagating one-dimensional combustion wave in a reactive mixture. Collectively, these works marked the first rigorous thermodynamic treatment of deflagration and detonation waves and has been historically referred to as the CJ theory. The remainder of this subsection focuses on the complete formulation of the CJ theory and the thermodynamic differences between detonations and deflagrations.

Chapman and Jouguet separately applied the RH relations to a steadily propagating one-dimensional combustion wave in a reactive mixture. As noted by Chapman and Jouguet, all steadily propagating detonation or deflagration waves must satisfy these fundamental conservation equations. The approach taken by Chapman and Jouguet deviates from that of Rankine and Hugoniot for non-reactive shock waves in that the upstream and downstream conditions of the combustion wave were taken as the reactant and products, respectively. Therefore, by assuming the products approach equilibrium at the downstream condition, one is able to determine the chemical composition of the combustion products and corresponding heat release across the combustion wave. Such a steadily propagating one-dimensional combustion wave is depicted in Fig. 1.1 with the associated gaseous reactant and product state nomenclature.

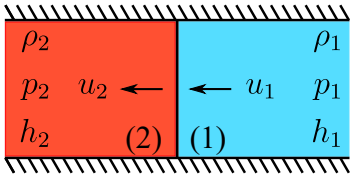

Figure 1.1. Chapman–Jouguet combustion wave schematic and state nomenclature.

The conservation of mass, momentum, and energy for one-dimensional flow across the combustion wave in Fig. 1.1 in the absence of mass addition, friction, and heat transfer, are given by

$$\rho_1 u_1 = \rho_2 u_2 \tag{1.1}$$

$$p_1 + \rho_1 u_1^2 = p_2 + \rho_2 u_2^2 \tag{1.2}$$

$$h_1 + \frac{1}{2}u_1^2 + q = h_2 + \frac{1}{2}u_2^2 \tag{1.3}$$

where states 1 and 2 correspond to the reactants and products, respectively. Additionally, thermodynamic equations of state for the reactants and products of the form

$$h_1 = f(\rho_1, p_1) \tag{1.4}$$

$$h_2 = f(\rho_2, p_2) \tag{1.5}$$

provide two additional equations. Note, h_1 and h_2 in Eqs. (1.3)–(1.5) represent the specific sensible enthalpy of the products and reactants, respectively. Similarly, q accounts for any heat added by means of chemical energy release per unit mass, which is equal to the difference in chemical enthalpy, or enthalpy of formation h_f°, between the reactants and products

$$q = \sum_i^{\text{reactants}} Y_i h_{f,i}^\circ - \sum_j^{\text{products}} Y_j h_{f,j}^\circ \tag{1.6}$$

Given a reactant mixture with a specified thermodynamic state, ρ_1, p_1, and h_1, application of Eqs. (1.1)–(1.3) with Eq. (1.5) yields a set of four equations with five unknowns, namely, ρ_2, p_2, u_2, h_2, and u_1. Hence, an additional condition or criterion is required for proper closure of the equation set. Chapman and Jouguet provided a separate, yet physically consistent, criterion for the solution of deflagration and detonation waves, which is detailed in the following paragraphs.

Before discussing the criterion proposed by Chapman and Jouguet, it is convenient to obtain the expression for the general reactive Hugoniot in order to assess the domain of physically plausible deflagration and detonation wave solutions. Solving Eq. (1.1) for u_2 and substituting into Eq. (1.2), after algebraic manipulation, yields

$$u_1^2 = \frac{1}{\rho_1^2}\left[(p_2 - p_1)\left(\frac{1}{\rho_1} - \frac{1}{\rho_2}\right)\right] \tag{1.7}$$

Note, Eq. (1.7) represents the Rayleigh line for a combustion wave, which defines the thermodynamic path in which the reactants transition to the product state across the combustion wave. This expression will be used in the subsequent analysis to identify plausible regions

of detonation and deflagration solutions. In a similar manner, substituting into Eq. (1.1), or simply solving Eq. (1.1) for u_1 and substituting into Eq. (1.2), yields

$$u_2^2 = \frac{1}{\rho_2^2}\left[(p_2 - p_1)\left(\frac{1}{\rho_1} - \frac{1}{\rho_2}\right)\right] \tag{1.8}$$

Subtracting (1.7) from (1.8) yields

$$u_1^2 - u_2^2 = (p_2 - p_1)\left(\frac{1}{\rho_1} + \frac{1}{\rho_2}\right) \tag{1.9}$$

Lastly, substituting back into Eq. (1.3) yields

$$h_2 - h_1 = q + \frac{1}{2}\left(\frac{1}{\rho_1} + \frac{1}{\rho_2}\right)(p_2 - p_1) \tag{1.10}$$

The above expression is the general reactive Hugoniot relation, and represents the locus of all possible thermodynamic equilibrium states behind a combustion wave that is accompanied by the addition of heat q from the release of chemical energy. Given a reactant mixture with a specified thermodynamic state, ρ_1, p_1, and h_1, Eq. (1.10) can be used to construct the product Hugoniot curve in the p–ρ^{-1} plane for all cases of equilibrium heat release.

If it is assumed that the reactants are calorically perfect, i.e., constant specific heats, then the general reactive Hugoniot can be simplified to

$$q = \frac{\gamma}{\gamma - 1}\left(\frac{p_2}{\rho_2} - \frac{p_1}{\rho_1}\right) - \frac{1}{2}(p_2 - p_1)\left(\frac{1}{\rho_1} + \frac{1}{\rho_2}\right) \tag{1.11}$$

where the sensible enthalpy is taken as $h = c_p T$, and the specific heat at constant pressure as $c_p = R[\gamma/(\gamma - 1)]$. Although not particularly useful for the analysis of detonation and deflagration waves, the expression in Eq. (1.11) represents the simplified calorically perfect Hugoniot relation, which is typically provided in the literature. Note, if no heat is released across the wave, then $q \equiv 0$, and the Hugoniot relation in Eq. (1.11) represents the locus of all possible solutions behind a non-reactive shock wave. Such an expression is identical to the expressions developed by Rankine [19] and Hugoniot [20] for their thermodynamic analysis of shock waves. Therefore, given an upstream gas with a specified thermodynamic state, ρ_1 and p_1, Eq. (1.11) with $q = 0$ can be used to construct the non-reactive Hugoniot curve in the p–ρ^{-1} plane.

For the non-reactive shock, Eq. (1.11) is used with given values of ρ_1 and p_1 to construct the appropriate curve. However, construction of the reactive Hugoniot relation requires a numerical routine with Eq. (1.10) to properly compute the locus of equilibrium solutions behind a combustion wave. Such a routine can be implemented for a given ρ_2 and guessed equilibrium temperature, T_2. At these conditions, the equilibrium pressure, p_2, sensible enthalpy, h_2, and change in chemical enthalpy, q, can be determined with a conventional Gibb's free energy minimization solver. Further, with knowledge of the equilibrium density, ρ_2, pressure, p_2, and heat release, q, application of Eq. (1.10) permits determination of the equilibrium sensible enthalpy behind the combustion wave from mass, momentum, and energy conservation across the wave. With such a calculation, the equilibrium sensible enthalpy, h_2, is predicted at a given ρ_2 by a guessed equilibrium temperature, T_2, and a chemical equilibrium solver, and by mass, momentum, and energy conservation from Eq. (1.10). Therefore, application of the iterative secant method with a new T_2 permits minimization of the difference in h_2 predicted by the two methods, and the resulting converged equilibrium solution. For the purpose of implementing this numerical routine and constructing the reactive Hugoniot, the chemical equilibrium and kinetics program Cantera is utilized within a Matlab environment [24].

For a stoichiometric H_2–air mixture initially at 1 atm and 300 K, the non-reactive and reactive Hugoniot curves are shown in Fig. 1.2. The initial gas state is denoted by the square marker, which takes the value of $\rho_2/\rho_1 = 1$ and $p_2/p_1 = 1$ and represents the origin of the Hugoniot curves. In effect, the addition of heat q from combustion pushes the reactive Hugoniot (red line) to the right of the non-reactive Hugoniot (blue line). Further, not all of the solutions to Eqs. (1.10) and (1.11) are physically plausible. For instance, in the case of a non-reactive shock wave, only solutions where $p_2/p_1 \geq 1$ and $\rho_2/\rho_1 \geq 1$ are physically possible. Solutions of the opposite nature corresponds to an expansive shock wave, which is physically impossible on the basis of entropy considerations provided by Rayleigh [25] and Taylor [26] in 1910. For this reason, the bottom branch of the non-reactive Hugoniot

is denoted by a dashed line to indicate a non-physical solution. Moreover, in the case of a reactive combustion wave, inspection of the Rayleigh line in Eq. (1.7) yields two possible regions where a solution can physically exist. For instance, if $\rho_2/\rho_1 < 1$ while $p_2/p_1 > 1$, then the mass flux through the combustion wave is complex, or non-physical, which is indicated by the dashed region on the reactive Hugoniot. The limiting cases of physically possible combustion waves correspond to the constant-volume combustion (CVC) solution, i.e., $\rho_2/\rho_1 = 1$, and the constant-pressure combustion (CPC) solution, i.e., $p_2/p_1 = 1$. All other physical solutions lie on two separate branches of the reactive Hugoniot, corresponding to the deflagration and detonation regimes.

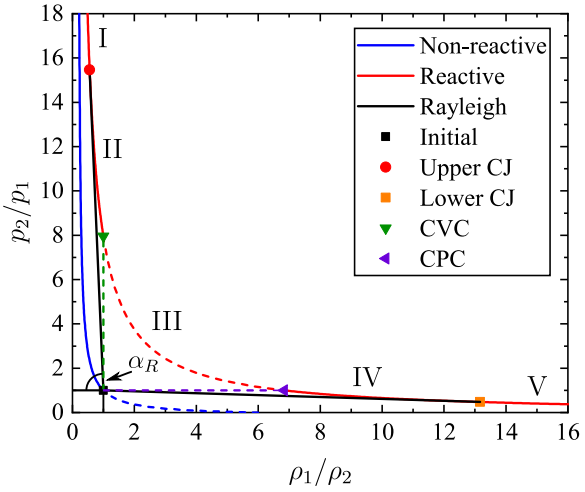

Figure 1.2. Non-reactive and reactive Hugoniot curves for shock and combustion wave in stoichiometric H_2–air mixture at 1 atm and 300 K.

All physically attainable deflagration and detonation wave solutions must satisfy both the reactive Hugoniot relation in Eq. (1.10) and the expression for the Rayleigh line in Eq. (1.7). Recognizing that the Rayleigh line is linear in the p–ρ^{-1} plane, it is convenient to write the Rayleigh line in the form

$$u_1 = \frac{\tan^{1/2}(\alpha_R)}{\rho_1} \tag{1.12}$$

where

$$\tan(\alpha_R) = \frac{p_2 - p_1}{1/\rho_1 - 1/\rho_2} \tag{1.13}$$

In this form, it is clear that the Rayleigh line originates from the initial state at $\rho_2/\rho_1 = 1$ and $p_2/p_1 = 1$ with an inclination angle α_R. Therefore only when the Rayleigh line intersects the reactive Hugoniot curve is a detonation or deflagration solution possible. Because the Hugoniot curve represents a hyperbola in the p–ρ^{-1} plane, there are characteristic angles of α_R for which a solution can exist. For instance, the minimum possible angle is when the Rayleigh line is tangent to the upper branch of the reactive Hugoniot, which represents a unique detonation (compression wave) solution. This Rayleigh line (black line) and tangency point, labeled by the upper CJ point, are shown in Fig. 1.2. Any increase in α_R above this value results in two intersection locations with the upper branch of the reactive Hugoniot, until α_R approaches 90 degrees, in which case the CVC solution is obtained. The two solution regimes on the upper branch of the reactive Hugoniot are labeled with the numerals I and II, which represents the cases of strong and weak detonation solutions, respectively. For α_R between 90 and 180 degrees, the Rayleigh line falls on the non-physical branch of the reactive Hugoniot with a complex mass flux, and is labeled with the numeral III. As α_R reaches 180 degrees, the CPC solution is obtained. Any increase in α_R above 180 degrees results in the intersection of the Rayleigh line and bottom branch of the reactive Hugoniot at two distinct locations. These distinct regimes are labeled with the numerals IV and V, and represent the weak and strong deflagration solutions, respectively. Lastly, the maximum value of α_R for which a solution is obtained is when the Rayleigh line becomes tangent with the lower branch of the reactive Hugoniot curve, representing a unique deflagration (expansion wave) solution. This Rayleigh line (black line) and tangency point, labeled by the lower CJ point, are shown in Fig. 1.2.

A few comments can be made about the nature of the detonation solutions in regions I and II, and the deflagration solutions in regions IV and V, before discussing the tangency CJ points. In region I, or the the strong detonation regime, the detonation wave moves with

a supersonic Mach number with respect to the reactants, whereas the Mach number behind the detonation is subsonic. This permits disturbances originating from behind the wave to propagate forward and overtake the wave from behind, rendering the wave unstable, and attenuating the solution towards the upper CJ tangency point where the post-detonation Mach number is sonic. In region II, or the weak detonation regime, the detonation wave also moves with a supersonic Mach number with respect to the reactants; however, the Mach number behind the detonation is supersonic. When considering the typical wave structure of a detonation, namely, adiabatic shock compression followed by heat release, reaching region II along the Rayleigh line is usually deemed a physically unrealizable process as more energy would have to be expended beyond the equilibrium CJ point. For this reason, weak detonation solutions are often disregarded as physically obtainable solutions. However, as noted by Lee [2] and Kuo [10], it may be possible to obtain the weak detonation solution in practice with reactant mixtures featuring rapid chemical kinetics. In this case, the solution would proceed along the Rayleigh line to region II without the adiabatic compression of a shock wave, although; they concede that such a unique wave would seldom be observed in practice.

In region IV, or the weak deflagration solution regime, the deflagration wave moves with a subsonic Mach number with respect to the reactants and the Mach number behind the deflagration is subsonic. Reactants passing through a weak deflagration are accelerated from a low to high subsonic velocity as they transition to burned products behind the wave. Solutions in this regime are frequently encountered in practice and are often treated using classical flame structure theories, such as those of Mallard and Le Chatelier [3] and Zel'dovich and Frank-Kamenetskii [5]. Moving further down the weak deflagration regime in region IV, the post-deflagration Mach number is increasing until finally reaching a sonic condition at the lower CJ tangency point. In region V downstream of this lower tangency point lies the strong deflagration regime, where the wave moves with a subsonic Mach number with respect to the reactants, and a supersonic Mach number behind. Reactants passing

through a strong deflagration are accelerated from a low subsonic velocity to supersonic as they transition to burned products behind the wave. Such waves are considered physically impossible on the basis of Rayleigh heat addition and the wave structure, in that a gas in a constant-area duct cannot be accelerated to a supersonic velocity by heat addition alone. Additionally, the lower CJ tangency point is only observed during the acceleration of a deflagration wave while undergoing DDT [2]. Therefore, of the possible detonation and deflagration regimes, only the stable upper CJ solution and weak deflagration solutions are commonly encountered in practice.

As previously mentioned, Eqs. (1.1)–(1.3) with Eq. (1.5) yield an indeterminate equation set requiring an additional expression or criterion. For detonations, Chapman and Jouguet provided the required criterion; although, arrived at by different phenomenological arguments. By analyzing the detonation wave velocity variation along the reactive Hugoniot curve, Chapman discovered that when the Rayleigh line is tangent to the reactive Hugoniot, the detonation wave velocity reaches a minimum [21]. Moreover, this condition provides a unique solution for a detonation wave velocity in a reactive mixture, which agrees with experimental observations, in that a unique detonation wave velocity is observed in a detonable mixture at given initial conditions. Therefore, Chapman postulated that the minimum wave velocity at the tangency point must be the correct detonation solution [2]. In contrast, Jouguet investigated the variation of post-detonation Mach number and entropy along the reactive Hugoniot and discovered that the post-detonation Mach number reaches the sonic condition, while the entropy reaches a minimum, as the Rayleigh line becomes tangent to the reactive Hugoniot [22,23]. Jouguet then postulated that these conditions must yield the correct detonation solution, given the unstable nature of the strong detonations, and the physical impracticality of weak detonations [2]. The simultaneous occurrence of the minimum velocity, post-detonation sonic flow, and minimum entropy conditions at the upper tangency point was later shown by Crussard in 1907 [27], and the resulting condition has

since been referred to as the CJ criterion. For mathematical closure, Eqs. (1.1)–(1.3) with Eq. (1.5) require the CJ criterion:

$$u_2^2 = a_2^2 = \left(\frac{\partial p_2}{\partial \rho_2}\right)_{s_2} \tag{1.14}$$

With this criterion, all the detonation wave properties, namely, ρ_2, p_2, u_2, h_2, and u_1, can be determined given the initial state of a detonable mixture, ρ_1, p_1, and h_1, which completes the CJ theory. A general solution requires the use of a sophisticated nonlinear equation solver coupled with a chemical equilibrium solver. Such solvers exist, which include the NASA chemical equilibrium applications (CEA) code [28], or the shock and detonation toolbox developed at Caltech [29,30], which makes use of the previously mentioned Cantera chemical equilibrium and kinetics solvers [24].

The results of the CJ theory can be used to demonstrate the fundamental motivation for pursuing detonations as a means of combustion in an aerospace propulsion system. Analysis of the entropy variation along the reactive Hugoniot curve highlights the amount of entropy generated for the various combustion processes that can be used in a given engine system. Fundamentally, a combustion process that generates less entropy is a more efficient means of heat addition in a thermodynamic cycle, since the heat addition is closer to a reversible process and less heat is wasted. Figure 1.3 shows the entropy variation along the reactive Hugoniot for stoichiometric H_2–air combustion that is initially at 1 atm and 300 K. As first noted in the work of Jouguet [22, 23], the minimum and maximum entropy points correspond to the CJ detonation and deflagration solutions, namely, the upper and lower CJ points, respectively. As previously mentioned, the upper CJ point is the stable detonation solution that is commonly encountered in practice. However, CJ deflagration is really only observed near the DDT limit of an accelerating deflagration wave. In practice, deflagration solutions commonly encountered lie on the weak deflagration regime, or region IV, towards the idealized CPC solution. For the sake of a conservative estimate, the idealized CPC solution can be used as a benchmark to evaluate the reduction in entropy generation by means of detonation combustion as opposed to deflagration. For the conditions shown in

Fig. 1.3, the reduction in entropy between a CJ detonation and idealized CPC deflagration is 19.2 percent. This is a substantial difference that can be exploited in aerospace propulsion applications by simply changing the method in which fuels are burned. For completeness, the entropy variation along the reactive Hugoniot for stoichiometric H_2–air combustion at different initial pressures and temperatures is shown in Figs. 1.4(a) and 1.4(b), respectively. Moreover, the reduction in entropy between the CJ detonation solution and the idealized CPC deflagration for the respective initial conditions is tabulated in Table 1.2. Again, over this initial pressure and temperature variation range, the reduction in entropy for detonation as opposed to deflagration is roughly 19 percent.

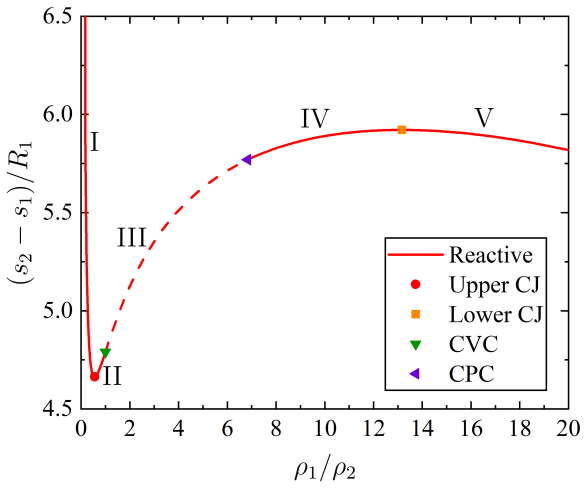

Figure 1.3. Entropy variation along reactive Hugoniot for stoichiometric H_2–air mixture at 1 atm and 300 K.

Before continuing, it is worth mentioning that the CJ criterion is a heuristic postulate with no rigorous mathematical underpinnings based on analysis of the conservation laws. Physical reasoning can be used to justify the disregard of strong and weak detonation solutions, such as the stability of strong detonations, and the wave structure for weak detonations, however; a formal rigorous analysis has yet to demonstrate the validity of the CJ criterion. Despite this, the CJ detonation theory has excellent agreement with

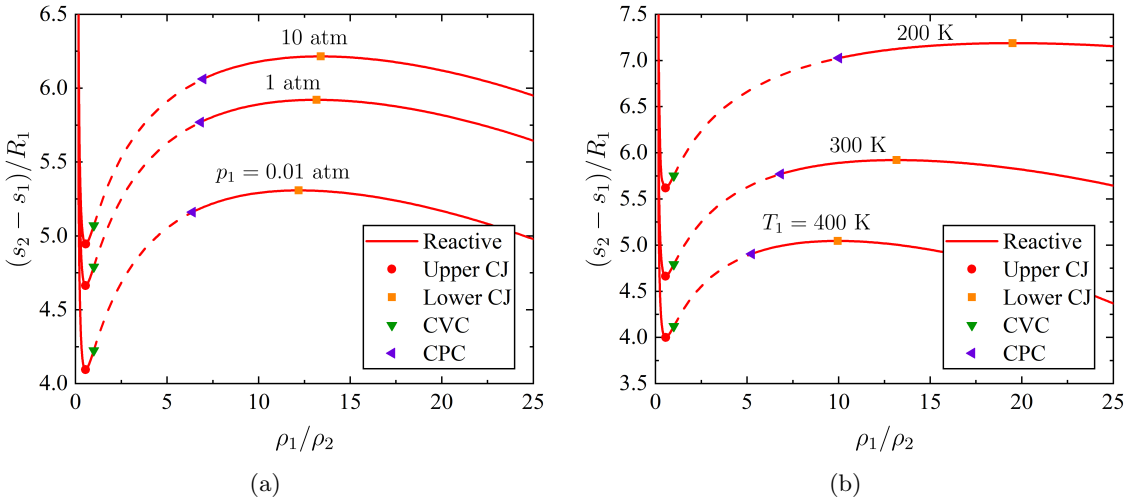

Figure 1.4. Entropy variation along reactive Hugoniot for stoichiometric H_2–air mixture at (a) 300 K and (b) 1 atm.

Table 1.2. Detonation and deflagration entropy change at various initial conditions for stoichiometric H_2–air mixture.

p_1 (atm)	T_1 (K)	$(s_2 - s_1)/R_1$ CPC	$(s_2 - s_1)/R_1$ CJ Det.	% Decrease
0.01	300	5.16	4.09	20.7
1	300	5.77	4.66	19.2
10	300	6.06	4.95	18.3
1	200	7.03	5.62	20.1
1	400	4.90	4.00	18.4

experimental observations, even near the limits of detonability. On the other hand, as noted by Lee [2], the agreement with experimental observations is merely fortuitous, unless a formal justification of the CJ criterion can be provided.

Lastly, it should be noted that the derivation of the above CJ theory bypasses details of the wave structure, or mechanisms, by which a detonation or deflagration propagates. In fact, only the RH relations are used to connect the initial and final equilibrium states of a reactive mixture that has passed through a combustion wave. Consequently, CJ theory fails

to explain the mechanism by which a detonation or deflagration self-propagates through a reactive mixture. Such explanations require detailed analysis of the respective wave structures and dynamics of the reaction products. For deflagrations, the theories of of Mallard and Le Chatelier [3] and Zel'dovich and Frank-Kamenetskii [5] bridge this gap for flame propagation in premixed reactive mixtures. Notably, the theory of Zel'dovich and Frank-Kamenetskii demonstrate that a deflagration wave propagates into the reactants by means of transport processes, such as heat conduction and diffusion of radicals, as a result of sharp gradients in temperature and chemical species concentration. In the case of detonations, the Zel'dovich–von Neumann–Döring (ZND) theory describes the one-dimensional structure of detonations and the behavior of products across the reaction zone, which explains the mechanism by which a one-dimensional detonation wave can self propagate. Since the ZND theory is used in the subsequent analysis, the following subsection provides a brief description of the theory and idealized one-dimensional detonation wave structure.

1.1.3 Zel'dovich–von Neumann–Döring Theory

Following the work of Mallard and Le Chatelier [3] and Berthelot and Vieille [15–18], it was apparent that the supersonic nature of detonation waves must be accompanied by adiabatic shock compression that aids the initiation of chemical reactions behind a detonation. Subsequently, the Soviet physicist Zel'dovich [31] provided the first rigorous analysis of the one-dimensional detonation wave structure in 1940. In Zel'dovich's work, the detonation wave was headed by a shock wave to provide the required adiabatic compression for the reactant to subsequently undergo chemical reactions in a closely coupled exothermic reaction zone behind the shock front. By including the effects of heat and momentum losses in the detonation wave structure, Zel'dovich was able to demonstrate the existence of a unique detonation wave velocity and detonation structure when the sonic and chemical equilibrium conditions coincide at the same location within the detonation structure. This condition results in a unique detonation wave velocity and is often referred to as regularity at the

sonic singularity, which has since been regarded as an eigenvalue detonation solution [2]. Shortly thereafter in 1942 and 1943, unaware of Zel'dovich's work, the Hungarian-American mathematician and physicist von Neumann [32] and the German physicist Döring [33] independently provided similar treatments of the one-dimensional detonation wave structure. Their work described a detonation wave that was headed by a shock wave and followed by a closely coupled chemical reaction zone. In von Neumann's work, attention was focused on the existence of weak detonation and the associated wave structure that must exist for such a wave to be physically realizable. A reaction progress variable was used to connect intermediate Hugoniot curves from the immediate post-shock state to the equilibrium detonation state. Further, Döring also made use of reaction progress variables, and directly integrated the resulting detonation wave structure with the associated chemical kinetics, which revealed the path of thermodynamic states through the detonation wave. Collectively, these three independent works marked the first formal analysis of a one-dimensional detonation wave structure and has since been referred to as the ZND detonation theory after the contributing researchers.

The general ZND detonation wave structure is shown schematically in Fig. 1.5, which details the temperature, pressure, and density profiles across the wave. Formally, the ZND theory states that the detonation wave structure consists of a leading shock front and coupled induction and chemical reaction zones, which together steadily moves through the reactants at the CJ detonation velocity for a given reactive mixture. As the reactants pass through the leading shock front, the reactants are adiabatically compressed to the post-shock state referred to as the von Neumann (vN) peak, which can readily be calculated with the RH shock jump relations. Immediately behind the shock, the adiabatic shock compression brings the reactants to a temperature where thermal dissociation of the reactants into radical species begins to take place. This dissociation region is referred to as the induction zone, and is almost thermally neutral with a thermodynamic state that is relatively constant [2]. Once sufficient concentration of active radical species are produced, rapid chain-branching

chemical reactions convert the reactants to products. This region is referred to as the reaction zone, which is accompanied by rapid exothermic chemical energy release. As shown in Fig. 1.5, within the reaction zone the temperature rapidly increases while the pressure and density simultaneously decrease. Across the reaction zone, the chemical reactions progress until eventually reaching chemical equilibrium, which is equal to the thermodynamic state predicted by the CJ detonation theory. As noted by Zel'dovich, von Neumann, and Döring, the adiabatic compression of the leading shock and the rapid expansion of products across the reaction zone provide the mechanisms by which a detonation wave ignites and self-propagates through a reactive mixture.

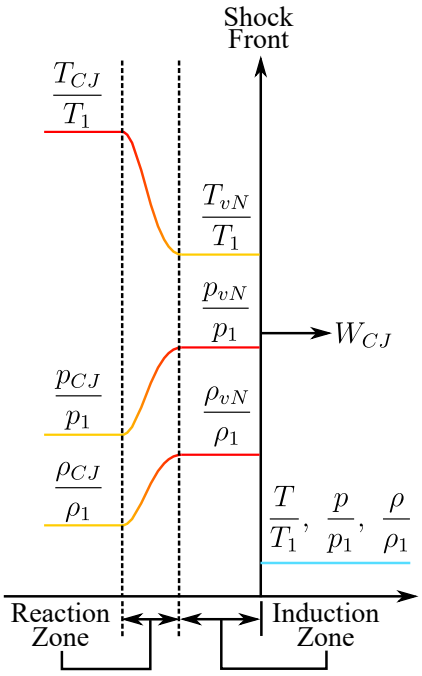

Figure 1.5. Zel'dovich–von Neumann–Döring detonation wave structure.

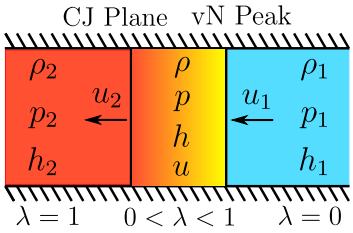

Figure 1.6. Zel'dovich–von Neumann–Döring detonation wave schematic and state nomenclature.

For a calorically perfect gas, the conservation of mass, momentum, and energy for as steady one-dimensional planar flow across the detonation wave in Fig. 1.6 in the absence of mass addition and friction are given by

$$\frac{d}{dx}(\rho u) = 0 \tag{1.15}$$

$$\frac{d}{dx}\left(p + \rho u^2\right) = 0 \tag{1.16}$$

$$\frac{d}{dx}\left(h + \frac{u^2}{2}\right) = 0 \tag{1.17}$$

where the specific enthalpy, h, in Eq. (1.17) is expressed as

$$h = \frac{\gamma}{\gamma - 1}\frac{p}{\rho} - \lambda q \tag{1.18}$$

In this form, $0 \leq \lambda \leq 1$ represents the reaction progress variable across the induction and reaction zones and q accounts for the heat added by means of chemical energy release per unit mass. At the von Neumann peak, the reaction progress variable is exactly equal to 0, and proceeds to unity at the equilibrium CJ plane in Fig. 1.6. Differentiating Eqs. (1.17) and (1.18) and combining yields

$$\frac{\gamma}{\gamma - 1}\left(\frac{1}{\rho}\frac{dp}{dx} - \frac{p}{\rho^2}\frac{d\rho}{dx}\right) - q\frac{d\lambda}{dx} + u\frac{du}{dx} = 0 \tag{1.19}$$

where dp/dx and $d\rho/dx$ can be replaced with Eqs. (1.15) and (1.16) to yield

$$\frac{1}{u}\frac{du}{dx} = \frac{(\gamma - 1)\, q}{a^2 - u^2}\frac{d\lambda}{dx} \tag{1.20}$$

Lastly, noting that $dx/dt = u$, the governing coupled ordinary differential equations across the induction and reaction zones of the ZND detonation wave structure are

$$\frac{du}{dx} = \frac{(\gamma - 1)\, q}{a^2 - u^2} \frac{d\lambda}{dt} \tag{1.21}$$

$$\frac{d\lambda}{dt} = k\,(1 - \lambda)\, \mathrm{e}^{E_a/RT} \tag{1.22}$$

where Eq. (1.22) is simply a single-step Arrhenius expression connecting the chemical kinetics to the dynamics of the detonation products.

Therefore, given a reactant mixture with a specified thermodynamic state, ρ_1, p_1, and h_1, pre-exponential factor, k, and activation energy, E_a, application of Eqs. (1.21)–(1.22) with the results of the CJ theory permits determination of the ZND wave structure. A typical solution method requires first determining the equilibrium CJ detonation wave solution using the CJ detonation theory discussed in the previous subsection. With knowledge of the detonation wave velocity, W_{CJ}, application of the RH shock jump conditions permits determination of the von Neumann peak, or $\lambda = 0$ state, which act as the initial conditions for the two coupled ordinary differential equations in Eqs. (1.21) and (1.22). Henceforth, starting from the von Neumann peak and numerically integrating these equations across the induction and reaction zones until the sonic solution is obtained yields the resulting detonation wave structure.

Although the above derivation is for a calorically perfect gas with constant γ, realistic reactive systems will feature numerous reaction progress variables representing the various chemical species that are present at the equilibrium CJ state. A detailed derivation of the governing ordinary differential equations across the detonation structure for a general reactive mixture can be found in Lee [2]. Moreover, CJ and ZND detonation solutions to general reactive mixtures can be obtained using a shock and detonation toolbox [29, 30] in conjunction with the computer program Cantera [24] in a Matlab environment. Together, these packages are very useful for rapidly computing the CJ and ZND detonation properties of general reactive mixtures.

For stoichiometric H_2–air initially at 1 atm and 300 K, the path of thermodynamic states for the ZND detonation is shown in Fig. 1.7. As explained above, the initial state proceeds along the shock adiabat until reaching the von Neumann peak. From this point, the subsequent thermodynamic states proceed along the Rayleigh line towards the equilibrium CJ tangency point on the reactive Hugoniot. With the ZND theory, it is now evident that this Rayleigh line path represents the progression of thermodynamic states across the induction and reaction zones of the ZND detonation wave. Hence, the fundamental result of the ZND theory is connecting the chemical kinetics of the reactive mixture with the dynamics of the detonation products along the Rayleigh line to reveal the structure of a steadily propagating one-dimensional detonation wave and associated length and timescales of the reaction zone. Figures 1.8(a)–1.8(c) show the corresponding ZND pressure, temperature, and species mole fraction profiles across the detonation wave structure, respectively. Note, $x_{1/2}$ represents the half-reaction zone length, which is equal to 0.27 mm for the current stoichiometric H_2–air mixture.

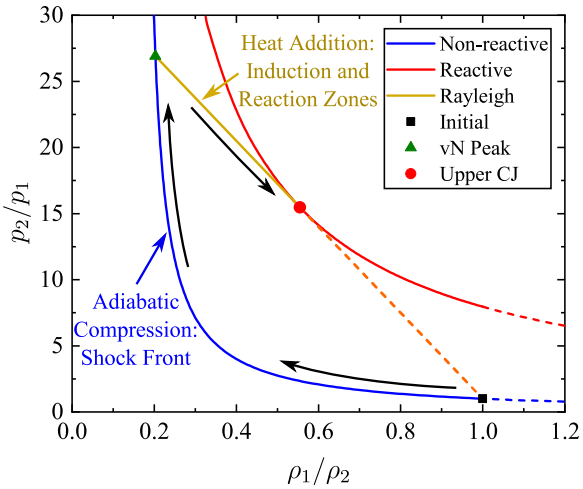

Figure 1.7. ZND detonation wave path along non-reactive Hugoniot, Rayleigh line, and reactive Hugoniot for stoichiometric H_2–air mixture at 1 atm and 300 K.

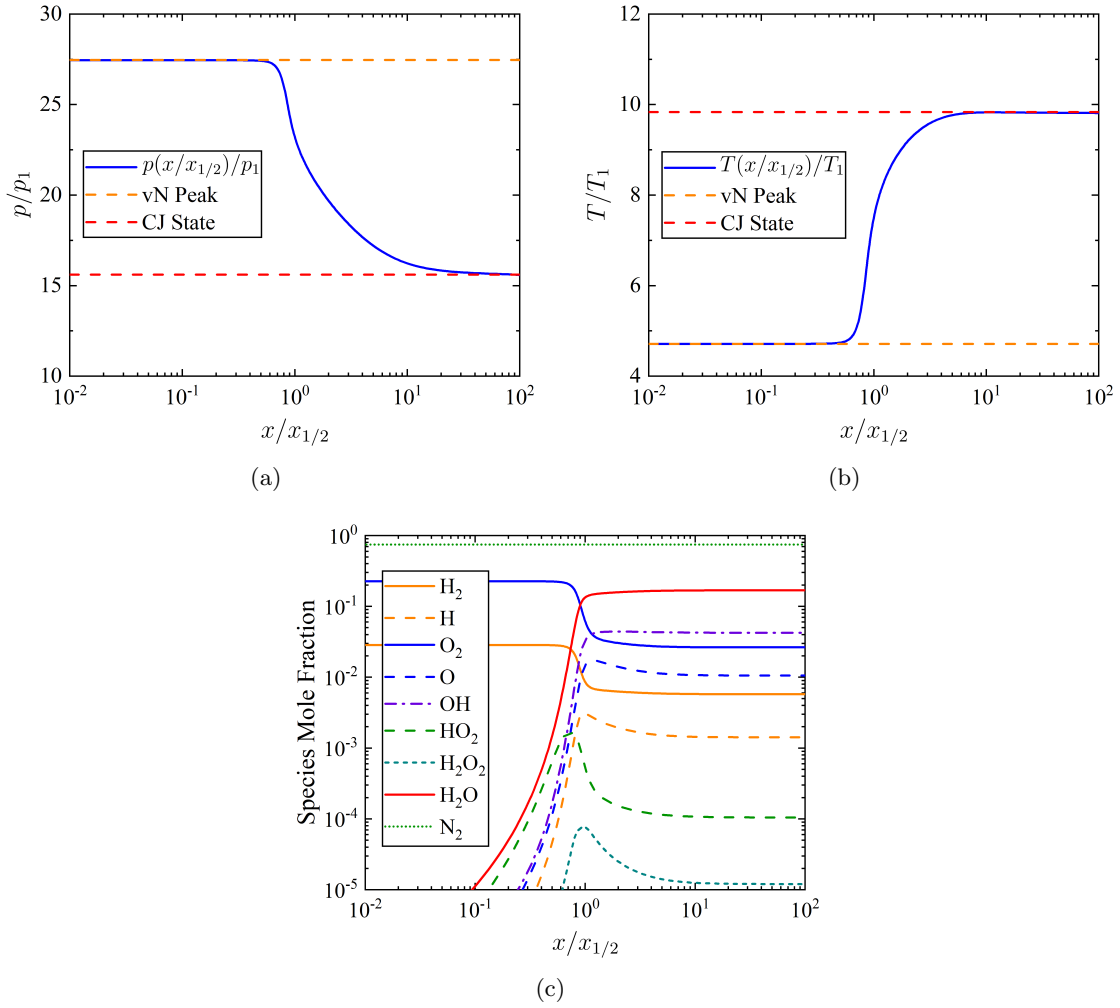

Figure 1.8. (a) Pressure, (b) temperature, and (c) species mole fraction across ZND detonation wave structure for stoichiometric H_2–air mixture at 1 atm and 300 K.

It can be noted that the ZND wave structure is seldom observed in practice because detonation waves are inherently unstable. Additionally, as will be discussed in the next subsection, a detonation wave is composed of an unsteady three-dimensional cellular structure for which a one-dimensional detonation theory is simply unable to capture. However, the ZND theory bridges the gap between the CJ theory and the mechanism by which a detonation wave can ignite and self-propagate through a reactive mixture. Additionally, ZND theory explains the transition path of thermodynamic states from the reactants to products

via adiabatic shock compression followed by heat release in an induction and reaction zone. Lastly, ZND theory provides a method to obtain characteristic length and timescales of the detonation wave structure which are paramount in fundamental detonation wave physics studies [2].

1.1.4 Experimental Observation

Despite the success of the CJ and ZND detonation wave theories, overwhelming experimental evidence has demonstrated that detonation waves are neither one-dimensional nor steady, but three-dimensional and transient [2]. This was demonstrated in the experiments of Soviet researchers Denisov and Troshin [34] in 1960, where the carbon soot-foil technique was used to reveal the multidimensional structure and propagation behavior of a detonation wave. Additionally, in the experiments of the American researcher White [35] in 1961, an interferometer with short-duration electric sparks as the light source was used to visualize a self-sustained detonation wave, revealing the multi-headed shock front structure. From these experiments, it was clear that the detonation front was composed of curved intersecting shocks, where soot-foil traces revealed the transient trajectory of the shock intersection points and pulsating nature of the detonation front. Following these discoveries, an abundance of research has revealed the physical nature of detonation wave using piezoelectric transducers and high-speed schlieren photography and interferometry techniques [2]. Accordingly, the detonation front and the accompanying transient phenomena inherent to its sustained propagation have been strenuously analyzed. The remainder of this section is intended to provide a brief description of the experimentally observed multi-dimensional and transient structure of detonation waves, and the corresponding implications for detonation-based engine design.

The simplest structure of a detonation wave front is depicted in Fig. 1.9, which represents a two-dimensional propagating detonation wave, although the following description can be extended to three-dimensions. The detonation wave features a leading shock front

that is composed of two distinct shock waves, namely, the incident shock and Mach stem, which are convex towards the upstream flow. The incident shock and Mach stem join at triple-shock Mach intersections, or triple points, from which weaker transverse shock waves extend into the burned products downstream of the detonation front. These transverse waves propagate unsteadily across the detonation front and normal to the detonation wave motion. This detonation wave structure is shown in the schlieren images from Lee and Radulescu in Figs. 1.10(a) and 1.10(b) for H_2–O_2–40% Ar detonations at different pressures [36]. Moreover, behind the Mach stems, the pressure and temperature are higher than that behind the incident shock. Consequently, the induction and reaction zones are shorter and more closely coupled to the shock front at the Mach stem locations than those behind the incident shocks. The higher pressure and temperature, and subsequently faster heat release, behind the Mach stems is the mechanism that drives the weaker transverse waves across the incident shock fronts. Moreover, when two transverse waves collide after sweeping across a given incident shock front, the transverse waves reflect, leaving behind another high pressure and temperature region and a newly formed Mach stem. As such, while the detonation wave propagates, the sweeping motion of the transverse waves and triple points trace out the trajectories shown in Fig. 1.9. Behind a triple point, the reactants pass trough either the Mach stem or incident shock, which causes the gases to have a discontinuity in velocity and density giving rise to the formation of a shear layer immediately behind the triple point. It is believed that this region of high shear accompanying the shear layer is the mechanism that traces the triple point trajectories onto carbon soot-foils [37]. The triple point trajectories trace out what is often referred to as detonation cells, which have a characteristic height denoted by λ (not to be confused with the reaction progress variable), and is depicted in Fig. 1.9.

The beginning of a cell marks the collision of two transverse waves and the subsequent formation of a strong Mach stem. The maximum height is associated with the collision and reflection of transverse waves at the outer edge of neighboring cells. At this point, the

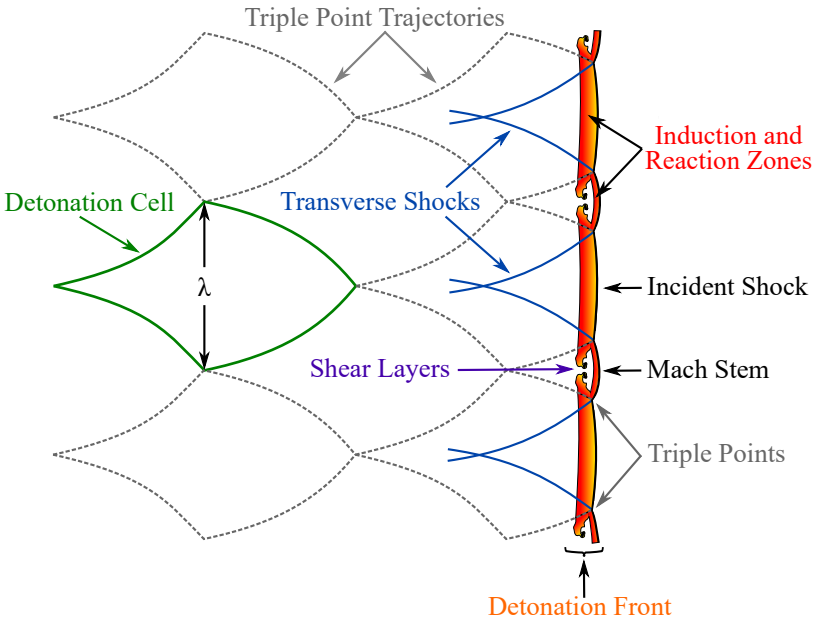

Figure 1.9. Schematic of multi-headed detonation front commonly observed in practice with triple point trajectories and definition of detonation cell (modified from [38]).

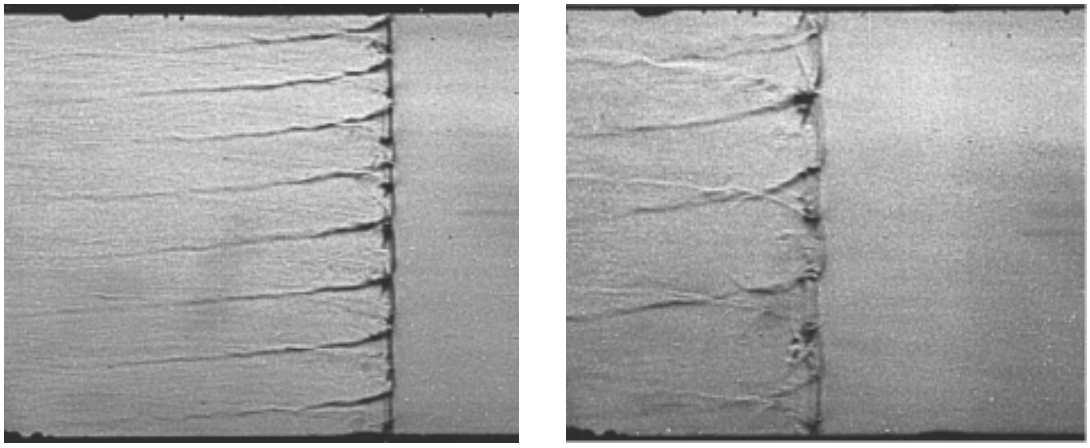

(a) (b)

Figure 1.10. Schlieren photographs in H_2–O_2–40% Ar at initial pressures of (a) 13 and (b) 8 kPa from Lee and Radulescu [36].

Mach stem of the detonation cell becomes an incident shock, until the transverse wave collide again at the end of the cell. This alternating wave pattern across the axial length of detonation cells causes a rapid change in the detonation front propagation velocity. For instance, because the reaction rates behind a Mach stem are much faster due to the elevated

pressure and temperature, the Mach stems travel with a faster velocity then the incident shocks. In fact, the maximum shock front velocity occurs at the beginning of the detonation cell, or collision point of transverse waves. Alternatively, the minimum velocity occurs just at the end of detonation cells, namely immediately before the re-collision of transverse wave and formation of a new Mach stem, which causes the various sections making up the detonation front to propagate in a pulsating manner. Experiments conducted by Strehlow and Crooker [39] using a laser streak schlieren photography method showed that along the axial distance of a detonation cell, the leading shock velocity can vary from roughly 1.6 to 0.7 times that predicted by the CJ theory. In effect, the overall mean propagation velocity of the detonation front is governed by the number density of collisions between triple points, which is a very different viewpoint regarding the nature of detonation propagation than that provided by the ZND theory.

The detonation cell height, or size, λ, has been shown to be a regularity in experimental observations and a fundamental length scale for detonation waves [2]. Fundamentally, the detonation cell size is the maximum distance traced by the triple points, or simply the maximum spacing between the transverse waves behind the detonation. Therefore, the detonation cell size is directly related to the properties of the induction and chemical reaction zones coupled to the Mach stem and incident shock. In fact, Lee [40] showed that the detonation cell size is linearly proportional to the induction zone length predicted by the ZND theory. As such, the detonation cell size is dependent on the initial state of the reactive mixture. Knystautas et al. [41] studied the pressure dependence on the detonation cell size in hydrogen–air and various hydrocarbon–air mixtures and showed that, in general, the cell size decreases with increasing pressure. Note, this is also shown in the schlieren photographs of Figs. 1.10(a) and 1.10(b), in that the transverse wave spacing decreases with increasing initial pressure. Similarly, the temperature dependence on the detonation cell size was investigated in the hydrogen–air experiments of Ciccarelli et al. [42] and hydrocarbon–air experiments of Tieszen et al. [43] and, in general, it was shown that detonation cell size de-

creases with increasing temperature. Therefore, it can be stated that, in general, increasing either the pressure or temperature increases the detonability of a given reactive mixture.

For common hydrogen and hydrocarbon reactive mixtures, the detonation cell size is listed in Table 1.3 for stoichiometric conditions at 1 atm and and 298 K. Note that changing the oxidizer from pure oxygen to air drastically increases the cell size of reactive mixtures. This is primarily attributed to the increased length of the induction zone and longer amount of time to thermally dissociate the reactants into sufficient concentrations of radicals for chemical reactions to take place. Similarly, Fig. 1.11 shows how the detonation cell size varies with equivalence ratio for hydrogen–air and hydrocarbon–air mixtures. In general, the minimum detonation cell size takes place at or near the stoichiometric condition; however, the cell size can vary drastically for reactive mixtures that are either fuel-lean or fuel-rich.

Table 1.3. Detonation cell size in various detonable mixtures at 1 atm and 298 K.

Mixture ($\phi = 1$)	Cell Size (mm)	Ref.
$H_2+\frac{1}{2}O_2$	2.08	Denisov and Troshin [34]
CH_4+2O_2	2.96	Manzhalei et al. [44]
$C_2H_2+\frac{5}{2}O_2$	0.17	Manzhalei et al. [44]
$C_2H_4+3O_2$	0.60	Bauer et al. [45]
$H_2+\frac{1}{2}(O_2+3.76N_2)$	15.10	Guirao et al. [46]
$CH_4+2(O_2+3.76N_2)$	349.53	Beeson et al. [47]
$C_2H_2+\frac{5}{2}(O_2+3.76N_2)$	5.80	Knystautas et al. [48]
$C_2H_4+3(O_2+3.76N_2)$	25.70	Knystautas et al. [48]

From the discussion above, it is evident that the detonation cell size is a fundamental length scale of detonations, which is also directly related to the detonability of a given reactive mixture. In fact, when the dimensions of the geometry containing the detonation, such as the diameter of a tube, approach the size of a single detonation cell, the detonation

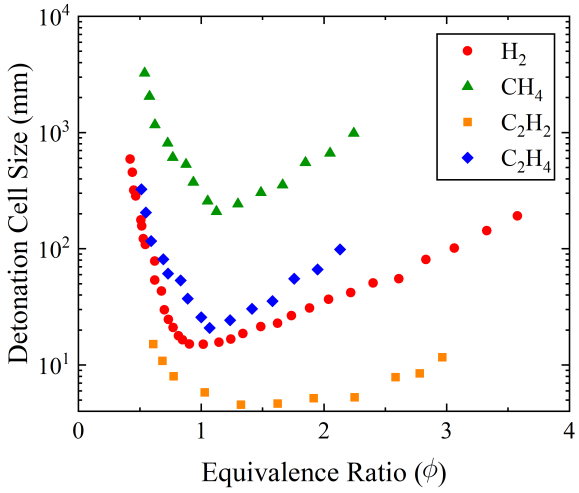

Figure 1.11. Detonation cell size for various fuel–air mixtures at different equivalence ratios at 1 atm and 298 K from [46, 48, 49].

propagation becomes unstable and usually results in the excitation of spinning, galloping, and stuttering instabilities [2]. Therefore, there is a minimum scalability limit for a detonation-based engine in which proper detonation can be adequately achieved. In general, it is preferred to have sufficient spacing in a combustion chamber for the stable propagation of several transverse waves along the detonation front. This ensures the stability of the front and proper detonation of the mixture. Consequently, this is a design consideration that must be addressed for detonation-based engines. For instance, when operating with hydrocarbon detonable mixtures such as methane, the detonation cell size can vary on the order of a meter at standard conditions when moving from a stoichiometric to fuel-lean mixture. As such, a properly designed thrust chamber must be capable of comfortably accommodating the fundamental length scale of a detonation wave.

1.2 Pulse Detonation Engines

1.2.1 Background

The pulse detonation engine (PDE) is a propulsion concept that makes use of intermittent detonations to supply thrust. Unlike existing chemical rocket and airbreathing engines

which operate using constant-pressure deflagrative combustion, the PDE makes use of the pressure-gain mode of combustion, namely, detonation. As discussed earlier in this chapter, detonations are capable of compressing the working fluid to pressures that are roughly an order-of-magnitude higher than that achieved through deflagration. An attractive feature of such pressure-gain combustion in an airbreathing engine design is the potential to reduce, or eliminate altogether, the need for mechanical compression and the associated complexities of intricate turbomachinery [50]. Further, in a pulse detonation rocket engine (PDRE), where the oxidizer is carried onboard, the propellant injection pressures are expected to be much lower than conventional rocket engines, which has the added advantage of eliminating the need for heavy and bulky turbopump machinery that drive propellant feed systems. Moreover, the use of detonation minimizes the entropy gain during the heat addition process of the engine cycle, which enables ideal thermal efficiency advantages over conventional rocket and airbreathing engines [51]. This aspect will be discussed in the following subsection, where a comparison of the thermodynamic cycle for a PDE-based system using the ZND detonation wave for heat addition is compared with the classical Brayton cycle, namely, the cycle used to model the thermal efficiency of conventional airbreathing engines employing isobaric heat addition. Direct consequences of higher thermal efficiency are superior specific impulse and better overall propulsive performance metrics, which are the primary motivation for pursuing PDEs as potentially viable propulsion systems.

The simplest PDE or PDRE configuration consists of a straight, constant-area thrust chamber that is closed at the head end, and open at the other. The head end usually features a number of fuel and oxidizer injection ports and an ignition source capable of providing the required activation energy to achieve a weak deflagration. The PDE operation usually consists of several phases during a single cycle, which typically include propellant fill, ignition, gasdynamic blowdown, and purge. Figure 1.12 shows a schematic of a typical PDE system and the corresponding general operating cycle. Phase 1 of the cycle consists of filling the thrust chamber with a gaseous fuel and oxidizer combination until the chamber

is fully filled with a detonable mixture at the desired mixture equivalence ratio. In phase 2, a weak spark from an ignition source is provided to initiate a deflagration wave at the head end of the chamber. As discussed previously, the deflagration wave will accelerate away from the closed end and abruptly transition into a self-propagating detonation wave, which accounts for the DDT process of phase 3. In phase 4, the detonation wave propagates through the remaining length of the PDE thrust chamber while converting all of the reactants into burned products. Once the detonation wave exits the chamber, a fairly complex gasdynamic blowdown process ensues, which features the interaction of multiple unsteady rarefaction waves that eventually reduces the pressure in the thrust chamber to the ambient condition. This exhausting gasdynamic blowdown phase is taken as phase 5 of the PDE cycle. Lastly, phase 6 consists of purging any remaining burned products at elevated temperatures from the thrust chamber with a colder inert purge gas so that refilling with fresh propellants can begin. Purging with the cold inert gas also ensures that the fresh propellants will not autoignite. Consequently, the PDE is an unsteady thrust producing propulsion system for which practical implementation for aerospace propulsion applications would necessitate that the system operate with a frequency of $\mathcal{O}(10^2)$ Hz [52]. Due to the gasdynamic nature of the PDE flow field, the maximum operating frequency is directly dependent on the length scale of the PDE system, such that scaling up the engine would inversely reduce the maximum operating frequency. In these cases, it is likely that a multi-tube PDE system would be required, such as the concept proposed by Bussing and Pappas [50]. However, even in multi-tube PDE systems, the operating characteristics of any single tube in a multi-tube arrangement would still follow the typical operation cycle shown in Figure 1.12. Before proceeding, it should be noted that the PDE is in fact one of multiple detonation-based engine concepts, and a comprehensive review of other systems such as the rotating detonation engine (RDE) and oblique detonation wave engine (ODWE) can be found in the 2000 review by Kailasanath [53], and the more recent 2013 and 2014 reviews by Wolański [54] and Lu and Braun [55], respectively.

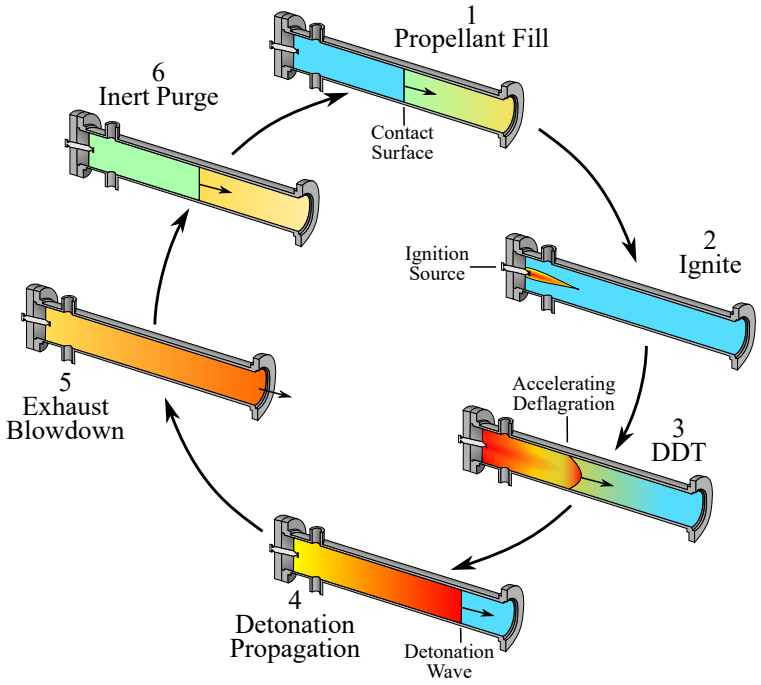

Figure 1.12. General pulse detonation engine operation cycle (modified from [56]).

The remainder of this section is intended to provide a summary of major research efforts directly influencing the development of PDEs. The summary is kept brief as many detailed and comprehensive reviews exist within the literature. For example, a comprehensive review of experimental and theoretical research efforts up to 1992 can be found in the review by Eidelman and Grossmann [57]. Additionally, the developments in PDE research up to 2003 on atomization and mixing, detonation initiation, experimental diagnostic techniques, and system-level and overall performance estimates can be found in the review by Kailasanath [58]. Finally, more recent developments in experimental, numerical, and analytical PDE research efforts can be found in the more recent review by Kailasanath [59].

The earliest experimental investigations of intermittent detonation devices for propulsion applications was carried out in Germany by Hoffman [60] in the late 1930s. In these early efforts, a laboratory-scale demonstrator was developed to investigate the feasibility of detonating various hydrocarbon mixtures in a combustor for potential use in a reaction propulsion system. Both gaseous acetylene and liquid benzene hydrocarbon fuels with oxy-

gen were investigated. The system, although valveless, operated much like that depicted in Fig. 1.12, in that a detonation tube was filled with a detonable mixture, ignited to achieve detonation, and exhausted into the ambient; however, a purge gas was not used. As noted by Bussing and Pappus [50], although performance characteristics were not reported, important operating characteristics such as fuel atomization, evaporation, and mixing were determined to be critical to the success of an intermittent detonation propulsion system.

Nearly two decades later in 1957, the feasibility of reaction devices operating on intermittent detonations was studied by Nicholls et al. [61] in the United States. A simplified analytical model was developed based on the stagnation properties behind the detonation wave to predict the average thrust and impulse of a detonation tube. Further, single-shot experiments using acetylene–oxygen were performed and the impulse was directly measured by suspending the setup in a ballistic pendulum arrangement. The setup consisted of a detonation tube that was open at one end, with fuel and oxidizer injection at the head end. Specific impulses above 1,200 seconds were reported for different acetylene–oxygen mixture ratios, although it is believed that proper detonation was not achieved and the combustion was a combination of deflagration and detonation [50]. Multi-cycle experiments were also performed with hydrogen–air mixtures, although dynamic thrust and impulse measurements were not recorded.

In the early 1960s, Krzycki [62] continued research efforts in the U.S. by conducting significant analytical and experimental investigations of an intermittent detonation device for propulsion applications. The analytical approach was based on the method of characteristics, in which wave diagrams were used to describe the spatial and temporal gasdynamic properties of the PDE flow field during the blowdown phase, and the transient nature of pressure loading on the thrust wall of the tube. Further, a vast experimental study was conducted with an intermittent detonation device similar to that of Nicholls et al. [61], which featured an air manifold, fuel injector, detonation tube, and spark igniter. The system was operated at frequencies from 0–60 Hz with propane–air mixtures, and it was concluded by

Krzycki that such an intermittent detonation system was not promising as a thrust producing mechanism because of the low operating frequency. However, according to Bussing and Pappus [50], the spark igniter did not feature the energy capacity required to directly initiate a detonation wave in propane–air mixtures, and the geometrical constraints of the detonation tube did not likely permit DDT to take place. For instance, the detonation tube used by Krzycki [62] featured a diameter of 25.4 mm, which is smaller than the detonation cell size of roughly 100 mm [63] for propane–air, making proper detonation very unlikely when considering the role detonation cells have on the stability of self-sustaining detonation waves. Hence, the system was in fact operating in a deflagrative pulse jet mode, and many researchers have since disregarded those conclusions.

The conclusions of Krzycki, however, impeded the progress of PDE development, and it was not until the mid 1980s that researchers began to re-examine the potential use of intermittent detonations as a viable propulsion system. In 1986, Helman et al. [64] experimentally investigated a pulsed detonation-based airbreathing engine design at 25 Hz using ethylene–oxygen mixtures. Ethylene and oxygen were injected intermittently and a synchronized spark plug was used to ignite the incoming mixture. Specific impulses were calculated based on the measured pressure history on the thrust wall from piezoelectric pressure transducers and reported to vary between 1,000–1,400 seconds. Although this system was very similar to the previous experimental devices of Hoffman [60], Nicholls et al. [61], and Krzycki [62], this work was the first to help initiate recent interest in PDEs.

Since the work of Helman [64], the PDE has been at the center of modern research efforts focused on practical implementation of a reliable detonation-based engine for aerospace propulsion applications [52]. The simple straight-tube thrust chamber configuration in both the airbreathing and rocket mode has received significant analytical [65–67], one-dimensional [68–76] and two-dimensional numerical [77–86], and single-cycle [87–92] and multi-cycle experimental [93–97] treatment in the literature. Extensive testing and analysis of the fully-filled, straight tube thrust chamber configuration, operating in a single-cycle or

multi-cycle pulsed manner with both hydrogen- and hydrocarbon-based fuels have shown promising results. Notably, the two-dimensional numerical studies of Harris et al. [84] and Ma et al. [85] demonstrated that a hydrogen-fueled airbreathing PDE operating over a Mach number range of 1.2–5 can provide a specific impulse of roughly 4,000–5,000 seconds when operated at frequencies ranging from 60–250 Hz, which is superior to conventional steady-flow ramjets at the same operating conditions. Further, in the two-dimensional numerical study of Ivanov and Frolov [86], a propane-fueled airbreathing PDE operating at Mach 3 and altitudes ranging from 9.3–16 km while operating with a frequency of 48 Hz provides specific impulse of approximately 1,700 seconds, which is superior to a ramjet under the same operating conditions. Unfortunately, experiments have yet to be conducted in direct-connect facilities for airbreathing PDEs operating under similar conditions. However, it is noteworthy to mention the performance results reported in the experimental work of Schauer et al. [95], where a hydrogen–air PDE was operated at frequencies of 12–16 Hz at static sea-level conditions. In those experiments, it was demonstrated that the PDE could achieve specific impulses of roughly 4,000 seconds with a fully-filled thrust chamber. These experimental results were also shown to validate the empirical single-cycle performance model of Wintenberger et al. [66, 67], and the theoretical performance model of Endo et al. [65].

In regard to rocket applications, the quasi-one-dimensional numerical study by Morris [76] showed that constant-area thrust chamber PDREs operating with a gaseous oxy-hydrogen propellant at 1 atm are capable of achieving single-cycle propulsive performance metrics superior to optimized steady-state rocket engines for blowdown pressure ratios of $\psi \lesssim 7$. Further, Kasahara et al. [96] successfully demonstrated a compact multi-cycle PDRE demonstrator, which featured a propellant and purge feed system comprised of three pressurized cylinders for ethylene, oxygen, and helium with solenoid injection valves. This PDRE demonstrator was shown to validate combined analytical thrust models from Endo et al. [65] and Sato et al. [98], and demonstrated that PDREs operating with propellant

injection pressures comparable to ambient pressure are realizable propulsion systems for aerospace applications. Collectively, the research and development efforts mentioned above yield promising results for the eventual implementation of PDEs and PDREs into specialized aerospace propulsion systems. Nonetheless, a number of design issues still remain to be solved, with the most important being efficient expansion of the detonation products during the transient blowdown phase of the cycle. This aspect will be elaborated on in the following subsections from the context of the PDE thermodynamic cycle and the importance of a high expansion efficiency, and the implementation of the partial filling technique and the use of a diverging nozzle to enhance performance metrics.

1.2.2 Thermodynamic Cycle

An idealized thermodynamic cycle analysis can be used to demonstrate the potential efficiency and performance advantages of detonation-based engines compared to their deflagration-based counterparts. In general, alongside providing adequate propulsive performance, the objective of a given propulsion system is to minimize the entropy rise of the working fluid. This ensures the system's actual thermodynamic cycle is closer to that of a reversible process, in which no heat is wasted and the maximum work output is achieved. Therefore, it is of interest to highlight the ideal thermodynamic advantages enabled by simply utilizing the pressure-gain detonative mode of combustion. Note, this brief analysis will also serve as a fundamental motivation for pursuing detonation-based engines in aerospace propulsion applications. For this comparison, an idealized thermodynamic cycle for an airbreathing PDE is compared with the ideal Brayton cycle. Such a comparison was made in the analysis by Heiser and Pratt [51] for a single-γ model, which was later extended to a two-γ model by Wu et al. [75]. The subsequent analysis closely follows that developed by Wu et al. [75], in which real thermophysical properties were used to compare the thermal efficiency of an airbreathing PDE with a conventional airbreathing engine operating on the Brayton cycle.

For the purposes of establishing state nomenclature, the schematics in Figs. 1.13(a) and 1.13(b) for an airbreathing ramjet and a PDE are used. Moreover, the forthcoming discussion regarding the ideal Brayton and PDE cycles are not constrained to these respective engine types. These are used merely as an aid to associate a given thermodynamic state to a location within a deflagration- or detonation-based airbreathing engine. In both the ideal Brayton and PDE cycles, the working fluid is subjected to four primary thermodynamic processes, namely, compression, heat addition, expansion, and heat rejection. In the case of the ideal Brayton cycle, the free stream, state 0, is assumed to be isentropically compressed to state 3, namely, the combustor entry state. In general, this compression can be achieved in numerous ways, such as ram compression, or a combination of ram and mechanical compression, much like that achieved in a turbojet. Once the free stream air enters the combustor, fuel is injected and the mixture passes through flame holders, effectively deflagrating the reactants which thereby releases heat. This deflagrative heat addition process is assumed to take place at constant pressure, which significantly raises the temperature and entropy of the working fluid to state 4 at the combustor exit. Subsequently, the burned products are assumed to expand isentropically to state 10 at the exit plane of the nozzle. In the ideal case, it is assumed that the gas pressure on the nozzle exit plane matches the free stream pressure, namely, $p_{10} = p_0$, whereby a fictitious constant-pressure heat rejection to the ambient is assumed to take place in order to close the cycle.

In the case of the ideal PDE cycle, the free stream, state 0, is assumed to be isentropically compressed to state 3, namely, the combustor entry state. This compression can be achieved in numerous ways, such as ram compression, or a combination of ram and mechanical compression. Within the combustor, the heat addition process is modeled by that described in the ZND detonation theory. As in Fig. 1.5, the detonation wave structure consists of a leading shock front, and coupled induction and chemical reaction zones, which together steadily moves through the reactants at the CJ detonation wave velocity for a given reactive mixture. Consequently, the reactants are adiabatically compressed further

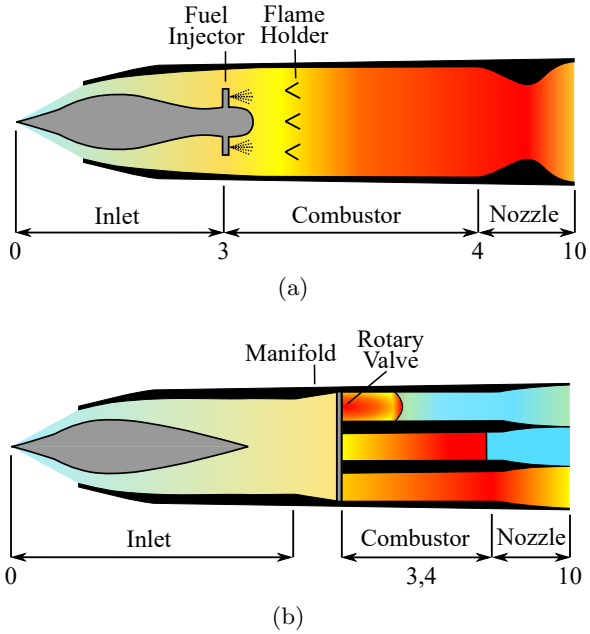

Figure 1.13. (a) Ramjet schematic and (b) airbreathing PDE schematic with state nomenclature.

through the shock front to the von Neumann peak, which will be denoted by state 3′. Additionally, the heat addition takes place within the reaction zone following the induction zone immediately behind the shock front, raising the temperature and entropy of the working fluid to state 4 within the combustor. Unlike the constant-pressure heat addition of the Brayton cycle, heat addition progresses with decreasing pressure along the Rayleigh line as shown in Fig. 1.7. Additionally, the heat addition increases the Mach number of the reaction products to a choking condition, which coincides with the equilibrium CJ state at the upper CJ point on the reactive Hugoniot. Following the heat addition, the burned products are assumed to expand isentropically to state 10 at the exit plane of the nozzle. In the ideal case, it is assumed that the gas pressure on the nozzle exit plane matches the free stream pressure, namely, $p_{10} = p_0$, and a fictitious constant-pressure heat rejection to the ambient takes place that closes the cycle. Note, the ideal expansion in this case assumes that each element of fluid within the PDE combustor is able to expand to the free stream

pressure, which does not actually take place in real PDE systems with a fixed geometry nozzle. This aspect will be elaborated on in the following discussion.

Figure 1.14(a) shows a comparison of the T–s diagrams for the respective cycles for a stoichiometric H_2–air fuel mixture initially at 1 atm and 300 K. In this diagram, the heat addition processes where computed using the chemical kinetics and equilibrium program Cantera [24]. Additionally, the ZND detonation heat addition was obtained by using a shock and detonation toolbox [29, 30] in conjunction with Cantera. Note that both cycles have a compression static temperature ratio of $\psi = 3$ in this comparison. Additionally, the solid black line is the previously discussed reactive Hugoniot curve, now shown in T–s space. As such, the heat addition for the PDE cycle terminates at the upper CJ point, which coincides with the minimum entropy point on the reactive Hugoniot. On the other hand, the heat addition for the Brayton cycle terminates at the CPC point, which coincides with the weakest possible deflagration solution. Consequently, the entropy gained during the heat addition process for both cycles is drastically different. In the case of the Brayton cycle, all of the entropy generated from states 3–4 is the result of constant-pressure heat addition. Alternatively, only the entropy generated through the reaction zone along the Rayleigh line from 3′–4 constitutes heat addition in the PDE cycle. In fact, all of the entropy generated from 3–3′ is generated irreversibly as a result of the adiabatic shock compression through the detonation wave. Subsequently, to close the cycle, all of the entropy generated during the cycle from states 0–10, whether it be by reversible or irreversible processes, must be rejected to the ambient. Hence, it becomes desirable to minimize the amount of irreversible entropy generated during a cycle since this component of entropy generation eventually becomes rejected waste heat, and reduces the amount of work one can output from the cycle.

Given the T–s diagram for the idealized PDE and Brayton cycles, it is of interest to evaluate and compare their respective thermal efficiencies. The thermal efficiency for a general heat engine is simply the ratio of work output to heat addition. Further, for a closed

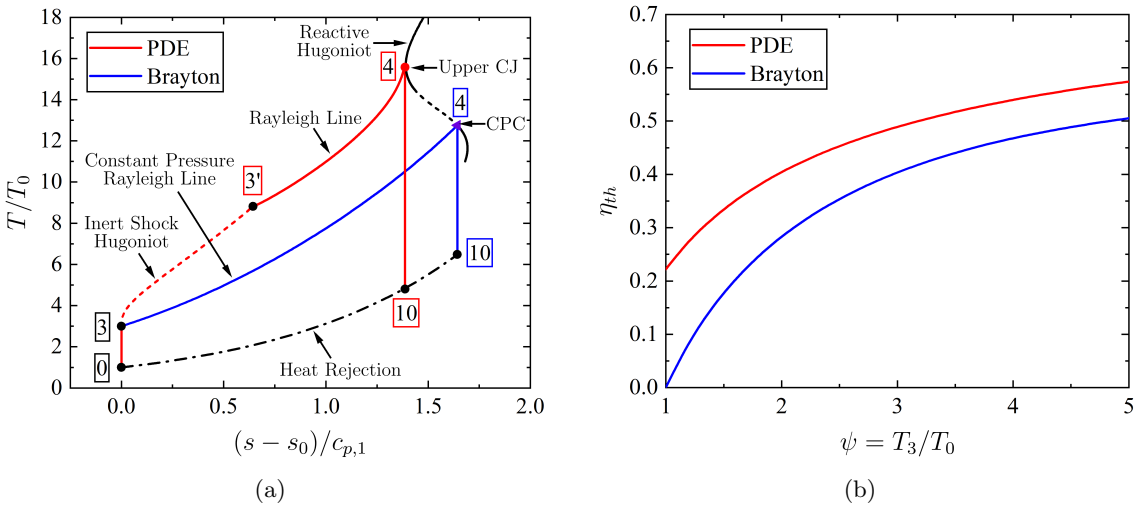

(a) (b)

Figure 1.14. (a) T–s diagram of Brayton and PDE cycles for stoichiometric H_2–air mixture at $p_0 = 1$ atm and $T_0 = 300$ K with $\psi = T_3/T_0 = 3$, and (b) comparison of thermal efficiency for various $\psi = T_3/T_0$.

cycle, the change in energy for the system becomes zero and the net work can be expressed as the difference in heat added and heat rejected. Consequently, for a heat engine with a closed cycle, the thermal efficiency becomes

$$\eta_{th} = \frac{w_{net}}{q_{add}} = \frac{q_{add} - q_{rej}}{q_{add}} = 1 - \frac{q_{rej}}{q_{add}} \tag{1.23}$$

The heat added in both cases is simply $q_{add} = f h_{pr}$, where f is the fuel–air ratio and h_{pr} is the heat of reaction, respectively. Moreover, since the heat rejection is assumed to be a quasi-static process at constant pressure, the heat rejection to the ambient can be expressed as

$$q_{rej} = \int_{10}^{0} T \, ds \tag{1.24}$$

Moreover, substitution of the combined first and second laws reduces Eq. (1.24) to

$$q_{rej} = \int_{10}^{0} dh = h_{10} - h_0 = c_{p,2} T_{10} - c_{p,1} T_0 \tag{1.25}$$

since the process is isobaric. In this expression, the subscripts 1 and 2 correspond to the reactant and product states following the heat addition. As such, the goal of the cycle

analysis becomes expressing the heat rejection in terms of the isentropic compression from 0–3, heat addition from 3–4, and isentropic compression from 4–10. Therefore, rearranging Eq. (1.25) as

$$q_{rej} = c_{p,1}T_0\left(\frac{c_{p,2}T_{10}}{c_{p,1}T_0} - 1\right) \tag{1.26}$$

In this form, the thermal efficiency in Eq. (1.23) becomes

$$\eta_{th} = 1 - \frac{\dfrac{c_{p,2}T_{10}}{c_{p,1}T_0} - 1}{\bar{q}} \tag{1.27}$$

where $\bar{q} = q_{add}/c_{p,1}T_0$. Expressions for T_{10}/T_0 have been derived in Appendix A for the PDE and Brayton cycles. As such, these expressions are given as:

$$\left.\frac{T_{10}}{T_0}\right|_{PDE} = \frac{R_1\gamma_1}{R_2\gamma_2 M_{CJ}^2}\left(\frac{\gamma_1 M_{CJ}^2 + 1}{\gamma_2 + 1}\right)^{\frac{\gamma_2+1}{\gamma_2}} \psi^{1-\frac{\gamma_1(\gamma_2-1)}{\gamma_2(\gamma_1-1)}} \tag{1.28}$$

$$\left.\frac{T_{10}}{T_0}\right|_{Brayton} = \frac{c_{p,1}}{c_{p,2}}\left(\frac{\bar{q}}{\psi} + 1\right)\psi^{1-\frac{\gamma_1(\gamma_2-1)}{\gamma_2(\gamma_1-1)}} \tag{1.29}$$

Substituting these expressions into Eq. (1.27) yields the resulting thermal efficiencies.

$$\eta_{th,PDE} = 1 - \frac{\dfrac{\gamma_1 - 1}{\gamma_2 - 1}\left(\dfrac{\gamma_2}{\gamma_1 M_{CJ}}\right)^2\left(\dfrac{\gamma_1 M_{CJ}^2 + 1}{\gamma_2 + 1}\right)^{(\gamma_2+1)/\gamma_2}\psi^{1-\frac{\gamma_1(\gamma_2-1)}{\gamma_2(\gamma_1-1)}} - 1}{\bar{q}} \tag{1.30}$$

$$\eta_{th,Brayton} = 1 - \frac{\left(\dfrac{\bar{q}}{\psi} + 1\right)\psi^{1-\frac{\gamma_1(\gamma_2-1)}{\gamma_2(\gamma_1-1)}} - 1}{\bar{q}} \tag{1.31}$$

Figure 1.14(b) shows a comparison of the thermal efficiencies for the PDE and Brayton cycles in Eqs. 1.30 and 1.31, respectively. For this comparison, the free stream initial conditions are 1 atm and 300 K. In Eqs. 1.30 and 1.31, $\bar{q}$ and γ_2 were obtained with Cantera by computing the equilibrium heat of reaction between states 3–4 for both cycles. Further, the shock and detonation toolbox was used to evaluate M_{CJ} for a given reactive mixture. It is noted that the thermal efficiency of the PDE cycle outperforms that of the Brayton cycle for the compression static temperature ratios shown. This suggests that the PDE cycle is able to more efficiently convert the heat added by means of detonative combustion

into useful work than the conventional Brayton cycle. Further, it is emphasized that this efficiency estimate also includes the work lost due to the irreversible adiabatic compression from states 3–3′ as this irreversible entropy gain becomes rejected heat. Additionally, unlike the Brayton cycle, the pressure-gain combustion used in the PDE cycle permits the cycle to operate without the need for inlet or mechanical compression. This is an attractive feature that can potentially be exploited in an airbreathing engine designs to reduce, or eliminate altogether, the need for mechanical compression and the associated complexities of intricate turbomachinery. Hence, these results serve as a primary motivation for researching design aspects of a detonation-based engine for potential use in aerospace propulsion applications.

Recall that the above idealized cycle analysis assumes that every fluid element in the PDE thrust chamber perfectly expands from state 4 to state 10, whereby the exit plane pressure is equal to the ambient, namely, $p_{10} = p_0$. For a general PDE operation, this is a mostly unrealistic assumption given the variation in pressure on the exit plane of the PDE. For instance, in a PDE comprised of a constant-area thrust chamber without a nozzle, the pressure can vary on the exit plane from roughly the ambient condition to as high as the post-detonation pressure within a single cycle of operation [76]. Moreover, because the pressure profile on the exit plane is transient, each fluid element passing across the exit plane at a given instant in time is expanding to a different state 10 with a unique kinetic energy. By extension, it is reasonable to assume that the pressure profile on the exit plane of a nozzle will also have a considerable variation during a single cycle of operation. This is expected to remain true for even optimum nozzles at a given operation condition, as any fixed geometry nozzle will not be able to expand all fluid elements passing from the nozzle throat to the same state 10. Therefore, it is of interest to investigate how sensitive the PDE cycle is to an adiabatic expansion efficiency, whereby the nozzle does not achieve the maximum kinetic energy of the exhausting products.

If the expansion efficiency is defined as the ratio of real change in static enthalpy to that of a ideal change for the same static pressure change, then the expansion efficiency can be written as [99]

$$\eta_e = \frac{h_4 - h_{10}}{h_4 - h_{10,i}} = \frac{c_{p,2}T_4 - c_{p,2}T_{10}}{c_{p,2}T_4 - c_{p,2}T_{10,i}} = \frac{T_4 - T_{10}}{T_4 - T_{10,i}} \tag{1.32}$$

where the subscript 10 is now the actual exit plane state and $10, i$ is the ideal state. Rearranging Eq. (1.32) for T_{10} yields

$$T_{10} = (1 - \eta_e)\, T_4 + \eta_e T_{10,i} \tag{1.33}$$

Next, substituting Eq. (1.33) into Eq. (1.27) yields the thermal efficiency for the real cycle as

$$\bar{\eta}_{th} = 1 - \frac{\dfrac{c_{p,2}}{c_{p,1}}\left[(1 - \eta_e)\,\dfrac{T_4}{T_0} + \eta_e \dfrac{T_{10,i}}{T_0}\right] - 1}{\bar{q}} \tag{1.34}$$

or equivalently,

$$\bar{\eta}_{th} = 1 - (1 - \eta_e)\,\frac{\dfrac{c_{p,2}}{c_{p,1}}\dfrac{T_4}{T_3}\psi - 1}{\bar{q}} - \eta_e\,(1 - \eta_{th}) \tag{1.35}$$

Substituting T_4/T_3 for the PDE and Brayton cycles (Eqs. (A.7) and (A.11)) yields the thermal efficiencies for the real cycles

$$\bar{\eta}_{th,PDE} = 1 - (1 - \eta_e)\,\frac{\dfrac{\gamma_1 - 1}{\gamma_2 - 1}\left(\dfrac{\gamma_2}{\gamma_1 M_{CJ}}\right)^2 \left(\dfrac{\gamma_1 M_{CJ}^2 + 1}{\gamma_2 + 1}\right)^{(\gamma_2+1)/\gamma_2} \psi - 1}{\bar{q}} - \eta_e\,(1 - \eta_{th,PDE}) \tag{1.36}$$

$$\bar{\eta}_{th,Brayton} = 1 - (1 - \eta_e)\,\frac{\left(\dfrac{\bar{q}}{\psi} + 1\right)\psi - 1}{\bar{q}} - \eta_e\,(1 - \eta_{th,Brayton}) \tag{1.37}$$

For brevity, these real thermal efficiency expressions are simplified in terms of their ideal thermal efficiencies.

Figures 1.15(a) and 1.15(b) show a comparison of the real thermal efficiency of the PDE and Brayton cycles as a function of the expansion efficiency for $\psi = 2$ and 4, respectively. Note that the real PDE thermal efficiency is more sensitive to the expansion efficiency

compared to the Brayton cycle. Consequently, for $\eta_e < 0.67$ while $\psi = 2$, and $\eta_e < 0.73$ while $\psi = 4$, the Brayton cycle outperforms the PDE cycle, respectively. Moreover, for continuous steady flow propulsion systems operating on the Brayton cycle, realistic expansion efficiencies of approximately 0.9, or better, are to be expected [99, 100]. Therefore, for the PDE cycle to remain competitive against the Brayton cycle, it is likely that any design aimed at efficiently expanding the burned products of a PDE cycle, should operate with a nominal expansion efficiency of at least roughly 0.8.

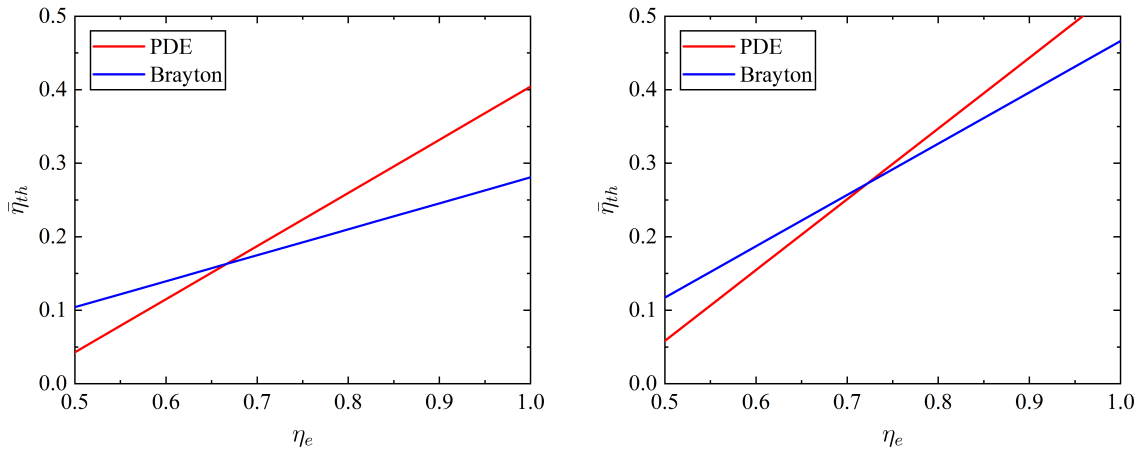

Figure 1.15. Effects of expansion efficiency η_e on cycle thermal efficiency $\bar{\eta}_{th}$ for for stoichiometric H_2–air mixture initially at $p_0 = 1$ atm and $T_0 = 300$ K with (a) $T_3/T_0 = 2$ (b) $T_3/T_0 = 4$.

In summary, thermodynamic cycle analysis can be used to demonstrate the potential advantages of using detonative combustion in propulsion system compared to their deflagrative combustion counterparts. In this case, a comparison of the idealized PDE and Brayton cycles show that the PDE cycle features a better thermal efficiency for most operating conditions. However, this advantage in thermal efficiency is predicated on the assumption that a PDE nozzle system can expand each fluid element of the burned products to the ambient condition, thereby maximizing the kinetic energy of the burned products. In practice, this

does not usually occur and there is a significant pressure variation on the exit plane of the engine, or nozzle. As a result, the analysis was extended to demonstrate the sensitivity of the PDE cycle to an adiabatic expansion efficiency. It was shown that the real thermal efficiency of the PDE cycle is more sensitive to the expansion efficiency than the Brayton cycle. Additionally, unless the PDE can maintain a reasonably high expansion efficiency compared to an engine operating on the Brayton cycle, then the performance advantages become fairly minimal. Thus, it is crucial that a rigorous analysis of potential nozzle devices for PDE propulsion systems be conducted to obtain a better understanding of the primary gasdynamic processes that govern the nozzle and overall engine performance. The following subsections discuss the advantages of partially filling the engine thrust chamber and the use of diverging nozzles.

1.2.3 Method of Partial Filling

When operating a PDE in the fully-filled mode, such that the detonable mixture fills the entire thrust chamber length, a significant propulsive performance loss arises. This is because, in this mode of operation, the detonation wave travels the full length of the thrust chamber before transmitting as a non-reactive decaying shock wave into the ambient. Consequently, as the detonation wave exits the PDE, a considerable portion of the available energy in the form of high-pressure burned products exits along with the detonation wave without performing useful propulsive work. Additionally, because a fully-filled, constant-area thrust chamber does not feature a device that efficiently converts the enthalpy of the burned products into kinetic energy, elevated exhausting pressures are observed at the exit plane of the PDE. As a result, this particular loss restricts the ideal maximum propulsive performance of fully-filled PDEs to propellant-based specific impulses of only 100–200 seconds at sea level static conditions, for both hydrogen- and hydrocarbon-based fuels [65, 66, 70]. The above observations have led researchers to explore further methods of

improving and optimizing the performance of the PDE in order to more efficiently capture the available energy of the exhausting burned products.

One of the commonly studied methods for enhancing the specific impulse includes partially filling the PDE thrust chamber volume with a detonable propellant mixture. In this mode of operation, as shown in the schematic of Fig. 1.16, only a fraction of the thrust chamber at the head is filled with a detonable propellant and the remaining portion of the chamber is filled with a non-combustible inert mixture. The additional chamber length that is not filled with the detonable propellant is sometimes thought of as behaving like a straight-extension nozzle; however, unlike conventional nozzles, the straight-extension section does not effectively convert enthalpy into kinetic energy, but simply prolongs the gasdynamic blowdown process of the engine due to the inertia of the non-combustible gas. In general, the presence of the non-combustible gas downstream of the detonable propellant provides a buffer between the burned detonation products and ambient condition, which allows the burned products to further expand before reaching the engine exit plane. Similarly, the inert gas provides a mechanism for which the burned products are impeded before exhausting from the PDE, which can lengthen the duration of transient impulse generation for the PDE cycle. Further, because less propellant is used in an individual cycle, the partial-filling method can be used to significantly raise the PDE specific impulse, although usually with a corresponding reduction in the total impulse and time-averaged thrust. Many previous experimental, numerical, and analytical studies have focused on various aspects of the performance benefits of partial filling, including the effect of propellant fill length-to-overall thrust chamber length, $\alpha = L_f/L$, namely, the propellant fill fraction, and the role of the inert gas. As a result, much progress has been made towards quantifying the performance gains associated with partial filling although only limited progress has been made in regard to the understanding of physical gasdynamic processes within the thrust chamber flow field that directly govern these observed performance gains. Therefore, the following paragraphs are intended to provide a brief summary of the important findings from

these various works and highlight fundamental performance characteristics that remain to be understood.

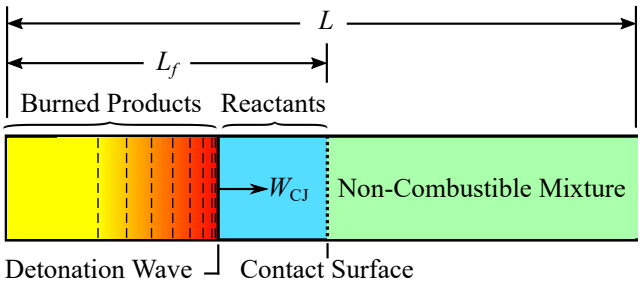

Figure 1.16. Schematic of partially-filled PDE operation.

In recent years, several experimental studies have investigated the performance benefits of partially-filled PDEs by conducting idealized single-shot detonation tube studies, and by performing more practical multi-cycle PDE studies. In single-shot studies, the detonable and non-combustible inert mixtures are usually separated by a thin diaphragm, as in [87, 89, 101, 102], which aids to create the most ideal distribution of detonable and non-combustible mixtures at a desired fill fraction. Similarly, the fill fraction is controlled by the diaphragm placement, which is usually varied by using segmented detonation tube sections, or by coupling straight tube extensions to the end of a fixed-length detonation tube. Alternatively, in multi-cycle PDE studies, the thrust chamber fill fraction is usually varied by precision timing of fuel injection valves, as in [95,97,103], and the non-combustible mixture normally consists of the purge gas from the previous cycle, or the ambient condition. Moreover, the impulse of the PDE is frequently obtained by integrated pressure histories on thrust surfaces [89], or by using ballistic pendulums [87,101,102], as in the case of the single shot studies, or by means of dynamic thrust measurements with dynamic load cells [95, 97, 103], as in the case of multi-cycle PDE studies.

Early experimental studies primarily focused on the performance scaling effects of varying the propellant fill fraction by means of single-shot experiments. Notably, in the

single-shot study of Zhdan et al. [87], it was demonstrated that the specific impulse of a partially-filled detonation tube could be increased by a factor of approximately 2 by reducing the propellant fill fraction from 1 to 0.14, while operating with stoichiometric acetylene–oxygen detonable mixtures and air as the inert gas. These performance gains were later confirmed in the single-shot studies of Daniau et al. [104] which showed that the specific impulse could be increased by a factor of roughly 2.5 by reducing the propellant fill fraction from 1 to 0.15, while operating with stoichiometric ethylene–oxygen detonable mixtures and air as the inert gas. Similarly, Kasahara et al. [101] demonstrated through single-shot experiments that the specific impulse of a detonation tube could be increased by a factor of approximately 1.8 by reducing the fill fraction from 1 to 0.44, while operating with stoichiometric hydrogen–oxygen detonable mixtures and air as the inert gas. More important, these experiments showed that at a first-order approximation, the ratio of specific impulse for the partially- to fully-filled tube appears to be inversely proportional to the fill fraction, namely, $I_{sp}/I_{sp,full} \propto 1/\alpha$, where α is the tube fill fraction. Therefore, it follows that a reduction in the tube fill fraction results in an observed increase in the single-shot specific impulse.

Following the single-shot experimental findings of [87, 101, 104], it became of immediate interest to determine whether or not the single-shot partial filling performance of detonation tubes was realizable in more practical multi-cycle PDE operations, where the fuel distribution is less ideal and the fill fraction is controlled by precision timing of injection valves. Notably, Schauer et al. [95] successfully demonstrated the performance benefits of partially-filled PDEs using a damped thrust stand facility, and a PDE operating at 12 and 16 Hz. In those experiments, the specific impulse of the PDE was increased by a factor of roughly 1.9 by reducing the fill fraction from 1 to 0.3, while operating with stoichiometric hydrogen–air detonable mixtures and purge air as the inert gas. Likewise, Joshi and Lu [97] demonstrated similar results using dynamic thrust measurements and a PDE operating at 1–20 Hz. However, in those experiments, the PDE was operated with sto-

ichiometric hydrogen–oxygen detonable mixtures and purge air as the inert gas, and the specific impulse was raised by a factor of approximately 1.7 by reducing the fill fraction from 1 to 0.58. Additionally, Kasahara et al. [103] demonstrated similar results with a multi-cycle PDE setup using a spring-damper mechanism while operating between 2.5–8.3 Hz with ethylene–oxygen mixtures at fill fractions of 0.13–0.26. In those experiments, it was also shown that for fill fractions less than 0.13, the combined effects of diffusion across the fuel-purge interface and shortened DDT distance results in improper detonation that ultimately reduces the performance benefit of partial filling. Lastly, it is worth noting that comparable results were also reported in the liquid fueled multi-cycle PDE facilities of Li et al. [105] and Wang et al. [106], where kerosene–oxygen with nitrogen purge, and gasoline–air (oxygen enriched) with no purge, were operated at 5–50 Hz and 10–110 Hz, respectively.

Among the various multi-cycle experiments mentioned above, it was demonstrated that the performance benefits observed in single-shot detonation tube facilities are also realizable in the more practical multi-cycle PDE facilities. However, most important, these experiments showed that the multi-cycle partial filling performance scales in the same manner as that observed in the single-shot partial filling studies. This indicates that the governing gasdynamic processes associated with the partial filling method can readily be studied by simply analyzing the single-cycle thrust chamber flow field of a PDE. Hence, recent analytical and numerical studies have investigated the single-cycle gasdynamic flow field characteristics and performance aspects of partially-filled PDEs.

Using an inviscid two-dimensional numerical model with a coupled two-step induction-parameter finite-rate chemistry model, Li and Kailasanath [107] investigated the single-cycle performance of partially-filled PDEs operating with stoichiometric ethylene–oxygen detonable mixtures with air as the inert gas. It was shown that the thrust production is primarily dominated by the dynamics of three distinct wave types, namely, the detonation, transmitted shock, and interface and exhausting rarefaction waves. Additionally, they showed how each wave type influences the pressure history on the thrust wall, which ultimately governs

the thrust profile and impulse in a single cycle. In a similar study by Sato et al. [98], an inviscid one- and two-dimensional axisymmetric numerical model with a coupled multi-step finite-rate chemistry model was used to investigate the single-cycle performance of partially-filled PDEs. In that study, in order to investigate the effects of the inert gas, PDEs operating with hydrogen and hydrocarbon-based detonable mixtures were investigated, and the inert gas was varied between air, argon, and helium. It was shown that the detonable and inert gas acoustic impedances appear to govern the resulting gasdynamic flow field following the collision of the detonation wave with the contact surface separating the respective mixtures. More specifically, it was shown that either a reflected shock or rarefaction wave can result from the interface collision, depending on the ratio of acoustic impedance across the gaseous interface. This was shown to yield a considerably different starting thrust chamber flow field, which in turn alters the pressure history on the thrust wall and the associated partial-filling performance gains. Consequently, the specific impulse gains over a fully-filled PDE are significantly more with a light–heavy detonable–inert mixture combination, such as oxyhydrogen–argon, than those obtained using a heavy–light detonable–inert mixture combination, such as oxyhydrogen–helium. Morris [76] obtained similar results while investigating the single-cycle performance benefits of straight-extension nozzles on PDEs using an inviscid quasi-one-dimensional numerical model with a coupled multi-step finite-rate chemistry model. In that study, the PDE was operated with a stoichiometric oxyhydrogen detonable mixture, and the inert was varied between hydrogen, helium, and nitrogen. Similar to the findings of Sato et al. [98], it was determined that a heavier inert gas could yield a significantly larger specific impulse compared to that of a fully-filled PDE; however, this performance gain was shown to become drastically diminished as the blowdown pressure ratio of the system increases, namely, when the pressure of the inert gas and ambient are reduced.

Due to the performance benefits of partial filling, there have been various efforts at modeling the performance characteristics of partially-filled PDEs. As a first-order estimate,

Li and Kailasanath [107] used their stoichiometric ethylene–oxygen numerical results to establish a correlation for fuel-based $I_{sp}/I_{sp,full}$ as a function of $1/\alpha = L/L_f$, namely, the inverse fill fraction. Similarly, Cooper and Shepherd [108] used the experimental results of [87,89,90,109] and numerical results of [107] to develop empirical piecewise correlations for the total impulse ratio $I_t/I_{t,full}$ and specific impulse ratio $I_{sp}/I_{sp,full}$ as functions of the fill fraction α. It was shown that the partially-filled impulse appears to scale as $I_t/I_{t,full} \propto \alpha$, whereas the partially-filled specific impulse scales as $I_{sp}/I_{sp,full} \propto 1/\alpha$ for $\alpha > 0.0676$. Cooper [110] later extended the Gurney energetics-based explosives model [111] in order to predict the total impulse and specific impulse of a partially-filled PDE operating with general detonable and inert mixtures. This model showed that the mass fraction of detonable-to-total mass (detonable plus inert) is a unique governing parameter that accurately scales the partially-filled PDE specific impulse. The model was shown to have good agreement with existing numerical and experimental results; however, the model is only appropriate for mass fractions greater than roughly 0.15, and fails in the limit where the fill and mass fractions approach zero. Further, Sato et al. [98] derived a scaling law in terms of the detonable-to-total mass fraction for the specific impulse ratio $I_{sp}/I_{sp,full}$, based on the assumption that the thermal efficiency of the partially-filled PDE is approximately equal to that of the fully-filled PDE. This model was shown to successfully collapse the results of [101,107] using general detonable and inert combinations for mass fractions above roughly 0.05.

In principle, the model of Sato et al. [98] is also based on energetics, and suffers from the same defect as that proposed by Cooper [110] in the limit of zero mass fraction. In order to approximate the specific impulse ratio in the limit of zero fill fraction, Cooper [110] proposed a separate model that considered the isentropic expansion of burned products, bounded by the thrust wall and contact surface, to estimate the impulse on the thrust wall. This model, was shown to have good agreement with the numerical results of Li and Kailasanath [107] in the limit of small fill fraction. However, it should be noted that [107] used a rather non-ideal detonation initiation scheme in their study, which is known to

largely influence the performance results at lower fill fractions. Lastly, the analytical work of Endo et al. [112] provided a way of estimating the performance of a partially-filled PDE by transforming the partially-filled PDE to an equivalent, homogeneous diluted, fully-filled PDE. Their model is based on the hypothesis that performance parameters of the PDE thrust chamber are predominantly governed by only the amount of energy and mass content in the chamber. Good agreement was obtained with the data of [95, 98, 107]; however, only for larger values of initial mole fraction of the detonable gas, or larger fill fractions. Moreover, despite being an energetics-based model, a finite value of specific impulse is predicted in the limit of zero fill fraction, which is approximately double that predicted using the expanding bubble model of Cooper [110].

As discussed above, much progress has been made towards the understanding of performance gains that accompany the partial filling method for PDEs. Notably, the work of Li and Kailasanath [107] and Sato et al. [98] provided fundamental insights to the single-cycle evolution of gasdynamic discontinuities and waves within the thrust chamber flow field, and their corresponding influence on the thrust wall pressure history and overall engine impulse. Similarly, the analytical models of Cooper [110], Sato et al. [98], and Endo [112] provided methods to estimate the performance of partially-filled PDEs, and established insights in regard to fundamental performance scaling parameters of partially-filled PDEs. However, it should be noted that these analytical models are primarily based on energetics, and do not treat the complex gasdynamic flow field encountered in a partially-filled PDE thrust chamber. Unfortunately, this limits the understanding of performance gains of partial filling as important details of the flow field are neglected, such as those discussed in the numerical studies of [98,107]. Additionally, there is no consensus in the literature as to which of the previous performance models most accurately captures the performance scaling of partially-filled PDEs, especially at lower fill fractions. In fact, a recent study by Kasahara et al. [113] investigated the partial-fill effect through an open-ended shock tube to better understand the gasdynamic mechanisms that govern the performance gains of the partial

filling method in PDEs. In that study, it was demonstrated that the acoustic impedance of the driver and driven sections can significantly influence the impulse generated by the shock tube. Moreover, most important, they determined that at lower fill fractions, the contact surface could trap acoustic waves between the thrust wall and contact surface, given the appropriate acoustic impedance ratio across the contact surface. This gasdynamic process was shown to be a critical part of the performance gains associated with partial filling at lower fill fractions, which previous analytical performance models fail to capture. Hence, a major goal of the current work is to understand the performance gains of partially-filled PDEs through identifying the manner in which the fill fraction and properties of the detonable and non-combustible mixture, such as acoustic impedance, combine to influence the propulsive performance.

1.2.4 Diverging Nozzles

Another common method used for enhancing the performance of PDEs is coupling a nozzle to the thrust chamber exit. Like conventional propulsion systems, the addition of a nozzle at the chamber exit provides a means of more efficiently expanding the enthalpy of the burned products into exhaust kinetic energy, which can drastically improve the specific impulse and attainable thrust levels. In fact, such performance enhancement has been demonstrated for PDEs equipped with straight, converging, diverging, and converging-diverging nozzle configurations [76, 114, 115], where the straight-extension nozzle is simply that of the partially-filled PDE configuration discussed in the previous subsection. As such, it is important to briefly comment on the findings of previous studies regarding the use of nozzles with PDEs, and establish which nozzle configurations have shown the most promising results. It is noted that only a brief review is provided here to highlight the major contributions and results from previous numerical and experimental efforts. A more comprehensive review of early research on various PDE nozzle configurations can be found in the work of Kailasanath [116].

In the study of Eidelman and Yang [114], an inviscid two-dimensional numerical model with a coupled single-step finite-rate chemistry model was used to investigate the effects of various nozzle configurations on the single-cycle performance of PDEs operating with stoichiometric ethylene–air propellant. In that study, only the PDE thrust chamber was filled with propellant, such that the nozzle extensions were filled with ambient air, with both initially at 1 atm. Under these operating conditions, it was demonstrated that a fixed length PDE coupled to either a converging, diverging, or straight-extension nozzle will provide performance that is superior to the baseline fully-filled PDE. However, more important, it was shown that diverging nozzles could deliver roughly 13 percent more impulse than converging nozzles, while simultaneously achieving the maximum cycle frequency. Similarly, He and Karagozian [115] investigated the effects of various nozzle configurations on the single-cycle performance of PDEs operating with methane–oxygen propellant using an inviscid quasi-one-dimensional and a two-dimensional numerical model with a coupled single-step finite-rate chemistry model. Like the study of [114], both the detonable and ambient condition were initially at 1 atm, and only the PDE thrust chamber was filled with propellant, with the nozzle extensions filled with ambient air. In He and Karagozian's study, it was also shown that a diverging nozzle geometry provides the best overall impulse, which was estimated to be roughly 8 percent higher than that of the converging nozzle, and 4 percent higher than that of the straight-extension nozzle. Further, unlike diverging nozzles, it was demonstrated that converging nozzles create a reflected shock in the thrust chamber flow field, which results in increased thrust at the head end of the chamber once the shock reflects from the thrust wall. It was also shown that this increase in thrust at the thrust wall is not able to overcome the corresponding negative thrust at the converging nozzle walls, due to the relatively high pressure loading along the converging walls during the nozzle startup and gasdynamic blowdown. In fact, it is this negative thrust loading mechanism that prevents converging nozzles from achieving performance metrics that are superior to those obtained when using a diverging nozzle in PDE applications. Additionally,

it should also be noted that the reflected shocks caused by the converging portion of the nozzle adversely increase the overall gasdynamic blowdown time of the cycle, which was recently shown by Zhang et al. [117] to hinder the high-frequency operation of valveless PDEs.

In regard to a comparison of diverging and converging-diverging nozzles, it was shown in the single-cycle numerical and experimental study of Owens and Hanson [118] that a PDE equipped with a purely diverging nozzle yields better performance than one that is equipped with a converging-diverging nozzle. In that study, the PDE was operating with a stoichiometric ethylene–oxygen detonable propellant and the nozzle was filled with ambient air, where a fill-to-ambient pressure ratio of unity was used in all cases. Based on the numerical results, it was determined in [118] that the single-cycle PDE specific impulse reduces with increasing throat obstruction in converging-diverging nozzles. Moreover, this was determined to be a direct result of the losses incurred at the converging portion of the nozzle during the nozzle startup and subsequent gasdynamic blowdown, where high pressure loading was shown to cause a large resultant negative thrust. Similarly, this was confirmed in the experiments conducted in [118], where the single-shot impulse was determined by integrating pressure measurements at the thrust wall and along the nozzle walls. In those experiments, it was shown that a diverging nozzle can provide nearly 12 percent higher specific impulse than that obtained with a converging-diverging nozzle with the same expansion area ratio. Likewise, Cooper and Shepherd [102] also confirmed the performance benefit of diverging nozzles over converging-diverging nozzles for detonation tubes operating with stoichiometric ethylene–oxygen detonable propellants. However, in their experiments, the detonation tube was suspended on a ballistic pendulum arrangement inside of a dump tank, and the impulse was measured for various diverging and converging-diverging nozzle configurations in sub-atmospheric environments ranging from 1.4–100 kPa. Like the results of [118], Cooper and Shepherd [102] showed that the detonation tube impulse reduces with increasing throat obstruction at a given blowdown pressure ratio, although this loss was

shown to reduce as the blowdown pressure ratio increases. Despite this, it was demonstrated in all test cases that diverging nozzles provide superior specific impulse compared to converging-diverging nozzles, due to the losses produced at the throat obstruction for converging-diverging nozzles.

Given the above observations, it can be said that purely diverging nozzles usually yield more impulse for the PDE compared to that of a purely converging and converging-diverging nozzle at the same operating condition. It is carefully noted that this remains true provided the diverging nozzle is not operating in a severely over-expanded state during the gasdynamic blowdown process, in which case significant losses can occur due to negative net thrust production from the nozzle. However, a few important results should be noted in regard to the use of diverging nozzles in PDE applications. Firstly, it is noted that a converging section of the nozzle is not required to achieve choked flow at the nozzle entrance or throat. In fact, choked flow is established at the entrance of a diverging nozzle due to the formation of rarefaction waves in the thrust chamber flow field once the detonation wave reaches the area change. Most important, this choking condition was confirmed in the schlieren flow visualization experiments of Owens and Hanson [118], where expansion fans were observed to emanate from the nozzle throat upon the passage of the detonation wave. Note, this flow field characteristic is counter to what is usually required to achieve a choked flow within a conventional-steady flow nozzle, which could prove to simplify the design of PDE nozzles. Lastly, in the numerical study of Cambier and Tegnér [119], a two-dimensional axisymmetric numerical model with a coupled finite-rate chemistry model was used to investigate the effects of diverging nozzle wall curvature on PDE performance. In that study, the diverging nozzles were varied between bell-shaped nozzles with negative curvature, a conventional conical nozzle with zero curvature, and a flared nozzles with positive curvature. It was demonstrated that a bell-shaped nozzle with negative curvature provides the best overall performance compared to other diverging nozzle shapes. However, unlike the nozzle studies of [102,114,115,118], the thrust chamber and nozzle were filled with

propellant, and a corresponding decrease in specific impulse was observed with increasing nozzle expansion area ratio. Consequently, this performance loss can be attributed to the lost thrust potential of high pressure burned products at the nozzle exit during the nozzle starting process, and to the large amount of detonable mixture required to fill diverging nozzles. Hence, it is not advantageous to fill a diverging nozzle with detonable mixture since any performance gain associated with the nozzle is not able to overcome the penalty of using excess fuel to fill the nozzle. As such, Fig. 1.17 shows a general schematic of the PDE with a diverging nozzle configuration that will be the focus of the current research.

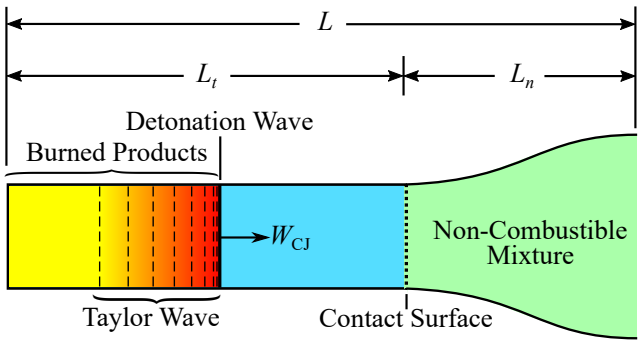

Figure 1.17. Schematic of PDE with diverging nozzle operation.

As shown in Fig. 1.17, only the constant-area portion of the thrust chamber is filled with detonable propellant, while the remaining nozzle volume is filled with a non-combustible gas. In practice, the non-combustible gas usually corresponds to the inert purge gas used to exhaust the PDE of any remaining burned products from the previous cycle, or simply the ambient condition. Additionally, the constant-area portion of the thrust chamber is denoted by the length, L_t, and the nozzle by length, L_n, such that the overall length of the PDE system is $L = L_t + L_n$. Moreover, the PDE and diverging nozzle configuration can readily be characterized with the ratios $\alpha_0 = L_t/L$, and $\epsilon = A_e/A_0$, which represent the axial fill fraction and nozzle expansion area ratio, respectively. In this case, the axial fill fraction is analogous to the partially-filled PDE fill fraction defined in the previous

subsection, such that the nozzle length has the relationship, $L_n/L = 1 - \alpha_0$. It is noted that in the limit $\epsilon = A_e/A_0 \to 1$, the PDE configuration depicted in 1.17 simply reduces to that of a partially-filled PDE depicted in 1.16, whereby the performance is governed purely by the gasdynamics associated with the method of partial filling. Conversely, when $\epsilon > 1$, the PDE configuration features geometric expansion in the nozzle, and the accompanying thrust chamber flow field will evolve in a manner that is distinctly different from that observed in partially-filled PDEs, due to the choking condition at the nozzle inlet. Hence, the performance of a PDE with a given diverging nozzle will be governed by a coupling of the gasdynamic expansion from the geometric area change in the nozzle, and the partial-fill effect due to the presence of the non-combustible gas.

The coupling of the partial-fill effect and the performance of diverging nozzles has been observed in previous numerical and experimental studies. For instance, in the experimental work conducted by Falempin et al. [109] the influence of various diverging and straight-extension nozzle configurations on the impulse of detonation tubes operating with stoichiometric ethylene–oxygen were investigated using a ballistic pendulum setup. In that study, it was shown in one particular case that the detonation tube specific impulse could be increased by a factor of roughly 1.4 by simply changing α_0 from 0.5 to 0.33 while using a diverging nozzle with the same expansion area ratio. Such performance behavior indicates that the partial-fill effect, namely, where the specific impulse increases with decreasing fill fraction, also influences the effectiveness of a given diverging nozzle. It is also worth noting that these experiments were conducted with the ambient and initial propellant pressure each at 1 atm. In the previously mentioned sub-atmospheric experimental work of Cooper and Shepherd [102], it was shown that a straight-extension nozzle with $\alpha_0 = 0.63$ provides superior specific impulse over a diverging nozzle with $\alpha_0 = 0.77$ and $\epsilon = 5.7$ when the ratio of ambient to initial propellant pressure is greater than roughly 0.5. However, once the ambient pressure drops below roughly half the initial propellant pressure, it was shown that the diverging nozzle provides superior performance. Lastly, it is noted that similar results

were obtained in the multi-cycle PDE experimental study of Allgood et al. [120], where it was shown that exhaust nozzles provide a performance benefit when the chamber fill fraction was greater than 0.5; however, when the fill fraction reduces below 0.5 the optimum performance is achieved with a straight-extension nozzle.

Based on the results mentioned above, it is evident that the fill fraction and acoustic impedance of the non-combustible mixture governs the effectiveness of a given diverging nozzle when compared to a straight-extension nozzle, or partially-filled PDE. Moreover, given the discussion in the previous subsection regarding the method of partial filling, these performance trends can best be explained by the effects of ambient acoustic impedance in the nozzle. For instance, the partial-fill effect is known to have a strong presence when the acoustic impedance of the non-combustible is high, namely, when the pressure of the ambient is of similar order as the initial propellant pressure. However, as the ambient pressure is reduced, the partial-fill effect attenuates and the effects of gasdynamic expansion in the nozzle becomes the dominating factor that governs the performance. This observation was first noted by Cooper [110], and was described in terms of the tamper mass effects regarding the non-combustible mixture. Further, as discussed in [102], this suggests that the nozzle flow can be characterized by a minimum of two distinct flow regimes, termed the unsteady- or quasi-steady flow regimes, depending on the acoustic impedance of the non-combustible. In the unsteady-flow regime, the partial-fill effect is said to dominate the impulse generation of a PDE, and the most favorable performance gains are achieved with a simple straight-extension nozzle. Further, in the quasi-steady-flow regime, the addition of a nozzle with the corresponding gasdynamic expansion is said to dominate the impulse generation of a PDE, and the most favorable performance gains are achieved with a diverging nozzle. However, a PDE can still operate in the intermediate regime with an overlap of the unsteady- and quasi-steady regimes, whereby the performance of the nozzle is governed by a more complicated coupling of the partial-fill effect and the gasdynamic expansion in the nozzle.

It is of interest to be able to quantify the performance metrics associated with a given nozzle design at general operating conditions. However, the complex nozzle flow inherent to the operation of a PDE has made analytical performance modeling of PDE nozzles especially challenging, except in a few restricted cases. For instance, in the unsteady-flow regime, the performance of a nozzle is dominated by the partial-fill effect, and partial filling models of Cooper [110], Sato et al. [98], and Endo [112] can be used to obtain estimates of the associated performance. However, it is noted that these models are truly only appropriate when $\epsilon = 1$, namely, when no geometric expansion exists to further expand the products during the gasdynamic blowdown. Moreover, in the quasi-steady-flow regime, Cooper and Shepherd [102] proposed a very simple model based on the assumption that the nozzle operates with steady flow and expands perfectly to match the ambient condition. Additionally, the nozzle inlet state was chosen such that choked flow was achieved, but with a stagnation enthalpy equal to that at the thrust wall. This model was shown to qualitatively model the performance behavior of nozzles with increasing blowdown pressure ratio; however, the model largely overestimated the measured specific impulse in [102]. Similarly, Barbour and Hanson [121] proposed a correction to the steady-flow model of [102] based on the existence of an exhausting rarefaction wave in the actual thrust chamber flow field. In that case, the throat stagnation enthalpy was replaced with the actual stagnation enthalpy at the throat rather than that at the thrust wall, and slightly better agreement was obtained with the measured specific impulse in [102]; however, the corrected model was shown to still largely overestimate the specific impulse. Finally, Barbour and Hanson [121] proposed an analytical model to treat the performance of detonation tube diverging nozzles in the quasi-steady-flow regime. In this case, the combined analytical models for a fully-filled detonation tube proposed by Wintenberger et al. [66,67] and Cooper and Shepherd [92] were extended to the case of a diverging nozzle with quasi-steady flow. As discussed in [121], the choking condition at the nozzle inlet was exploited to separately treat the impulse generated from the detonation tube and coupled diverging nozzle. Moreover, the model was

shown to agree well with the numerical and experimental results of [83, 102], provided the acoustic impedance of the ambient and L_n/L are small, namely, when the partial fill effect is negligible and the nozzle starting process is nearly instantaneous. Although, it is noted that no reduced-order model currently exist that can accurately estimate the performance of PDE nozzles across the unsteady and quasi-steady nozzle flow regimes. Hence, a major goal of the current work is to understand the performance gains of general PDE diverging nozzles through identifying the manner in which the acoustic impedance of the detonable and non-combustible mixtures, nozzle length, and nozzle expansion area ratio combine to influence the propulsive performance.

1.3 Thesis Outline and Research Objectives

As discussed in the previous sections, much progress has been made towards the understanding of performance gains associated with partially-filled PDEs, and PDEs equipped with diverging nozzles. However, there is still no widely agreed upon model that can readily evaluate the performance of general PDE configurations over a broad range of operating conditions. Moreover, in order to establish comprehensive design methodologies for partially-filled PDEs, and those equipped with diverging nozzles, rigorous treatment of the unsteady thrust chamber and nozzle flow fields is required. In general, this can usually only be accomplished with high-fidelity numerical models, such as those discussed in [76, 81, 83, 98, 107, 114, 115, 119], whereby the performance is evaluated once the entire thrust chamber and nozzle flow fields are determined. Although accurate, this approach can become impractical when considering the computational expense of performing extensive parametric studies in order to explore the design space of various PDE configurations. Therefore, there is a need for simplified reduced-order models that can accurately and rapidly evaluate the performance of general PDEs, while still capturing the physical gasdynamic flow phenomena inherent to the unsteady thrust chamber and nozzle flow fields. The focus of the current research is to investigate and characterize the fundamental gasdynamic

processes that govern the propulsive performance of a general PDE. This research effort is separated into a series of related analytical, numerical, and experimental studies focused on various gasdynamic interactions within a PDE thrust chamber and nozzle flow field. The proposed work aims to investigate three distinct PDE operating configurations, namely, the fully- and partially-filled PDE, and PDEs equipped with diverging nozzles. The thesis outline and research objectives are listed below:

1. Chapter 1 discusses the fundamentals of detonations, which includes a detailed survey of historical contributions leading up to the one-dimensional CJ and ZND detonation theories. Additionally, the CJ theory is used to perform a comparative study of the fundamental differences associated with the thermodynamics of deflagration and detonation waves, which is subsequently used to demonstrate the primary motivation of pursuing detonation combustion in aerospace propulsion systems. Further, a comprehensive literature review of PDEs is provided, and a simple thermodynamic cycle analysis is used to emphasize the importance of a properly designed nozzle device in detonation-based propulsion systems. Consequently, a detailed review of the partial filling method and use of diverging nozzles in PDE propulsion systems is provided in order to detail the benefits of these respective performance enhancement methods. A detailed discussion of recent modeling efforts for partially-filled PDEs and PDEs equipped with diverging nozzles is provided, to highlight what phenomena appear to govern the performance of these respective PDE configurations, and demonstrate the limitations of existing models. As such, this discussion is used to establish the primary motivation of this research, which is to investigate and characterize the fundamental gasdynamic processes that govern the propulsive performance of a general PDE.
2. Chapter 2 provides a detailed description of the PDE thrust chamber flow field for a fully- and partially-filled PDE, and for a PDE equipped with a diverging nozzle. More important, this discussion is used to highlight the various gasdynamic discontinuities, waves, and subsequent interactions that will arise during a single-cycle operation of

a general PDE, which must be modeled appropriately in order to accurately evaluate the various propulsive performance metrics.

3. Chapter 3 provides a detailed analytical description for the one-dimensional interaction of a detonation wave with a contact discontinuity separating a detonable and non-combustible mixture using the ZND detonation theory. This particular gasdynamic interaction arises in PDEs when the detonation wave reaches the gaseous interface separating the detonable and non-combustible mixtures. Moreover, this gasdynamic interaction directly governs the incident properties of the shock that transmits into the non-combustible mixture, and the incident reflected wave type and strength that propagates upstream into the burned products, which can drastically influence the evolution of the entire thrust chamber flow field. Additionally, a detonation-driven shock tube facility is developed to experimentally investigate this particular gasdynamic interaction, whereby experiments are conducted at various detonable equivalence ratios and non-combustible inert mixture mole fractions. Finally, the experimental and analytical results are reduced in terms of the ratio of detonable and non-combustible mixture acoustic impedance.
4. In Chapter 4, a general quasi-one-dimensional method of characteristics (MOC) model is developed for rapidly evaluating the single-cycle evolution of gasdynamic waves and discontinuities in general PDE thrust chamber flow fields. The MOC model is developed using a simplified unit process approach with an explicit inverse time marching algorithm in order to readily construct the complex thrust chamber flow field along a predefined grid. Moreover, the model incorporates the detonation-contact surface interaction results of Ch. 3 in order to accurately treat the one-dimensional collision of a detonation wave with a contact discontinuity. A grid dependency study is carried out to determine the appropriate grid resolution for the purposes of minimizing computational expense without sacrificing numerical accuracy. Subsequently, a thorough validation of the model is presented over a broad range of operating conditions with

existing higher-fidelity numerical and experimental performance data for fully- and partially-filled PDEs, and PDEs equipped with diverging nozzles. This includes PDEs operating with a variety of detonable fuels, non-combustible inert gases, fill fractions, blowdown pressure ratios, and nozzle expansion area ratios. Lastly, a detailed description of the model limitations is provided, and particular operating conditions are addressed whereby the assumptions used in the development of the model become inaccurate.

5. In Chapter 5, a simplified analytical model is developed based on control volume analysis for evaluating the primary performance metrics of a general fully-filled PDE. In this case, the MOC model is used to justify and establish a simplified thrust relation based solely on the flow properties at the exit plane of a fully-filled PDE. A detailed analytical description of the thrust chamber flow field is provided, from which an analytical piecewise expression for thrust is derived based on the exit plane pressure history. This expression is then used to evaluate the specific impulse, total impulse, and time-averaged thrust of a fully-filled PDE. Lastly, this simplified model is validated against the current MOC model and existing higher-fidelity numerical and experimental performance data for a variety of detonable fuels, equivalence ratios, and blowdown pressure ratios.
6. In Chapter 6, the MOC model developed in Ch. 4 is used to conduct a broad parametric study of the partially-filled PDE, and PDE equipped with a diverging nozzle. In the case of partially-filled PDEs, the method of Ch. 3 is used to tailor the acoustic impedance of the non-combustible inert gas at a fixed fill fraction in order to demonstrate the sensitivity of thrust chamber flow field and PDE performance to the non-combustible acoustic impedance. Additionally, the detonable fill fraction and non-combustible acoustic impedance are varied simultaneously in order to highlight the general role of non-combustible acoustic impedance and fill fraction on the partially-filled PDE performance. Subsequently, a parametric investigation of non-combustible

mixture temperature is conducted to characterize the benefit of using moderately cold non-combustible gases at different fill fractions. Similarly, the benefit of partial filling is investigated for partially-filled PDEs operating in sub-atmospheric environments at different fill fractions. It is demonstrated that the specific impulse performance results generated with the MOC model from the various parametric investigations can successfully be collapsed using the scaling law proposed by Sato et al. [98]. Additionally, this scaling law is extended to other important performance metrics, such as the total impulse and time-averaged thrust ratios. In the case of PDEs with diverging nozzles, a parametric investigation is conducted to highlight the combined effects of nozzle expansion area ratio and blowdown pressure ratio on the thrust chamber and nozzle flow fields. In these cases, a detailed discussion of the transient nozzle starting flow field is provided in relation to the acoustic impedance of the non-combustible mixture and nozzle expansion area ratio. Similarly, a parametric investigation is conducted by simultaneously varying the nozzle expansion area ratio at different blowdown pressure ratios in order to determine the regimes of unsteady and quasi-steady flow, and the associated influence on nozzle performance. For the regime of quasi-steady flow, a simplified diverging nozzle performance model is developed based on the fully-filled analytical model in Ch. 5. Lastly, the optimum nozzle performance characteristics of PDEs are presented and discussed for diverging nozzles of different lengths, expansion area ratios, and blowdown pressure ratios.

7. Chapter 7 provides a rigorous analytical description for the quasi-one-dimensional dynamics of the transmitted shock wave inside a general contour diverging nozzle. This model is derived on the basis of a two-equation approximation of the generalized CCW theory for treating general shock dynamics in non-uniform channels. Additionally, unlike previous models, the present model includes the effects of both area change and flow non-uniformity behind the transmitted shock, which is essential for accurate modeling of the transmitted shock dynamics in PDE nozzles. In application

to diverging PDE nozzles, this model is used to demonstrate how the thrust chamber length governs the magnitude of flow non-uniformity behind the transmitted shock entering the nozzle, and how drastically this can influence the nature of shock attenuation within a nozzle. Moreover, the shock dynamics model is used in conjunction with the MOC model to demonstrate how different nozzle wall curvature influences the PDE propulsive performance, due to the changes in transmitted shock attenuation and gasdynamic over-expansion in the nozzle flow field during the nozzle starting process.

8. Finally, in Chapter 8, a summary of the major research contributions from each chapter is provided, and suggestions aimed at guiding further research of PDE propulsion systems are discussed.

CHAPTER 2

GASDYNAMIC FLOW FIELD IN PULSE DETONATION ENGINES

2.1 Fully-Filled Thrust Chamber

Before discussing details of analytical and numerical models, a discussion of the dominant one-dimensional gasdynamic features of a fully- and partially-filled PDE flow fields, as well as PDEs with diverging nozzles is provided. The intent of this chapter is to highlight the important gasdynamic interactions and processes that must be considered when developing a MOC-based solver for general PDE single-cycle flow fields. In this section, the case of a fully-filled PDE is considered, and the subsequent sections are used to address the additional flow features that arise in a partially-filled PDE, and PDEs equipped with diverging nozzles.

Consider a straight and constant-area PDE thrust chamber with an overall length L, which is fully filled with gaseous detonable propellant. The detonable propellant is separated from the ambient by an idealized contact surface at the chamber exit plane. For simplicity, it is assumed that the detonable propellant and contact surface are initially stationary. After ignition, it is further assumed that a detonation wave is instantaneously formed at the head end of the thrust chamber and propagates down the chamber away from the thrust wall. In practice, such direct detonation initiation can be achieved using exploding wire devices such as those used in the experiments of Zitoun and Desbordes [89]. However, in more practical operations, detonations are achieved using spark ignition with DDT transition aided by Shchelkin spirals or various obstacles, such as those used in the experiments of Schauer [95] and Cooper [90]. Once the detonation wave is formed, the detonation is immediately followed by a self-similar rarefaction wave, also known as the Taylor wave [122]. This rarefaction wave decelerates the gas from a high velocity to rest, satisfying the closed wall boundary condition at the head end of the chamber. Figure

2.1(a) shows a schematic of the developing gasdynamic flow field following initiation of a detonation wave in the fully-filled PDE thrust chamber configuration under consideration.

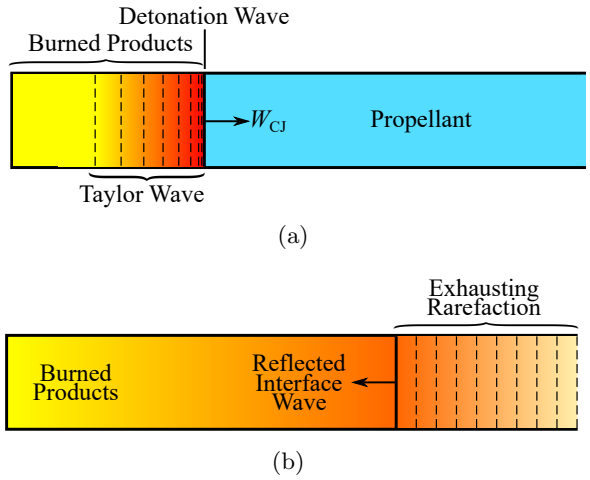

Figure 2.1. Schematic of (a) starting flow field following detonation initiation in fully-filled PDE and (b) exhausting flow field after entrance of exhausting rarefaction at the thrust chamber exit.

When the detonation wave collides with the contact surface, an unsteady shock wave is transmitted into the surrounding. The incident strength of the transmitted shock depends on the acoustic impedance change across the contact surface, which will be discussed in detail in the following chapter. Simultaneously, a reflected wave propagates upstream into the burned detonation products towards the head-end of the chamber. The strength of this reflected wave is also governed by the acoustic impedance change across the contact surface and can take the form of a reflected shock, a Mach wave, or rarefaction wave. The reflected interface wave is immediately followed by an exhausting rarefaction wave that propagates towards the thrust wall at the head end of the chamber. Moreover, the exhausting rarefaction wave is the mechanism that accelerates the high pressure burned products of the detonation wave out of the chamber and creates a sonic condition on the exit plane of the PDE. This gasdynamic process is shown schematically in Fig. 2.1(b).

Once the exhausting rarefaction reaches the head end of the chamber, the wave reflects, causing the pressure on the thrust wall to start decreasing, which initiates the gasdynamic blowdown of the thrust chamber to the ambient condition. This complete gasdynamic flow field is depicted in the x–t diagram of Fig. 2.2, which highlights the behavior of the detonation wave, Taylor wave, reflected interface wave, and exhausting rarefaction wave. The generalized flow field description above details the dominant wave interaction processes in a fully-filled PDE, which must be modeled appropriately in order to investigate the single-cycle performance aspects of fully-filled PDEs.

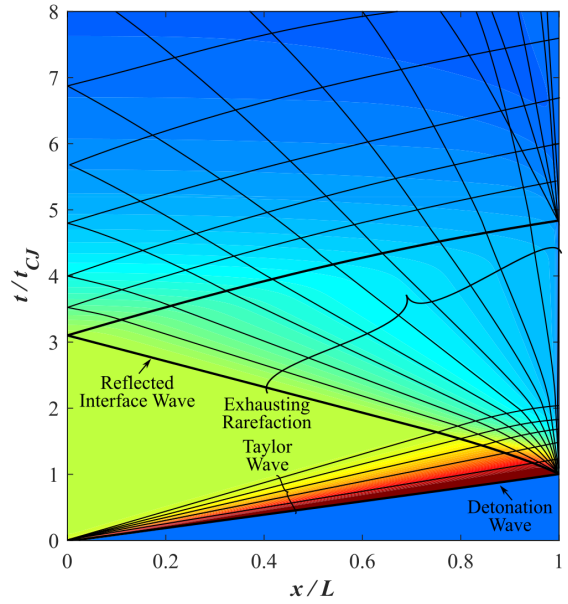

Figure 2.2. x–t diagram of fully-filled PDE flow field where the color corresponds to pressure.

2.2 Partially-Filled Thrust Chamber

In the partially-filled case, only a portion of the PDE thrust chamber is filled with detonable propellant, while the remaining portion of the chamber is filled with a non-combustible gas. The non-combustible gas can either be ambient air outside the PDE, or as

commonly encountered in practice, the inert gas used to purge the PDE from any remaining combustion products from a previous cycle. The filled length is denoted by L_f, whereby the parameter commonly referred to as the fill fraction for a constant-area thrust chamber is simply the ratio of filled length-to-total chamber length, $\alpha = L_f/L$. The detonable and non-combustible mixtures are separated by a contact surface and are assumed to be initially stationary. In practice, this is likely not the case as the fuel is being injected with a finite velocity. However, for the sake of this discussion and subsequent idealized analysis, the contact surface is assumed to be initially stationary. After ignition, the flow field begins to evolve in a similar manner to that of a fully-filled PDE, with the propagating detonation wave and following self-similar Taylor rarefaction wave. Figure 2.3(a) shows a schematic of the developing gasdynamic flow field following initiation of a detonation wave for the partially-filled PDE thrust chamber configuration under consideration.

As the detonation wave collides with the contact surface, an unsteady shock wave is transmitted into the non-combustible gas. Simultaneously, a reflected wave propagates upstream into the burned detonation products towards the head-end of the chamber. As in the case of a fully-filled PDE, the strength of the transmitted shock and reflected wave are directly governed by the acoustic impedance change across the contact surface. However, unlike the fully-filled case, the exhausting rarefaction only enters the thrust chamber once the transmitted shock exits the chamber. Following the detonation wave collision with the contact surface, the transmitted shock and contact surface begin propagating towards the PDE exit. While traveling towards the exit, both the contact surface and transmitted shock wave decelerate as they are continually being overtaken by the transmitted Taylor rarefaction wave from behind. Moreover, it is during this time that the burned products, now bounded between the thrust wall and traveling contact surface, are continually expanded before reaching the chamber exit plane. The reflected wave from the interface collision travels upstream through the burned products until eventually reaching the thrust wall. In the case of a reflected shock or Mach wave from the interface collision, the wave is immedi-

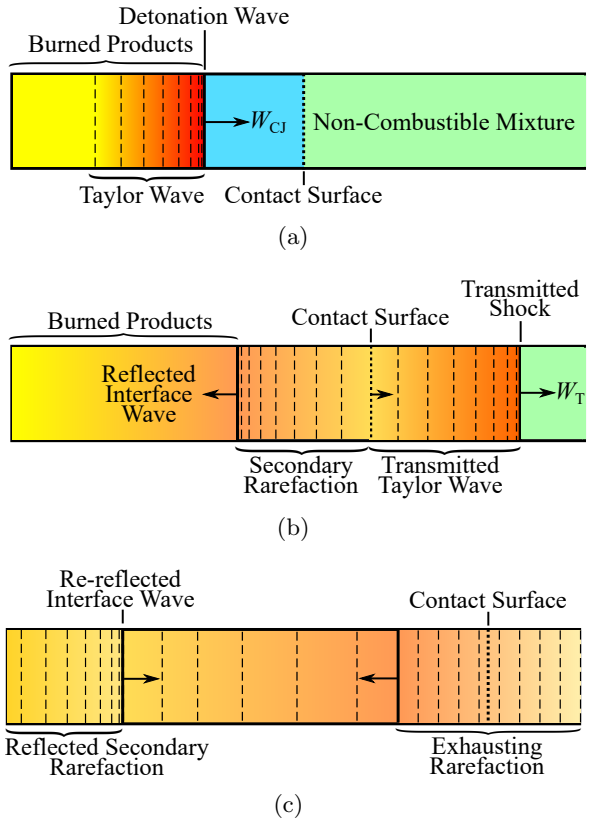

Figure 2.3. Schematic of (a) starting flow field following detonation initiation in partially-filled PDE, (b) intermediate flow field with transmitted shock, contact surface, reflected interface wave, and following secondary rarefaction, and (c) exhausting flow field after entrance of exhausting rarefaction at the thrust chamber exit.

ately followed by a secondary rarefaction wave. This secondary rarefaction wave forms to relieve the gas behind the reflected shock or Mach wave to match the decaying pressure at the contact surface traveling behind the decaying transmitted shock. Additionally, for the sake of discussion in the subsequent analysis, the secondary rarefaction wave also includes the reflected Taylor wave from the contact surface. This more complex flow field is shown schematically in Fig. 2.3(b). As the contact surface encounters the exhausting rarefaction wave, the contact surface accelerates through the rarefaction wave until eventually exiting the chamber. Similarly, once the reflected interface wave and secondary rarefaction reach the head end of the chamber, the wave reflects causing the pressure on the thrust wall to

start decreasing, which initiates the intermediate phase of the gasdynamic blowdown. This gasdynamic process is shown schematically in Fig. 2.3(c).

It can be noted that if the secondary rarefaction is led by a reflected shock from the interface collision, then the pressure history on the thrust wall will experience an instantaneous increase from the shock reflection off the thrust wall, which is immediately followed by a subsequent relaxation from the reflected secondary rarefaction. Once the secondary rarefaction wave has completely reflected from the wall, the pressure history on the thrust wall has decayed to an intermediate value that is above the ambient condition. In this case, the exhausting rarefaction is the mechanism that returns the thrust wall pressure back to the ambient condition. Hence, the exhausting rarefaction traveling towards the thrust wall collides head on with the reflected secondary rarefaction and eventually reaches and reflects off the thrust wall, initiating the remainder of the gasdynamic blowdown to the ambient condition. This complete gasdynamic flow field is depicted in the x–t diagram of Fig. 2.4, which highlights the behavior of the detonation wave, Taylor wave, reflected interface wave, secondary rarefaction, and exhausting rarefaction.

Although not mentioned above, it is noted that the contact surface and exhausting rarefaction interaction can result in reflected secondary compression waves that travel towards the PDE exit. However, in most cases, these compression waves are weak and will not significantly influence the performance of a partially-filled PDE. Further, it can be noted that as the fill fraction becomes very low, it is possible to have cases where the reflected wave from the interface collision propagates back towards the thrust wall, reflects, and eventually intersects the contact surface before the contact surface has exited the PDE. This situation is representative of the contact surface wave trapping mechanics studied by Kasahara et al. [113] in an open-ended shock tube. Similarly, it is possible to get secondary reflected compression or shock waves from the contact surface that reflect back towards the thrust wall. These wave reflections can cause momentary pressure rises on the thrust wall during

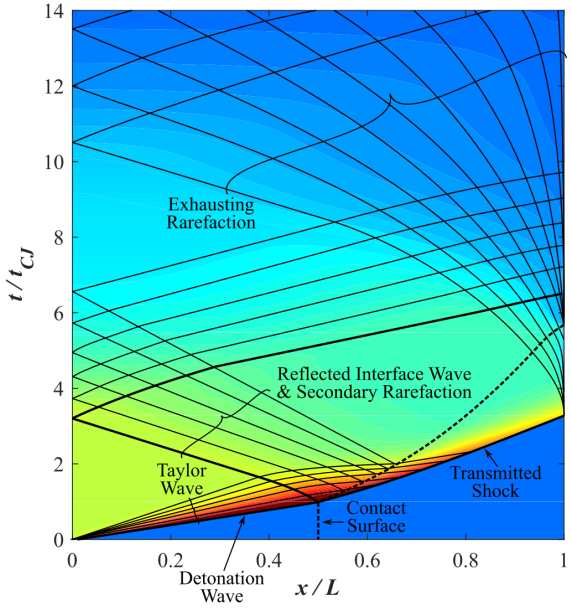

Figure 2.4. x–t diagram of partially-filled PDE flow field where the color corresponds to pressure.

the incident decay, and are regarded as a secondary flow phenomenon that only occur at lower fill fractions.

2.3 Pulse Detonation Engines with Diverging Nozzles

A PDE with a diverging nozzle consists of a straight and constant area thrust chamber that is coupled to a diverging nozzle section. The constant area portion of the PDE thrust chamber is fully filled with detonable propellant up to the nozzle entrance, while the volume occupied by the diverging nozzle is filled with a non-combustible gas. Similar to the partially-filled PDE case, the non-combustible gas can either be ambient air outside the PDE, or as commonly encountered in practice, the inert gas used to purge the PDE from any remaining combustion products from a previous cycle. The detonable and non-combustible mixtures are separated by a contact surface at the chamber exit and nozzle inlet, and are assumed to be initially stationary. After ignition, the flow field begins to evolve in a similar manner to that of a fully-filled PDE, with the propagating detonation

wave and following self-similar Taylor rarefaction wave. Figure 2.5(a) shows a schematic of the developing gasdynamic flow field following initiation of a detonation wave for the PDE thrust chamber configuration with a diverging nozzle under consideration.

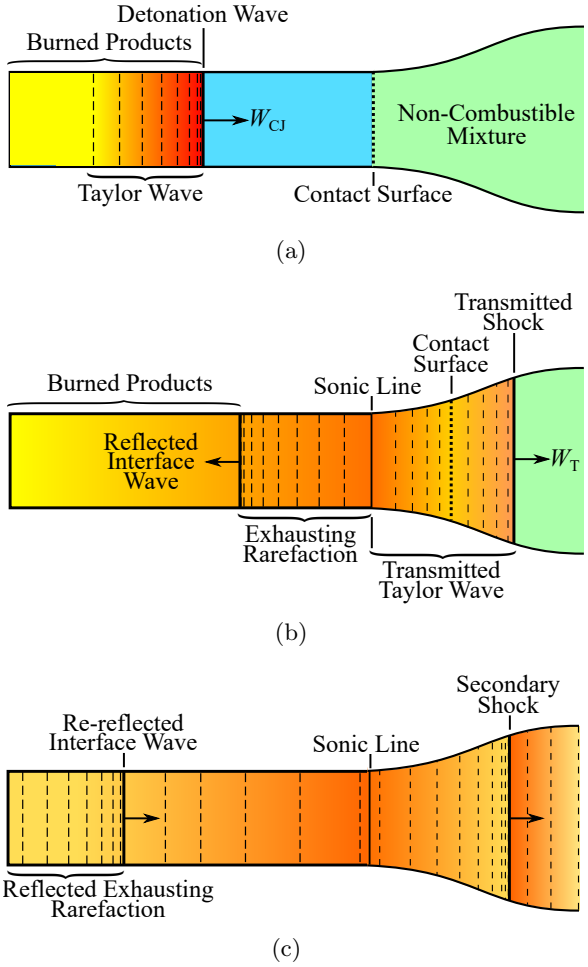

Figure 2.5. Schematic of (a) starting flow field following detonation initiation in PDE with a diverging nozzle, (b) intermediate and starting nozzle flow field with thrust chamber reflected interface wave and exhausting rarefaction, nozzle transmitted shock and contact surface, and (c) exhausting flow field after reflected exhausting rarefaction and formation of secondary shock inside nozzle.

As the detonation wave collides with the contact surface, an unsteady shock wave is transmitted into the non-combustible gas. Similarly, as in all previous cases, a reflected

wave propagates upstream into the burned detonation products towards the head-end of the chamber. The strength of the transmitted shock and reflected waves are directly governed by the acoustic impedance change across the contact surface. Because the PDE features a diverging nozzle, a sonic point forms at the inlet of the nozzle. The existence of this sonic point drastically alters the nature in which the thrust chamber flow field develops when compared with the partially-filled PDE, which features no area change. For instance, the sonic point creates a unique situation where the flow field inside the constant area portion of the thrust chamber is independent from the flow field within the nozzle. More strictly, the sonic point at the nozzle inlet creates a choking condition whereby disturbances from within the nozzle are unable to propagate into the constant area thrust chamber. Consequently, so long as the choking condition exist at the nozzle inlet, the flow field within the constant area portion of the thrust chamber is exact to that of a fully-filled PDE. Hence, after the detonation wave collision with the contact surface, the reflected interface wave is immediately followed by an exhausting rarefaction wave that together travel upstream through the burned products until eventually reaching, and reflecting from the thrust wall. Similar to the case of a fully-filled PDE, the exhausting rarefaction is the mechanism that accelerates the gas within the thrust chamber to the sonic condition at the nozzle inlet where the area change takes place, and relaxes the thrust chamber flow field back to the ambient condition.

Immediately following the detonation and contact surface collision, the nozzle starting flow begins with the transmitted shock and contact surface propagating through the nozzle towards the nozzle exit. Similar to the case of a partially-filled PDE, while traveling towards the exit, the transmitted shock wave decelerates as a result of continually being overtaken by the transmitted Taylor rarefaction wave from behind. However, when the PDE is equipped with a nozzle, the shock also decays as a result of the increasing area change within the nozzle. This more complex flow field is shown schematically in Fig. 2.5(b). As the transmitted shock travels the length of the nozzle, the gas behind the shock is expanding

through the nozzle. If the expansion is rapid enough as a consequence of a rapidly increasing area change, such that the gas coming from the nozzle inlet approaches pressures below that behind the transmitted shock, then a secondary shock forms that brings the gas pressure back up to that behind the transmitted shock. This gasdynamic process is shown schematically in Fig. 2.5(c). Moreover, the strength of the secondary shock in the nozzle starting process is governed by the degree of over-expansion in the gas behind the transmitted shock. Hence, cases of severe over-expansion yield fairly strong secondary shocks, whereas slight over-expansion yields fairly weak secondary shocks. Note, that this type of unsteady nozzle starting process has similarities to the starting process found in hypersonic nozzles for reflected shock tunnels [123–125]. In either case, the secondary shock is swept downstream through the nozzle until eventually exiting. Once the transmitted shock, contact surface, and secondary shock exit the nozzle, the unsteady nozzle starting process has completed and a mostly quasi-steady flow field ensues, which is governed by the choking condition at the nozzle inlet. In this case, the behavior of the exhausting rarefaction within the constant area thrust chamber governs the flow properties at the choking condition at the nozzle inlet, and the quasi-steady flow in the nozzle. This quasi-steady nozzle flow continues during the thrust chamber blowdown until the head end pressure in the thrust chamber returns back to the ambient condition. This complete gasdynamic flow field is depicted in the x–t diagram of Fig. 2.6, which highlights the behavior of the detonation wave, Taylor wave, reflected interface wave, exhausting rarefaction, transmitted shock, contact surface, and secondary shock. To reiterate, the thrust chamber flow appears separate from the nozzle flow field due to the sonic choking condition at the nozzle inlet at $x/L = 0.7$.

The generalized flow field description in this chapter details the dominant wave and discontinuity interaction processes in fully- and partially-filled PDEs, as well as PDEs equipped with diverging nozzles. In order to appropriately investigate the single-cycle performance aspects of such PDE configurations with analytical or numerical methods, it is critical that these gasdynamic processes be properly modeled. One of the most crucial pro-

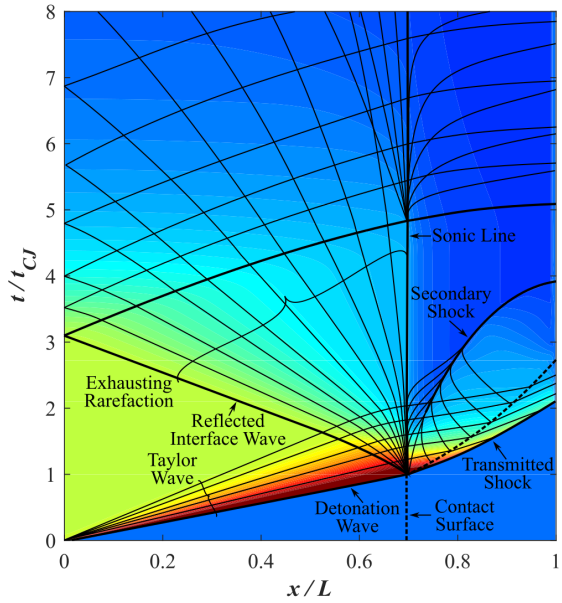

Figure 2.6. x–t diagram of PDE flow field with diverging nozzle where the color corresponds to pressure.

cesses that governs the evolution of the resulting flow field in all cases is the collision of the detonation wave with the contact surface. This particular gasdynamic interaction governs the incident strength and velocity of the transmitted shock and reflected wave, which can take the form of a shock, Mach wave, or rarefaction. Therefore, the next chapter is used to investigate the one-dimensional collision of a detonation wave with a contact surface discontinuity in order to gain insights regarding the underlying physical parameters governing this gasdynamic interaction.

CHAPTER 3

DETONATION WAVE–CONTACT SURFACE INTERACTION [1]

3.1 Background

The collision of a detonation wave with a contact surface discontinuity is a fundamental gasdynamic interaction process that takes place during the operation of a fully- or partially-filled PDE, and PDEs operating with diverging nozzles. As mentioned in the previous chapter, the results of this gasdynamic collision drastically influences the evolving flow field within the thrust chamber of a PDE, and the subsequent propulsive performance metrics. As such, properly capturing the underlying physics governing this gasdynamic collision is vital to the success of analytical and numerical models for the propulsive performance of general PDE based systems. The goal of this chapter is to provide a rigorous investigation of this interface collision and demonstrate what properties of detonable and non-combustible mixtures govern the transmission of a shock into the non-combustible mixture, and the reflected interface wave into the burned products. Additionally, the results of this chapter can be used to properly tailor the reflected interface wave behavior in PDE thrust chambers, which can be used as a means to adjust and control propulsive performance metrics.

Before discussing the interaction of a detonation with a contact surface discontinuity, it is worth mentioning the insights gained from studies focused on the interaction of a shock wave with a contact discontinuity. The one-dimensional transmission of a shock wave into a gas as the result of a shock wave collision with a contact discontinuity has received analytical and experimental coverage in previous studies [126–130]. This particular interaction arises, for example, in shock tube flows where the reflected shock wave interacts

[1] Parts of this chapter were published in Peace, J.T. and Lu, F.K., "Detonation-to-Shock Wave Transmission at a Contact Discontinuity," *Shock Waves*, vol. 28, no. 5, pp. 981–992, 2018. doi: 10.1007/s00193-018-0804-6

with the contact surface separating the post-shock and driver gases. In this particular flow process, a shock wave is transmitted through the contact surface and a simultaneous reflected shock or rarefaction occurs in the opposite direction. In the studies conducted by Bitondo et al. [127, 128], the exact reflection type has been shown to depend on the ratio of internal energies across the contact surface and can either amplify or attenuate the transmitted shock. This work was later used to tailor shock tube flows such that a Mach wave reflection could be obtained from the interaction of the shock wave and contact surface [131]. It is noteworthy that the shock collision with a contact discontinuity, in fact, gives rise to a Richtmyer–Meshkov instability which is beyond the scope of the current investigation [132].

Unlike the extensive treatment of the normal incidence of a shock wave on a contact discontinuity, there has been less treatment of the transmitted shock wave from the one-dimensional interaction of a detonation wave with a contact discontinuity separating a detonable and non-combustible mixture. Morrison [133] conducted the first theoretical treatment of this gasdynamic interaction while investigating the use of a detonation driver to induce shocks in the test section of a shock tube. An analytical expression was provided for the strength of the transmitted shock, namely, the pressure ratio following the collision for the cases of reflected shock, rarefaction, and Mach wave by matching the pressure and gas velocity across the resulting interface. Similarly, Paterson [134] provided further analytical treatment by calculating the properties of a transmitted shock wave into a reactive and non-reactive medium following the collision of a detonation wave onto a contact surface. Calculations were carried out assuming an equilibrium CJ detonation state and waves reflecting into stoichiometric oxyhydrogen and stoichiometric oxygen and carbon monoxide detonation products. The criterion for the reflection type was determined by use of pressure–velocity diagrams and the locus of transmitted shock solutions relative to the equilibrium detonation state. In Pack's [135] analysis, a criterion was derived to uniquely determine the nature of the reflected wave based on the relative shock impedances of the

detonable medium and the medium for which the transmitted wave passes. In that study, the shock impedance was defined as the product of equilibrium density of the medium and the velocity of the shock relative to the medium. Lastly, this interaction was also treated in an analytical study conducted by Fickett [136], where the incident interaction was used to determine the trajectory of the transmitted shock in an inert medium with lower shock impedance. Experiments were conducted by Thomas et al. [137] to determine the properties of a transmitted shock wave as the result of a detonation wave incident on both an abrupt planar gaseous interface and a diffuse concentration gradient. In the case of an abrupt planar interface, the measured transmitted shock was shown to agree well with the theory of Paterson for stoichiometric acetylene–oxygen detonations and helium, air, argon, and carbon dioxide inert gases. It is noted that each of these cases would result in a reflected rarefaction from the contact surface.

The current work provides a general analytical treatment of the interaction of a detonation wave with a stationary contact discontinuity and discusses the analytical results obtained for oxyhydrogen detonations. In all known previous analytical studies, the detonation state has been modeled by the equilibrium CJ state, such that the effects of the leading shock front, and the induction and reaction zones were not considered in the one-dimensional analysis. The methods used in the current study are similar to that implemented in the works of Paterson [134], Pack [135], and Fickett [136]; however, the one-dimensional detonation wave is modeled using the ZND detonation wave representation. Making use of this simplified detonation model allows one to investigate the effects of selecting various representative post-detonation states across the one-dimensional detonation structure on the transmitted shock wave properties. In actuality, a detailed rigorous treatment of this gasdynamic interaction would encompass using the von Neumann peak [32] to determine the incident transmitted shock and reflected wave strengths, and then computing the subsequent interaction of the reflected wave with the reaction zone structure of the ZND wave profile in order to establish the final transmitted shock strength following the collision. How-

ever, such analysis is well beyond the capabilities of any analytical treatment and would require high-fidelity numerical investigations featuring spatial resolution several orders of magnitude less than that of the reaction zone thickness of a detonation wave. Therefore, the goal of the current work is to simplify this gasdynamic interaction, and use a representative post-detonation state from within the detonation wave structure to obtain adequate results regarding the transmitted shock wave properties. Concurrently, an experimental investigation was conducted using a detonation-driven shock tube facility operating with oxyhydrogen detonable mixtures and helium–air inert mixtures, and the measured transmitted shock velocities are compared with the analytical results. Further, the acoustic impedances of the detonable and non-combustible gases are used to develop a relationship with the transmitted shock and detonation wave velocities that can assist in tailoring the reflection type when a detonation wave is incident on a contact discontinuity.

3.2 Theory

The focus of this chapter is to analytically describe the one-dimensional interaction of a detonation wave with a contact discontinuity. Consider a constant area, closed tube which is partially filled with a gaseous detonable mixture with the remaining length filled with an inert, non-combustible gas, which are separated by a contact surface discontinuity. This setup was previously depicted in Fig. 2.3(a) of Ch. 2, which shows a detonation wave traveling towards the contact surface in a partially-filled PDE. The initial pressure and density of the gases on either side of the contact surface are denoted by p_1, ρ_1, p_0, and ρ_0, where the subscripts 1 and 0 represent the detonable and inert gases, respectively. Similarly, the ratio of specific heats for the detonable and inert gases is denoted by γ_1 and γ_0, respectively. The detonation wave is modeled by the one-dimensional ZND theory [31–33]. In this representation, the detonation wave has a finite thickness as a result of the induction and reaction zones following the detonation front. The ZND detonation wave representation is utilized to preserve the theoretical, one-dimensional planar structure of the detonation

wave from the von Neumann (vN) peak, a characteristic of the leading shock front, to the equilibrium CJ detonation state. Consistent with this representation and depicted in Fig. 3.1(a), the planar detonation wave travels towards the contact surface at the characteristic CJ velocity of the detonable mixture W_{CJ}. As mentioned previously, when the detonation wave collides with the contact surface, distinct reflection types can occur that determine the transmitted shock wave properties. For example, Figs. 3.1(b) and 3.1(c) depict the cases of a reflected shock and rarefaction from the contact surface, respectively. In these figures, the post-detonation, reflected characteristic, and transmitted shock states are denoted by 2, $2'$ and $0'$, respectively. Although not shown in Fig. 3.1, a third degenerate case can exist such that a reflected Mach wave, namely, an infinitely weak wave, propagates into the detonation products. This reflection type can only occur under specified conditions and will also be discussed further in the subsequent sections.

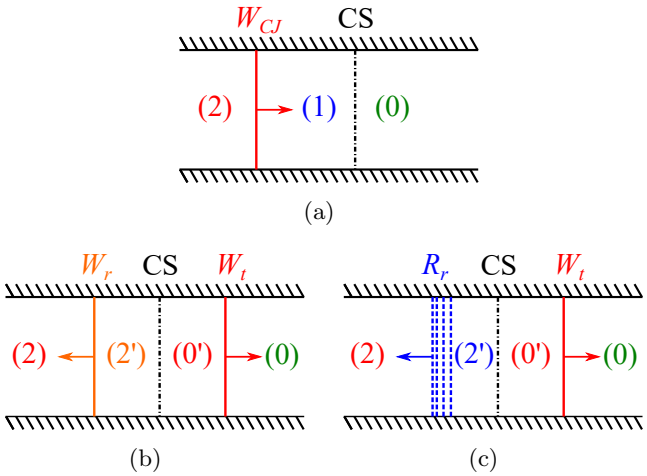

Figure 3.1. (a) One-dimensional gasdynamic interaction and associated states for detonation wave collision with contact surface (CS) with formation of (b) a reflected shock wave and (c) a reflected rarefaction wave at the contact surface.

Following Paterson [134] and Pack [135], the properties of the transmitted shock wave can be determined by considering a reflected shock, a rarefaction, or a Mach wave from the contact surface following the collision. Consider a shock wave, where for idealized flow

in the absence of friction and heat transfer, the locus of all possible instantaneous states behind a reflected shock wave from the contact surface is given by [138]

$$u_{2'} = u_2 - a_2 \left(\frac{p_{2'}}{p_2} - 1\right) \left[\frac{\gamma_2 (\gamma_2 - 1)}{2} \left(1 + \frac{\gamma_2 + 1}{\gamma_2 - 1} \frac{p_{2'}}{p_2}\right)\right]^{-1/2} = u_2 - \phi (p_{2'}) \tag{3.1}$$

Similarly, the locus of all possible instantaneous states behind a reflected, (isentropic) rarefaction wave from the contact surface is given by [138]

$$u_{2'} = u_2 - \frac{2a_2}{\gamma_2 - 1} \left[\left(\frac{p_{2'}}{p_2}\right)^{(\gamma_2 - 1)/2\gamma_2} - 1\right] = u_2 - \psi(p_{2'}) \tag{3.2}$$

Lastly, the locus of all possible instantaneous states behind the transmitted shock wave is given by

$$u_{0'} = u_0 + a_0 \left(\frac{p_{0'}}{p_0} - 1\right) \left[\frac{\gamma_0 (\gamma_0 - 1)}{2} \left(1 + \frac{\gamma_0 + 1}{\gamma_0 - 1} \frac{p_{0'}}{p_0}\right)\right]^{-1/2} = u_0 + \chi (p_{0'}) \tag{3.3}$$

The strength and velocity of the transmitted shock wave into the inert gas can be solved for given appropriate constraints to (3.1), (3.2) and (3.3). The constraints for this particular interaction require the pressure and gas velocity behind the transmitted shock be exactly equal to the pressure and gas velocity following the reflected characteristic at the contact surface, namely $p_{0'} = p_{2'}$ and $u_{0'} = u_{2'}$. Therefore, for the cases of a shock, a rarefaction, or a Mach reflection from a stationary contact surface ($u_0 = 0$), the following three conditions exist, respectively:

$$u_2 - \phi (p_{2'}) = \chi (p_{0'}) \qquad (p_{2'} > p_2) \tag{3.4}$$

$$u_2 - \psi (p_{2'}) = \chi (p_{0'}) \qquad (p_{2'} < p_2) \tag{3.5}$$

$$u_2 = u_{2'} \qquad (p_{2'} = p_2) \tag{3.6}$$

Further, with p_2, u_2, a_2 and γ_2 solely dependent on the selection of the detonation state, and with the constraint $p_{0'} = p_{2'}$, (3.4)–(3.6) provide separate equations for a single unknown, namely $p_{2'}$, depending on whether $p_{2'} \gtrless p_2$ or equal to p_2. Therefore, by numerically solving for $p_{0'} = p_{2'}$ in (3.4)–(3.6), the transmitted shock strength and wave velocity can be obtained for an arbitrary gaseous detonable mixture for conditions that result in one of

three possibilities, namely, a reflected shock, a rarefaction or a Mach wave occurs at the contact surface, respectively.

To determine the final transmitted shock solution, the post-detonation state 2 must be specified, namely, the post-detonation pressure p_2, gas velocity u_2, sound speed a_2, and ratio of specific heats γ_2 must be known. The most obvious state to consider would be the vN state immediately behind the leading shock front of the detonation wave. This selection is consistent with the gasdynamic interaction depicted in Fig. 3.1. It is noted here that making use of the ZND model widens the versatility of the current theoretical work to a family of solutions that can be obtained based on the selection of state 2. At this point, it is convenient to make use of the reaction progress variable λ that is associated with a particular post-detonation state. The different states of reactants passing through the ZND detonation wave structure can be uniquely assigned a value of λ from zero to unity, depending on the given location in the combined induction and reaction zones. At the leading shock front, the gas is assumed to be adiabatically compressed to the vN state, which can be regarded as $\lambda = 0$. Similarly, at the equilibrium CJ plane, all relevant chemical reactions have fully terminated and the reaction progress variable is taken as $\lambda = 1$. The intermediate, quasi-equilibrium states residing in the induction and reaction zones will have a λ value ranging from zero through unity. For an appropriately considered family of solutions, the cases of $\lambda = 0$, $1/2$ and 1 are chosen in this study, where only the case of $\lambda = 1/2$ is arbitrary. It is noted that for general detonable mixtures, there are usually numerous reaction progress variables that correspond to the various species in the post-detonation equilibrium state. Hence, for this study, the state corresponding to $\lambda = 1/2$ is taken as the average temperature location within the reaction between the vN and CJ equilibrium state. Note that the case of $\lambda = 1$ is identical to the theoretical approach taken by Paterson [134].

For $\lambda = 0$, where the detonation state 2 is defined by the vN peak, the pressure, gas velocity in the wave reference frame, and sound speed are given by

$$p_{vN} = \frac{2\gamma_1 M_{CJ}^2 - (\gamma_1 - 1)}{\gamma_1 + 1} p_1 \tag{3.7}$$

$$u_{vN} = \frac{2 + (\gamma_1 - 1)M_{CJ}^2}{(\gamma_1 + 1)M_{CJ}^2} W_{CJ} \tag{3.8}$$

$$a_{vN} = \frac{\left\{\left[2\gamma_1 M_{CJ}^2 - (\gamma_1 - 1)\right]\left[(\gamma_1 - 1)M_{CJ}^2 + 2\right]\right\}^{1/2}}{(\gamma_1 - 1)M_{CJ}^2} W_{CJ} \tag{3.9}$$

Additionally, the vN state can be regarded as calorically perfect such that, $\gamma_{vN} = \gamma_1$. For $\lambda = 1$, where the detonation state 2 is defined by the equilibrium CJ state, the pressure, gas velocity in the wave reference frame, and sound speed are given by [65]

$$p_{CJ} = \frac{\gamma_1 M_{CJ}^2 + 1}{\gamma_2 + 1} p_1 \tag{3.10}$$

$$u_{CJ} = \frac{\gamma_1 M_{CJ}^2 - \gamma_2}{\gamma_1 M_{CJ}^2} \frac{1}{\gamma_2 + 1} W_{CJ} \tag{3.11}$$

$$a_{CJ} = \frac{\gamma_1 M_{CJ}^2 + 1}{\gamma_1 M_{CJ}^2} \frac{\gamma_2}{\gamma_2 + 1} W_{CJ} \tag{3.12}$$

In the above equations, γ_2 represents the equilibrium ratio of specific heats at the rear surface of the chemical reaction zone. Lastly, to calculate the detonation properties and the $\lambda = 1/2$ state, the chemical kinetics computer program Cantera with a Matlab shock and detonation toolbox are utilized [24, 29, 30]. The three distinct detonation states utilized in this study are summarized in Table 3.1.

Table 3.1. Denotation of state 2 using ZND detonation wave model.

λ	p_2	u_2	a_2	γ_2
0	p_{vN}	u_{vN}	a_{vN}	γ_{vN}
1/2	$p_{1/2}$	$u_{1/2}$	$a_{1/2}$	$\gamma_{1/2}$
1	p_{CJ}	u_{CJ}	a_{CJ}	γ_{CJ}

The gasdynamics of a reflected shock and rarefaction from the contact surface are demonstrated in the form of an x–t diagram in Fig. 3.2. As shown in Fig. 3.2(a), the incident transmitted shock wave propagates with a slower wave velocity than the detonation wave velocity yielding a reflected shock wave from the contact surface. Alternatively, as shown in Fig. 3.2(b), the incident transmitted shock wave propagates with a faster wave velocity compared to the detonation wave velocity in the event of a rarefaction reflection from the contact surface. The third scenario, not depicted in Fig. 3.2, is a reflected Mach wave. In this case, the incident transmitted shock velocity is equal to the detonation wave velocity. The characteristics of these incident shock wave velocities will be discussed in a later section from the context of the relative acoustic impedance between the detonable and inert gases.

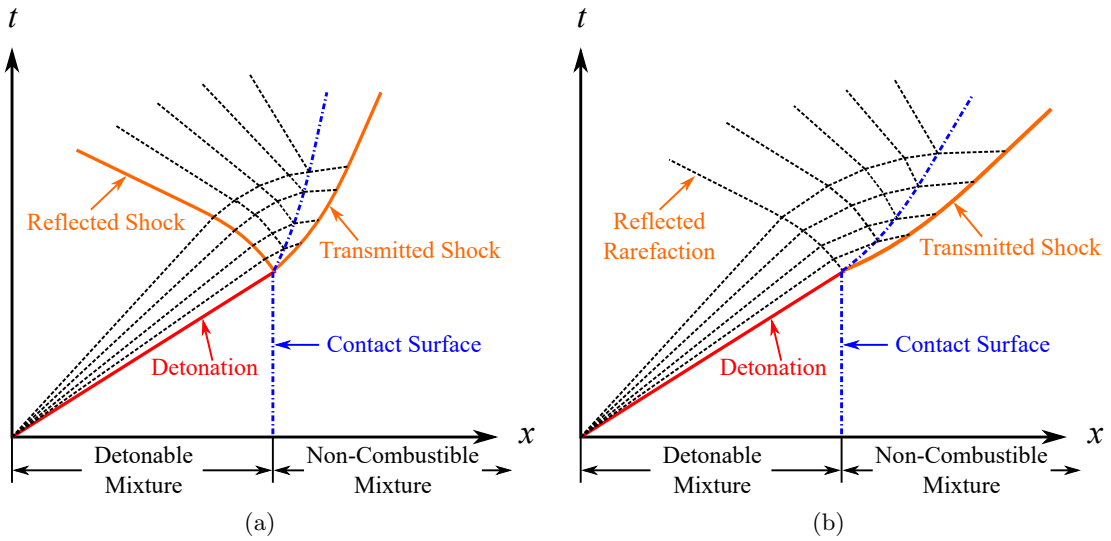

Figure 3.2. x–t-diagram of (a) shock reflection and (b) rarefaction reflection at the contact surface.

For completeness, it is worth considering the effects of vibrational excitation in the gas immediately following the transmitted shock, especially when comparing with experimental measurements made in the detonation-driven shock tube facility in the following subsec-

tion. In the region just downstream of the diaphragm where time-of-flight measurements are taken, it is possible for the post-transmitted shock gas to be in a state of vibrational nonequilibrium or complete vibrational equilibrium. In the current study, the temperatures experienced behind the shock are on the order of 2,000 K, which is high enough to vibrationally excite any oxygen molecules present in the driven section. Therefore, it is pertinent to estimate the distance for which the shock reaches a state of vibrational equilibrium regarding the experimental cases of 100 and 20 percent air by volume in the driven section. In the case of 20 percent air by volume, the remaining gas is helium, which will effectively lower the vibrational relaxation time as a result of oxygen molecules more frequently colliding with a monatomic partner. Thus, it is to be expected that the case of a driven section helium mole fraction equal to 0.8 will yield transmitted shock solutions where vibrational equilibrium is reached within a shorter distance downstream of the diaphragm.

From the RH shock jump conditions, the nonequilibrium post-shock temperature and pressure can be estimated by averaging the frozen and equilibrium states. Further, using the estimated nonequilibrium pressure and temperature, the vibrational relaxation time can be approximated with empirical correlations based on conventional Landau–Teller plots ($\ln p\tau_{vib}$ vs. $T^{-1/3}$) [139, 140]. Thus, considering a transmitted shock moving at Mach 5 in air and a helium–air mixture with a helium mole fraction of 0.8, the approximate vibrational relaxation time is calculated to be 0.82 μs and 0.013 μs, respectively. These relaxation times indicate that the transmitted shock will reach a state of vibrational equilibrium within approximately 1.4 mm and 43 μm downstream of the diaphragm in the respective cases specified above. Note, this is before the first pressure transducer used to conduct time-of-flight measurements for the transmitted shock. Therefore, it is expected that the experimentally created transmitted shock waves would be in a state of vibrational equilibrium when passing the first transducer used in the time-of-flight measurement. For this reason, equilibrium solutions have been computed and included in the results alongside calorically perfect gas solutions discussed at the beginning of this section. It is worth not-

ing that the vibrational equilibrium transmitted shock solutions deviate from the calorically perfect gas solutions by a maximum of 2.5 percent in the case of 100 percent air by volume in the driven section. This small deviation is attributed to the relatively small fraction of O_2 present in the air mixture, which is roughly 21 percent by volume in the case of air, and only roughly 4.2 percent by volume in the case of helium mole fraction equal to 0.8. Additionally, it is noted that these curves provide the upper and lower bounds for transmitted shock solutions where vibrational non-equilibrium is present.

A final comment is made regarding the range of application and validity of the current theoretical work. As seen in Fig. 3.2, the Taylor wave following the detonation wave transmits through the reflection type and now traveling contact surface following the collision. This allows the Taylor wave to overtake the transmitted shock wave, which causes the transmitted shock to decay from its incident strength as it continues to propagate into the inert gas. However, the current theoretical work only treats the incident transmitted shock strength and velocity. The decay behavior of the wave is not accounted for and requires additional theoretical treatment, such as that discussed by Fickett [136]. Further, the simplified one-dimensional ZND structure of a detonation wave is purely theoretical and not entirely in concert with experimental observation. As discussed previously in Ch. 1, a physical detonation wave is composed of a transient three-dimensional cellular structure for which the steady, planar, and one-dimensional ZND theory fails to capture. Despite this aspect of the experimentally observed detonation wave structure, the theoretical work presented herein remains suitable for providing insights regarding the role of selecting various states within the simplified detonation structure and the corresponding effect on the transmitted shock properties.

3.3 Experimental Setup

An experiment was constructed to validate the theoretical analysis discussed above. The setup comprised of a 1.91 cm diameter detonation tube with an overall length of 1.93

m and a detonation driver section length of 1.22 m. The driver and driven sections featured an array of eight high-frequency PCB model 111A24 pressure transducers for obtaining pressure and time-of-flight measurements of the incident detonation wave and transmitted shock. For the experiments, only detonable mixtures of H_2 and O_2 were considered. To provide an appropriate sweep of test conditions, the equivalence ratio of the oxyhydrogen mixture was varied from $0.5 \leq \phi \leq 1.5$. Similarly, the driven section was filled with a non-combustible mixture of helium and air where the helium mole fraction was varied from $0.0 \leq X_{He} \leq 1.0$. This enabled a large range of experimental testing conditions for both a reflected shock and rarefaction to be observed from the contact surface. Fig. 3.3 shows a schematic of the experimental setup and the transducer locations. Table 3.2 provides the location of each transducer relative to the diaphragm. Here the negative dimensions indicate the transducers upstream in the driver section.

For each test, both the driver and driven sections were evacuated down to roughly 1 kPa before filling each section with the desired oxyhydrogen and helium–air mixtures. To mitigate the possibility of contaminants or impurities in the desired mixtures, the sections were then refilled with either O_2 or helium and evacuated two additional times. This ensured the remaining gas left in each sections was the appropriate gas for establishing the correct mixture. The desired oxyhydrogen equivalence ratio and helium–air mixtures were obtained by using partial pressures measured by two analog pressure gauges with a resolution of 3.4 kPa. This gauge resolution permits setting the desired oxyhydrogen mixture equivalence ratio with a minimum and maximum uncertainty of $\pm$ 0.026 and $\pm$ 0.111, corresponding to the fuel lean and fuel rich equivalence ratios of 0.5 and 1.5, respectively. Further, this gauge resolution permits setting the driven section helium mole fraction with a minimum and maximum uncertainty of $\pm$ 0.017 and $\pm$ 0.021, corresponding to the cases of helium–air mixtures with helium mole fractions of 0.2 and 0.8, respectively. An automotive spark plug was used in order to obtain a detonation wave in the driver section of the setup. Moreover, to aid in the DDT transition process, a Shchelkin spiral with a blockage ratio

$BR = 1.58/2.85 = 0.55$ was placed at the head end of the driver section. To allow for proper mixing of the oxyhydrogen mixture after filling, the static detonable mixture was left undisturbed in the driver section for 15 minutes prior to spark ignition of the detonable driver mixture.

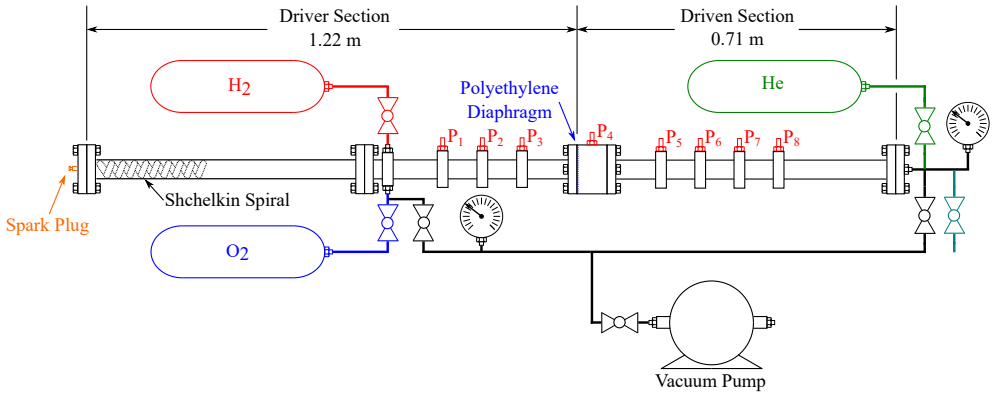

Figure 3.3. Schematic of detonation-driven shock tube experimental setup.

Table 3.2. Pressure transducer location relative to diaphragm (all dimensions in cm).

P_1	P_2	P_3	P_4	P_5	P_6	P_7	P_8
-30.48	-20.32	-10.61	1.91	13.97	24.13	34.29	44.45

To determine the influence of using a thin diaphragm as a contact surface, a sweep of stacked 12.7 μm thick, low-density polyethylene diaphragms was conducted to determine the differential rupture pressure and ratio of transmitted-to-detonation wave velocity. Fig. 3.4(a) shows the results of rupture pressure versus the number of diaphragms. The relationship can be seen to be adequately linear over the range of tested diaphragms with a minimum differential rupture pressure of approximately 46 ± 3.5 kPa corresponding to a single diaphragm.

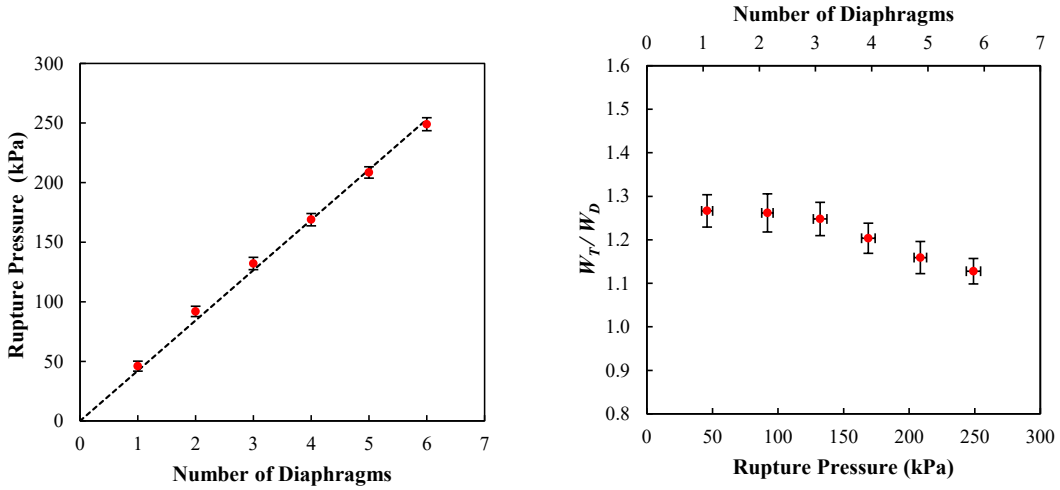

Figure 3.4. (a) Rupture pressure vs. number of diaphragms and (b) ratio of transmitted shock to detonation wave velocity vs. diaphragm rupture pressure for a stoichiometric oxyhydrogen detonation driver and helium driven section.

Figure 3.4(b) shows the results of the transmitted shock to detonation wave velocity ratio for the sweep of diaphragms and associated rupture pressures. In this case, the H_2/O_2 mixture was stoichiometric and the inert gas was He. These conditions should result in a reflected rarefaction from the contact surface and are most sensitive to the nature of the reflection type that takes place at the contact surface. Further, it is noted that during these diaphragm experiments, the average peak detonation pressure was measured to be roughly 2,609 $\pm$ 37.3 kPa, which was well above that required to rupture all of the various diaphragms. Additionally, if reflected shocks were observed as a result of the physical diaphragm, then these conditions will make it most evident. It is clear from Fig. 3.4(b) that there was a negligible effect of diaphragm rupture pressures on the ratio of transmitted shock to detonation wave velocity for rupture pressures less than approximately 140 kPa. Further, for diaphragm rupture pressures less than 140 kPa, there was no observed shock reflection at transducer P_3 following the collision, which further indicated the single diaphragm had a negligible effect. Similar results were obtained by Li et al. [141], where the effects of diaphragms were investigated for detonation transmission across an interface

of two detonable mixtures. Although rupture pressures were not reported in that study, Li et al. [141] showed that polyester diaphragms less than 50 μm thick yielded detonation wave propagation velocities that approached the case of no diaphragm when a slide gate valve was utilized. Therefore, for these experiments, the driver and driven sections of the setup were separated by a single 12.7 μm low-density polyethylene diaphragm to act as the contact surface of the detonable and non-combustible mixtures.

3.4 Comparison of Theoretical and Experimental Results

To ensure that a meaningful comparison can be made between the analysis and experimental results, it must be shown that a detonation wave traveling near the CJ velocity is established for the range of oxyhydrogen mixtures used within this study. Fig. 3.5 shows the measured detonation wave velocity results from applying a time-of-flight method with the array of pressure transducers in the driver side. For fuel-rich equivalence ratios, the error between the measured detonation wave velocity and the CJ theory was less than one percent. However, for the fuel lean mixtures, an average error of approximately seven percent was observed. These error margins are thought to be acceptable for carrying out the full experimental sweep of test conditions for validating the theoretical work. Thomas et al. [137] never directly quoted the incident detonation wave velocity in their study; however, similar error with the CJ theory can be deduced from various plots. It can also be noted that a fully-developed detonation wave was observed in the present study by the first pressure transducer P_1 at a distance of 91.5 cm from the ignition source at the head end of the driver section. Subsequent pressure histories also indicated the presence of a fully-developed detonation wave which adds evidence that such a wave was properly established.

For the transmitted shock, the wave velocity is determined by using a time-of-flight method between pressure transducers P_4 and P_5, where transducer P_4 is located 1.91 cm from the diaphragm and 12.1 cm from transducer P_5. Fig. 3.6 compares the present analysis and the measured transmitted shock wave velocities, where Fig. 3.6(a) corresponds to taking

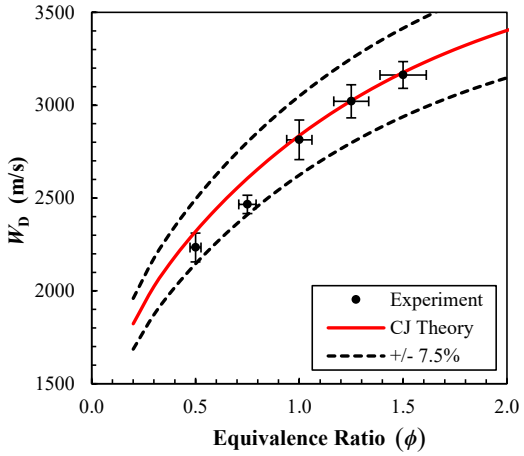

Figure 3.5. Measured detonation wave velocity for different oxyhydrogen mixtures compared with the CJ theory.

state 2 as the $\lambda = 0$ or vN state, Fig. 3.6(b) corresponds to the $\lambda = 1/2$ or half-reaction quasi-equilibrium state, and Fig. 3.6(c) corresponds to the $\lambda = 1$ or equilibrium CJ state. In these experiments, a reflected shock was observed for all equivalence ratios when the driven section is filled with 100 percent air, namely, when $X_{He} = 0$. However, a reflected rarefaction was observed for all other tested equivalence ratios when the driven side contains a mixture of helium–air with $X_{\mathrm{He}} = 0.8$ and 1.0.

Comparison of the measured shock wave velocities and the theoretical predictions suggested that using either the vN state or half-reaction quasi-equilibrium state as the post-detonation state yielded the best agreement in the case of a reflected rarefaction. However, the accuracy became diminished when reflected shock waves are observed from the contact surface. This is true for both the calorically perfect and equilibrium transmitted shock solutions. The opposite results were obtained when using the equilibrium CJ state as the post-detonation state in the analytical calculations. Fig. 3.6(c) shows that moderate agreement is achieved when the driven side was filled with air only and a reflected shock was observed from the contact surface. However, mostly poor agreement is obtained in the case of reflected rarefaction. The average error over the full test range between the measured transmitted shock wave velocities and theoretical predictions based on various selections of

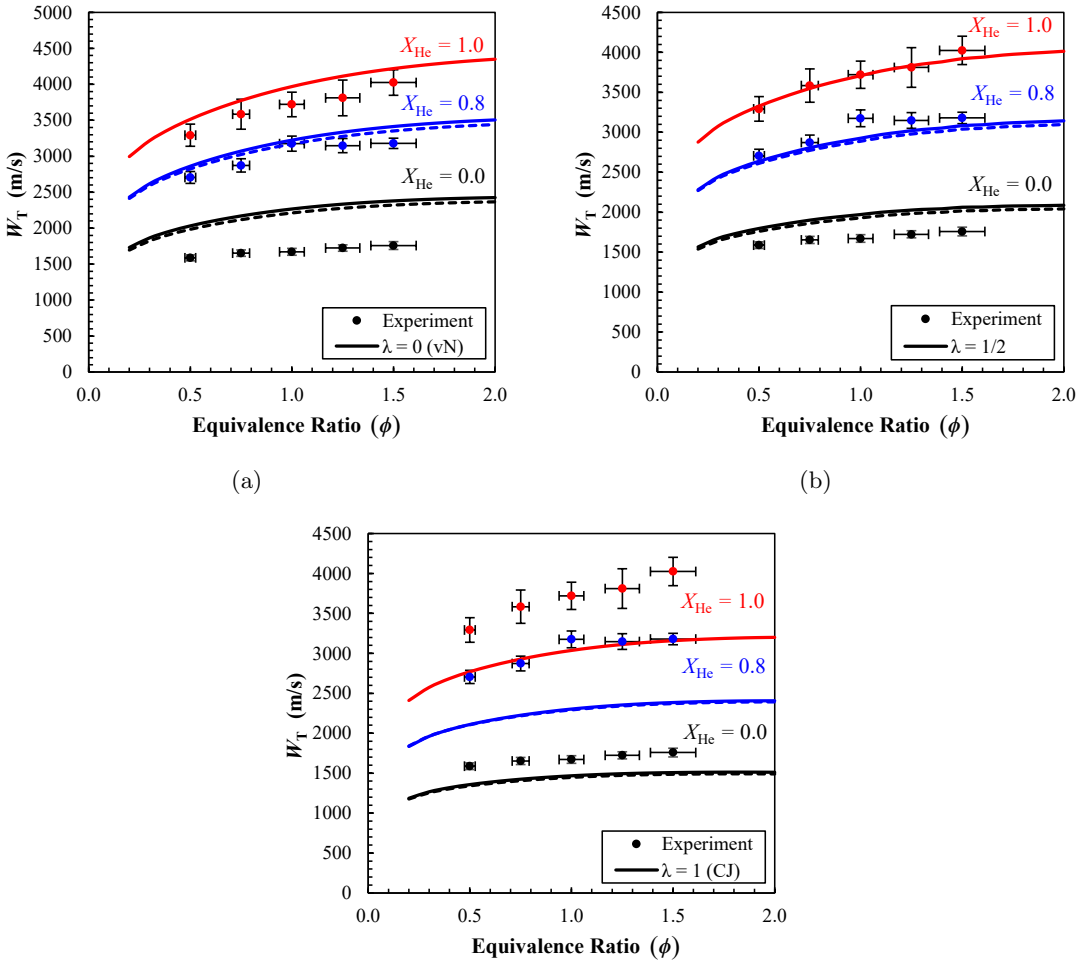

Figure 3.6. Comparison of measured and theoretical transmitted shock velocity for (a) $\lambda = 0$, (b) $\lambda = 1/2$, and (c) $\lambda = 1$ vs. oxyhydrogen mixture equivalence ratio at helium mole fractions of 0.0, 0.8, and 1.0, where the solid and dashed lines represent the calorically perfect and equilibrium solutions.

the post-detonation state is summarized as 15.3, 6.8, and 18.7 percent for $\lambda = 0$, 1/2 and 1, respectively. In the case of a reflected rarefaction from the contact surface, the average error is summarized as 6.1, 2.1, and 21.4 percent for $\lambda = 0$, 1/2, and 1, respectively. Lastly, in the case of a reflected shock from the contact surface, the average error is summarized as 33.5, 16.4, and 13.4 percent for $\lambda = 0$, 1/2, and 1, respectively.

The second range of test conditions consisted of sweeping the helium–air mixture ratio by sweeping the helium mole fraction in the driven section from 0.0–1.0 at driver oxyhydrogen mixture equivalence ratios of 0.5, 1.0, and 1.5. The measured transmitted shock wave velocity and theoretical prediction are provided in Fig. 3.7 where Fig. 3.7(a) corresponds to taking state 2 as the $\lambda = 0$ or vN state, Fig. 3.7(b) corresponds to the $\lambda = 1/2$ or half-reaction, quasi-equilibrium state, and Fig. 3.7(c) corresponds to the $\lambda = 1$ or equilibrium CJ state. For these conditions, a reflected shock from the contact surface was observed for helium mole fractions of less than 0.4, 0.6 and 0.8 for oxyhydrogen mixture equivalence ratios of 0.5, 1.0 and 1.5, respectively. Similar behavior regarding the comparison of theoretical and measured transmitted shock wave velocities are shown in Fig. 3.7. For instance, better agreement is observed when using the vN or half-reaction quasi-equilibrium states as the post-detonation state in the case of a reflected rarefaction from the contact surface. Alternatively, the agreement becomes diminished as the helium mole fraction in the driven section reduced to zero and the driven section consisted solely of air. Once again, the reverse behavior is true for the case of selecting the equilibrium CJ state as the post-detonation state. An average error is not reported in this case as the range of test conditions yields both reflected shock and rarefaction waves from the contact surface for a sweep of helium mole fraction at all test equivalence ratios.

3.5 Non-Dimensional Acoustic Impedance Results

It is desirable to introduce non-dimensional parameters to aid in collapsing the data into a characteristic physical relationship regarding the interaction of a detonation wave with a contact surface. An additional interpretation regarding the nature of the reflection type can be established by making use of the transmitted shock and detonation wave acoustic impedance. Past numerical studies have shown that the generalized acoustic impedance for a shock wave can be used to predict the reflection type at the contact surface following the collision of a detonation wave [98]. In essence, the nature of the reflection type is governed

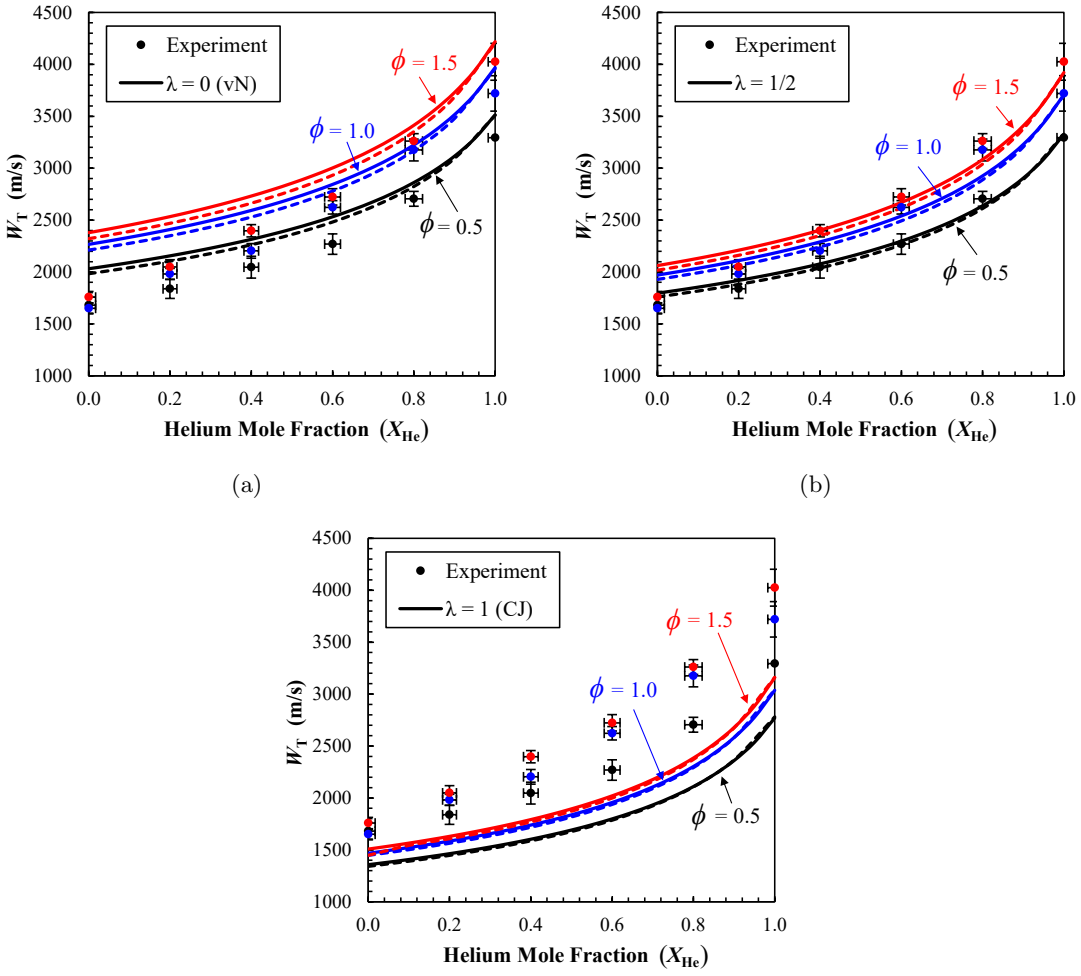

Figure 3.7. Comparison of measured and theoretical transmitted shock velocity for (a) $\lambda = 0$, (b) $\lambda = 1/2$ and (c) $\lambda = 1$ vs. helium mole fraction at oxyhydrogen mixture equivalence ratios of 0.5, 1.0, and 1.5, where the solid and dashed lines represent the calorically perfect and equilibrium solutions.

by the ratio of acoustic impedance across the contact surface. The generalized acoustic impedance depends on the density, specific heat ratio, incident detonation and transmitted shock wave pressure ratio, and are given by [142]

$$z_0 = \left\{ \frac{\rho_0 p_0}{2} \left[(\gamma_0 + 1) \frac{p_{0\prime}}{p_0} + (\gamma_0 - 1) \right] \right\}^{1/2} \tag{3.13}$$

$$z_1 = \left\{ \frac{\rho_1 p_1}{2} \left[(\gamma_1 + 1) \frac{p_2}{p_1} + (\gamma_1 - 1) \right] \right\}^{1/2} \tag{3.14}$$

where the subscript 2 and $0'$ correspond to the post-detonation state selected for the theoretical calculations, and the resulting post-transmitted shock state, respectively. In this representation, the acoustic impedance is simply a measure of the mass flux through the shock front of the detonation wave as a consequence of the upstream gas properties. This definition is really only appropriate for a shock wave or, likewise, the vN state of a detonation wave. Nonetheless, the definition can be extended to any general moving discontinuity including the quasi-equilibrium state within the detonation wave structure in which heat release is observed. It follows that in the case of $\lambda = 0$, if $z_0/z_1 > 1$ then a reflected shock wave will occur when the detonation wave collides with the contact surface. Similarly, if $z_0/z_1 < 1$ then a reflected rarefaction will result from the detonation contact surface collision. Lastly, if $z_0/z_1 = 1$, namely, the acoustic impedances between the detonable and non-combustible mixtures are identical, then the resulting reflection type is a Mach wave. Therefore, the first non-dimensional parameter is taken as the ratio of acoustic impedance between driven and driver sections, respectively.

$$Z = \frac{z_0}{z_1} \tag{3.15}$$

The second non-dimensional parameter can be taken as the ratio of transmitted shock wave velocity to detonation wave velocity.

$$\Gamma = \frac{W_T}{W_{CJ}} \tag{3.16}$$

This is an effective way of normalizing the results to unity in the case of a reflected Mach wave where $\Gamma = 1$ when $Z = 1$. The experimental acoustic impedance is determined using the measured detonation and transmitted wave velocities and scaling by the appropriate gas density to recover the mass flux ratio. Fig. 3.8 shows the results of all the experimental tests collapsed into a single plot using the non-dimensional relationships in (3.15) and (3.16).

In this representation, it is evident that the selection of state 2 in the theoretical calculations influences the observed agreement over the range of conditions yielding reflected shock and rarefaction waves. In the case of a reflected rarefaction, $Z < 1$, the ratio of

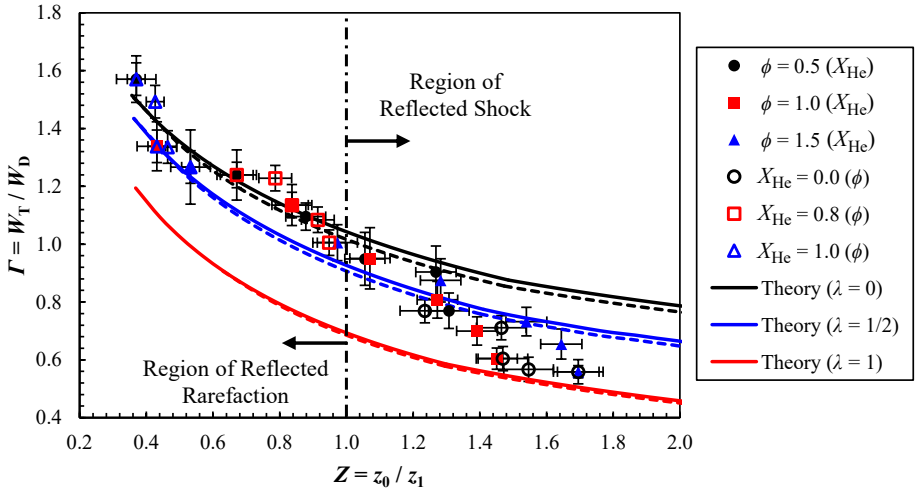

Figure 3.8. Non-dimensional transmitted shock to detonation wave velocity ratio vs. ratio of acoustic impedance, where the solid and dashed lines represent the calorically perfect and equilibrium solutions. The experimental parameter in parentheses in the legend title represents the sweep parameter at the given condition.

transmitted-to-detonation wave velocity Γ is best represented by taking $\lambda = 0$ as the post-detonation state. This is despite the fact that taking $\lambda = 1/2$ provides the best estimate for the physical transmitted shock wave velocity. As seen in Fig. 3.8, when $Z > 1$, the experimental data appear to begin converging toward the theoretical curve associated with taking the equilibrium CJ state as state 2 in the theoretical calculations. It is unknown if the experimental data actually converges toward the $\lambda = 1$ or CJ curve for larger values of Z, and appropriate confirmation would require further experimentation with heavier gases in the driven section. Despite this, the current work has shown that making use of the non-dimensional parameters Γ and Z is an effective approach that provides insightful results regarding the role of the post-detonation state and the subsequent transmitted shock properties.

To demonstrate the experimental cases of reflected shock and rarefaction from the contact surface, Fig. 3.9 provides experimental pressure traces of transducer P_3 for the case of $Z = 0.36$ (reflected rarefaction) and $Z = 1.69$ (reflected shock), respectively. For plotting purposes, the time has been scaled such that the reflected shock or rarefaction reached

transducer P_3 at $t/t_{ref} = 1$, where t_{ref} is the time at which the reflection type reaches the transducer location. Note that a reflected shock appeared when using an inert gas with an acoustic impedance substantially higher than that of the detonable mixture. As will be shown in the following chapters, this gasdynamic process can drastically affect the evolving flow field in a PDE thrust chamber.

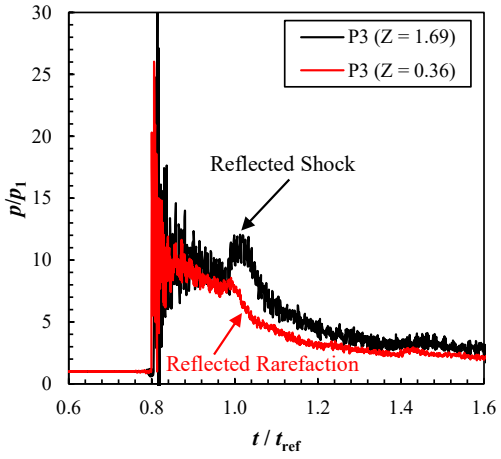

Figure 3.9. Experimental pressure trace of transducer P3 for the case of shock reflection ($Z = 1.69$) and rarefaction reflection ($Z = 0.36$).

In summary, a theoretical model is formulated such that an arbitrary selection of the post-detonation state can be chosen based on the reaction progress variable λ within the one-dimensional ZND detonation wave structure. With this, the transmitted shock properties into a non-combustible gas mixture can be determined for the cases of a reflected shock, rarefaction, and Mach wave at the contact surface separating the detonable and non-combustible mixtures. Further, a detonation-driven shock tube facility was used to experimentally investigate the behavior of transmitted shock waves into a non-combustible helium–air mixture for a range of oxyhydrogen driver equivalence ratios. Over the range of considered test conditions, it was shown that selecting the half-reaction quasi-equilibrium state ($\lambda = 1/2$) as the representative post-detonation state, yields the best prediction for

the transmitted shock wave velocity into the non-combustible mixture. Additionally, non-dimensional parameters were formulated based on the ratio of acoustic impedance between the non-combustible and detonable mixtures, and transmitted shock and detonation wave velocities. This non-dimensional relationship demonstrated that in the range of reflected rarefaction waves from the contact surface where $Z < 1$, the ratio of transmitted shock to detonation wave velocity is best represented by taking the vN state ($\lambda = 0$) as the representative post-detonation state in the theoretical calculations. Similarly, in the range of reflected shock waves from the contact surface where $Z > 1$, the ratio of transmitted shock to detonation wave velocity is best represented by taking an intermediate state between the vN peak ($\lambda = 0$) and equilibrium CJ states ($\lambda = 1$) as the representative post-detonation state in the theoretical calculations. Moreover, for cases of $Z \gg 1$, the the ratio of transmitted shock to detonation wave velocity appears to be best represented by taking the equilibrium CJ state ($\lambda = 1$) as the representative post-detonation state in the theoretical calculations. For this reason, the $\lambda = 1/2$ state will be used in all of the subsequent analysis, as this state provides the best overall agreement with the experimentally measured transmitted shock velocities W_T, and provides the least error for $\Gamma = W_T/W_{CJ}$ in Fig. 3.8 for the complete range of tested acoustic impedance ratios.

CHAPTER 4

METHOD OF CHARACTERISTICS MODELING [1]

4.1 Introduction

A major part of this research is to perform a broad parametric study of PDEs under various operating conditions in order to gain insightful understanding of the gasdynamic phenomena that governs the primary performance metrics. For the purposes of modeling general PDE thrust chamber flow fields, an unsteady, quasi-one-dimensional, MOC-based solver is developed. This type of solver is a computationally inexpensive approach that takes advantage of the hyperbolic nature of the governing equations for an idealized unsteady, quasi-one-dimensional flow, and directly integrates the transient flow field using a simple time-marching algorithm. With a simple MOC-based model, the thrust chamber flow field can readily be computed along the characteristic pathlines and left- and right-running Mach lines [143, 144]. Moreover, a MOC-based solver treats discontinuities such as detonations, shocks, and contact surfaces exactly, thereby eliminating the need for elaborate shock capturing and gradient-based mesh refinement techniques commonly employed in higher-fidelity numerical models. Consequently, complex interface collisions such as detonation waves colliding with contact surfaces can be treated exactly without being dependent on grid refinement. When implemented, these advantages permit convenient and rapid modeling of general PDE thrust chamber flow fields and the associated propulsive performance.

Previously, Morris [70] developed a simplified one-dimensional MOC model in order to perform parametric studies of the single-cycle performance of fully-filled PDEs operating with various propellants and at different blowdown pressure ratios. Similarly, Guzik

[1] Parts of this chapter were published in Peace, J.T. and Lu, F.K., "Performance Modeling of Pulse Detonation Engines Using the Method of Characteristics," *Aerospace Science and Technology*, vol. 88, pp. 51–64, 2019. doi: 10.1016/j.ast.2019.03.015

et al. [71] developed a simplified quasi-one-dimensional MOC model based on the left- and right-running Mach lines in order to evaluate the single-cycle gasdynamic flow field and performance of fully- and partially-filled PDEs, as well as PDEs fitted with quasi-steady ideal nozzles. In the current study, a general quasi-one-dimensional MOC model is developed using the approach of [143, 144] in order to model the single-cycle evolution of gasdynamic waves and discontinuities in general PDE thrust chamber flow fields and the associated performance. The current MOC model differs from that of [71, 145], in that three characteristics are used to develop the thrust chamber flow field solution, namely the characteristic left- and right-running Mach lines and pathlines. Similarly, the quasi-one-dimensional nozzle flow is treated directly and no restriction is made regarding the nozzle length, thereby eliminating the need for a quasi-steady nozzle flow assumption. For the purposes of treating the one-dimensional interaction of the detonation wave with the contact surface separating the detonable and non-combustible mixtures, the method detailed in Ch. 3 is utilized. Moreover, to aid the development of the model, a detailed description of the necessary unit process algorithms required to accurately solve the PDE thrust chamber flow field is provided. Finally, the MOC model is validated against existing numerical and experimental data for both hydrogen and hydrocarbon detonable propellants operating over a range of fill fractions, blowdown pressure ratios, and nozzle expansion area ratios.

4.2 Governing Equations

The governing equations for an unsteady, quasi-one-dimensional flow in the absence of friction, mass addition, and heat transfer take the form

$$\frac{\partial \rho}{\partial t} + u\frac{\partial \rho}{\partial x} + \rho\frac{\partial u}{\partial x} + \rho u\frac{A'(x)}{A(x)} = 0 \tag{4.1}$$

$$\frac{\partial u}{\partial t} + u\frac{\partial u}{\partial x} + \frac{1}{\rho}\frac{\partial p}{\partial x} = 0 \tag{4.2}$$

$$\frac{\partial p}{\partial t} + u\frac{\partial p}{\partial x} - a^2\left(\frac{\partial \rho}{\partial t} + u\frac{\partial \rho}{\partial x}\right) = 0 \tag{4.3}$$

Note that the energy equation has been replaced by the combined entropy and sound speed equations, a simplification specific to isentropic flow fields. Because these governing equations are restricted to isentropic flow without heat addition, all the heat release from the detonation wave must be assumed to take place at a discontinuity. In such a flow field, the above equations are then only appropriate for treating transient flow gradients between boundary conditions and discontinuities. This aspect will be discussed throughout the remainder of this section. Application of the MOC to the governing equations in (4.1)-(4.3), which is carried out in Appendix B, yields the following ordinary differential characteristic and compatibility equations [143, 144]

$$\left(\frac{dt}{dx}\right)_0 = \lambda_0 = \frac{1}{u} \tag{4.4}$$

$$\left(\frac{dt}{dx}\right)_\pm = \lambda_\pm = \frac{1}{u \pm a} \tag{4.5}$$

$$dp_0 - a^2 d\rho_0 = 0 \tag{4.6}$$

$$dp_\pm \pm \rho a du_\pm = -\rho a^2 u \frac{A'(x)}{A(x)} dt_\pm \tag{4.7}$$

where Eqs. (4.4) and (4.6) apply along pathlines and denoted by the subscript 0, and Eqs. (4.5) and (4.7) apply along the right- and left-running Mach lines and denoted by the subscript $\pm$. This approach differs from previous MOC-based analysis of PDE flow fields, such as that carried out by Guzik et al. [71, 145], in that three distinct characteristics are used presently to develop the flow field solution at each point. In Guzik et al.'s MOC approach [71, 145], a homentropic assumption was employed which only requires the right- and left-running Mach lines to develop the flow field at each solution point. In that model, entropy changes were assumed to only take place at discontinuities, and isentropic regions were approximated by strips of homentropic regions.

In the current approach, entropy changes are also only assumed to take place at discontinuities; however, isentropic regions are directly treated with the isentropic assumption and the additional pathline characteristic. An example of such a flow field occurs in both

the partially-filled PDE and PDE equipped with a diverging nozzle in the region that develops behind the decaying transmitted shock wave. As the shock decays, each pathline passing through the shock is subjected to a different entropy jump, such that an entropy gradient forms in the flow field behind the decaying shock. Moreover, the current MOC approach directly treats the starting nozzle flow field, such that no quasi-steady nozzle flow assumption is required. This permits treating nozzles of general length and aids to capture the effects of the transient nozzle starting process on thrust production.

With a MOC-based method, the solution is developed in x–t space by numerically integrating Eqs. (4.4)–(4.7), namely, integrating along the characteristic pathlines and right- and left-running Mach lines coupled with their respective compatibility equations. Compared to a conventional unsteady, one-dimensional Euler solver, a MOC-based solver permits rapid solutions at low computational expense. The MOC approach provides a convenient and, as it turns out, accurate approach for performing parametric sweeps of PDE flow fields. Moreover, a MOC-based solver treats discontinuities such as detonations, shocks, and contact surfaces exactly, including complex interface collisions such as detonation waves colliding with contact surfaces without being dependent on grid resolution.

4.3 Method of Characteristics Unit Processes

The MOC model developed for this study closely follows the procedure presented by Zucrow and Hoffman [143, 144]. This procedure was also used in the parametric study of Morris [70]; however, only fully-filled PDEs were investigated. Similar to [70], the unit process procedures discussed in [143,144] are utilized to solve each of the different gasdynamic conditions that occur in the thrust chamber flow field during a single-cycle of operation. These include interior, solid boundary, open-end, detonation wave, shock wave, and contact surface points, each with a specific algorithm. For the purposes of this study, an inverse time-marching method is utilized with a predefined grid based on a specified spacing in the

x–t plane. The finite difference relations for the characteristic and compatibility equations along the pathlines and right- and left-running Mach lines take the form

$$\Delta t_0 = \lambda_0 (x_{i,j} - x_0) \tag{4.8}$$

$$\Delta t_\pm = \lambda_\pm (x_{i,j} - x_\pm) \tag{4.9}$$

$$p_{i,j} - a_0^2 \rho_{i,j} = p_0 - a_0^2 \rho_0 \tag{4.10}$$

$$p_{i,j} \pm \rho_\pm a_\pm u_{i,j} = p_\pm \pm \rho_\pm a_\pm u_\pm - \rho_\pm a_\pm^2 u_\pm \frac{A'(x_\pm)}{A(x_\pm)} \Delta t_\pm \tag{4.11}$$

where Eqs. (4.8) and (4.10) apply along the C_0 pathline, and Eqs. (4.9) and (4.11) apply along the right- and left-running $C_\pm$ Mach lines, respectively. Note that the solution points are denoted by the subscripts i, j, where the gas properties with subscripts 0, $+$, and $-$ represent the averaged properties along the discretized pathline, and right- and left-running Mach lines, respectively. The advantage of this method is the ability to compute and develop the solution on predefined points for an unsteady flow field. However, an inverse marching grid requires tracking of discontinuities such as shock waves and contact surfaces since their location at any given time is likely to fall between any two predefined grid points. The details of each unit process regarding the application of Eqs. (4.8)–(4.11), as well as tracking of discontinuities, are discussed in the following paragraphs.

The algorithm for the unit process for an interior point is the most frequently used in the evolving flow field. Interior points make up the flow field between discontinuities and boundary conditions at any given time. Figure 4.1 is a schematic of the finite difference grid utilized for calculating interior points. In this schematic, and in all subsequent schematics, the black points represent the predefined grid points while the colored points represent interpolated points from the intersection of the pathline and right- and left-running Mach waves on the previous t–line. For obtaining a solution at $x_{i,j}$, a modified Euler predictor–corrector method is used to numerically integrate Eqs. (4.8)–(4.10) along the right- and left-running C_+, and C_- Mach lines, as well as the C_0 pathline that passes through the point $x_{i,j}$. This integration procedure encompasses solving for the intersection location of

the C_+, C_- and C_0 characteristics on the previous t–line, which are denoted by x_+, x_-, and x_0 in Fig. 4.1, respectively. For the predictor step, the solution is achieved by first iteratively determining the location where each characteristic intersects the previous t–line using Eqs. (4.8) and (4.9). Since the solution is known to pass through $x_{i,j}$, this procedure simply backward propagates the characteristics in order to determine where each characteristic intersects the previous t–line. Additionally, for each iteration, λ_0 and $\lambda_\pm$ are refined with the interpolated u and a at x_+, x_-, and x_0 using the neighboring points on the previous solution at $x_{i-1,j-1}$, $x_{i,j-1}$, and $x_{i+1,j-1}$. Iteration of this procedure is carried out until the change in intersection location of all characteristics on the previous t–line satisfies a desired tolerance, where a tolerance of 10^{-8} is used in the current study for all instances where convergence is required. The predictor solution at $x_{i,j}$ is obtained by applying Eqs. (4.10) and (4.11) along the C_0, C_+, and C_- characteristics to simultaneously obtain $p_{i,j}$, $\rho_{i,j}$, and $u_{i,j}$. Lastly, the corrector step is applied in a similar iterative method using the averaged flow properties along the characteristics to refine the solution at $x_{i,j}$ until the change $p_{i,j}$, $\rho_{i,j}$, and $u_{i,j}$ satisfies the desired tolerance.

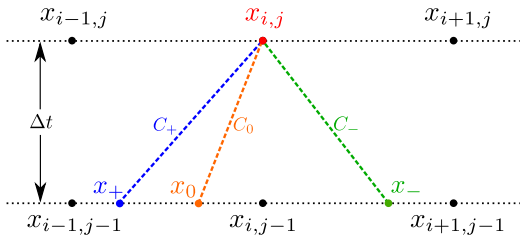

Figure 4.1. Finite difference grid for interior point.

At the thrust wall, a unit process for a solid wall is utilized to impose a zero velocity boundary condition. The finite difference grid utilized for calculating the thrust wall point is shown in Fig. 4.2. Note that the C_0 pathline characteristic follows the stationary wall, which enforces the zero-velocity boundary condition. Similar to the interior point, a modified Euler predictor–corrector method is utilized to determine $p_{i,j}$ and $\rho_{i,j}$ at $x_{i,j}$. In this

case, the predictor solution at $x_{i,j}$ is determined by iteratively applying (4.9) to the C_- characteristic until the location of x_- on the previous t–line satisfies the desired tolerance. Then, application of Eqs. (4.10) and (4.11) along the C_0 and C_- characteristics permits computation of $p_{i,j}$ and $\rho_{i,j}$ at $x_{i,j}$. Lastly, the corrector step is iteratively applied in a similar manner with the averaged flow properties to refine the solution at $x_{i,j}$ until the change in $p_{i,j}$ and $\rho_{i,j}$ satisfies the desired tolerance.

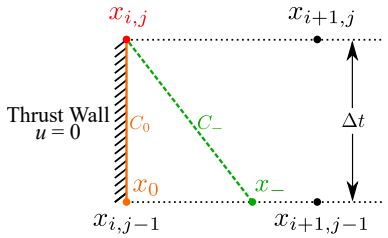

Figure 4.2. Finite difference grid for wall point.

At the exit of the thrust chamber, a unit process for an open-end point is utilized to determine the flow condition on the boundary exit. In general, partially-filled PDEs and PDEs with diverging nozzles can have a combination of subsonic and supersonic outflow on the exit boundary. As indicated in the computational PDE study of Kailasanath et al. [69], the open-end boundary condition can have a significant effect on the relaxation of flow properties on the exit boundary, and consequently, in the thrust chamber. This is especially true if the flow is subsonic, such that the external flow field outside the computational domain can influence the solution at the exit. For the purposes of this study, a conditional open-end point unit process is utilized on the exit boundary subject to subsonic or supersonic outflow. The finite difference grids for subsonic and supersonic outflow at the open-end point are shown in Figs. 4.3(a) and 4.3(b), respectively. Note, in Fig. 4.3(a), the C_- characteristic does not originate from inside the computational domain which complicates the boundary condition for subsonic outflow. In such a situation, it is assumed that $p_{i,j}$ is fixed at the ambient condition, namely, p_{amb}. Subsequently, the intersection location of the

C_+ and C_0 characteristics with the previous t–line are iteratively determined using Eqs. (4.8) and (4.9) until convergence is obtained. Likewise, the predictor $\rho_{i,j}$ and $u_{i,j}$ at $x_{i,j}$ are simultaneously determined by application Eqs. (4.10) and (4.11) along the C_+ and C_0 characteristics. Lastly, the corrector is iteratively applied until $\rho_{i,j}$ and $u_{i,j}$ at $x_{i,j}$ satisfy the desired tolerance.

In the event of supersonic outflow, all three characteristics originate from within the computational domain, as indicated in Fig. 4.3(b). This simplifies the solution point, as no external disturbance from outside the PDE thrust chamber can influence the exit boundary condition. Therefore, in the event of supersonic outflow, the solution point at $x_{i,j}$ is readily obtained by the same algorithm used to compute an interior point, and the pressure boundary condition is removed.

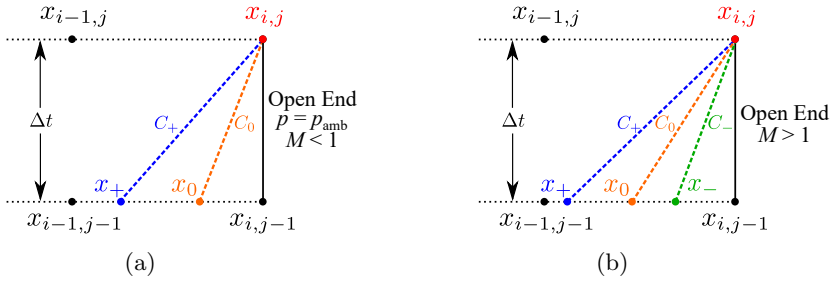

Figure 4.3. Finite difference grid for (a) subsonic outflow flow and (b) supersonic outflow at an open-end point.

In order to treat shock waves such as the unsteady transmitted shock into the non-combustible mixture, a unit process for a shock wave point is required. Figure 4.4 is a schematic showing the finite difference grid for a general shock point. In this schematic, the red square points represent the location of the shock wave. In general, the shock wave point solution will not coincide with a point in the predefined grid. The solution can readily be obtained by iteratively applying unit processes to the pre- and post-shock states separately until convergence is achieved. Such a scheme is initiated by propagating the shock wave forward with a guessed shock velocity equal to the shock velocity at the previous t–line.

This provides the new location of the shock solution point denoted by $x_{sL,j}$ and $x_{sR,j}$, namely, the left- and right-side locations of the shock wave, respectively. For the right-hand side of the shock wave, the unit process for an interior point is utilized to determine the pre-shock $p_{sR,j}$, $\rho_{sR,j}$, and $u_{sR,j}$ at $x_{sR,j}$. With knowledge of the shock velocity and pre-shock flow condition, application of the Rankine–Hugoniot (RH) shock jump conditions permits calculation of the post-shock $p_{sL,j}$, $\rho_{sL,j}$, and $u_{sL,j}$ at $x_{sL,j}$. Likewise, the pressure at $x_{sL,j}$ can be obtained by applying Eqs. (4.9) and (4.11) along the forward propagating C_+ characteristic that overtakes the shock from behind. With this procedure, $p_{sL,j}$ is obtained by two methods, namely, by estimating the shock velocity and applying the RH shock jump conditions, and by applying Eqs. (4.9) and (4.11) along the C_+ characteristic behind the shock. Such a routine can be converged with application of root-finding scheme such as the secant method. In this case, a new shock velocity is iterated until the error in $p_{sL,j}$ determined from the RH shock jump condition and the C_+ characteristic behind the shock satisfies the desired tolerance.

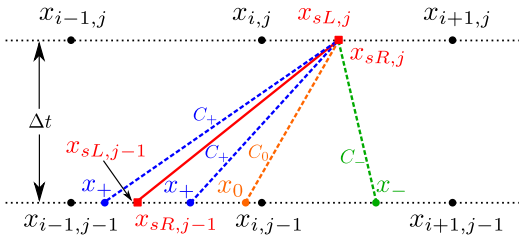

Figure 4.4. Finite difference grid for shock wave point.

As mentioned in the general flow description for partially-filled PDE thrust chambers and PDEs with diverging nozzles, following the collision of the detonation wave with the contact surface, the contact surface is set into motion towards the exit of the thrust chamber. Similar to the transmitted shock wave, the contact surface also moves unsteadily and interacts with both the overtaking Taylor rarefaction, as well as the head on interaction with the exhausting rarefaction. Treatment of the contact surface motion through the grid

is carried out using a unit process for a contact surface point. Figure 4.5 is a schematic of the finite difference grid used to calculate the contact surface point, where the red square points represent the contact surface point. Note that the contact surface coincides with the C_0 characteristic, a necessary condition that ensures the contact surface moves along a pathline. In general, similar to the shock wave, the contact surface solution will not coincide with the predefined grid. In this case, a similar modified Euler predictor–corrector algorithm is applied to both the right- and left-hand sides of the contact surface until p and u across the contact surface converges. Hence, the solution method requires guessing λ_0, λ_+, and λ_- and using Eqs. (4.8) and (4.9) to simultaneously solve for the intersection locations of $x_{cL,j}$, $x_{cR,j}$ on the new t–line, and x_+ and x_- on the previous t–line. Similar to previous unit processes, this method is carried out iteratively until the change in location of x_+ and x_- satisfies the desired tolerance. Subsequently, the predictor solutions for $x_{cL,j}$ and $x_{cR,j}$ are obtained from Eqs. (4.10) and (4.11), where the compatibility equation for the C_0 pathline is separated according to the right- and left-hand sides of the contact surface. Lastly, the corrector is applied in a similar manner using the averaged flow properties until p, $\rho_{cL,j}$, $\rho_{cR,j}$, and u at the contact surface point satisfies the desired tolerance.

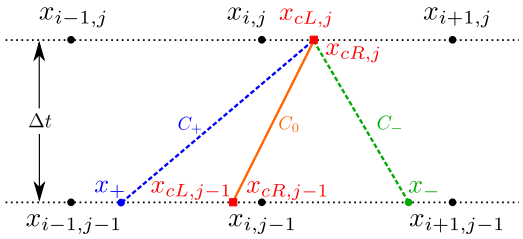

Figure 4.5. Finite difference grid for contact surface point.

As previously mentioned, an isentropic flow field is assumed in developing the governing equations for the MOC model. This restricts the model in that a detonation wave must be modeled as a distinct discontinuity where all the heat release takes place within the discontinuity. This type of detonation wave representation is consistent with the one-

dimensional Chapman–Jouguet (CJ) detonation wave theory [21–23]. In the CJ theory, it is assumed that all of the chemical reactions and heat release takes place within the shock front, and the coupled induction and reaction zones following the shock front have zero width. Therefore, for the purposes of modeling a detonation wave using the MOC, the CJ detonation wave representation is utilized. Unlike the shock and contact surface discontinuity points previously discussed, the CJ detonation wave propagates at a constant velocity for a given detonable propellant. In this case, the detonation wave is assumed to steadily propagate through the gaseous propellant until finally reaching the contact surface. Note, the Taylor rarefaction wave that develops behind the detonation wave cannot physically overtake the detonation due to the sonic CJ condition associated with the post-detonation state. Similarly, the propellant flow field ahead of the detonation is initially uniform, which will not perturb the detonation wave velocity away from the CJ value. Therefore, the unit process used to treat the detonation wave is simply a matter of propagating the CJ detonation state through the predefined grid points at given time steps. Note, this method requires selecting an appropriate time step to ensure the detonation location for each new time step coincides with the predefined grid points. The implementation of this method will be discussed in the following subsections.

A few comments can be made about the unit processes detailed above and the nature of the solution points. To ensure the computed solutions are numerically stable, the unit process algorithms must satisfy the Courant–Friedrichs–Lewy (CFL) stability criterion. This requires that the intersection points x_0, x_+, and x_- for the C_+, C_- and C_0 characteristics intersect the previous t–line between the points used for interpolation, namely, $x_{i-1,j-1}$, $x_{i,j-1}$, and $x_{i+1,j-1}$. This ensures that the flow properties interpolated at x_0, x_+, and x_- use the appropriate neighboring points to perform the interpolation procedure. Additionally, as noted in [143, 144], the act of interpolating to determine the flow properties at the characteristic intersection locations on the previous t–line tends to reduce the accuracy of the solution. In fact, smearing of the solution can occur since some of the neighboring points

used in the interpolation scheme lie outside of the domain of dependence for the solution points. This is a numerical artifact of such a MOC solution method that cannot be avoided, but only mitigated by utilizing a finer grid spacing. Despite these numerical inaccuracies, as will be seen in the following sections, the PDE modeling carried out in this study has very good agreement with both theoretical and numerical models and various experiments.

4.4 Application to Pulse Detonation Engines

The solution procedure for generalized PDE thrust chamber flow fields requires the application of all of the previously discussed unit processes. For this purpose, all of the unit process algorithms are developed within a Matlab environment. In the case of a fully-filled PDE, the grid spacing in x is selected and the time step is determined by, $\Delta t = \Delta x / W_{CJ}$, which ensures the detonation wave propagation through the grid coincides with a predefined grid point at each time step. Similarly, in the partially-filled or diverging nozzle case, the time step for the solution prior to the detonation wave collision with the contact surface is defined in the same manner. In each case, detonation initiation is assumed to take place instantly at the head end of the thrust chamber, such that the equilibrium CJ detonation solution is implemented at the first grid point adjacent to the thrust wall. Once the detonation wave collides with the contact surface, the incident transmitted shock strength and type of reflection are determined using the method in Ch. 3. The results of this instantaneous interface interaction are constructed exactly on the t–line immediately following the interface collision. Similarly, following the detonation wave collision with the contact surface, if the transmitted shock velocity is larger than the detonation wave velocity, then the time step is reduced according to, $\Delta t = \Delta x / W_T$, where W_T is the incident transmitted shock velocity. This ensures that the CFL stability criterion is always satisfied throughout the complete gasdynamic blowdown process.

A two-γ model is utilized for the propellant and detonation products, where the ratio of specific heats behind the detonation wave is fixed at the equilibrium γ_{CJ}, and the chemical

composition of the burned products are assumed to remain frozen for the remainder of the blowdown process. Although this is a great simplification, Povinelli and Yungster [146,147] demonstrated that recombination and chemical nonequilibrium only have small effects on the performance of PDEs operating with both hydrogen- and hydrocarbon-air mixtures. This is primarily attributed to the rather modest changes in γ across regions of frozen, nonequilibrium, and equilibrium flow within the PDE flow field. Further, for the purposes of computing the equilibrium CJ detonation wave properties, the chemical kinetics computer program Cantera with a Matlab shock and detonation toolbox is utilized [24,29,30]. Lastly, for the transmitted shock, a calorically perfect shock solution is assumed, such that the specific heat ratio of the non-combustible mixture remains fixed across the transmitted shock. Hence, across the contact surface following the interface interaction, γ changes from γ_{CJ} behind the contact surface to γ_0 associated with the purge or ambient condition ahead of the contact surface.

The transient resultant force is simply expressed as a function of the pressure history on the internal thrust surfaces as

$$\boldsymbol{F}(t) = -\iint_S (p - p_0)\, d\boldsymbol{S} \tag{4.12}$$

Note, due to symmetry and the quasi-one-dimensional assumption, the only non-zero component of thrust occurs in the x-direction, namely, $F_x(t) = \boldsymbol{F}(t) \cdot \hat{i}$, and is the component of thrust utilized in all of the subsequent performance analysis. Moreover, it is noted that the thrust force can also be computed using a control volume surrounding the PDE and summing the time rate of change of momentum integrated over the control volume, momentum flux through the control surfaces, and pressure area force acting on the PDE exit. In fact, the difference in thrust computed between the two methods is less than 0.1 percent; however, due to simplicity, the thrust obtained using Eq. (4.12) is used in the subsequent analysis. If, however, viscous losses were included in the model, then Eq. (4.12) must modified to include such losses to maintain valid agreement with the control volume approach. In fact, it is only in the inviscid limit that Eq. (4.12) becomes exact to the thrust force

predicted by a complete control volume analysis. Moreover, the time-averaged thrust is determined by

$$\bar{F} = \frac{1}{t_f} \int_0^{t_f} F_x(t)\ dt \tag{4.13}$$

where t_f is the time at which the pressure at the head end of the thrust chamber returns back to the ambient condition. Similarly, the thrust force can be integrated over the duration of the cycle, namely, t_f, in order to obtain the total impulse for the single-cycle operation of the PDE

$$I_t = \int_0^{t_f} F_x(t)\, dt \tag{4.14}$$

Lastly, the propellant-based specific impulse is determined from the total impulse by

$$I_{sp} = \frac{I_t}{m_d g} \tag{4.15}$$

where m_d is the mass of detonable propellant (fuel and oxidizer).

4.4.1 Effects of Grid Resolution

A grid dependency study is carried out to find a suitable grid spacing for minimizing computational expense, but still able to properly model the thrust chamber flow field with negligible error. For this purpose, the specific impulse of a fully-filled PDE is computed by varying the total number of grid points, N, used to discretize the thrust chamber length. Figure 4.6 shows how the specific impulse computed with the MOC model compares with the theory of Endo et al. [65] and the model of Wintenberger et al. [66,67] for stoichiometric H_2–O_2 and C_2H_4–O_2 propellants in a 1 m long thrust chamber using grids with total number of nodes ranging from 20–1,000. Note that for H_2–O_2 propellant, the specific impulse calculated by the MOC model is slightly higher than that predicted by the theory of [65], but converges towards that predicted by the model of [66, 67]. Similarly, for C_2H_4–O_2 propellant, the specific impulse calculated by the MOC model is slightly higher than the specific impulse predicted by both the theory of [65] and the model of [66,67]. Although not shown in Fig. 4.6, the specific impulse calculated with the MOC model at the finest grid

spacing for both propellants is within one percent of the values reported in the MOC study by Morris [70]. It is noted that the computational time for 100 nodes is approximately 20 seconds, whereas the 1,000 node case requires more than 15 minutes of machine time in a Matlab environment. Therefore, it is concluded that approximately 200 nodes provides the best compromise between computational expense and negligible convergence error.

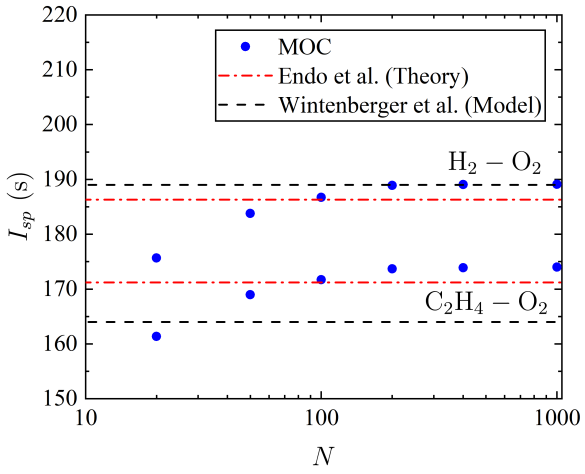

Figure 4.6. Dependence of specific impulse on grid resolution N for fully-filled PDE with stoichiometric H_2-O_2 propellant ($\psi = 1$) and comparison with the theory of [65] and model of [66, 67].

4.5 Model Validation

It is desired to validate the current MOC model in order to ensure the model produces adequate performance results for fully- and partially-filled PDEs, and PDEs equipped with a diverging nozzle before conducting detailed parametric studies. As such, this section is used to conduct a rigorous comparison of the current MOC model with existing numerical and experimental results within the literature for a wide range of PDE operating conditions.

4.5.1 Fully-Filled Pulse Detonation Engine

The first case of validation is to ensure the current MOC model can properly capture the gasdynamic flow field evolution for a fully-filled PDE. For this, the MOC model results are compared with experimental pressure traces obtained in a PDE test facility that was previously used by Joshi and Lu [97] for unsteady thrust measurements. The PDE consists of a constant-area stainless-steel tube with an overall length of 660 mm and an internal diameter of 25.4 mm. In this case, the PDE was operated in a single shot manner, and an array of high frequency pressure transducers (PCB model 111A24) were used to obtain the experimental pressure traces. For the fully-filled configuration, a single 6.0 μm thick Mylar diaphragm was used at the engine exit plane to separate a stoichiometric H_2–O_2 detonable mixture from the ambient air. Additionally, for the purposes of achieving direct detonation initiation within the PDE chamber, a small perpendicular pre-detonator was employed at the head end of the tube. Within the pre-detonator, detonation is achieved by means of energy deposition from an automotive spark plug and DDT transition.

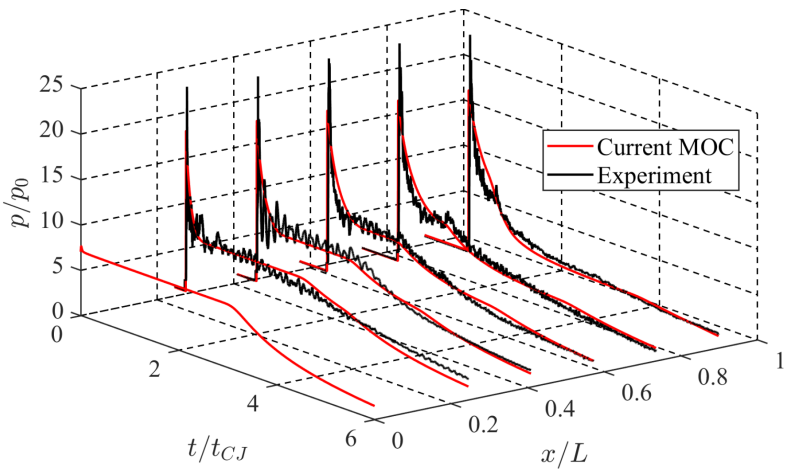

Figure 4.7. Comparison of fully-filled ($\alpha = 1$) PDE pressure flow field from MOC with experimental results for $2H_2$–O_2 propellant.

The temporal and spatial evolution of pressure for the fully-filled PDE operating with stoichiometric H_2–O_2 detonable mixture and air as the ambient gas, both initially at

1 atm and 300 K, is shown in Fig. 4.7. In this figure, t_{CJ} represents the time at which the detonation wave reaches the end of the engine. Hence, at $t/t_{CJ} = 1$, the detonation reaches the diaphragm at the exit plane of the engine. Note that the MOC model is in very good agreement with the experimental pressure traces. In fact, an average error of less than 10 percent is obtained across the distributed pressure flow field during the full blowdown process, which indicates that the MOC model can adequately capture the dominant gasdynamic processes and interactions within a fully-filled PDE.

It is also desired to ensure that the current MOC model properly captures the effects of varying the propellant equivalence ratio and blowdown pressure ratio on specific impulse for a fully-filled PDE. Figures 4.8(a) and 4.8(b) show a comparison of the MOC model with the previously mentioned MOC model of [70], higher-fidelity numerical models of [76,83,98], and experimental results of [92, 95] for hydrogen and hydrocarbon propellants at various equivalence and blowdown pressure ratios. In the experiments of [95], the PDE was operated at 12–16 Hz with a H_2–O_2+3.76N_2 propellant mixture with air as the purge gas, and the equivalence ratio was varied from roughly 0.4–2.8. Moreover, the thrust was directly measured using a damped thrust stand, and similar to previous experimental efforts, a Shchelkin spiral was used to aid the DDT process within the PDE. In the experiments of [92], single-shot tests were conducted using a detonation tube with stoichiometric C_2H_4–O_2 and air as the ambient. In those experiments, the detonation tube was suspended on a ballistic pendulum setup and enclosed inside of a dump tank in order to control the sub-atmospheric ambient environment, and thin Mylar diaphragms where used to separate the detonable and ambient mixtures. Note, very good agreement is obtained in Fig. 4.8(a) with previous H_2–O_2 results, such that an average difference of 0.7 percent is obtained with the MOC results of [70], and 7.9 percent for the numerical results of [98]. Additionally, in the case of H_2–air propellant, an average error of 6.1 percent is obtained with the measurements of [95] for the equivalence ratio range shown. Moreover, in Fig. 4.8(b), very good agreement is also obtained with previous results, such that an average difference of 4.4 percent is

obtained with the MOC results of [70], and 1.7 percent for the numerical results of [76, 83] over the range of blowdown pressure ratios shown for H_2–O_2 and C_2H_4–O_2 propellants, respectively. Lastly, in the case of stoichiometric C_2H_4–O_2 propellant, an average error of 12 percent is obtained with the measurements of [92] for the blowdown pressure ratio range shown.

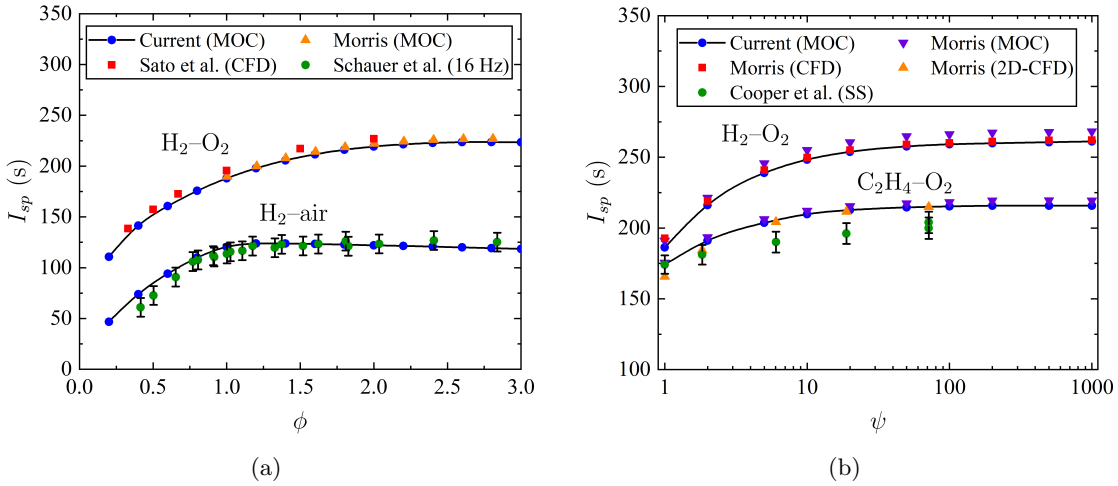

Figure 4.8. Comparison of current MOC model with existing numerical and experimental data of [70, 76, 83, 92, 95, 98] for H_2–(O_2+3.76N_2), H_2–O_2, and C_2H_4–O_2 propellants at various (a) equivalence ratios and (b) blowdown pressure ratios.

Finally, it is desired to ensure that the current MOC model provides an accurate prediction for time-averaged thrust. In this case, this is primarily to ensure that the cycle blowdown time is accurately determined. For this, a comparison is made with the experimental results of [95] for a fully-filled PDE operating at 16 Hz and at various equivalence ratios. Figure 4.9 shows that fairly good agreement is obtained with the experimental results of [95], in that an average error of 8.3 percent is obtained over the equivalence ratio range shown. In general, the comparison of the MOC model with the results of [95] becomes worse as the equivalence ratio increases. This is largely attributed to the increased DDT run-up distance with increasing propellant equivalence ratio, which can result in severe non-ideal

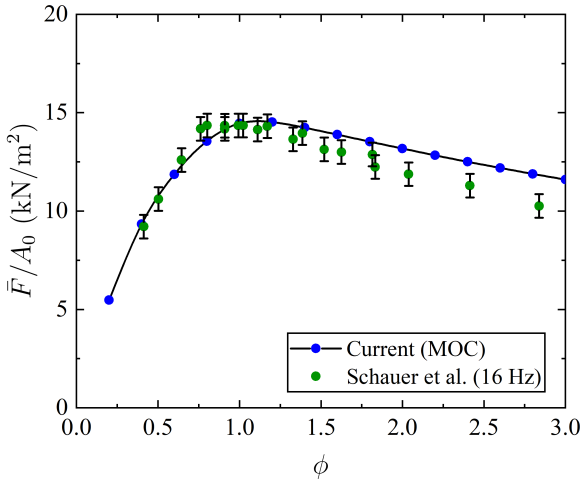

Figure 4.9. Comparison of time-averaged thrust predicted by the current MOC model with the experiments of [95] for H_2–air propellant at different equivalence ratios ($\psi = 1$).

detonation initiation. In fact, this non-ideal initiation behavior was studied by Kiyanda et al. [148] for oxyhydrogen mixtures at various equivalence ratios, where it was shown that DDT run-up distance is very sensitive to the mixture equivalence ratio. Consequently, the pressure history on the thrust wall can be significantly reduced with a corresponding increase in the overall cycle blowdown time. Despite this, the above results suggests that the current MOC model properly captures the manner in which the propellant equivalence ratio and system blowdown pressure ratio influences the ideal fully-filled PDE performance.

4.5.2 Partially-Filled Pulse Detonation Engine

Similar to the fully-filled PDE, the first case of validation is to ensure the current MOC model can properly capture the gasdynamic flow field evolution for partially-filled PDEs. For this, the MOC model results are compared with experimental pressure traces obtained in a partially-filled PDE test facility that was previously used by Joshi and Lu [97] for unsteady thrust measurements. In this case, a 485 mm straight-extension section with the same diameter was coupled to the end of the PDE in order to emulate a fill fraction of $\alpha = 0.58$. Additionally, a single 6.0 μm thick Mylar diaphragm was used to separate a

stoichiometric H_2–O_2 detonable mixture from ambient air. As before, the PDE was operated in a single-shot manner, whereby a small perpendicular pre-detonator was employed at the head end of the tube to achieve direct initiation.

The temporal and spatial evolution of pressure for the partially-filled PDE operating with stoichiometric H_2–O_2 detonable mixture and air as the ambient gas, both initially at 1 atm and 300 K, is shown in Fig. 4.10. In this figure, t_{CJ} represents the time at which the detonation wave reaches the end of the filled length. Hence, at $t/t_{CJ} = 1$, the detonation reaches the diaphragm at $0.58L$. Note that, similar to the fully-filled case, the MOC model is in very good agreement with the experimental pressure traces. An average error of less than 10 percent is obtained across the distributed pressure flow field during the full blowdown process, which indicates that the MOC model can adequately capture the dominant gasdynamic processes and interactions within of a partially-filled PDE.

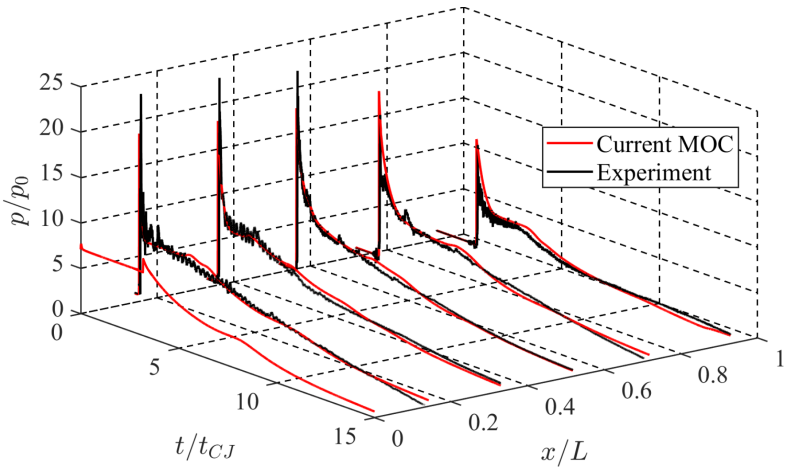

Figure 4.10. Comparison of partially-filled ($\alpha = 0.58$) PDE pressure flow field from MOC with experimental results for $2H_2$–O_2 propellant.

The next case of validation is to ensure that the current MOC model can properly capture the performance of a partially-filled PDE thrust chamber. This is done by calculating the performance while varying the fill fraction at a blowdown pressure ratio of $\psi = 1$. In partial filling studies, it is common to investigate the partial-fill effect on per-

formance by examining the ratio of specific impulse for a partially-filled PDE to that of a fully-filled PDE. The results of the MOC model are compared in Fig. 4.11 with existing numerical and experimental data for partially-filled PDEs using H_2–O_2 (filled symbols) and H_2–O_2+3.76N_2 (open symbols) propellant mixtures and air as the inert gas. It is important to note that comparing the MOC model with experimental data in this normalized manner will suppress variation in experimental data associated with separate detonation initiation schemes and performance measurement techniques. However, this also provides a way to help isolate the fundamental performance scaling associated with partially filling a PDE, for which the MOC model can be validated against. The experiments by Kasahara et al. [101] were single-shot (SS) tests using stoichiometric H_2–O_2 propellant, and the impulse was measured using a ballistic pendulum setup. Thin Mylar diaphragms were used at different locations in a fixed length tube to vary the fill fraction from 0.2–1, which also served to separate the detonable mixture from the non-combustible ambient air. A Shchelkin spiral was used to aid the DDT process. In the experiments conducted by Joshi and Lu [97], the PDE was operated between 1–20 Hz using a H_2–O_2 propellant mixture with an air purge, and the fill fraction was varied by precision timing controls of gaseous fuel injectors. The thrust was directly measured using an innovative dynamic thrust measurement technique based on an effective inertial force for the PDE system and a deconvolved force from the dynamic response of the PDE system. Because the specific impulse for a fully-filled PDE was not reported for these experiments, the specific impulse was normalized using an interpolated value between experimental fill fractions of 0.88 and 1.15. It is noted that a Shchelkin spiral was also used in those experiments to enhance the DDT process. Moreover, as previously mentioned, in the experiments conducted by Schauer et al. [95], the PDE was operated between 12–16 Hz using a H_2–O_2+3.76N_2 propellant mixture with air as the purge gas. In these experiments, the fill fraction was varied from 0.2–1.6, but only the data with fill fractions less than or equal to unity are used for validation in the present study. The thrust was measured using a damped thrust stand, and similar to previous experimental

efforts, a Shchelkin spiral was used to aid the DDT process within the PDE. The computational study of Sato et al. [98] is also used for validation since a wide range of single-cycle PDE operating conditions was investigated. In this study, both H_2–O_2 and H_2–O_2+3.76N_2 propellant mixtures were considered. The propellant fill fraction was varied from 0.3–1.0 with air as the inert gas. Further, these computations were carried out by modeling the exhausting PDE flow field using a two-dimensional computational domain. This removes the complications of specifying a boundary condition directly at the exit of the PDE, and allows capturing of any multi-dimensional exhausting phenomena that influences the PDE performance characteristics. Note, for H_2–O_2 (filled symbols), the agreement is very good with the experiments of Kasahara et al. [101] and Joshi and Lu [97]. In fact, the average error for fill fractions ranging from 0.44–1.0 is 7.6 percent. Moreover, for H_2–O_2+3.76N_2 (open symbols), the agreement is excellent with the experiments of Schauer et al. [95] over the fill fractions ranging from approximately 0.3–1.0. In this case, the average error with the experiments is only 3.5 percent. Additionally, for the numerical results of Sato et al. [98], the agreement is excellent over the fill fraction range of 0.3–1.0, with an average difference of 3.1 percent.

The results of the MOC model are also compared in Fig. 4.12 with existing computational and experimental data for partially-filled PDEs using a stoichiometric C_2H_4–O_2 propellant mixture and air as the inert gas. The experiments conducted by Zitoun and Desbordes [89] were single-shot (SS) tests using an exploding wire in order to achieve direct detonation initiation, and the impulse was measured by integrating Eq. (4.12) at the head end. The fill fraction was varied from 0.82–0.98 by adding straight tube extensions, and thin Mylar diaphragms were used to separate the detonable mixture from the non-combustible ambient air. Note, a fully-filled specific impulse value was not reported in that study; however, the data was normalized using the theory of Endo et al. [65]. The agreement with these experiments is very good over the fill fraction range of 0.82–1.0, with an average error of 4.5 percent. Similarly, the MOC model is shown to have excellent agree-

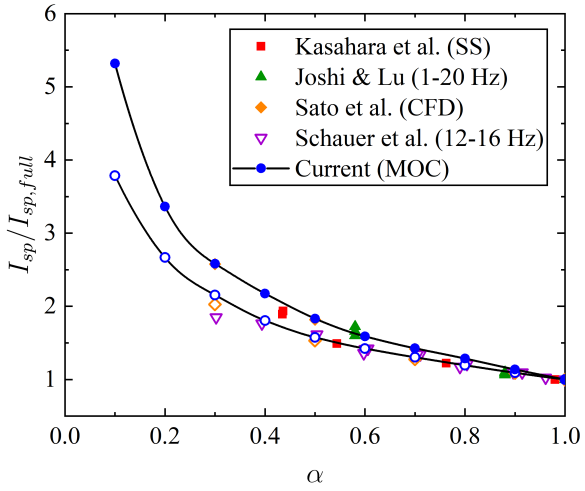

Figure 4.11. Comparison of specific impulse ratio from MOC with published data in [95, 97, 98, 101] for $2H_2$–O_2 (filled symbols) and $2H_2$–(O_2+$3.76N_2$) (open symbols) propellants and air as the inert gas ($\psi = 1$).

ment with the previously mentioned computational study of Sato et al. [98]. Over the fill fraction range of 0.1–1.0, the MOC results differ from those reported results by 1.2 percent. Lastly, the computational study carried out by Li and Kailasanath [107] is also used for the purposes of validation. In that study, the partially-filled solutions were computed using a two-dimensional computational domain and the exhausting PDE flow field was directly calculated. For fill fractions greater than 0.5, the MOC model is shown to have very good agreement; however, this agreement starts to deviate at very low fill fractions. As the fill fraction approaches zero, the MOC model has the tendency to over-predict the computational results of [107]. This is primarily attributed to the mostly non-ideal detonation initiation scheme employed in [107], which featured only a 4 atm region near the thrust wall; meanwhile, the current MOC model uses an idealized direct detonation initiation with the CJ theory. Although not shown in Figs. 4.11 and 4.12, in the limit the fill fraction approaches zero, the partial filling performance ratio $I_{sp}/I_{sp,full}$ approaches 8.9 and 6.3 for H_2–O_2 and C_2H_4–O_2 with air as the inert gas, respectively. Note, these performance values are for a fill fraction of $\alpha = 0.01$, since the current MOC model cannot actually approach a

fill fraction of zero. Further, these values are merely idealized representations of the upper limit of partially-filled PDE performance, as this is an area with minimal numerical and experimental results. However, it is interesting to note that these upper limits agree very well with those obtained using the homogeneous dilution model of Endo et al. [112], and are about a factor of 2 higher than those obtained using the bubble model of Cooper [110]. Despite these results, caution should be taken when using a MOC-based model to evaluate the performance of partially-filled PDEs in the limit of small fill fraction. It is likely that these reported values largely overestimate the actual performance due to the effects of non-ideal detonation initiation. Alternatively, the MOC model is shown to have very good agreement with both experimental and two-dimensional computational results for larger fill fractions with the initial blowdown pressure ratio of the PDE system equal to unity.

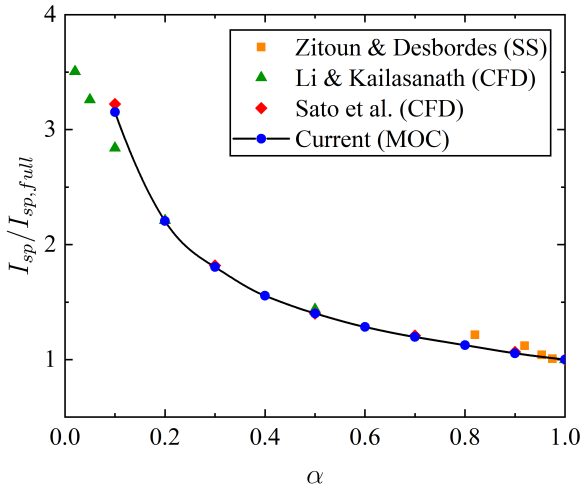

Figure 4.12. Comparison of specific impulse ratio from MOC with published data in [89, 98, 107] for C_2H_4–$3O_2$ propellant and air as the inert gas ($\psi = 1$).

The final case for validation is ensuring the current MOC model can properly capture the combined effects of partially filling the PDE while varying the blowdown pressure ratio. This operating condition would be encountered when using partially-filled PDEs in sub-atmospheric environments. In this case, the magnitude of specific impulse is directly

determined rather than the ratio of specific impulse of a partially-filled to fully-filled PDE. Comparing the current MOC model with existing data in this manner better highlights any potential deviation from previous results at a given blowdown pressure ratio. For the purposes of comparing H_2–O_2 propellant mixtures, the one-dimensional computational study of Morris [76] is used. In [76], stoichiometric H_2–O_2 propellant is used with an H_2 ambient condition. The exit boundary condition was modeled using a conditional supersonic and subsonic flow condition, and an idealized diaphragm was assumed to separate the propellants from the ambient condition until the detonation wave reached the diaphragm location. Moreover, the fill fraction was varied from 0.33–1.0 by adding straight-extensions, and the blowdown pressure ratio was varied from 1–1,000. Figure 4.13 shows the comparison of the current MOC model with the results of [76]. It can be seen from Fig. 4.13 that excellent agreement is obtained for fill fractions ranging from 0.5–1.0, and blowdown pressure ratio ranging from 1–1,000. In those cases, the average error is 0.6 percent. It is noted that the MOC model slightly underestimates the specific impulse as the fill fraction reaches 0.33, which has an average error of roughly 1.4 percent over the full blowdown pressure ratio range. In this case, the deviation is believed to be a result of the finite-rate chemistry model used in [76], in that more chemical recombination is permitted to take place as the fill fraction is decreased, which ultimately increases the specific impulse.

Lastly, the current MOC model is compared in Fig. 4.14 with existing numerical and experimental data for partially-filled PDEs in sub-atmospheric environments using a C_2H_4–O_2 propellant mixture and air as the inert gas. The numerical results of Morris [83] were computed using an axisymmetric two-dimensional numerical domain, and the exhausting flow field was directly computed without requiring the specification of a boundary condition on the PDE exit plane. In those computations, the PDE was filled with a stoichiometric C_2H_4–O_2 propellant mixture with air as the ambient. The fill fraction was fixed at 0.63 by using a straight tube extension and an idealized diaphragm was used to separate the propellant from the ambient condition, which varied from 1.4–100 kPa. Further, the experiments

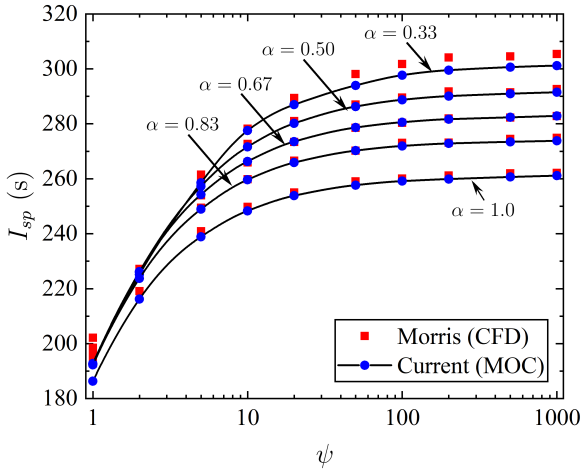

Figure 4.13. Comparison of specific impulse from MOC with published data in [76] at various blowdown pressure ratios and fill fractions for $2H_2$–O_2 propellant and H_2 ambient.

conducted by Cooper and Shepherd [102] were single-shot (SS) tests using stoichiometric C_2H_4–O_2 and air as the ambient. The detonation tube was suspended on a ballistic pendulum setup and enclosed inside of a dump tank in order to control the ambient environment. The fill fraction was fixed at 0.63 by coupling a straight tube extension to the detonation tube, and a thin Mylar diaphragm was used to separate the detonable propellant from the ambient condition. In those experiments, the detonation tube was filled to 80 kPa with the stoichiometric C_2H_4–O_2 detonable mixture and the ambient air was varied from 1.4–100 kPa. As shown in Fig. 4.14, excellent agreement is obtained between the current MOC model and the results reported by Morris [83], such that an average difference of one percent is obtained for fill fractions cases of 0.63 and 1. Similarly, agreement is very good with the experimental results of Cooper and Shepherd [102], such that an average error of 3.7 percent is obtained over the blowdown pressure ratio range test for fill fractions of 0.63 and 1.

4.5.3 Pulse Detonation Engine with Diverging Nozzles

Finally, it is desired to ensure the current MOC model can properly capture the gasdynamic flow field evolution and resulting performance for PDEs equipped with diverging

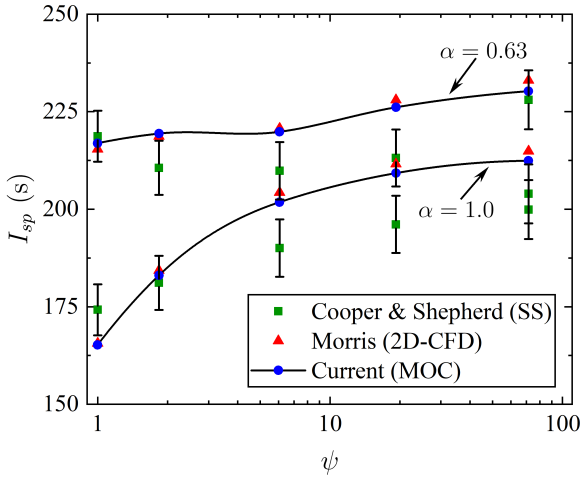

Figure 4.14. Comparison of specific impulse from MOC with published data in [83, 102] at various blowdown pressure ratios for C_2H_4–$3O_2$ propellant and air as the inert gas.

nozzles. As such, the first case of validation requires ensuring the MOC results accurately model the experimental pressure traces obtained in the previously discussed test facility of Joshi and Lu [97]. In this case, the 660 mm length PDE tube is coupled to a conical diverging nozzle with a length, conical half-angle, and expansion area ratio of 165 mm, 8.4°, and 8.0, respectively. Further, the PDE was operated in a similar single-shot manner, where a single 6.0 μm thick Mylar diaphragm at the nozzle inlet was used to separate the detonable mixture from the ambient air. The temporal and spatial evolution of pressure for stoichiometric H_2–O_2 detonable mixture and air as the ambient gas, both initially at 1 atm and 300 K, is shown in Fig. 4.15. Note, t_{CJ} represents the time at which the detonation wave reaches the end of the filled length, which corresponds to $0.8L$ for the present nozzle case. Note that the MOC model is in very good agreement with the experimental pressure traces. In fact, similar to the fully- and partially-filled cases, an average error of less than 10 percent is obtained across the distributed pressure flow field during the full blowdown process, indicating that the MOC model can adequately capture the dominant gasdynamic processes and interactions within a PDE coupled to a diverging nozzle.

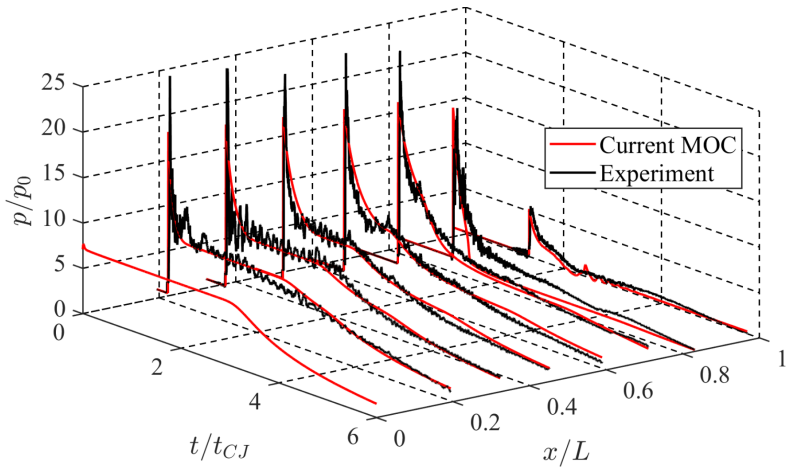

Figure 4.15. Comparison of pressure flow field from MOC with experimental results for PDE featuring a diverging nozzle ($\epsilon = 8.0$) and $2H_2$–O_2 propellant.

Lastly, the final case of validation is ensuring the current MOC model can properly capture the combined effects of varying the nozzle expansion area ratio and blowdown pressure ratio. For this, the MOC model is compared in Figs. 4.16 and 4.17 with existing numerical and experimental data for PDEs equipped with diverging nozzles operating in sub-atmospheric environments. It is noted that the cases of $\epsilon = 1$ in these figures correspond to the previously discussed fully-filled PDE results of [83,102], and the data is simply repeated here to emphasize the performance benefit of diverging nozzles. As before, the experiments conducted by Cooper and Shepherd [102] were single-shot tests using stoichiometric C_2H_4–O_2 and air as the ambient. Additionally, the detonation tube was suspended on a ballistic pendulum setup and enclosed inside of a dump tank in order to control the ambient environment. In those experiments, the detonation tube was fitted with two separate conical diverging nozzles featuring expansion area ratios of $\epsilon = 5.7$ and $\epsilon = 6.5$ with half-angles of 8 and 12 degrees, respectively. Additionally, a thin Mylar diaphragm was placed at the tube exit, or nozzle inlet, in order to separate the detonable propellant within the tube from the ambient condition within the nozzle. During operation, the detonation tube was filled to 80 kPa with a stoichiometric C_2H_4–O_2 detonable mixture and the ambient air was varied from 1.4–100 kPa. In the case of $\epsilon = 6.5$, Morris also used the experimental

results of [102] to validate the previously mentioned two-dimensional axisymmetric numerical model of [83]. Therefore, these numerical results have been included in the current validation.

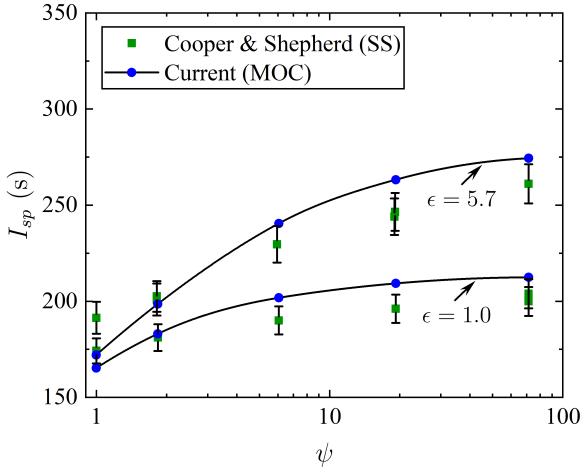

Figure 4.16. Comparison of specific impulse from MOC with published data in [102] for conical diverging nozzles with $\epsilon = 5.7$ at various blowdown pressure ratios for C_2H_4–$3O_2$ propellant and air as the inert gas.

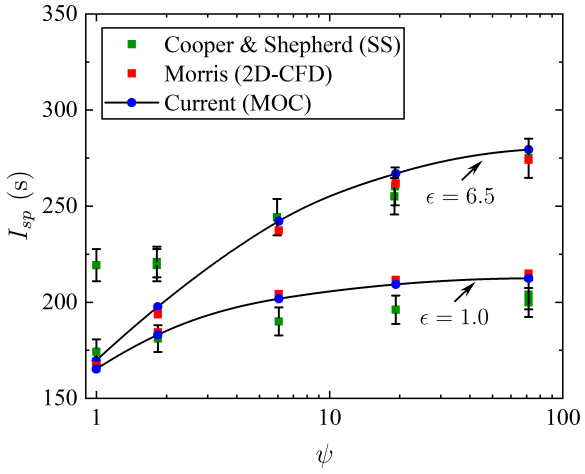

Figure 4.17. Comparison of specific impulse from MOC with published data in [83, 102] for conical diverging nozzles with $\epsilon = 6.5$ at various blowdown pressure ratios for C_2H_4–$3O_2$ propellant and air as the inert gas.

As shown in Fig. 4.16, very good agreement is obtained between the current MOC model and the experimental results of [102] for $\epsilon = 5.7$. In this case, an average error of 5.7 percent is obtained over the blowdown pressure ratio of roughly 1–75. Similarly, as shown in Fig. 4.17 for the case of $\epsilon = 6.5$, excellent agreement is obtained with the two-dimensional axisymmetric numerical model of Morris [83]. In this case, an average error of 1.8 percent is obtained over the same blowdown pressure range. However, the current MOC results and the results of Morris only share good agreement with the results of [102] for larger blowdown pressure ratios, and deviate at lower blowdown pressure ratios near unity. This was explained in [83] by the inability of an inviscid model to capture the shock wave-boundary layer interaction that leads to flow separation during the cases of severely over-expanded flow in the nozzle. For instance, in the study conducted by Owens and Hanson [118], it was found that a PDE operating with stoichiometric C_2H_4–O_2 propellant and with a blowdown pressure ratio of $\psi = 1$ will achieve optimum performance for a nozzle expansion area ratio of approximately $\epsilon = 1.8$. Consequently, severely over-expanded flow exists in the nozzle for the cases of $\epsilon = 5.7$ and 6.5 at lower blowdown pressure ratios. In fact, the nozzle flow for these cases resembles the over-expanded flow shown in Fig. 2.5, where a strong secondary shock forms during the nozzle startup and blowdown. In practice, such a strong shock can create a severe adverse pressure gradient within the wall boundary layer that ultimately induces flow separation. Subsequently, the gas downstream of the separation point expands in accordance with the boundary of the resulting core jet flow rather than the physical nozzle wall. As a result, this mechanism causes inviscid models to over-predict the losses accrued during severe over-expansion in the nozzle since the gas expansion follows the nozzle wall geometry rather than the separated core flow. This leads to the disagreement between the current MOC model and the experiments of Cooper and Shepherd [102] in Figs. 4.16 and 4.17 at lower blowdown pressure ratios. Despite this, an average error of 9.6 percent is obtained over the full blowdown pressure ratio shown; however, this error reduces to only 2.3 percent for $\psi \gtrsim 6$.

4.5.4 Model Limitations

Based on the above comparisons with the existing numerical and experimental results, the current MOC model is capable of accurately reproducing the performance of PDEs that are both fully- and partially-filled, and operating with diverging nozzles. This included operating in standard conditions where the propellant and ambient are at equal pressure, and in sub-atmospheric environments, where the initial blowdown pressure ratio is greater than unity. It is also noted that a variety of different numerical schemes were used for PDE performance comparison including one-dimensional, two-dimensional, and axisymmetric, with various exit boundary conditions. Similarly, a variety of different experimental results were used for comparison for both hydrogen and hydrocarbon based propellant mixtures, using single-shot and multi-cycle operations, and various thrust and impulse measurement techniques including ballistic pendulums, damped thrust stands, and dynamic thrust measurements. In most cases, the MOC model accurately reproduces the performance results; however, a few limitations should be mentioned.

It is possible to encounter situations where the inviscid and adiabatic assumptions used in the development of the MOC model begin to breakdown, yielding in an isentropic assumption that is inaccurate. For instance, as the L/d of the engine increases, where L is the tube length and d is the diameter, the effects of frictional losses and heat transfer through the walls become more apparent causing deviations from the isentropic solution. In general, heat losses will result in a reduction in pressure within the thrust chamber, whereby larger localized pressure drops within the PDE flow field correlate with higher local heat flux at the wall. Consequently, this heat transfer loss mechanism yields a plateau pressure deficit at the thrust wall, and a corresponding decrease in this component of integrated thrust. Similarly, frictional losses are a result of the boundary layer development along the internal surfaces of the thrust chamber, which form a shear stress distribution over the internal surfaces that counteract the thrust force. The characteristics of these performance losses

have been discussed in detail in the fully-filled PDE studies of Radulescu and Hanson [149], Owens and Hanson [150], and Kawane et al. [151].

Notably, Radulescu [149] demonstrated that the specific impulse losses in a fully-filled PDE due to heat transfer through the walls approximately scales quasi-linearly with increasing L/d. To arrive at this result, it is first necessary to recognize that the square of specific impulse is directly proportional to the amount of heat released per unit mass of the propellant, namely, q.

$$I_{sp} \propto q^{1/2} = Cq^{1/2} \tag{4.16}$$

This is a fundamental relationship that was reported in the analytical model of Wintenberger et al. [66, 67], and later demonstrated in the experiments of Kiyanda et al. [148]. In Eq. (4.16), C simply represents a proportionality constant, which was shown to be approximately 0.058 s^2/m in [67] for various hydrogen- and hydrocarbon-based detonable mixtures with air and oxygen as the oxidizer. It follows, after differentiating Eq. (4.16), that

$$dI_{sp} = \frac{1}{2} C q^{-1/2} dq \tag{4.17}$$

Or equivalently,

$$\Delta I_{sp}\Big|_{q_{loss}} = I_{sp,isentropic} - I_{sp,q_{loss}} = \left(\frac{1}{2} C q^{-1/2}\right) q_{loss} \tag{4.18}$$

Additionally, q_{loss} can be approximated by an averaged wall heat flux for the cycle as

$$q_{loss} = \frac{Q_{loss}}{m_d} \approx \frac{\overline{q''} A_s t_f}{m_d} \approx \frac{4\overline{q''}\pi d L t_f}{\rho_1 \pi d^2 L} \approx \frac{4\overline{q''} t_f}{\rho_1 d} \approx \frac{24\overline{q''} L}{\rho_1 d W_{CJ}} \tag{4.19}$$

In this expression, it has been assumed that the fully-filled cycle time is approximated by $t_f \approx 6t_{CJ} \approx 6L/W_{CJ}$. Combining Eqs. (4.19) and (4.18) yields

$$\Delta I_{sp}\Big|_{q_{loss}} \approx \left[\frac{12C\overline{q''}}{\rho_1 W_{CJ} q^{1/2}}\right] \frac{L}{d} \approx K_1 \frac{L}{d} \tag{4.20}$$

Note, a similar result was first reported in [149] using similar arguments. Thus, at a first-order approximation, the decrement in specific impulse due to heat loss is proportional to the L/d of the thrust chamber. In a given case, the value of K_1 can be determined from

the theoretical properties of the detonable mixture, and an empirically measured average wall heat flux $\overline{q''}$.

A similar derivation can also be made for the decrement in specific impulse due to frictional losses within the thrust chamber. In general, the specific impulse decrement from frictional forces takes the form

$$\Delta I_{sp}\Big|_{F_{visc}} = I_{sp,isentropic} - I_{sp,F_{visc}} = \frac{\int_0^{t_f} F_{visc}(t)\,dt}{m_d g} \tag{4.21}$$

Further, if it is assumed that the contribution of the viscous frictional force can be replaced by a representative averaged shear stress over the internal surface, namely, $F_{visc}(t) \approx \overline{\tau}_w A_s$, then it follows that the specific impulse decrement from frictional losses takes the form

$$\Delta I_{sp}\Big|_{F_{visc}} \approx \frac{\int_0^{t_f} \overline{\tau}_w A_s\,dt}{m_d g} \approx \frac{\overline{\tau}_w A_s t_f}{m_d g} \approx \frac{4\overline{\tau}_w \pi d L t_f}{\rho_1 \pi d^2 L g} \approx \frac{24\overline{\tau}_w L}{\rho_1 d g W_{CJ}} \tag{4.22}$$

As before, it has been assumed that the fully-filled cycle time is approximated by $t_f \approx 6t_{CJ} \approx 6L/W_{CJ}$. Finally, rewriting Eq. (4.22) to the form

$$\Delta I_{sp}\Big|_{F_{visc}} \approx \left[\frac{24\overline{\tau}_w}{\rho_1 W_{CJ} g}\right]\frac{L}{d} \approx K_2 \frac{L}{d} \tag{4.23}$$

Thus, at a first-order approximation, the decrement in specific impulse due to frictional losses is also proportional to the L/d of the thrust chamber. Furthermore, the value of K_2 can be determined from the theoretical properties of the detonable mixture, and an empirically measured average wall shear stress $\overline{\tau}_w$.

With Eqs. (4.20) and (4.23), an estimate for the actual fully-filled PDE specific impulse can be written as

$$I_{sp,actual} \approx I_{sp,isentropic} - \Delta I_{sp}\Big|_{q_{loss}} - \Delta I_{sp}\Big|_{F_{visc}} \tag{4.24}$$

Or equivalently,

$$I_{sp,actual} \approx I_{sp,isentropic} - K_1\frac{L}{d} - K_2\frac{L}{d} \approx I_{sp,isentropic} - (K_1 + K_2)\frac{L}{d} \tag{4.25}$$

where the definitions of K_1 and K_2 are shown in Eqs. (4.20) and (4.23), respectively. Combining K_1 and K_2 into a single constant, K, and after manipulation of Eq. (4.25), a useful

form of the desired expression for the performance decrement in a fully-filled PDE due to heat and frictional losses can be obtained.

$$\frac{I_{sp,actual}}{I_{sp,isentropic}} \approx 1 - K\frac{L}{d} \tag{4.26}$$

Note, in this form, $K = (K_1 + K_2)/I_{sp,isentropic}$, which is dependent on physical properties of the detonable propellant, averaged heat flux through the wall, averaged shear stress distribution along the internal surface, and ideal performance. Although simple, Eq. (4.26) provides a very useful relationship for estimating how the heat and frictional losses combine and scale with the thrust chamber L/d. To demonstrate this, a normalized specific impulse comparison of the MOC model is made in Fig. 4.18 with existing published data for fully-filled PDEs of varying L/d ranging from 8–200 and operating with $2H_2$–O_2, C_2H_4–$3O_2$, and C_3H_8–$5O_2$ propellants. In this case, a least-squares fit to the aggregate experimental data in Fig. 4.18 of the form: $I_{sp}/I_{sp,MOC} \approx 1 - K(L/d)$, yields $K = 3.37 \times 10^{-3}$. Note, this is an averaged representation of K based on several experimental results with different detonable mixtures. In practice, and for more accurate results, K should be estimated based on the detonation properties of the respective propellant and physical conditions of the actual setup. Despite this, it follows, albeit crudely, that the current MOC model will overestimate the actual fully-filled PDE performance by more than 20 percent for $L/d \gtrsim 60$, which is similar to the findings of [149, 151]. Additionally, although these results are for fully-filled PDEs, similar trends are expected for the partially-filled PDE and PDEs featuring diverging nozzles. It should also be noted that the self-similarity of the flow begins to breakdown as $L/d \to 1$, which causes an additional deviation in the experimental observations from that of the ideal PDE performance. Details regarding the breakdown of self-similarity can be found in [149].

It is also possible to encounter flow field situations whereby the frozen flow assumption used in the development of the current MOC model is not entirely accurate. In the present model, the frozen flow assumption implies that the burned products behave as a calorically perfect gas, such that the distribution of molecular internal energy states and chemical

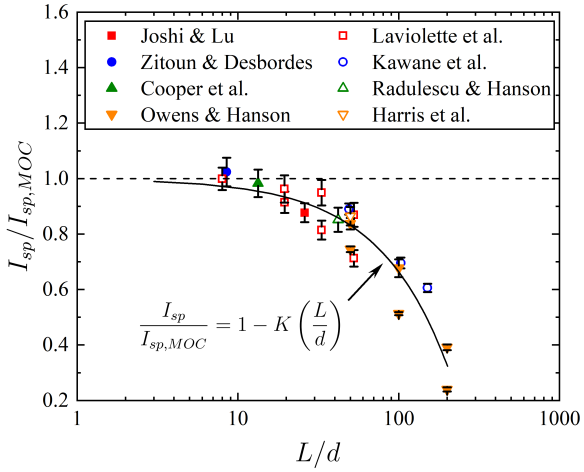

Figure 4.18. Comparison of normalized specific impulse from MOC model with published data in [89,90,97,149–153] for various L/d and $2H_2$–O_2, C_2H_4–$3O_2$, and C_3H_8–$5O_2$ propellants.

composition are invariant to changes in pressure and temperature in the thrust chamber flow field. Another way of stating this, is that the current model assumes that the timescales associated with the readjustment of thermodynamic and chemical equilibrium are infinitely long compared to that of the characteristic flow timescale of a moving fluid element within the thrust chamber flow field. In actuality, this is not true as the timescales associated with chemical reactions and the translational, rotational, and vibrational relaxation processes are in fact finite, and can be of the same order or smaller than that of the flow timescale. In such cases, exothermic recombination of atomic species will take place across expansive regions of the flow field, which will ultimately raise the PDE performance. Therefore, it is important to comment on the limitations of the frozen flow assumption used in the development of the current MOC model, and mention to what extent this assumption will influence the model results in comparison to experimental measurements.

The degree to which the flow is locally frozen, in a state of equilibrium, or nonequilibrium, can be determined by use of the Damköler number, Da. In general, the Damköler number is simply defined as,

$$Da = \frac{t_f}{t_r} \tag{4.27}$$

where t_f is the local characteristic flow time, and t_r is the local time required to reach equilibrium from either thermodynamic relaxation or chemical reaction processes. In this case, t_f corresponds to the amount of time required for a fluid element to traverse a distance of interest, l, within the thrust chamber flow field. In application to the quasi-one-dimensional PDE flow field, l would simply be the length of a pathline that traverses across any number of gasdynamic waves within the thrust chamber flow field, such as the Taylor, secondary, and exhausting rarefaction waves. Hence, $t_f = l/u$, where u is the local velocity along the fluid element pathline. However, it is worth noting that different selections of l, such as the detonation or shock wave structure length, can yield drastically shorter flow time scales. In essence, when $Da \ll 1$, namely, $t_f \ll t_r$, then it follows that the flow can be described by a frozen flow assumption. Alternatively, when $Da \gg 1$, namely, $t_f \gg t_r$, then it follows that the flow can be described by a local equilibrium assumption. Lastly, if $Da \approx 1$, namely, $t_f \approx t_r$, then it follows that the flow is in a state of nonequilibrium. Before evaluating Da for processes in the PDE flow field, it is necessary to first establish which of the timescales associated with various relaxation and chemical reaction processes are of importance. In general, the timescales required to reach thermodynamic equilibrium vary widely among translational, rotational, and vibrational relaxation, which are also generally different from the chemical reaction timescales. As discussed by Vincenti and Kruger [154] and Zel'dovich and Raizer [155], equilibrium is generally established orders of magnitude faster in high temperature gas flows for translational and rotational relaxation processes compared to the much slower vibrational relaxation and chemical reaction processes. Additionally, Bray [156] demonstrated that most of the nonequilibrium effects on thrust performance for conventional rocket engines can be adequately captured when only considering vibrational relaxation and chemical reaction processes. Therefore, only these respective timescales will be considered in the following discussion.

The dynamics of burned products across the Taylor rarefaction will be used for the purposes of estimating the flow timescale, and the associated vibrational relaxation and

chemical timescales, as this rarefaction wave is the first rapid expansion process that a fluid element encounters upon passing through the detonation wave. Moreover, these timescales can then be used to create a first-order estimate of Da, whereby locally frozen, nonequilibrium, or equilibrium flow can be determined. As previously discussed, once a fluid element passes through a detonation wave, the fluid element approaches a state of local thermodynamic and chemical equilibrium upon reaching the equilibrium CJ point. Additionally, once the fluid element begins to traverse across the Taylor rarefaction wave following the detonation, rapid pressure and temperature changes cause the fluid element to undergo readjustment towards a new thermodynamic and chemical equilibrium. The vibrational relaxation timescale can be approximated with empirical correlations based on conventional Landau–Teller plots ($\ln p\tau_{vib}$ vs. $T^{-1/3}$) [139] given the post-detonation mixture and representative bath gas. For instance, in stoichiometric H_2–O_2 detonable mixtures, the post-detonation state primarily consists of diatomic and polyatomic species H_2O, H_2, OH, and O_2 with mole fractions of $X_{H_2O} = 0.534$, $X_{H_2} = 0.162$, $X_{OH} = 0.135$, and $X_{O_2} = 0.048$, respectively. Consequently, H_2O can be taken as the representative bath gas, and the vibrational relaxation timescale can be estimated for the various species with H_2O as the most frequent collision partner. At the temperatures and pressures encountered across the Taylor rarefaction wave for stoichiometric H_2–O_2, the vibrational relaxation timescale of H_2O in H_2O is estimated to be $\tau_{vib} \sim \mathcal{O}(10^{-8})$ seconds using the empirical results of Kung and Center [157]. Similarly, a rough approximation for the vibrational relaxation timescale of the diatomic species in H_2O can be determined using N_2 as a representative diatomic species. In this case, the vibrational relaxation timescales of H_2, OH, and O_2 in H_2O are roughly $\tau_{vib} \sim \mathcal{O}(10^{-7})$ sec, using the empirical results of Center and Newton [158].

In stoichiometric H_2–air detonable mixtures, the post-detonation state primarily consists of diatomic and polyatomic species N_2, H_2O, H_2, OH, and O_2 with mole fractions of $X_{N_2} = 0.632$, $X_{H_2O} = 0.295$, $X_{H_2} = 0.031$, $X_{OH} = 0.018$, and $X_{O_2} = 0.008$, respectively. Consequently, N_2 can be taken as the representative bath gas, and the vibrational relaxation

timescale can be estimated for the various species with N_2 as the most frequent collision partner. At the temperatures and pressures encountered across the Taylor rarefaction wave for stoichiometric H_2–air, the vibrational relaxation timescale of N_2 in N_2 is estimated to be $\tau_{vib} \sim \mathcal{O}(10^{-6})$ seconds using the empirical results of Millikan and White [140]. Similarly, the vibrational relaxation timescale of H_2O in N_2 is estimated to be $\tau_{vib} \sim \mathcal{O}(10^{-8})$ seconds using the empirical results of Kung and Center [157]. Lastly, a rough estimate for the remaining diatomic species in N_2 can be determined using the empirical results of [140] to be approximately $\tau_{vib} \sim \mathcal{O}(10^{-7})$ seconds.

As previously discussed, it is also desired to estimate the timescales of the chemical reactions upon departure from the equilibrium CJ state. A simple method for approximating the chemical reaction timescales was discussed by Gou et al. [159] for combustion modeling with reduced and detailed chemical kinetic mechanisms. In that study, it was demonstrated that the chemical timescale could be approximated by,

$$\tau_{chem,i} = \frac{Y_i}{D_i} \tag{4.28}$$

where Y_i and D_i are the mass fraction and mass fraction destruction rate of the i^{th} species, respectively. It is noted, that the primary reactions to take place will be recombination as the gas expands to lower pressures and temperatures during the gasdynamic blowdown process. The mass fraction and destruction rates can be evaluated with the chemical kinetics program Cantera [24] for all of the post-detonation species by perturbing the reaction system away from chemical equilibrium across the Taylor rarefaction wave. As such, for stoichiometric H_2–O_2 detonable mixtures, the dominant chemical recombination timescales occur on a range $\tau_{chem} \sim \mathcal{O}(10^{-5}$–$10^{-6})$ seconds. Similarly, for stoichiometric H_2–air detonable mixtures, the dominant chemical recombination timescales occur on a range $\tau_{chem} \sim \mathcal{O}(10^{-4}$–$10^{-6})$ seconds. One of the more significant conclusions to draw from these estimates is that the PDE thrust chamber flow field is likely to always be in, or near, a state of local thermodynamic equilibrium. This comes about from the result that $\tau_{vib} < \tau_{chem}$ by roughly an order of magnitude for hydrogen-based detonable mixtures. Fur-

ther, this indicates that most nonequilibrium effects associated with PDE flow fields come in the form of chemical nonequilibrium as opposed to thermodynamic nonequilibrium, in which case the flow field chemical kinetics can be accurately modeled with Arrhenius-based finite-rate chemistry models.

Based on the above discussion, the magnitude of the Damköler number can be estimated by assuming $t_r \approx \tau_{chem}$. Moreover, for the purposes of estimating the flow timescales, it will be assumed that chemical equilibrium or nonequilibrium effects do not heavily influence the time required for a fluid element to traverse across the Taylor rarefaction wave. Therefore, by use of the MOC model, it follows that the flow timescale for a fluid element starting at $x_0 = 0.1$, 0.5, and 1 m from the thrust wall, are characterized by 5.5×10^{-5}, 2.7×10^{-4}, and 5.4×10^{-4} seconds for H_2–O_2 detonable mixtures, and 7.5×10^{-5}, 3.7×10^{-4}, and 7.4×10^{-4} seconds for H_2–air detonable mixtures, respectively. Consequently, within the thrust chamber flow field, $1 \lesssim Da \lesssim 100$ for H_2–O_2 detonable mixtures and $0.1 \lesssim Da \lesssim 100$ for H_2–air detonable mixtures. Further, recognizing that the subsequent expansion processes within the PDE flow field usually happen slower than that within the Taylor rarefaction wave, it can be said that the H_2–O_2 PDE flow field is mostly characterized by an equilibrium flow assumption, while the H_2–air PDE flow field is characterized by regions of chemical nonequilibrium and equilibrium. Although this analysis only pertains to the Taylor rarefaction wave and subsequent gasdynamic expansion processes in the thrust chamber flow field, the presence of chemical nonequilibrium is expected to be more significant in the event the PDE is partially-filled, and even more severe when a diverging nozzle is coupled to the end of the PDE. In the latter case, the diverging nozzle permits geometric expansion of the gas, whereas the fully- and partially-filled PDEs only allow for gasdynamic expansion through the various rarefaction waves. Consequently, the rate of expansion through a nozzle will be considerably larger compared to rarefaction waves alone, which will in turn amplify the effects of chemical nonequilibrium.

The above discussion indicates that the frozen flow assumption utilized in the development of the MOC model is not a very accurate description of the actual PDE flow field. As such, it is necessary to highlight the consequences of employing such a simplifying assumption. For instance, Kailasanath et al. [160] and Povinelli and Yungster [146] studied the effects of dissociation and recombination on the performance of fully-filled PDEs using a multi-step finite-rate chemistry model. They demonstrated that the heat released during recombination of atomic species could raise the specific impulse by approximately 5 percent over that of the idealized PDE with frozen chemistry for PDEs operating with H_2–air. Similarly, using a multi-step finite-rate chemistry model for H_2–O_2, Morris [76] and Sato et al. [98] reported fully-filled PDE specific impulses that where 4.7 and 3.3 percent higher than that predicted by the current MOC model with frozen chemistry, respectively. Further, Povinelli and Yungster [147] and Sato et al. [98] also reported fully-filled PDE specific impulses that were roughly 6.6 and 3.4 percent higher than that predicted by the current MOC model for both stoichiometric C_2H_4–air and C_2H_4–O_2 mixtures, respectively. Based on these comparative results, it is anticipated that current MOC model will underestimate the fully-filled performance of a PDE by roughly 5 percent due to freezing the chemistry of the burned products and neglecting recombination during the gasdynamic blowdown processes. Additionally, it follows that this deviation could be more severe with longer PDE geometries (greater than 1 m in length) where the overall time for recombination is lengthened, thereby increasing the performance increase from more efficient recombination.

In the case of partially-filled PDEs and PDEs with diverging nozzles, this deviation due to the frozen flow assumption is expected to become more severe, as the gasdynamic blowdown features more expansion of the burned products, and more time is allowed for further recombination reactions to occur. For instance, in the case of partially-filled PDEs, the current MOC model underestimates the specific impulse results reported by Sato et al. [98] by 4.9 and 5.1 percent for stoichiometric H_2–O_2 and C_2H_4–O_2 detonable mixtures with air as the inert gas at a fill fraction of $\alpha = 0.5$. Similarly, Barbour and Hanson [161]

investigated the effects of chemical nonequilibrium on PDEs with diverging nozzles using a multi-step finite-rate chemistry model. They showed that chemical nonequilibrium due to incomplete recombination in the nozzle could lead to a 9 percent loss compared to the chemical equilibrium solution for PDEs operating with stoichiometric H_2–O_2 and C_2H_4–O_2 propellant and featuring diverging nozzles with a 12 degree half-angle and an expansion area ratio of $\epsilon = 100$. In comparison to the current frozen flow MOC model, this correlates to an underestimation of 13 and 15 percent for stoichiometric H_2–O_2 and C_2H_4–O_2 propellants, respectively. However, it is interesting to note that when Barbour and Hanson [161] included the losses due to friction and heat transfer, the agreement between the current MOC model and those reported results reduced to only 3.0 and 4.8 percent, respectively. This result is merely fortuitous, due to the simplifying assumptions of the MOC model. Although, it does indicate that in some cases the performance gains due to recombination are similar in magnitude to the performance losses associated with friction and heat transfer, such that the PDE performance can be represented by an idealized model that neglects all of these details. Despite this, it follows that by neglecting equilibrium or nonequilibrium chemical recombination in the PDE flow field, the frozen flow assumption will have the tendency to underestimate the actual PDE performance.

Finally, an additional limitation of the current MOC model is the ability to properly model the exhausting nozzle flow field in cases where severe over-expansion manifests in the nozzle. This usually occurs in scenarios with low ψ and large ϵ. In these cases, the inviscid and quasi-one-dimensional assumptions fail to account for the shock wave-boundary layer interaction and multi-dimensional core flow that develops past the separation point in the nozzle. Consequently, this leads to an underestimation of the real PDE performance. As a general note, the Summerfield criterion [162] can be used to estimate when a severely over-expanded nozzle will result in flow separation, namely, when the nozzle exit pressure reaches roughly 40 percent of the ambient condition. Although this criterion is based on conventional steady flow nozzles, its accuracy should increase in the event quasi-steady flow

is established in the nozzle after the transmitted and secondary shock passage. However, it should also be noted that such severely over-expanded cases usually occur far away from the conditions associated with optimum performance. Therefore, this limitation should not prevent the MOC model from being used to accurately determine the optimum nozzle expansion area ratio for a given blowdown pressure ratio.

CHAPTER 5

ANALYTICAL MODEL OF FULLY-FILLED PULSE DETONATION ENGINE

5.1 Control Volume Analysis

It will be of use in the forthcoming analysis and discussion to have a simplified analytical performance model for the fully-filled PDE. As will be seen in the following chapter, performance scaling laws developed for partially-filled PDEs are normalized by that of a fully-filled PDE operating under similar conditions. Therefore, it is of importance to develop a simplified analytical model that can accurately predict the primary performance metrics of a fully-filled PDE, such as time-averaged thrust, total impulse, and specific impulse, without the need of performing a MOC-based computation. Additionally, it will be of use in the following chapter to establish the upper limit of idealized optimum performance for a PDE using a quasi-steady nozzle. Hence, it is desired first formulate a simplified analytical model for the fully-filed PDE that can readily be extended the case of a quasi-steady nozzle. In the development of such a simplified fully-filled performance model, a detailed control volume analysis is advantageous, since the primary gasdynamic processes that govern the impulse and thrust generation of a fully-filled PDE can be identified. For this, the results from the MOC model are used to assist in the control volume analysis, as the entire flow field can readily be calculated for the complete gasdynamic blowdown in a single-cycle. Such analysis provides the opportunity to gain useful physical insights regarding the nature of transient thrust and impulse generation, which can aid the identification of conditions for which a fully-filled PDE performance model can be simplified. For the subsequent control volume derivation and discussion, the control volume under consideration is depicted in Fig. 5.1. Note, the control volume surrounds the entire PDE thrust chamber; hence, the unsteady momentum within the control volume, momentum flux, and pressure-area force at the exit control surface all contribute to the overall thrust and impulse. For

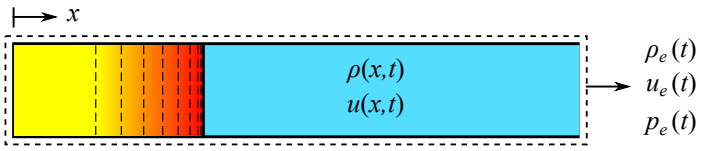

Figure 5.1. Control volume (dashed line) for simplified analytical performance model of fully-filled PDE.

this model, it is assumed that the gasdynamics are one-dimensional, unsteady, inviscid, and absent from any heat transfer. Note, these assumptions were shown to be in agreement with the actual gasdynamic flow field in a PDE thrust chamber during the development and validation of the MOC model in Ch. 4. As such, they are used to simplify the current control volume analysis. The general linear momentum equation for the closed control volume in Fig. 5.1 is given by

$$R_x = \frac{\partial}{\partial t}\left[\int_{cv} \rho(x,t)u(x,t)\ d\mathcal{V}\right] + u_e(t)\dot{m}_e(t) + \left[p_e(t) - p_0\right]A_e \tag{5.1}$$

In this form, R_x is the resultant thrust force on the control volume, and the first, second, and third terms on the right-hand side of Eq. (5.1) represents the time rate of change of internal momentum integrated over the control volume, momentum flux at the exit control surface, and the net pressure-area force at the exit control surface, respectively. Additionally, the actual reaction thrust force on the PDE thrust chamber is obtained by application of Newton's third law, $F_x = -R_x$, namely, equal and opposite the net force on the control volume. However, without loss of generality, the negative sign can be neglected in the subsequent analysis.

5.1.1 Transient Thrust and Impulse Generation

It is now of interest to investigate the behavior of each term in Eq. (5.1) for the single-cycle gasdynamic blowdown of a fully-filled PDE. More specifically, it is of interest to determine what fraction of the overall impulse is attributed to the unsteady momentum within the chamber, momentum flux out of the chamber, and pressure-area force at the chamber exit plane during a single-cycle of operation. For this, the MOC model is used to

calculate the complete flow field of a fully-filled PDE. Fig. 5.2(a) shows the the integrated unsteady momentum and time-rate of change of that momentum for a thrust chamber that is 1 m in length with an L/d of 10, initially filled with stoichiometric H_2-O_2 propellant at 1 atm and 300 K, and at an initial blowdown pressure ratio of unity. In this case, the black curve represents the integrated momentum over the control volume at each instance in time during the blowdown, and the red curve represents the time rate of change of that integrated momentum.

For $t/t_{CJ} < 1$, the detonation wave is steadily propagating down the length of the thrust chamber until eventually exiting the chamber at $t/t_{CJ} = 1$. Consequently, there is a sharp rise in the integrated momentum being imparted on the propellant that is initially at rest. Recall that the Taylor rarefaction wave behind the detonation wave decelerates the gas to rest as a result of the thrust wall boundary condition. As a result, although the detonation wave imparts momentum to the burned products, the Taylor wave subsequently removes some of this momentum, or kinetic energy, and converts it back into internal energy in the stagnation region following the rarefaction wave. This causes the sharp drop in integrated momentum across the chamber volume immediately following the exit of the detonation wave. Additionally, the exhausting rarefaction wave enters the chamber immediately following the exit of the detonation wave, which accelerates the burned products out of the chamber. Consequently, as the exhausting rarefaction continues propagating into the thrust chamber, the internal energy of the burned products is converted back into kinetic energy, which begins to increase the momentum near the chamber exit. Eventually, the exhausting rarefaction begins increasing the integrated momentum of the burned products more than the Taylor rarefaction wave is able to attenuate the momentum, which results in the minimum point on the black curve at $t/t_{CJ} \approx 1.7$ in Fig. 5.2(a). After the minimum point, the exhausting rarefaction continues propagating into the chamber until the leading characteristic of the rarefaction wave reaches the thrust wall at $t/t_{CJ} \approx 3$. Subsequently, as the exhausting rarefaction reflects from the thrust wall, the integrated momentum reaches

a secondary maximum at roughly $t/t_{CJ} \approx 3.5$, in which case the chamber begins to enter a mostly quasi-steady constant volume blowdown, where the gas properties are nearly uniformly distributed and the integrated momentum slowly returns back to zero at the end of the cycle.

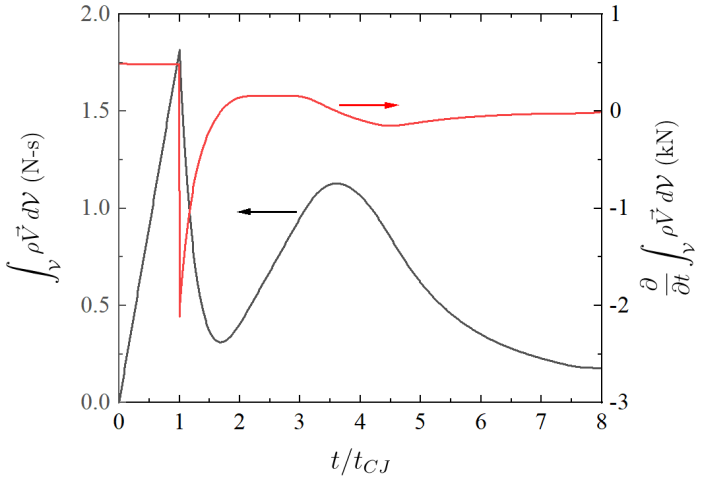

(a)

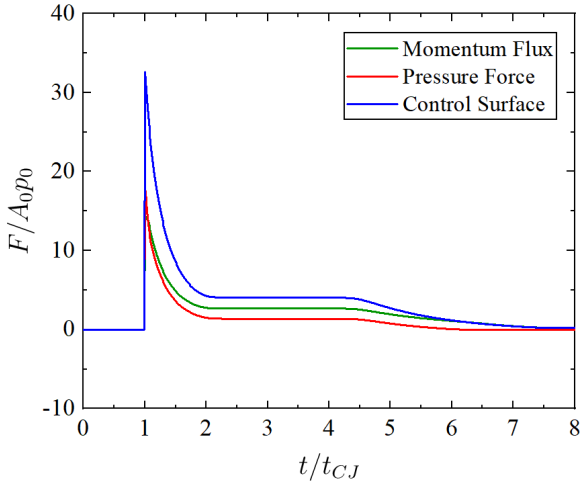

(b)

Figure 5.2. (a) Integrated momentum over control volume (black) and time rate of change (red), and (b) control surface force components (blue): momentum flux (green) and pressure-area force (red) for fully-filled PDE operating with $2H_2$-O_2 propellant at 1 atm and 300 K ($\psi - 1$).

As previously mentioned, the time rate of change of integrated momentum is given by the red curve in Fig. 5.2(a). Physically, the magnitude of the red curve corresponds to the slope of the integrated momentum (black curve), which is exactly equal to the net force acting on the control volume due to the unsteady momentum within the chamber. As such, given the steady propagation of the detonation for $t/t_{CJ} < 1$, momentum is being linearly imparted onto the burned products, which results in the constant positive force on the control volume. However, after the detonation wave exits and the integrated momentum begins decreasing due to the Taylor rarefaction, the net force from integrated momentum across the volume becomes negative. Additionally, the net force remains negative until the exhausting rarefaction begins imparting more momentum to the burned products than the Taylor wave is able to attenuate, which takes place at $t/t_{CJ} \approx 1.7$, at which case the net force equals zero. After this point, the exhausting rarefaction is accelerating the burned products towards the chamber exit causing an increase in integrated momentum that is mostly linear, resulting in the constant positive force until the instant in time when the leading edge of the exhausting rarefaction reaches the thrust wall at $t/t_{CJ} \approx 3$. After this point, the net force due to integrated momentum in the control volume passes back through zero at the secondary peak on the black curve at $t/t_{CJ} \approx 3.5$, and remains negative for the rest of the mostly quasi-steady constant volume blowdown. It is noted that the secondary maximum negative force occurs at $t/t_{CJ} \approx 4.5$, which corresponds to the time at which the leading characteristic of the exhausting rarefaction wave reaches the chamber exit after reflecting from the thrust wall. Eventually, the net force from integrated momentum inside the control volume returns back to zero at the end of the cycle. The important thing to note about the time rate of change of integrated momentum in the control volume for a fully-filled PDE, is the fact that the net force can be both positive and negative. As will be seen in the following discussion, this will have a significant implication regarding the overall impulse that is contributed by the first term on the right-hand side of Eq. (5.1).

The last two terms on the right-hand-side of Eq. (5.1), namely, momentum flux and the pressure-area force at the chamber exit plane, are shown in Fig. 5.2(b) in nondimensional form. In this case, the momentum flux is shown with the green curve, while the pressure-area force is shown with the red curve. The sum total of the two forces, which makes up the net force at the exit control surface is shown by the blue curve. As expected, both the momentum flux and pressure-area force on the exit plane are exactly zero for $t/t_{CJ} < 1$, since the detonation wave has not actually reached the exit plane of the chamber. However, at $t/t_{CJ} = 1$, the maximum momentum flux and pressure-area force are observed on the exit plane. The relaxation in momentum flux and pressure on the exit plane from $1 \leq t/t_{CJ} \lesssim 2$ is due to the interaction of the exhausting rarefaction and Taylor rarefaction waves, which subsides to a steady value once the Taylor rarefaction wave has exited the chamber at $t/t_{CJ} \approx 2$. From $2 \lesssim t/t_{CJ} \lesssim 4.5$, a quasi-steady flow persists on the exit plane, which is indicated by the mostly steady momentum flux and pressure-area force, and net control surface force. As previously mentioned, $t/t_{CJ} \approx 4.5$ corresponds to the time at which the leading characteristic of the exhausting rarefaction wave reaches the chamber exit after reflecting from the thrust wall, in which case both the momentum flux and pressure-area force on the exit plane begin to relax in accordance with a quasi-steady constant volume blowdown. This continues until the thrust chamber completely exhausts into the surrounding and the net control surface force returns back to zero at the end of the cycle. The important thing to note for the net momentum flux and pressure-area force at the chamber exit, is the fact that the net control surface force is always positive. It is also worth noting that the exhausting rarefaction wave accelerates the burned products to a choking condition at the exit plane of the PDE, such that sonic flow exists at the exit plane for the majority of the blowdown. As will be seen in the following subsections, this aspect will have significant simplifying implications when modeling the exhausting flow properties on the exit plane.

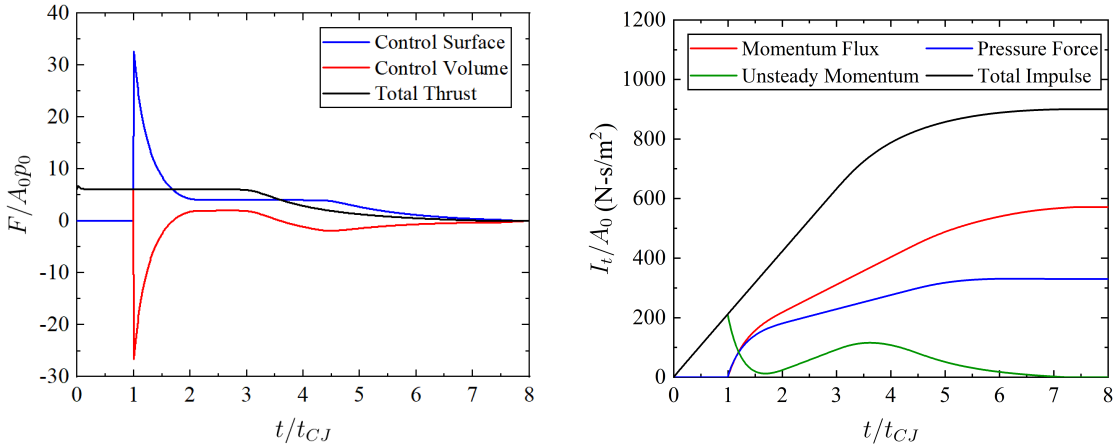

Figure 5.3. (a) Components of total thrust (black): net control surface momentum flux and pressure-area force (blue) and time rate of change of integrated momentum over the control volume (red), and (b) impulse generation for fully-filled PDE operating with $2H_2$-O_2 propellant at 1 atm and 300 K ($\psi - 1$).

A comparison of the net control surface force, namely, the addition of momentum flux and pressure-area force on the exit plane, and the control volume force, namely, the time rate of change of integrated momentum over the control volume, are shown in Fig. 5.3(a). In this figure, the blue curve represents the net control surface force, while the red curve represents the net control volume force. Additionally, the black curve represents the total sum of the control surface and volume forces, which accounts for all three terms on the right-hand-side of Eq. (5.1). As expected, the total thrust profile is identical to the profile that would be obtained by simply evaluating the pressure-area force history on the thrust wall, is in the case of [65]. However, in the current control volume analysis, it is easier to visualize the behavior and breakdown of terms that contribute to the thrust. Although the transient thrust profile and time-averaged thrust are important performance considerations, the integrated impulse for the cycle is more indicative of which terms actually contribute to the overall single-cycle performance. As such, Fig. 5.3(b) shows the breakdown of impulse per unit thrust area from each of the three terms on the right-hand-side of Eq. (5.1). In this figure, the green curve represents the integrated impulse as a result of the net control

volume force, namely, time rate of change of integrated momentum over the control volume, the blue curve represents the integrated impulse as a result of the net pressure-area force on chamber exit plane, and the red curve represents the integrated impulse from the net momentum flux at the chamber exit plane. Lastly, the black curve represents the sum total of all three components, representing the total net impulse during a single-cycle.

Due to the manner in which momentum spatially changes throughout the control volume during the blowdown, the contribution from the time rate of change of integrated momentum contributes to a small fraction of the impulse during the cycle. In fact, because of the positive and negative variation in the control volume force, the net area under the red curve in Fig. 5.3(a) is effectively zero by the end of the cycle. This is indicated by the green curve in Fig. 5.3(b) approaching zero towards the end of the cycle. This result indicates that the net time rate of change of integrated momentum over the control volume is a negligible quantity over the duration of a single-cycle of a fully-filled PDE, and minimally contributes to the overall impulse. Physically, the above results indicates that

$$\int_0^{t_f} \left\{ \frac{\partial}{\partial t} \left[\int_{cv} \rho(x,t) u(x,t) \, d\mathcal{V} \right] \right\} dt \ll \int_0^{t_f} \left\{ u_e(t) \dot{m}_e(t) + \left[p_e(t) - p_0 \right] A_e \right\} dt \tag{5.2}$$

where t_f represents the duration of a single-cycle. Therefore, if it is desired to derive an analytical model such that the primary performance metrics are based on the complete cycle, i.e. time-averaged thrust, total impulse, and specific impulse, as opposed to the transient evolution of thrust and impulse, then the general thrust equation for a fully-filled PDE in Eq. (5.1) can be reduced to

$$F_x = u_e(t) \dot{m}_e(t) + \left[p_e(t) - p_0 \right] A_e \tag{5.3}$$

Note, in this form the negative sign for the reaction force on the thrust chamber has been dropped. It should be emphasized that an expression this simple will not provide the correct temporal evolution of thrust and impulse generation during a single cycle of operation. However, because the time rate of change of integrated momentum over the control volume

negligibly contributes to the total impulse at the end of the cycle, the simplified expression can be especially useful at modeling complete cycle performance metrics.

A comparison of the full thrust equation in Eq. (5.1) and the simplified expression in Eq. (5.3) is shown in Fig. 5.4. In this figure, the black curve represents the total integrated impulse from all three terms in Eq. (5.1), while the red curve simply represents the net control surface force, namely, the momentum flux and pressure-area force at the chamber exit in Eq. (5.3). As expected, the temporal evolution in impulse is very different for the respective thrust equations; however, the total impulse at the end of the cycle is effectively identical due to the behavior of the time rate of change of integrated momentum over the control volume throughout the complete cycle.

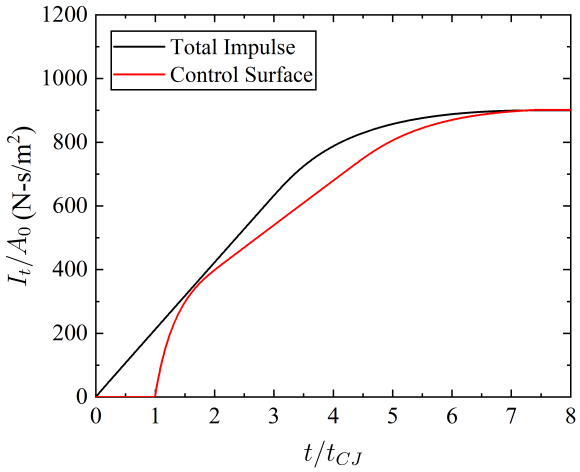

Figure 5.4. Comparison of integrated impulse from complete control volume expression (black) Eq. (5.1) and simplified expression (red) Eq. (5.3) for fully-filled PDE operating with $2H_2$-O_2 propellant at 1 atm and 300 K ($\psi - 1$).

Given the above control volume analysis and discussion, it is evident that a simplified fully-filled PDE model can be developed whereby the time rate of change of integrated momentum over the control volume is neglected. Such an assumption allows modeling efforts to be directed at the exit plane of the thrust chamber as opposed to the complete flow field, whereby the goal becomes to model the momentum flux and pressure-area force on the

chamber exit plane. Additionally, such an assumption restricts the performance model to single-cycle performance metrics such as time-averaged thrust, total impulse, and specific impulse; however, these are generally the primary figures of merit for evaluating preliminary PDE performance. Therefore, the following subsections is dedicated to developing a simplified fully-filled PDE performance model based on Eq. (5.3).

5.1.2 Simplified Thrust Equation

Before proceeding to a description of flow properties on the chamber exit plane, it is of interest to further simplify the thrust equation in Eq. (5.3). In the previous subsection, the general thrust equation in Eq. (5.1) was reduced to Eq. (5.3) based on the behavior and contribution of the unsteady momentum within the control volume. However, Eq. (5.3) can be simplified even further given certain conditions that exist on the exit plane of a fully-filled PDE during the gasdynamic blowdown process. It was previously mentioned that the exhausting rarefaction of a fully-filled PDE creates a choked sonic flow condition on the exit plane for the majority of the gasdynamic blowdown. Fortunately, this condition reduces the number flow properties required to properly evaluate Eq. (5.3). Further, for simplicity, it is assumed that the burnt products are chemically frozen during the gasdynamic blowdown. This reduces the modeling of exit plane properties to a one-γ model, where the ratio of specific heats is simply given by $\gamma_2 = \gamma_{CJ}$, namely, the equilibrium value behind the detonation wave. With the above assumptions, it follows that the exit gas velocity can be replace by

$$u_e(t) = a_4(t) = \sqrt{\gamma_2 R_2 T_4(t)} \tag{5.4}$$

Similarly, the mass flow rate can be replaced by

$$\dot{m}_e(t) = \rho_4(t) A_e u_4(t) = \rho_4(t) A_e \sqrt{\gamma_2 R_2 T_4(t)} \tag{5.5}$$

where it is noted that the subscript 4 refers to the gas state on the exit plane at $x = L$. Substituting these quantities into Eq. (5.3) yields

$$F_x = \gamma_2 R_2 T_4(t) \rho_4(t) A_e + [p_4(t) - p_0] A_e \tag{5.6}$$

Replacing the density using the thermal equation of state for an ideal gas yields

$$F_x = \gamma_2 p_4(t) A_e + [p_4(t) - p_0] A_e \tag{5.7}$$

Lastly, regrouping terms results in the final simplified thrust equation:

$$F_x = p_4(t) A_e \left[\gamma_2 + 1 - \frac{p_0}{p_4(t)} \right] \tag{5.8}$$

With this final simplified thrust expression in Eq. (5.8), it is noted that the only time varying quantity is $p_4(t)$, namely, the transient pressure profile on the chamber exit plane. Therefore, the goal of the following subsections is to describe this pressure history at the chamber exit plane for a generalized fully-filled PDE.

5.2 Model Description

Consider a straight and constant-area PDE thrust chamber with an overall length L, which is fully-filled with gaseous detonable propellant. The propellant is separated from the ambient by an idealized contact surface at the chamber exit plane. For simplicity, it is assumed that the propellant and contact surface are initially stationary. Recall that a detailed description of the gasdynamic flow field was provided in Ch. 2 for a fully-filled PDE, therefore only a brief description is provided here. Following ignition, a detonation wave is assumed to instantaneously form at the head end of the thrust chamber and propagate down the chamber away from the thrust wall. The detonation wave is immediately followed by the self-similar Taylor rarefaction wave, which decelerates the gas from a high velocity to rest, satisfying the closed wall boundary condition at the head end of the chamber. As the detonation wave reaches the exit, the detonation wave collides with the contact surface at the chamber exit. Note, the full description of this gasdynamic interaction was provided

in Ch. 3 for the cases of reflected shock, Mach, or rarefaction wave from the contact surface, depending on the conditions across the discontinuity. Following the collision, a transmitted shock propagates into the surrounding while a reflected wave propagates into the burned products. Similarly, the exhausting rarefaction wave enters the chamber and immediately follows the reflected interface wave, which together propagate towards the head end of the chamber. A labeled x–t diagram is provided in Fig. 5.5 for the entire flow field of a fully-filled PDE with the accompanying labeled state nomenclature for the current analytical model. In this case, 1 denotes the initial propellant state, 2 the post-detonation state, 3 the stagnation state behind the Taylor rarefaction wave, and 4 the properties on the exit plane of the PDE where $x = L$.

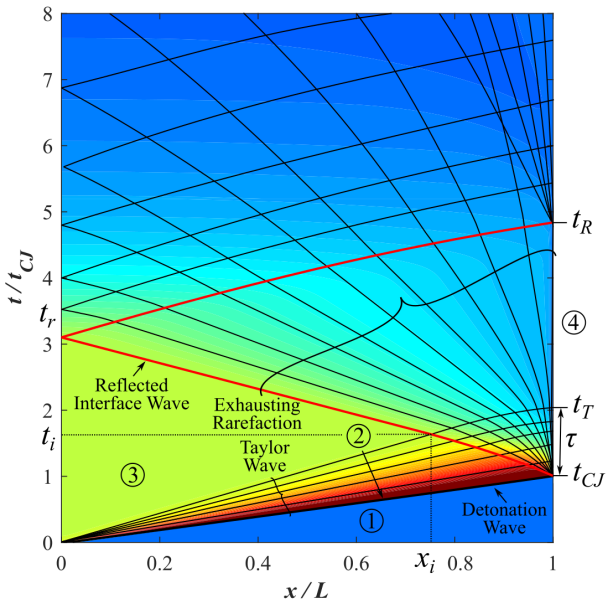

Figure 5.5. x–t diagram of fully-filled PDE flow field and associated important time instances for analytical model where the color corresponds to pressure.

The flow condition on the exit plane can be described by four distinct phases. The first is simply a quiescent phase prior to the arrival of the detonation wave, which has a

duration of $0 < t < t_{CJ}$, where $t_{CJ} = L/W_{CJ}$. Similarly, the second phase accounts for the starting flow process on the exit plane, which is caused by the arrival of the detonation wave and passage of the Taylor rarefaction wave. The duration of the second phase is defined by $t_{CJ} < t < t_T$, where t_T is the time at which the trailing characteristic of the Taylor rarefaction wave reaches the exit plane. Further, the third phase is a steady choked state that arises due to the exhausting rarefaction accelerating the gas in the stagnation region of state 3 to a sonic velocity on the exit plane at state 4. The duration of this steady choked phase is defined by $t_T < t < t_R$, where t_R is defined by the time at which the leading characteristic of the exhausting rarefaction wave reflects from the thrust wall and propagates back to the exit plane of the thrust chamber. Note, the leading characteristic of the exhausting rarefaction has been colored red in Fig. 5.5. In this depiction, it is clear that t_R is governed by the dynamics of the leading characteristic of the exhausting rarefaction wave. Lastly, the final phase is a mostly constant-volume blowdown of the thrust chamber for $t > t_R$. It is noted that the flow condition is not actually a constant-volume blowdown; however, due to the spatial uniformity of flow properties in the PDE for $t > t_R$, a constant-volume blowdown is a reasonable approximation [121]. In summary, the flow condition on the exit plane can be described by a quiescent condition, detonation wave arrival and Taylor wave passage, steady choked flow, and a constant-volume blowdown. As such, the goal of the following subsections is to provide an analytical description of state 4 on the exit plane throughout these distinct flow phases. Lastly, before proceeding to a description of the flow properties at state 4, it will be convenient to provide an analytical description of states 1, 2, and 3, as these states are required for evaluating state 4. Moreover, the variation in flow properties through the Taylor rarefaction wave and exhausting rarefaction wave will be required to properly define state 3 and t_R.

State 1 is simply described by the initially quiescent propellant with $u_1 = 0$, where p_1 and T_1 are defined as part of the propellant initial conditions. Similarly, state 2 is represented by the equilibrium post-detonation state, which was provided in Eqs. (3.10)-

(3.12) for a CJ detonation in Ch. 3. In order to determine state 3, it is required to evaluate the properties along the trailing characteristic of the Taylor rarefaction wave where $u_3 = 0$. The variation in flow properties through the Taylor rarefaction wave can readily be obtained by considering a self-similar centered rarefaction wave, where the leading characteristic travels at the detonation wave velocity, and the trailing characteristic travels at the local sound speed once the gas has isentropically decelerated to rest. The variation in pressure, sound speed, and gas velocity through the wave was given in [65] as

$$p(x,t) = \left(1 - \frac{\gamma_2 - 1}{\gamma_2 + 1}\frac{x_2 - x}{a_2 t}\right)^{2\gamma_2/(\gamma_2-1)} \frac{\gamma_1 M_{CJ}^2 + 1}{\gamma_2 + 1} p_1 \tag{5.9}$$

$$a(x,t) = \frac{\gamma_1 M_{CJ}^2 + \gamma_2}{\gamma_1 M_{CJ}^2}\frac{1}{\gamma_2 + 1} W_{CJ} + \frac{\gamma_2 - 1}{\gamma_2 + 1}\frac{x}{t} \tag{5.10}$$

$$u(x,t) = -\frac{\gamma_1 M_{CJ}^2 + \gamma_2}{\gamma_1 M_{CJ}^2}\frac{1}{\gamma_2 + 1} W_{CJ} + \frac{2}{\gamma_2 + 1}\frac{x}{t} \tag{5.11}$$

In these expressions, x_2 represents the location of the leading characteristic and is given by $x_2 = W_{CJ}t$. Evaluating Eq. (5.11) at $u(x_3, t) = 0$, and solving for x_3/t reveals the path of the trailing characteristic. Moreover, substituting that expression into Eqs. (5.9) and (5.10) yields the resulting pressure and sound speed in the stagnation region of state 3.

$$p_3 = p_1 \left(\frac{\gamma_1 M_{CJ}^2 + \gamma_2}{2\gamma_2}\right)\left(\frac{\gamma_1 M_{CJ}^2 + \gamma_2}{\gamma_1 M_{CJ}^2 + 1}\frac{\gamma_2 + 1}{2\gamma_2}\right)^{(\gamma_2+1)/(\gamma_2-1)} \tag{5.12}$$

$$a_3 = \frac{\gamma_1 M_{CJ}^2 + \gamma_2}{2\gamma_1 M_{CJ}^2} W_{CJ} \tag{5.13}$$

$$u_3 = 0 \tag{5.14}$$

It is now of interest to determine how the gas properties in state 3 vary across the exhausting rarefaction wave upon reaching the desired state 4 at the chamber exit. In this case, state 4 is simply governed by the nature in which state 3 expands through the exhausting rarefaction. Recall that in the x–t diagram of Fig. 5.5, the exhausting rarefaction is headed by the reflected interface wave (red line) from the interaction of the detonation wave with the contact surface. If this reflected interface wave is a Mach wave, then the reflected interface wave is simply that of the C_- characteristic that leads the exhausting

rarefaction wave. Similarly, if the reflected interface wave is a rarefaction wave, then the reflected rarefaction and exhausting rarefaction waves become coincident. In this case, the leading characteristic of the two coincident waves becomes the C_- characteristic that leads the exhausting rarefaction wave. Alternatively, in the event of a shock reflection from the contact surface, the exhausting rarefaction is headed by a shock. The existence of this shock can greatly complicate the gasdynamic description of the exhausting rarefaction. However, if the reflected shock is fairly weak, such that $p_{2'}/p_2 \approx 1$, then it can be assumed that the reflected interface wave is simply that of the the C_- characteristic that leads the exhausting rarefaction. In fact, this assumption was also used in the performance model of [66,67], and as will be shown in Ch. 6, the operating conditions that yield a reflected shock from the contact surface usually result in a shock of relatively weak strength. Moreover, because the shock is continually being overtaken by the exhausting rarefaction wave from behind, the shock will significantly decay in strength as it propagates towards the thrust wall. Hence, it will be assumed that cases of a shock reflection from the contact surface yields a shock of weak strength that can be neglected. Thus, in general, if the exhausting rarefaction is assumed to closely resemble that of a self-similar centered rarefaction wave, then the pressure, sound speed, and gas velocity variation through the exhausting rarefaction are given by

$$p(x,t) = p_3 \left(\frac{2}{\gamma_2 + 1} - \frac{\gamma_2 - 1}{\gamma_2 + 1} \frac{x - L}{a_3 (t - t_{CJ})} \right)^{2\gamma_2/(\gamma_2 - 1)} \tag{5.15}$$

$$a(x,t) = \frac{2}{\gamma_2 + 1} a_3 - \frac{\gamma_2 - 1}{\gamma_2 + 1} \frac{x - L}{t - t_{CJ}} \tag{5.16}$$

$$u(x,t) = \frac{2}{\gamma_2 + 1} a_3 + \frac{2}{\gamma_2 + 1} \frac{x - L}{t - t_{CJ}} \tag{5.17}$$

It is noted that these expressions where derived based on the results in [163] for a centered rarefaction wave. With this generalized flow field description, it is now possible to describe the flow properties on the exit plane for a single-cycle of operation of a fully-filled PDE.

5.2.1 Passage of Taylor Rarefaction Wave

The starting flow on the exit plane begins when the detonation wave arrives at the chamber exit. The peak pressure on the exit plane at $t = t_{CJ}$ is denoted by $p_4(t_{CJ})$, and governed by the pressure condition immediately after the detonation wave collision with the contact surface. Note, the reflected wave strength can be directly calculated using the detonation-contact surface interaction theory of Ch. 3 for the cases of reflected shock, Mach, or rarefaction wave depending on the acoustic impedance ratio across the contact surface. Recognizing that in the event of a reflected shock, the pressure behind the reflected shock would be larger than the post-detonation pressure, namely, $p_{2'} > p_2$. Similarly, in the event of a reflected Mach or rarefaction wave, the pressure behind the reflected waves would either be equal to, or less than, the post-detonation pressure, namely, $p_{2'} = p_2$ or $p_{2'} < p_2$, respectively. This aspect must be considered when selecting the starting peak pressure on the chamber exit plane. For instance, because the detonation wave collision with the contact surface is modeled as a collision of discontinuities, the moment immediately following the collision yields two distinct pressures on either side of the resulting wave type at the same location. As such, the larger of the two pressures must be selected when considering what pressure manifests as the physical peak if one were to measure the pressure immediately following the collision. Hence, in the event of a reflected shock from the contact surface, $p_4(t_{CJ}) = p_{2'}$ as predicted by the procedure detailed in Ch. 3. Similarly, in the event of a reflected Mach or rarefaction from the contact surface, $p_4(t_{CJ}) = p_2$.

With the selection of peak pressure defined, it is now desired to formulate an expression for the remainder of the pressure relaxation during the Taylor rarefaction wave passage. This relaxation in pressure occurs over the duration $t_{CJ} < t < t_T$, and is caused by both the Taylor wave passage and interaction with the exhausting rarefaction at the exit plane. This gasdynamic interaction is characterized by a non-simple region in x–t space, where the Taylor and exhausting rarefaction wave interact in a manner similar to that of a head on collision between two rarefaction waves. Consequently, providing a closed form

analytical expression for $p_4(t)$ during the Taylor wave passage based solely on the governing gasdynamics becomes a difficult task. In most gasdynamic problems where the solution of interest lies within, or on the boundary of a non-simple region, the solution is usually obtained numerically with a method such as the MOC. However, as the goal is to provide an analytical expression for $p_4(t)$ during a complete PDE cycle, an approximate expression based on a nondimensional pressure decay function will suffice. For this, the MOC model was used to compute the pressure history on the thrust chamber exit plane for a wide range of operating conditions. For the decay portion associated with the Taylor rarefaction wave passage, the decay shape can be normalized based on $[p_4(t) - p_{4,s}]/[p_4(t_{CJ}) - p_{4,s}]$, where $p_4(t_{CJ})$ represents the peak pressure and $p_{4,s}$ represents the steady choked pressure at $t = t_T$. Moreover, the time can be scaled by $\tau = t_T - t_{CJ}$, which represents the duration of Taylor wave passage on the exit. Figure 5.6 shows the results for a wide range of PDE operating condition with both H_2–O_2 and C_2H_4–O_2 propellants at various equivalence ratios, initial propellant temperatures, and blowdown pressure ratios.

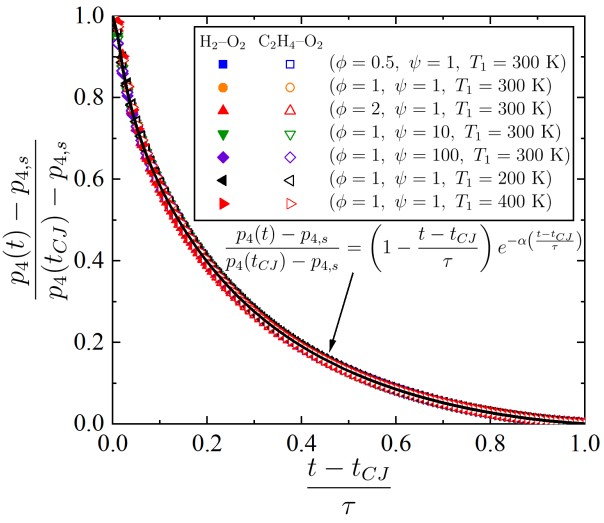

Figure 5.6. Normalized pressure decay at PDE exit for various operating conditions and comparison with Friedlander decay profile for α=3.

It is evident that all of the pressure decay profiles collapse when plotted as a normalized pressure decrement versus normalized overpressure duration, where the overpressure is referenced to the steady choked pressure during $t_T < t < t_R$. This is an indication that the trailing characteristic on the exit plane, which is on the far side of the non-simple region in the x–t diagram of Fig. 5.5, is characterized by a mostly similar flow that scales with L/τ. Additionally, it appears that the normalized decay shape is not sensitive to the propellant type or post-detonation properties. This permits for a model equation to represent the decay solely based on the decay shape, rather than a combination of the shape and gas properties. In this case, the modified Friedlander blast wave profile [164] can be used to model the normalized overpressure decay for the duration defined by τ. This modified decay profile is given by,

$$\frac{p_4(t) - p_{4,s}}{p_4(t_{CJ}) - p_{4,s}} = \left(1 - \frac{t - t_{CJ}}{\tau}\right) \mathrm{e}^{-\alpha\left(\frac{t-t_{CJ}}{\tau}\right)} \tag{5.18}$$

where α represents the shape factor. Based on a least-squares fit of the model equation to the aggregate MOC data in Fig. 5.6 yields an $\alpha = 3$. Note that application of Eq. (5.18) requires knowledge of $p_4(t_T) = p_{4,s}$ and $\tau = t_T - t_{CJ}$. The determination of $p_{4,s}$ will be carried out in the following subsection; however, t_T will be addressed in the following paragraphs.

A very good estimate for t_T can be made by assuming that the trailing characteristic of the Taylor rarefaction keeps a fairly constant slope as it traverses the full thrust chamber. In fact, as seen in Fig. 5.5, the slope of the trailing characteristic of the Taylor wave remains constant over the chamber length range $0 < x/L \lesssim 0.8$. However, as the characteristic encounters the exhausting rarefaction, the slope continues to decrease until finally reaching the chamber exit. If this slight decrease in the characteristics slope is neglected for $0.8 \lesssim x/L \leq 1$, then t_T can be approximated as,

$$t_T = \frac{L}{a_3} \tag{5.19}$$

where it is reminded that a_3 is the sound speed in the stagnation region of state 3 behind the Taylor rarefaction wave and given in Eq. (5.13). Substituting this expression into Eq. (5.19) yields an approximate general expression for t_T as

$$\frac{t_T}{t_{CJ}} = \frac{2\gamma_1 M_{CJ}^2}{\gamma_1 M_{CJ}^2 + \gamma_2} \tag{5.20}$$

Therefore, the expression for $\tau = t_T - t_{CJ}$ simply becomes

$$\tau = \left(\frac{2\gamma_1 M_{CJ}^2}{\gamma_1 M_{CJ}^2 + \gamma_2} - 1 \right) t_{CJ} \tag{5.21}$$

In summary, application of Eq. (5.18) with Eq. (5.21) yields an appropriate pressure decay profile for modeling the passage of the Taylor wave on the exit plane from $t_{CJ} < t < t_T$. The next subsection addresses the steady choked state on the chamber exit plane that follows the Taylor wave passage.

5.2.2 Steady Choked Flow

After the passage of the Taylor rarefaction wave, a steady choked flow condition develops on the exit plane for $t_T < t < t_R$. During this time interval, the exhausting rarefaction wave accelerates the burned products in the stagnation region of state 3 behind the Taylor rarefaction to a sonic velocity on the exit plane. As such, the steady choked state on the exit plane can be determined by evaluating Eqs. (5.15)-(5.17) at $x = L$. Hence, the steady choked flow condition on the exit plane is given by

$$p_{4,s} = p_3 \left(\frac{2}{\gamma_2 + 1} \right)^{2\gamma_2/(\gamma_2 - 1)} \tag{5.22}$$

$$a_{4,s} = \frac{2}{\gamma_2 + 1} a_3 \tag{5.23}$$

$$u_{4,s} = \frac{2}{\gamma_2 + 1} a_3 = a_{4,s} \tag{5.24}$$

It is now desired to evaluate the duration for which this steady choked condition persists on the exit plane. It is evident from Fig. 5.5 that t_R marks the end of the steady flow phase of the gasdynamic blowdown. This is caused by the arrival of the leading characteristic

of the exhausting rarefaction wave that reflects from the thrust wall and propagates back to the chamber exit. Consequently, it is required to derive an expression for t_R based on the dynamics of the leading characteristic of the exhausting rarefaction wave. Note that when the exhausting wave first enters the chamber, the leading characteristic is initially propagating through the Taylor rarefaction wave up until t_i at x_i. This causes a variable slope for the leading characteristic, which depends on the flow property variation across the Taylor rarefaction wave. Therefore, it becomes important to evaluate the time t_i and location x_i for which the leading characteristic of the exhausting rarefaction wave reaches the trailing characteristic of the Taylor rarefaction wave. This can readily be determined by applying the characteristic equation for a C_- characteristic that is propagating through the Taylor rarefaction wave. In this case, the governing ordinary differential equation becomes

$$\frac{dx}{dt} = u(x,t) - a(x,t) = -\frac{\gamma_1 M_{CJ}^2 + \gamma_2}{\gamma_2 M_{CJ}^2}\frac{2}{\gamma_2+1}W_{CJ} + \frac{3-\gamma_2}{\gamma_2+1}\frac{x}{t} \tag{5.25}$$

Solving this equation with the initial condition that $x = L$ when $t = t_{CJ}$ yields the path of the leading characteristic through the Taylor rarefaction wave as [65]

$$x(t) = \frac{W_{CJ}t}{\gamma_2 - 1}\left[\frac{\gamma_2\gamma_1 M_{CJ}^2 + \gamma_2}{\gamma_1 M_{CJ}^2}\left(\frac{t_{CJ}}{t}\right)^{2(\gamma_2-1)/(\gamma_2+1)} - \frac{\gamma_1 M_{CJ}^2 + \gamma_2}{\gamma_1 M_{CJ}^2}\right] \tag{5.26}$$

Similarly, solving (5.26) for the condition when $x(t_i) = a_3 t_i = x_i$ yields

$$\frac{t_i}{t_{CJ}} = \left(\frac{\gamma_1 M_{CJ}^2 + \gamma_2}{\gamma_1 M_{CJ}^2}\frac{\gamma_2+1}{2\gamma_2}\right)^{-(\gamma_2+1)/2(\gamma_2-1)} \tag{5.27}$$

$$\frac{x_i}{L} = \frac{\gamma_1 M_{CJ}^2 + \gamma_2}{2\gamma_1 M_{CJ}^2}\left(\frac{\gamma_1 M_{CJ}^2 + \gamma_2}{\gamma_1 M_{CJ}^2}\frac{\gamma_2+1}{2\gamma_2}\right)^{-(\gamma_2+1)/2(\gamma_2-1)} \tag{5.28}$$

After the leading characteristic of the exhausting rarefaction reaches the trailing characteristic in the Taylor rarefaction, the slope of the characteristic becomes constant and the characteristic continues propagating towards the thrust wall through the stagnation region of state 3. Consequently, the time at which the characteristic reaches the thrust wall, defined by t_r in Fig. 5.5, is simply

$$t_r = t_i + \frac{x_i}{a_3} \tag{5.29}$$

Substituting Eqs. (5.13), (5.27), and (5.28) into Eq. (5.29), after algebraic manipulation yields,

$$\frac{t_r}{t_{CJ}} = 2\left(\frac{\gamma_1 M_{CJ}^2 + \gamma_2}{\gamma_1 M_{CJ}^2}\frac{\gamma_2+1}{2\gamma_2}\right)^{-(\gamma_2+1)/2(\gamma_2-1)} \tag{5.30}$$

After the leading characteristic reaches the thrust wall at the head end of the chamber, the characteristic reflects and begins propagating back towards the chamber exit. In this case, the slope is variable and dependent on the flow property variation across the exhausting rarefaction. As such, the path of the characteristic can readily be determined by applying the characteristic equation for a C_+ characteristic that is propagating through the exhausting rarefaction wave. In this case, the governing differential equation becomes

$$\frac{dx}{dt} = u(x,t) + a(x,t) = \frac{4}{\gamma_2+1}a_3 + \frac{3-\gamma_2}{\gamma_2+1}\frac{x-L}{t-t_{CJ}} \tag{5.31}$$

Solving this equation with the initial condition that $x = 0$ when $t = t_r$ yields the path of the reflected leading characteristic through the exhausting rarefaction wave as

$$x(t) = L - a_3\left(t - t_{CJ}\right)\frac{\gamma_2+1}{\gamma_2-1}\left\{\left[\left(t-t_{CJ}\right)\frac{a_3}{L}\right]^{-2(\gamma_2-1)/(\gamma_2+1)} - \frac{2}{\gamma_2+1}\right\} \tag{5.32}$$

Similarly, solving (5.32) for the condition when $x(t_R) = L$ yields

$$\frac{t_R}{t_{CJ}} = \frac{t_r}{t_{CJ}} + \frac{\gamma_1 M_{CJ}^2}{\gamma_1 M_{CJ}^2 + \gamma_2}\left[\left(\frac{2}{\gamma_2+1}\right)^{-(\gamma_2+1)/2(\gamma_2-1)} - 1\right] \tag{5.33}$$

In summary, application of Eq. (5.22) over the duration $t_T < t < t_R$, where t_T and t_R are given in Eqs. (5.19) and (5.33) yields the appropriate pressure profile for steady choked flow phase of the blowdown. The following subsection addresses the final phase of the blowdown, namely, the constant-volume blowdown for $t > t_R$.

5.2.3 Constant Volume Blowdown

It was previously mentioned that the final portion of the gasdynamic blowdown closely resembles that of a constant-volume blowdown [121]. This is a consequence of the flow properties being nearly uniformly distributed across the thrust chamber for $t > t_R$. As a result, it may be assumed that the remainder of pressure relaxation on the exit plane

to the ambient closely follows that of a constant-volume blowdown. In such a case, the conservation of mass for the control volume in Fig. 5.1 becomes

$$\frac{\partial}{\partial t}\left[\int_{cv} \rho_e(t)\ d\mathcal{V}\right] + \dot{m}_e(t) = 0 \tag{5.34}$$

where $\rho(x,t)$ has been replaced with $\rho_e(t)$ due to the spatially uniform flow assumption. Performing the integration over the thrust chamber volume and noting that $\dot{m}_e(t) = \rho_4(t)A_e u_e(t)$ yields

$$\mathcal{V}\frac{d\rho_4(t)}{dt} = -\rho_4(t)A_e u_4(t) \tag{5.35}$$

If it is further assumed that the sonic flow exist on the chamber exit plane for the majority of the constant-volume blowdown, then $u_4(t) = a_4(t)$. Similarly, recognizing that the ratio of $\mathcal{V}/A_e = L$ for a constant area thrust chamber, then Eq. (5.35) can be further simplified to

$$L\frac{d\rho_4(t)}{dt} = -\rho_4(t)a_4(t) \tag{5.36}$$

It is convenient at this point to introduce the ratio $\rho_4(t)/\rho_{4,s}$ and $a_4(t)/a_{4,s}$ in order to relate the density and sound speed ratios on the exit plane through an isentropic expansion process with the initial condition at $t = t_R$. Hence, manipulating Eq. (5.36) to the form

$$L\frac{d}{dt}\left(\frac{\rho_4(t)}{\rho_{4,s}}\right) = -\left(\frac{\rho_4(t)}{\rho_{4,s}}\right)\left(\frac{a_4(t)}{a_{4,s}}\right)a_{4,s} \tag{5.37}$$

Further, substituting the isentropic relation $a_4(t)/a_{4,s} = [\rho_4(t)/\rho_{4,s}]^{(\gamma_2-1)/2}$, after algebraic manipulation yields

$$\left(\frac{\rho_4(t)}{\rho_{4,s}}\right)^{-(\gamma_2+1)/2} d\left(\frac{\rho_4(t)}{\rho_{4,s}}\right) = -\frac{a_{4,s}}{L}\ dt \tag{5.38}$$

Integrating this expression from $1 \leq \rho_4(t)/\rho_{4,s} < \rho_4(t)/\rho_{4,s}$ on the time interval $t_R < t < t$ yields the isentropic constant-volume decay in density on the chamber exit plane.

$$\rho_4(t) = \left[1 + \frac{\gamma_2 - 1}{2}\frac{a_{4,s}\,(t - t_R)}{L}\right]^{-2/(\gamma_2-1)} \rho_{4,s} \tag{5.39}$$

Subsequently, application of the isentropic relation for density and pressure yields the desired constant-volume decay in pressure on the chamber exit plane.

$$p_4(t) = \left[1 + \frac{\gamma_2 - 1}{2}\frac{a_{4,s}\,(t - t_R)}{L}\right]^{-2\gamma_2/(\gamma_2-1)} p_{4,s} \tag{5.40}$$

Note, an equivalent expression was derived following a similar procedure in the study of [121], which was used to evaluate the performance of detonation tubes coupled to diverging nozzles. In summary, application of Eq. (5.40) over the duration $t > t_R$, where t_R is given by (5.33) yields the appropriate pressure profile for constant-volume blowdown on the chamber exit.

5.2.4 Model Summary

Application of the model requires selecting a detonable propellant and setting the initial conditions of the thrust chamber, i.e. p_1, T_1, γ_1, and p_0. Similarly, the model requires computing the equilibrium CJ detonation wave properties, i.e. M_{CJ} and γ_2, using a chemical equilibrium solver such as the Cantera detonation toolbox [29, 30], or the NASA CEA code [28]. Additionally, application of the detonation-contact surface interaction theory of Ch. 3 is required to determine $p_4(t_{CJ})$, namely, the peak pressure on the exit plane following the collision of the detonation wave with the contact surface at the chamber exit. Finally, application of Eq. (5.8) below with Eqs. (5.41) and (5.42)–(5.45) permits evaluation of $F_x(t)$ over the cycle interval $0 \leq t \leq t_f$, where t_f represents the time at which $p_4(t) = p_0$ during the constant-volume blowdown. Lastly, application of Eqs. (4.13)–(4.15) permits determination of the primary single-cycle performance parameters for a fully-filled PDE.

$$F_x(t) = p_4(t) A_e \left[\gamma_2 + 1 - \frac{p_0}{p_4(t)} \right] \tag{5.8}$$

$$p_4(t) = \begin{cases} p_1 & t < t_{CJ} \\ \left[p_4(t_{CJ}) - p_{4,s} \right] \left(1 - \frac{t - t_{CJ}}{\tau} \right) \mathrm{e}^{-\alpha \left(\frac{t - t_{CJ}}{\tau} \right)} + p_{4,s} & t_{CJ} \leq t < t_T \\ p_1 \left(\frac{2}{\gamma_2 + 1} \right)^{2\gamma_2/(\gamma_2 - 1)} \left(\frac{\gamma_1 M_{CJ}^2 + \gamma_2}{2\gamma_2} \right) \left(\frac{\gamma_1 M_{CJ}^2 + \gamma_2}{\gamma_1 M_{CJ}^2 + 1} \frac{\gamma_2 + 1}{2\gamma_2} \right)^{(\gamma_2+1)/(\gamma_2-1)} & t_T \leq t < t_R \\ p_4(t) = p_{4,s} \left[1 + \frac{\gamma_2 - 1}{2} \frac{a_{4,s}(t - t_R)}{L} \right]^{-2\gamma_2/(\gamma_2 - 1)} & t_R \leq t \leq t_f \end{cases} \tag{5.41}$$

$$t_{CJ} = \frac{L}{W_{CJ}} \tag{5.42}$$

$$t_T = \frac{2\gamma_1 M_{CJ}^2}{\gamma_1 M_{CJ}^2 + \gamma_2} t_{CJ} \tag{5.43}$$

$$t_r = 2\left(\frac{\gamma_1 M_{CJ}^2 + \gamma_2}{\gamma_1 M_{CJ}^2}\frac{\gamma_2 + 1}{2\gamma_2}\right)^{-(\gamma_2+1)/2(\gamma_2-1)} t_{CJ} \tag{5.44}$$

$$t_R = t_r + \frac{\gamma_1 M_{CJ}^2}{\gamma_1 M_{CJ}^2 + \gamma_2}\left[\left(\frac{2}{\gamma_2 + 1}\right)^{-(\gamma_2+1)/2(\gamma_2-1)} - 1\right] t_{CJ} \tag{5.45}$$

5.3 Model Validation

In order to validate the current analytical performance model for a fully-filled PDE, a comparison is first made with the current MOC model to verify that the model accurately represents the pressure profile on the chamber exit plane. Additionally, a comparison is made with previously published numerical and experimental results for PDEs operating with different equivalence ratios and blowdown pressure ratios. Figure 5.7 shows a comparison of the current analytical model and MOC model regarding the pressure history on the exit plane. In these cases, excellent agreement is obtained for the Taylor rarefaction wave passage phase from $1 < t/t_{CJ} \lesssim 2$, and the steady choked flow phase from $2 \lesssim t/tCJ \lesssim 4.5$. Additionally, very good agreement is obtained during the approximated constant-volume blowdown phase for $t/tCJ \gtrsim 4.5$; however, the constant-volume blowdown phase terminates slightly prematurely compared to the full gasdynamic blowdown computed with the MOC model. This should not influence the integrated total impulse or specific impulse; however, this could cause an over-estimation for the time-averaged thrust. This will be shown in the following discussion when comparing against previous numerical and experimental data.

It is also desired to ensure that the current analytical model properly captures the effects of varying the propellant equivalence and blowdown pressure ratios on specific impulse for a fully-filled PDE. Figures 5.8(a) and 5.8(b) show a comparison of the analytical model with the current MOC model and the previously discussed MOC model of [70], higher-fidelity numerical models of [76, 83, 98], and experimental results of [92, 95] for hydrogen and hydrocarbon propellants at various equivalence ratios and blowdown pressure ratios. In Fig. 5.8(a), very good agreement is obtained with the current MOC model, such that an

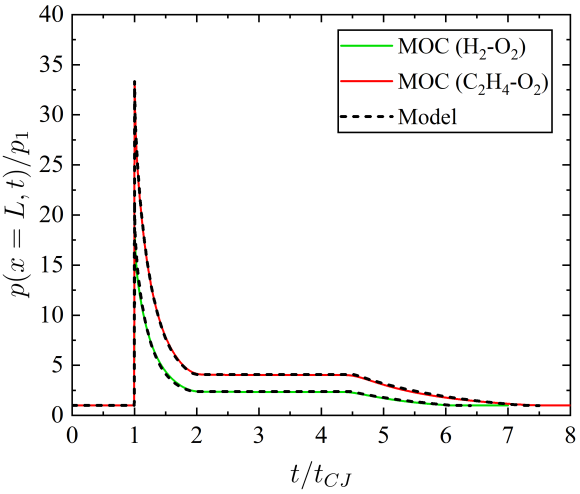

Figure 5.7. Comparison of pressure profile at PDE exit predicted by the analytical model and the MOC model for $2H_2$–O_2 and C_2H_4–$3O_2$ propellants at 1 atm and 300 K and $\psi = 1$.

average difference of 0.4 percent is obtained over the range of equivalence ratios shown for H_2–air and H_2–O_2 propellants. This suggests that the model properly captures the manner in which the equivalence ratio influences the pressure history on the chamber exit plane. Similarly, an average difference of 0.8 percent is obtained with the MOC results of [70], and 7.4 percent for the numerical results of [98]. Additionally, in the case of H_2–air propellant, an average error of 6.6 percent is obtained with the measurements of [95] for the equivalence ratio range shown. Moreover, in Fig. 5.8(b), very good agreement is also obtained with the current MOC model, such that an average difference of 0.6 and 1.1 percent is obtained over the range of blowdown pressure ratios shown for H_2–air and C_2H_4–O_2 propellants, respectively. This suggests that the model properly captures the manner in which the blowdown pressure ratio influences the pressure history on the chamber exit plane. Similarly, an average difference of 5.9 percent is obtained with the MOC results of [70], and 2.1 percent for the numerical results of [76, 83]. Lastly, in the case of stoichiometric C_2H_4–O_2 propellant, an average error of 12 percent is obtained with the measurements of [92] for the equivalence ratio range shown.

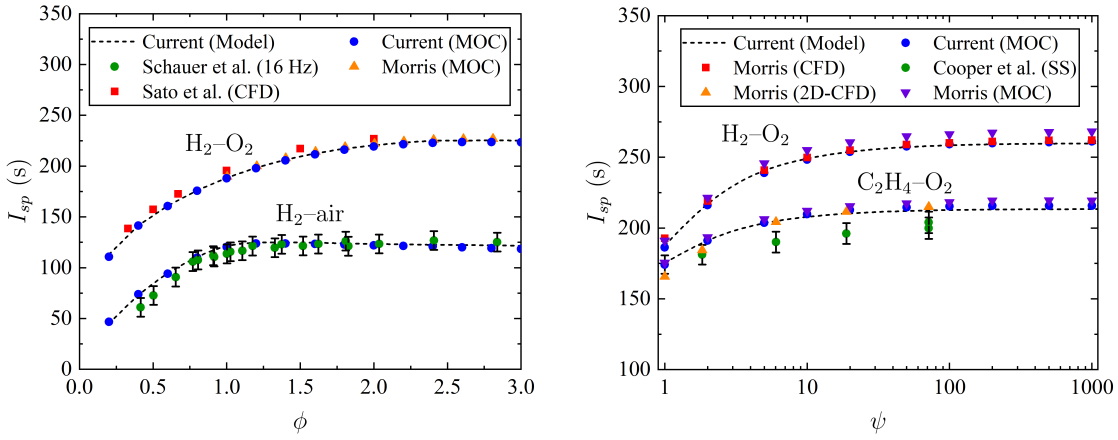

Figure 5.8. Comparison of current analytical model with current MOC and existing numerical and experimental data of [70, 76, 83, 92, 95, 98] for H_2–(O_2+3.76N_2), H_2–O_2, and C_2H_4–O_2 propellants at various (a) equivalence ratios and (b) blowdown pressure ratios.

Lastly, it is desired to ensure that the current analytical model provides an accurate prediction for time-averaged thrust given the premature termination of the constant-volume blowdown assumption. In this case, a comparison is made with the current MOC model where the fully blowdown is directly calculated, and with the experimental results of [95] for a fully-filled PDE operating at 16 Hz and at different equivalence ratios. Figure 5.9 shows that the current analytical and MOC models share very good agreement, where an average difference of 3.1 percent is obtained over the equivalence ratio range shown. Similarly, fairly good agreement is obtained with the experimental results of [95], in that an average error of 11.7 percent is obtained over the equivalence ratio range shown. In general, the analytical model slightly over-predicts the time-averaged thrust for a single-cycle as the constant-volume blowdown approaches the ambient condition faster than that of the full gasdynamic blowdown. However, despite this over-prediction for $\bar{F}$, the model still yields sufficiently accurate results for a reduced-order model. Lastly, it should be noted that the faster relaxation of the constant-volume blowdown assumption does not significantly affect the models ability to predict reliable total and specific impulse results, as the thrust level towards the end of the cycle is gradually approaches zero. Hence, the

accrued error becomes less significant for performance metrics that are not directly or inversely proportional to t_f. This is the reason for the excellent agreement shown in Fig. 5.8(a) between the analytical model and the specific impulse results of [95], namely, the constant-volume blowdown assumption does not significantly influence the integrated total impulse and subsequent specific impulse.

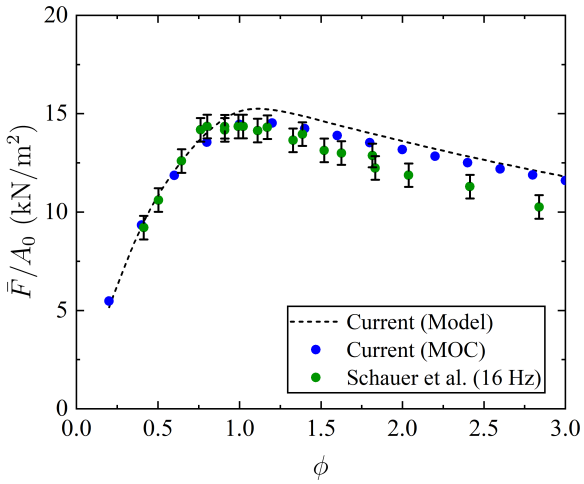

Figure 5.9. Comparison of time-averaged thrust predicted by the current analytical model and the MOC model with the experiments of [95] for H_2–air propellant at different equivalence ratios ($\psi = 1$).

CHAPTER 6

PERFORMANCE CHARACTERISTICS OF PULSE DETONATION ENGINES

6.1 Partially-Filled Pulse Detonation Engines

In this section, the single-cycle performance characteristics of partially-filled PDEs are discussed, including the effects of detonable and inert acoustic impedance, inert mixture temperature, and engine blowdown pressure ratio. Subsequently, partially-filled PDE performance scaling laws in the form of nondimensional specific impulse, total impulse, and time-averaged thrust ratios are discussed.

6.1.1 Effects of Detonable and Inert Acoustic Impedance

The reflection type that results from the collision of the detonation wave with the contact surface separating the detonable and non-combustible mixture can largely influence the pressure history on the thrust wall and corresponding PDE impulse. This was shown in the numerical study of Sato et al. [98] for various propellant mixtures, and helium, air, and argon as the inert gas. They showed that the ratio of acoustic impedance of the detonable and inert mixtures can be used to determine whether a compression or rarefaction wave reflects from the contact surface. Moreover, in Ch. 3, the acoustic impedance ratio across the contact surface, z_0/z_1, was determined to be the primary parameter governing the reflection type at the contact surface, which can take the form of a reflected rarefaction, a Mach wave, or a shock wave. Using the approach of Ch. 3, the strength of the reflected wave can be determined for a given acoustic impedance ratio across the contact surface. Figure 6.1 shows how the strength of the reflected wave varies with the ratio of acoustic impedance for stoichiometric H_2–O_2 and C_2H_4–O_2 propellant mixtures. It is noted that the solutions shown in Fig. 6.1 are obtained by sweeping the acoustic impedance z_0 of the inert mixture. Further, in Fig. 6.1, $p_{2'}$ and p_2 represent the post-reflected wave pressure and

post-detonation pressure, respectively. Hence, when the acoustic impedance ratio is less than unity, the reflected wave is a rarefaction wave with a strength $p_{2'}/p_2 < 1$. Similarly, when the acoustic impedance ratio is greater than unity, the reflected wave is a shock wave with a strength $p_{2'}/p_2 > 1$. Lastly, the unique case of a reflected Mach wave with a strength $p_{2'}/p_2 = 1$ results when the acoustic impedance ratio is exactly equal to unity. With a fixed propellant mixture, varying the gas properties of the inert mixture can influence the nature of the reflection type at the contact surface. Additionally, proper understanding of this interface interaction permits tailoring of the gasdynamic collision which can be used for PDE performance enhancement.

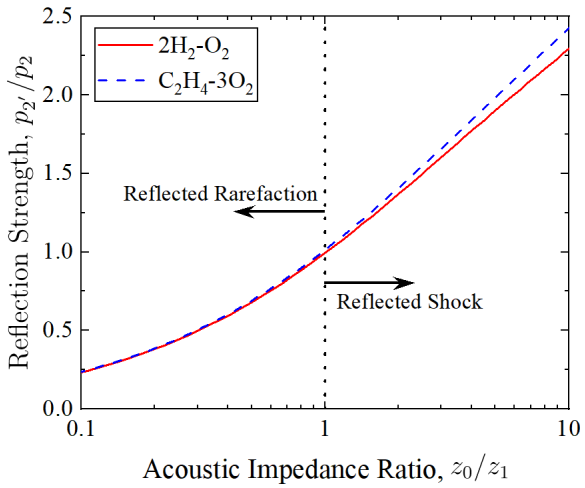

Figure 6.1. Strength of reflection type at contact surface as a function of acoustic impedance ratio across the contact surface for $2H_2$–O_2 and C_2H_4–$3O_2$ propellants.

In order to investigate the role of the interface interaction on the performance of a partially-filled PDE, the three types of reflections, namely, rarefaction, Mach and shock wave are considered. The method of Ch. 3 is used to tailor the interface collision of a stoichiometric H_2–O_2 detonable propellant with a helium–air inert mixture. For each case, the PDE is partially filled with a stoichiometric H_2–O_2 propellant mixture to a fill fraction of $\alpha = 0.5$, and the remaining portion of the chamber is filled with a helium–air inert

mixture, each at 1 atm and 300 K. In the case of helium as the inert mixture ($X_{He} = 1.0$), the acoustic impedance ratio across the contact surface is $z_0/z_1 = 0.36$, which results in a reflected rarefaction from the contact surface with a strength of $p_{2'}/p_2 = 0.58$. The starting flow field for this case is shown in the form of a non-dimensional x–t diagram pressure contour in Fig. 6.2. In this figure, t_{CJ} is defined by the time required for the detonation wave to propagate from the thrust wall to the contact surface location, $t_{CJ} = \alpha L/W_{CJ}$. The thrust chamber pressure distribution shown throughout the PDE corresponds to the constant dashed t–line in the x–t diagram pressure contour. Because the ratio of acoustic impedance is less than unity, a reflected rarefaction results from the interface collision and propagates upstream towards the thrust wall. Additionally, it is noted that the incident transmitted shock wave into the non-combustible mixture has a larger velocity than the detonation wave velocity. As will be shown later in this section, these two flow characteristics will yield a more rapid decay of the pressure history on the thrust wall and a lower overall impulse.

In the case of a helium–air inert mixture with a helium mole fraction of $X_{He} = 0.36$, the acoustic impedance ratio is $z_0/z_1 = 1.0$ and a reflected Mach wave with a strength of $p_{2'}/p_2 = 1.0$ results from the collision of the detonation wave with the contact surface. Figure 6.3 shows the corresponding non-dimensional x–t diagram pressure contour and thrust chamber pressure distribution on the constant dashed t–line. Note that the reflected Mach wave does not cause an increase or decrease in the pressure immediately behind the reflected interface wave. However, because the Mach wave is immediately followed by the secondary rarefaction wave, as described in Ch. 2, there is a slight decrease in pressure in order to match the decaying pressure at the contact surface behind the transmitted shock. In this case, the incident transmitted shock wave has a slower velocity than the detonation wave velocity, which will delay the time for which the exhausting rarefaction enters the thrust chamber.

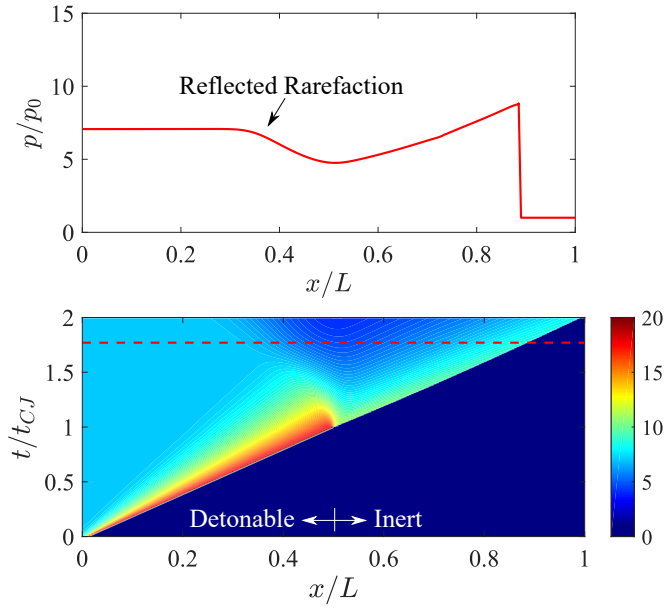

Figure 6.2. Non-dimensional x–t diagram of p/p_0 pressure contour (bottom) and pressure distribution on constant dashed t–line (top) for $2H_2$–O_2 propellant and helium as the inert gas yielding a reflected rarefaction wave at the contact surface ($\psi = 1$).

In the case of air as the inert mixture ($X_{He} = 0.0$), the acoustic impedance ratio is $z_0/z_1 = 1.24$ and a reflected shock wave with a strength of $p_{2'}/p_2 = 1.11$ results from the collision of the detonation wave with the contact surface. Figure 6.4 shows the corresponding x–t diagram pressure contour and thrust chamber pressure distribution on the constant dashed t–line. Notice that the reflected shock wave is accompanied by an increase in the pressure immediately behind the shock. Moreover, as previously mentioned, because the shock wave is immediately followed by the secondary rarefaction, there is a decrease in pressure in the flow field behind the shock in order to match the decaying pressure at the contact surface behind the transmitted shock. Once, the reflected shock wave reaches the thrust wall, the wave will reflect and cause a momentary rise in pressure on the thrust wall. Similar to the previous reflected Mach wave example, the incident transmitted shock wave has a slower velocity than the detonation wave velocity, which will delay the time for which the exhausting rarefaction enters the tube. Subsequently, these two gasdynamic processes

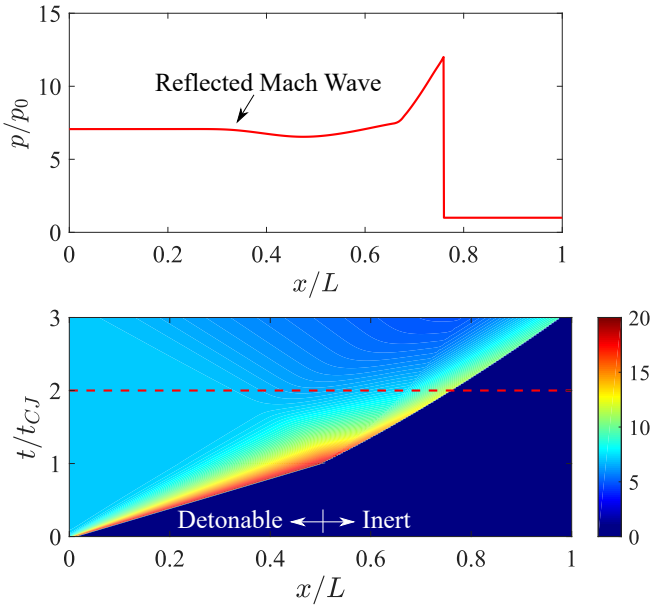

Figure 6.3. Non-dimensional x–t diagram of p/p_0 pressure contour (bottom) and pressure distribution on constant dashed t–line (top) for $2H_2$–O_2 propellant and helium–air mixture as the inert gas with $X_{He} = 0.36$ yielding a reflected Mach wave at the contact surface ($\psi = 1$).

will result in a longer positive pressure duration on the thrust wall and a higher impulse.

The corresponding pressure history, $p_w = p(0, t)$, on the thrust wall for the previously discussed cases of a reflected shock, Mach, and rarefaction wave from the contact surface for stoichiometric H_2–O_2 detonable mixture, and fill fraction of $\alpha = 0.5$, are shown in Fig. 6.5. Because t_{CJ} is defined as the time required for the detonation wave to travel the fill length of the thrust chamber, $t/t_{CJ} = 1$ represents the time at which the detonation wave collides with the contact surface. As shown in Fig. 6.5, the pressure history on the thrust wall for all cases starts as a steady plateau pressure. The magnitude of this pressure is equal to the pressure at the tail-end of the Taylor rarefaction wave, which is propellant dependent and provided in Eq. (5.12) based on the analytical work of [65]. Following the detonation wave collision with the contact surface, the reflected interface wave travels towards the thrust wall and reaches

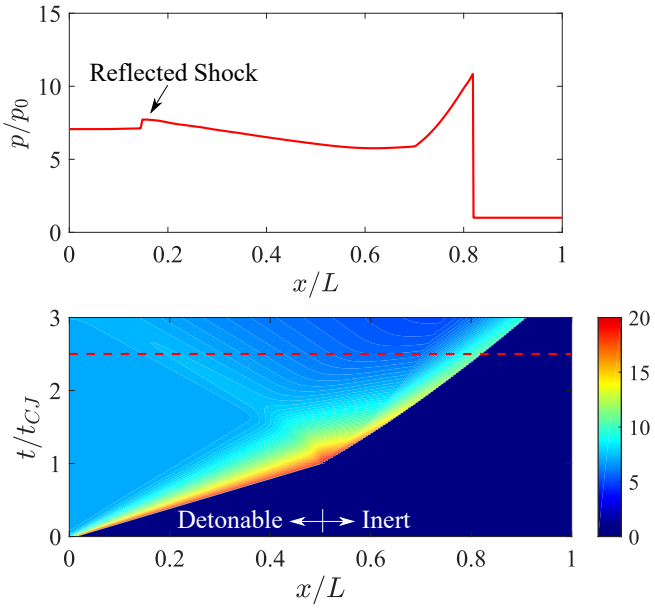

Figure 6.4. Non-dimensional x–t diagram of p/p_0 pressure contour (bottom) and pressure distribution on constant dashed t–line (top) for $2H_2$–O_2 propellant and air as the inert gas yielding a reflected shock at the contact surface ($\psi = 1$).

the head-end of the chamber at roughly $t/t_{CJ} \approx 3.5$, which initiates the pressure decay at the thrust wall. It is noted that this non-dimensional time is dependent on the fill fraction and strength of the reflection type at the interface, and the $t/t_{CJ} \approx 3.5$ condition shown in Fig. 6.5 is specific to the stoichiometric H_2–O_2 propellant, helium–air inert mixture, and $\alpha = 0.5$ case previously discussed. For the case of a reflected shock ($X_{He} = 0.0$), a spike in pressure is observed at the end of the plateau pressure history from the reflected shock on the thrust wall, which is then immediately followed by a subsequent pressure decay from the following secondary rarefaction wave. In the cases of reflected Mach ($X_{He} = 0.36$) and rarefaction wave ($X_{He} = 1.0$), the pressure history simply decays from the steady plateau pressure without any additional pressure rise. The behavior of the decay is very different given the strength of the reflection from the contact surface. For instance, the case of a Mach wave is the limiting lower bound for the strength of a rarefaction wave, as the reflected Mach wave leads the secondary rarefaction from the contact surface. Hence, the incident

decay on the thrust wall is solely dependent on the reflected secondary rarefaction wave. Alternatively, in the event of a reflected rarefaction from the contact surface, the reflected rarefaction and secondary rarefaction waves are coincident and identical. As shown in Fig. 6.5, the case of a reflected rarefaction from the contact surface yields a more rapid decay in pressure at the thrust wall. This remains true for any reflected rarefaction from the interface collision, such that stronger reflected rarefaction waves result in more rapid decay in pressure at the the thrust wall.

In any of the respective gasdynamic cases, once the reflected interface wave and secondary rarefaction reflect from the thrust wall, the pressure begins to relax towards an intermediate plateau value between the starting plateau pressure behind the Taylor rarefaction wave and the ambient condition. The magnitude of this secondary plateau is directly governed by the nature of the interface collision and strength of the secondary rarefaction wave. In general, a reflected shock from the contact surface yields a stronger transmitted shock wave into the non-combustible inert mixture than the case of a reflected Mach or rarefaction wave. This directly causes higher pressures at the now traveling contact surface, which separates the post-transmitted shock gas, and the gas being relieved through the secondary rarefaction wave. Hence, the case of a reflected shock from the contact surface yields the highest pressure conditions at the tail of the secondary rarefaction wave compared to the cases of a reflected Mach or rarefaction wave. It can then be expected that the pressure magnitude of the intermediate plateau is largest in the cases of a reflected shock, followed by a reflected Mach and rarefaction wave from the contact surface, respectively. This is demonstrated in Fig. 6.5; however, only the case of a reflected shock actually completely reaches the intermediate plateau pressure before the exhausting rarefaction wave reaches the thrust wall. Depending on how long it takes for the transmitted shock to reach the exit of the thrust chamber, namely, the time at which the exhausting rarefaction is able to begin propagating into the chamber, the pressure at the thrust wall may actually never completely reach the intermediate plateau value. This pressure decay behavior is shown for

the cases of a reflected rarefaction ($X_{He} = 1.0$) and Mach wave ($X_{He} = 0.36$) in Fig. 6.5. In these cases, the transmitted shock is moving with a faster velocity than the case of reflected shock, and a shorter time is required for the transmitted shock to exit the tube. This allows the exhausting rarefaction to reach the head-end of the chamber and begin relieving the gas at the thrust wall in a shorter amount of time, as indicated by the second decay in pressure at $t/t_{CJ} \approx 8$ and 9.5, respectively, whereas the exhausting rarefaction reaches the thrust wall at roughly $t/t_{CJ} \approx 10.5$ for a reflected shock. Consequently, these gasdynamic processes yield a more rapid decay in pressure at the thrust wall and shorter time for which the pressure history on the thrust wall returns to the ambient condition, yielding a lower overall impulse for the PDE cycle.

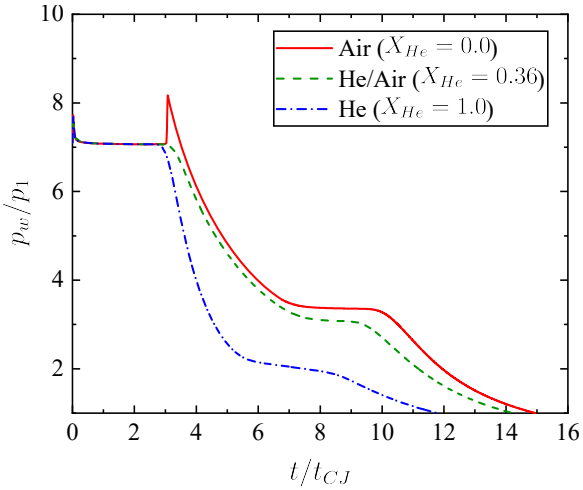

Figure 6.5. Pressure history at the thrust wall for $2H_2$–O_2 propellant and inert helium mole fractions of 0, 0.36, and 1, corresponding to reflected shock, Mach, and rarefaction waves at the contact surface, respectively ($\psi = 1$).

This transient variation in impulse for the complete cycle is shown in Fig. 6.6 As expected, the largest impulse obtained is for the case of a reflected shock at the contact surface. This is attributed to the reflected shock raising the pressure on the thrust wall after the steady plateau pressure, and the delayed entrance of the exhausting rarefaction wave into the PDE from the slower transmitted shock velocity. Similarly, the case of a reflected

Mach wave yields an integrated impulse that is less than that obtained for a reflected shock, but higher than that obtained for a reflected rarefaction. The total cycle impulse for the case of a reflected shock ($X_{He} = 0.0$) is approximately 24% and 57% higher than the cases of a reflected Mach ($X_{He} = 0.36$) and rarefaction wave ($X_{He} = 1.0$), respectively. Although the slower transmitted shock wave has the tendency to prolong the over-pressure duration on the thrust wall and increase the total impulse, the maximum operating frequency of the partially-filled PDE becomes reduced. In the cases of reflected shock, Mach, and rarefaction wave, the non-dimensional gasdynamic blowdown times of $t/t_{CJ} \approx 12$, 14, and 16, correspond to limit operating frequencies for a 1 m long thrust chamber of 363, 411, and 493 Hz, respectively. Namely, a 30 percent reduction in maximum operating frequency is obtained for the case of a reflected shock compared to a reflected rarefaction. This is an adverse performance characteristic that cannot be avoided in single-tube PDE systems; however, multi-tube systems could potentially manage the desired propulsive performance characteristics with reduced operating frequency in individual tubes [165–167].

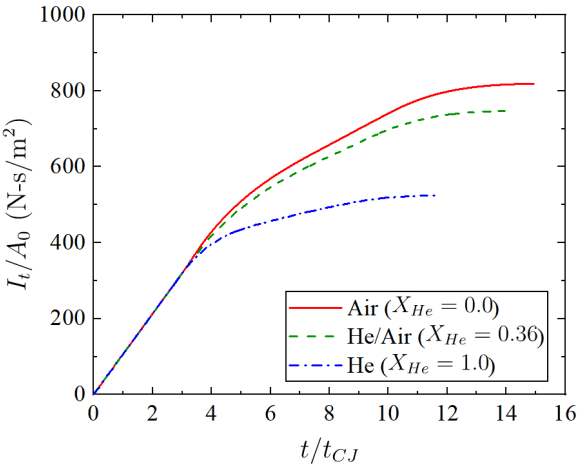

Figure 6.6. Integrated impulse history per unit area for $2H_2$–O_2 propellant and inert helium mole fractions of 0, 0.36, and 1, corresponding to reflected shock, Mach, and rarefaction waves at the contact surface, respectively ($\psi = 1$).

All of the above discussion is focused on the case of $\alpha = 0.5$ in order to highlight the primary gasdynamic phenomena that govern the pressure history on the thrust wall and resulting gasdynamic blowdown time. It is of interest to investigate how the combination of fill fraction and helium–air mixture influence the performance characteristics. For this purpose, the MOC model is used to perform a parametric sweep of helium mole fraction on the range $0 \leq X_{He} \leq 1$ for the non-combustible helium–air mixture, and the fill fraction on the range $0.2 \leq \alpha \leq 1$. The propellant-based specific impulse is calculated and plotted in Fig. 6.7(a) for the parametric ranges considered above. Similar to results from previous investigations, as the fill fraction is lowered, the specific impulse continually increases for a given inert helium mole fraction. Further, at a fixed fill fraction, the specific impulse is strongly dependent on the helium mole fraction, or effective acoustic impedance of the inert gas. Recall that a reflected Mach wave results from the collision of the detonation wave with the contact surface at $X_{He} = 0.36$, which is independent of fill fraction. Hence, for $X_{He} < 0.36$ and $X_{He} > 0.36$, a reflected shock and rarefaction results from the interface collision, respectively. With this knowledge, an important result is shown in Fig. 6.7(a), in that as the acoustic impedance ratio z_0/z_1 increases, the benefit of partial filling becomes more apparent. For instance, in the case of helium as the inert gas ($X_{He} = 1.0$), the performance gains of partial filling are respectable but only up to $I_{sp}/I_{sp,full} = 1.47$ at $\alpha = 0.2$. Alternatively, in the case of air as the inert gas ($X_{He} = 0.0$), the performance gains are quite significant with $I_{sp}/I_{sp,full} = 3.36$ at $\alpha = 0.2$. This is best explained by the gasdynamic processes discussed at the beginning of this section. As the helium mole fraction of the inert gas decreases, the acoustic impedance of the inert mixture increases. As a result, decreasing X_{He} from 1 to 0.36 results in weaker reflected rarefaction waves from the contact surface until ultimately reaching the limiting condition of a reflected Mach wave. Further, any decrease in X_{He} beyond 0.36 yields a reflected shock wave with increasing strength at the interface collision. As previously mentioned, in either of these cases, the following secondary rarefaction wave is now the only mechanism relieving the gas bounded

by the reflected Mach or shock wave and propagating contact surface. Hence, the nature of the first decay in pressure at the thrust wall following the initial steady plateau pressure becomes less rapid as the helium mole fraction is reduced, and even experiences an abrupt increase in the event of a reflected shock. The second major gasdynamic process governing the performance gains shown in Fig. 6.7(a) is the magnitude of the intermediate plateau pressure. As mentioned previously, the interface collision and resulting flow field is what governs the pressure behind the reflected secondary wave from the thrust wall, namely, the pressure magnitude of the second plateau. As X_{He} is decreased, the pressure behind the incident and decaying transmitted shock becomes much higher. Consequently, the pressure at the contact surface traveling behind the transmitted shock is also higher, which serves as the tail boundary condition for the secondary rarefaction wave. Hence, as X_{He} decreases, the intermediate plateau pressure on the thrust wall increases, which causes a corresponding increase in the total impulse. Lastly, the final gasdynamic process governing the performance shown in Fig. 6.7(a) is the propagation velocity of the transmitted shock while traveling through the non-combustible inert mixture. As X_{He} is decreased, the acoustic impedance of the inert mixture increases, which lowers the transmission velocity of the transmitted shock. Effectively, this delays the time at which the exhausting rarefaction enters the thrust chamber and propagates towards and reflects from the thrust wall, initiating the final decay in pressure to the ambient condition.

In addition to the performance characteristics, it is also of interest to investigate how the propellant fill fraction and helium mole fraction of the inert mixture influences the gasdynamic blowdown time. Figure 6.7(b) shows the corresponding blowdown time for the parametric sweep of fill fraction and X_{He} shown in Fig. 6.7(a). For the case of the strongest reflected rarefaction from the contact surface ($X_{He} = 1.0$), the time required to return the pressure history at the thrust wall to the ambient condition continually decreases with decreasing fill fraction. This is due to the initial rapid pressure decay experienced on the thrust wall from the reflected rarefaction, and the shorter time required for the exhausting

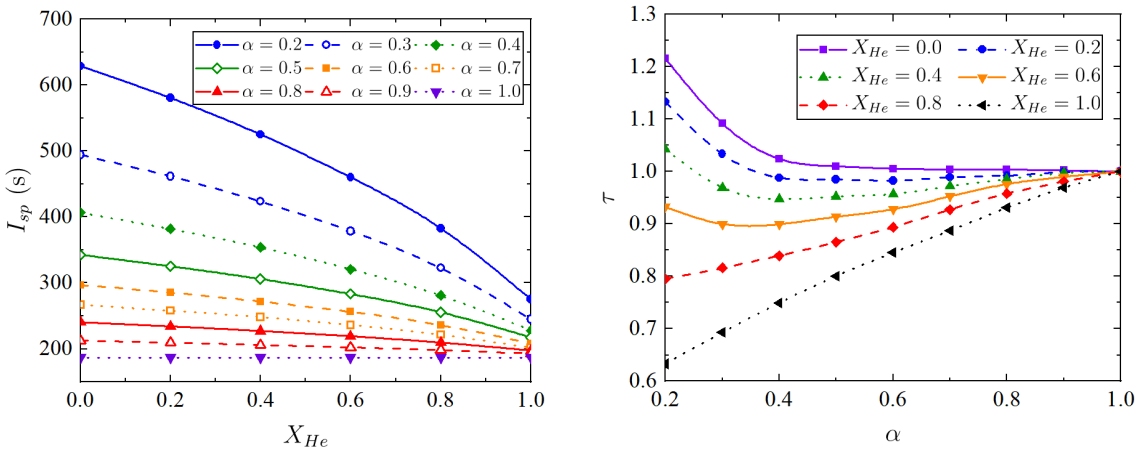

Figure 6.7. (a) Specific impulse and (b) normalized gasdynamic blowdown time for $2H_2$–O_2 propellant and helium–air inert mixtures at different fill fractions and helium mole fractions ($\psi = 1$).

rarefaction to begin propagating into the thrust chamber. For instance, in this case, the ratio of the transmitted shock to detonation wave velocity is $W_T/W_{CJ} = 1.07$; hence, the transmitted shock initially moves faster towards the PDE exit than the detonation wave velocity, and lower fill fractions result in shorter blowdown times than the case of a fully-filled PDE. Alternatively, in the case of the strongest shock reflection from the contact surface ($X_{He} = 0.0$), the time required to return the pressure history at the thrust wall to the ambient condition continually increases with decreasing fill fraction. This is caused by the reflected shock wave from the contact surface that slows the decay in pressure at the thrust wall, and the fact that a longer amount of time is required before the transmitted shock reaches the exit of the PDE, allowing the exhausting rarefaction to enter the thrust chamber. In this case, the ratio of the detonation wave velocity to the transmitted shock velocity is $W_T/W_{CJ} = 0.52$.

It is noted that some of the cases of X_{He} in Fig. 6.7(b) do not display the monotonic behavior of non-dimensional blowdown time versus fill fraction. For instance, the cases of $X_{He} = 0.4$ and 0.6 result in a reflected rarefaction from the contact surface; however, as

the fill fraction decreases below roughly 0.4, a minimum in $\tau = t_f/t_{f,full}$ is reached. As mentioned previously, at lower fill fractions, it is possible to have the reflected interface wave reflect from the thrust wall and catch the contact surface before the contact surface exits the thrust chamber. Additionally, depending on the acoustic impedance ratio across the contact surface separating the inert gas behind the decaying transmitted shock and the relieved burned products behind the secondary rarefaction, secondary reflected compression waves can reflect and propagate back towards the thrust wall. For $X_{He} \lesssim 0.6$ and $\alpha \lesssim 0.4$, secondary reflected compression waves form that slightly raise the intermediate plateau pressure and subsequently delay the time required for the pressure history on the thrust wall to return back to the ambient condition. Note, for the case of reflected shocks from the contact surface ($X_{He} < 0.36$), this becomes more evident as τ starts to increase much faster for $\alpha \lesssim 0.4$. As noted in the open-ended shock tube study of Kasahara et al. [113], any acoustic wave originating behind the contact surface will reflect with an amplitude of roughly 4/3 that of the incident value. Additionally, once the acoustic wave reflects from the contact surface and propagates back towards the thrust wall, the wall reflection results in a doubling of the wave amplitude. Their analysis showed that the impulse of the shock tube was primarily governed by the wave dynamics between the thrust wall and contact surface, rather than the inertia of the inert gas in the driven section. In essence, as the fill fraction reduces to the point where the reflected interface wave can catch the contact surface before it exits the thrust chamber, the contact surface can act as a barrier between the inert and burned mixtures that traps the gasdynamic waves between the thrust wall and contact surface. Moreover, as the inert acoustic impedance increases, the ability of the contact surface to trap acoustic waves starts to increase. Subsequently, each additional reflection between the thrust wall and contact surface raises the intermediate plateau pressure, which requires the exhausting rarefaction to relieve a higher pressure on the thrust wall, effectively lengthening the gasdynamic blowdown time. Such a description is applicable in the current

study for describing the minimum point behavior in τ in Fig. 6.7(b) and the corresponding rise in τ for lower fill fractions.

It is interesting to note that similar trends for τ in the case of $X_{He} = 0$ and 1 were reported in the analytical homogeneous dilution study of Endo et al. [112]. As previously discussed, [112] is primarily focused on describing the gasdynamics of an energetically equivalent fully-filled PDE that has been diluted based on the inert mixture of a partially-filled PDE. Because the model is focused on a diluted fully-filled PDE, there is no contact surface present in the flow field for which the mechanism of contact surface trapping can influence the ratio of τ. Despite this, their results imply that an energetics-based model can approximately capture the effects of this gasdynamic phenomenon by simply modeling the effective detonation wave and acoustic velocities in a diluted detonable mixture. Additionally, although the effects of compression waves reflecting from the contact surface become apparent for $\alpha \lesssim 0.4$, there is a region of lower fill fractions where the energetics-based models of [98, 110, 112] still accurately reflect the trends of higher-fidelity numerical and experimental results.

6.1.2 Effects of Non-Combustible Mixture Temperature

It is also of interest to investigate how the temperature of the inert mixture influences the performance gains of partially filling the PDE thrust chamber. In general, the acoustic impedance of the inert mixture is inversely proportional to the mixture temperature, which will ultimately influence the observed performance gains of partial filling. Additionally, varying the inert mixture temperature will highlight the importance of maintaining a cold purge gas during operation. For this parametric sweep, the detonable propellant is fixed at a stoichiometric H_2–O_2 mixture at 1 atm and 300 K, and the inert air mixture is varied from 150-800 K at 1 atm. The specific impulse results from this parametric variation are shown in Fig. 6.8(a) for fill fractions ranging from 0.2–1. By decreasing the inert mixture temperature T_i, the acoustic impedance of the non-combustible mixture simultaneously in-

creases, provided the pressure of the mixture is held constant. Additionally, with a fixed stoichiometric H_2–O_2 detonable propellant, a reflected Mach wave will result from the interface collision of the detonation wave and contact surface when $T_i = 418$ K. Subsequently, a reflected shock and rarefaction wave results from the interface collision when $T_i < 418$ K and $T_i > 418$ K, respectively. With this knowledge, it is evident from Fig. 6.8(a) that the performance gains from partial filling are significantly increased when the inert mixture temperature is relatively low. For instance, in the case of $T_i = 800$ K, the performance gains of partial filling are respectable but only up to $I_{sp}/I_{sp,full} = 2.10$ at $\alpha = 0.2$. Alternatively, in the case of air as the inert gas features a $T_i = 150$ K, the performance gains are quite significant with $I_{sp}/I_{sp,full} = 4.46$ at $\alpha = 0.2$. Again, this is best explained by the gasdynamic processes discussed at the beginning of this section in relation to the acoustic impedance of the inert mixture. In this case, as the inert mixture temperature decreases, the acoustic impedance of the inert mixture increases. As a result, decreasing T_i from 800 to 418 K results in weaker reflected rarefaction waves from the contact surface until ultimately reaching the limiting condition of a reflected Mach wave. Further, any decrease in T_i below 418 K yields a reflected shock wave with increasing strength at the interface collision. These results demonstrate that it is important to ensure the temperature of the purge gas is kept relatively low in order to maintain a high acoustic impedance, which serves to enhance the performance benefit of partially filling the PDE thrust chamber.

The normalized gasdynamic blowdown time behaves in a similar manner to that of the case of varying the acoustic impedance of the inert mixture by changing the helium mole fraction; however, in this case the acoustic impedance is lowered by increasing the inert mixture temperature. It is evident from Fig. 6.8(b) that the variation in normalized blowdown time, τ is strongly dependent on the acoustic impedance of the inert mixture. For instance, when $T_i < 300$ K, τ continually increases with decreasing fill fraction, whereby the rate of increase becomes more pronounced once the contact surface wave trapping mechanics discussed in [113] begin to take effect. Alternatively, for $T_i > 300$ K, the normalized

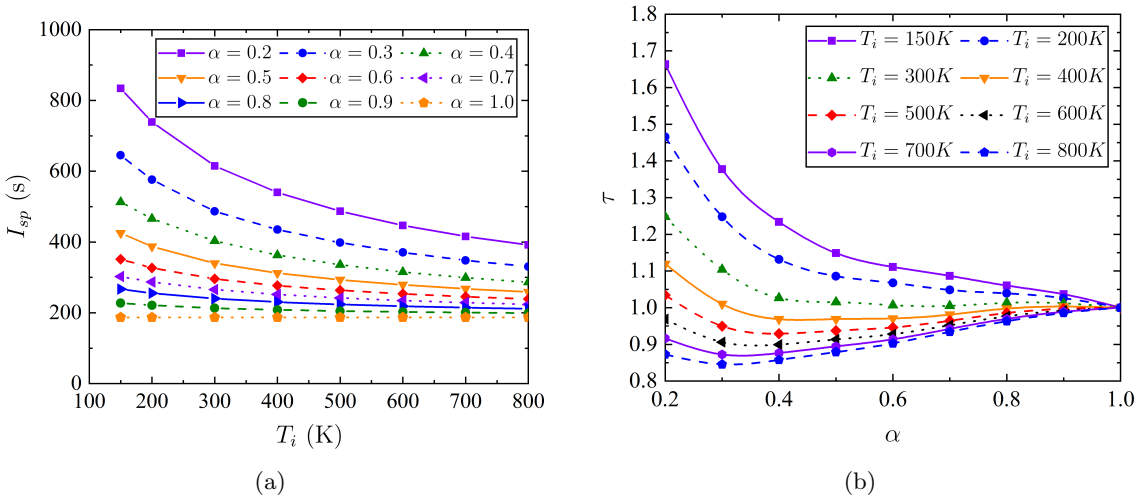

Figure 6.8. (a) Specific impulse and (b) normalized gasdynamic blowdown time for $2H_2$–O_2 propellant and air as the inert gas at different fill fractions and inert temperatures ($\psi = 1$).

blowdown time continually decreases with decreasing fill fraction until ultimately reaching a minimum point at roughly $0.3 \lesssim \alpha \lesssim 0.4$. As mentioned before, this minimum point behavior in τ coincides with the lowest fill fraction upon which the leading characteristic of the reflected secondary wave catches the contact surface from behind before exiting the chamber. Hence, any reduction in fill fraction for the given conditions results in reflected compression waves at the thrust wall and a associated increase in the time required to exhaust the PDE to the ambient condition.

6.1.3 Effects of Blowdown Pressure Ratio

It is also of interest to investigate how the blowdown pressure ratio of the PDE influences the performance gains of partially filling the PDE thrust chamber, since the acoustic impedance of the inert mixture is directly proportional to the mixture pressure. For these cases, the inert non-combustible mixture is taken as the ambient condition and an idealized diaphragm is assumed to separate the ambient from the propellant. Note, this is an idealized representation of PDEs operating in sub-atmospheric environments, as practical multi-cycle operations would not employ a diaphragm to separate the detonable

propellant from the ambient condition. However, the subsequent results are indicative of the ideal single-cycle performance of partially-filled PDEs. For this parametric sweep, the detonable propellant is fixed at a stoichiometric H_2–O_2 mixture at 1 atm and 300 K, and the ambient air is varied from 0.01–1 atm at 300 K, corresponding to a blowdown pressure ratio variation of $\psi = p_1/p_0 = 100$–1. The specific impulse results from this parametric variation are shown in Fig. 6.9(a) for fill fractions ranging from 0.2–1. By decreasing the ambient pressure p_0, the acoustic impedance of the non-combustible mixture simultaneously decreases. For sub-atmospheric operation with a fixed stoichiometric H_2–O_2 detonable propellant, a reflected shock and rarefaction wave results from the interface collision when $\psi < 1.35$ and $\psi > 1.35$, respectively. Hence, when $\psi = 1.35$ a reflected Mach wave is obtained. It is evident from Fig. 6.9(a) that the performance gains from partial filling in a sub-atmospheric environment is dependent on the operating fill fraction. For instance, in the fully-filled case and consistent with conventional rocket engine performance, the PDE specific impulse continually increases as the PDE exhausts into a lower back pressure. Conversely, in the case of $\alpha = 0.2$, the specific impulse reduces with increasing ψ. This trend remains true until the fill fraction increases to roughly 0.7, in which case the specific impulse becomes nearly independent of the blowdown pressure ratio. Increasing the fill fraction above 0.7 results in similar behavior for a fully-filled PDE operating in sub-atmospheric environments. This performance behavior is best explained using the acoustic impedance discussion from the forgoing section. In the case of $\psi = 1, 10$, and 100, the transmitted shock to detonation wave velocity ratio is equal to $W_T/W_{CJ} = 0.52, 1.03$, and 1.71, respectively. Hence, as the ambient back pressure drops while holding the propellant at 1 atm, the transmitted shock velocity into the ambient condition in the remaining portion of the thrust chamber increases. Consequently, the reflected rarefaction from the interface collision becomes stronger as ψ increases above 1.35. These two gasdynamic processes lower the intermediate plateau pressure on the thrust wall and allow for the exhausting rarefaction to enter the thrust chamber in a shorter amount of time, effectively lowering the specific

impulse and time required to return the pressure history on the thrust wall back to the ambient condition. These are the gasdynamic mechanisms that lower the specific impulse for $\alpha < 0.7$ with increasing ψ. For $\alpha \geq 0.7$, the partial-fill effect becomes reduced as the acoustic impedance of the ambient air reduces with increasing ψ, and the ability of the ambient air to impede the exhausting blowdown gasdynamics of the PDE is diminished.

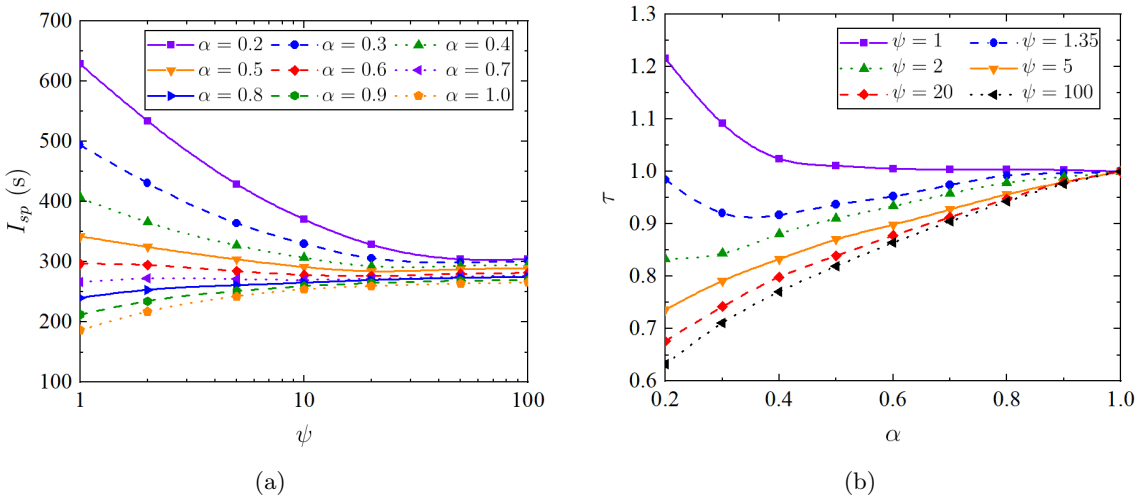

Figure 6.9. (a) Specific impulse and (b) normalized gasdynamic blowdown time for $2H_2$–O_2 propellant and air as the inert gas at different fill fractions and blowdown pressure ratios.

The normalized gasdynamic blowdown time behaves in a similar manner to that of the case of varying the acoustic impedance of the inert mixture by changing the helium mole fraction; however, in this case the acoustic impedance is lowered by decreasing the back pressure. It is evident from Fig. 6.9(b) that the normalized blowdown time continually decreases for all fill fractions when $\psi < 2$. Note, these are the cases that result in a reflected rarefaction from the contact surface, and subsequently result in faster transmitted shock waves into the non-combustible ambient air, which yields reduced shorter time intervals until the exhausting rarefaction is able to enter the thrust chamber. For the case of $\psi = 1.35$, a reflected Mach wave results from the interface collision and the normalized gasdynamic blowdown time decreases with decreasing fill fraction until $\alpha \approx 0.3$. At this point, the

fill fraction is low enough to allow the secondary rarefaction wave, lead by the reflected interface Mach wave, to reflect from the thrust wall and catch the contact surface before the contact surface leaves the PDE. Hence, a secondary reflected compression wave results from this interface interaction, which slightly raises the intermediate plateau pressure on the thrust wall and increases the gasdynamic blowdown time. Lastly, the case of $\psi = 1$ is identical to that of $X_{He} = 0.0$ in the previous discussion.

6.1.4 Performance Scaling Laws

It is of interest to normalize the previously discussed partial filling results with respect to the performance of a fully-filled PDE. Non-dimensional performance relations for the single-cycle specific impulse, total impulse, and time-averaged thrust of partially-filled PDEs are crucial for guiding the design of PDE based propulsion systems and engine scalability. Previously, there have been various efforts at normalizing the specific impulse of partially-filled PDEs. One of the first approaches was in the numerical study of Li and Kailasanath [107], where their numerical results were used to obtain an empirical correlation for $I_{sp}/I_{sp,full}$ as a function of fill fraction. Similarly, Cooper and Shepherd [108] used the experimental and numerical results of [87, 89, 90, 107, 109] to obtain an empirical piecewise correlation for $I_t/I_{t,full}$ and $I_{sp}/I_{sp,full}$ versus the ratio of propellant fill volume to PDE thrust chamber volume, namely, volumetric fill fraction. They adjusted experimental data using the Gurney model [111, 168] to correct for the tamping mass of the diaphragm. However, as mentioned previously and in [110], any correlation based solely on the fill fraction is not general, but specific to the respective detonable and inert mixture combination. In recognition of this, Cooper [110] used the Gurney model to normalize the specific impulse as a function of the inert and detonable gas mixture masses. In this form, the Gurney model was shown to successfully collapse $I_{sp}/I_{sp,full}$ versus the mass fraction of detonable-to-total mass (detonable plus inert) for generalized detonable and inert combinations. A comparison of the Gurney model was made in [110] with the experimental and numerical

results of [87, 89, 90, 98, 101, 107, 109], and the model was shown to represent the general trend well, with only a slight over-estimation of the experimental results. This was the first result that provided insights to a governing parameter, namely, the mass fraction of the detonable and inert mixtures, to collapse the ratio of $I_{sp}/I_{sp,full}$ for general detonable and inert mixture combinations. This was later confirmed by Sato et al. [98] where their analysis showed that $I_{sp}/I_{sp,full}$ is inversely related to the square root of mass fraction for any detonable propellant and inert gas mixture. The Gurney and Sato models are discussed in the following paragraphs.

The model proposed by Cooper [110] made use of the original Gurney model [111], which is an explosives model based on using momentum and energy conservation to associate the terminal velocity of an accelerating mass with the Gurney velocity. From that analysis, a relationship was developed for the impulse of the PDE in terms of the Gurney velocity, total thrust chamber mass, tamper mass fraction, m_i/m_d, and thrust chamber mass fraction, m_{tc}/m_d. Further, if it is assumed that $m_{tc}/m_d \to \infty$, which is appropriate for PDE propulsion systems, then the normalized expression for $I_{sp}/I_{sp,full}$ based on the Gurney model can be written as [113]

$$\frac{I_{sp}}{I_{sp,full}} = \sqrt{\frac{4}{3}} \left(\frac{m_i}{m_d} + \frac{1}{2} \right) \left(\frac{m_i}{m_d} + \frac{1}{3} \right)^{-1/2} \tag{6.1}$$

In the study by Sato et al. [98], an expression was derived for $I_{sp}/I_{sp,full}$ based on similar energy conservation considerations. They introduced the mass fraction parameter

$$Z = \frac{m_d}{m_d + m_i} = \left[1 + \left(\frac{1}{\alpha} - 1 \right) \frac{\rho_i}{\rho_d} \right]^{-1} \tag{6.2}$$

which is related to the ratio of heat released by means of combustion for fully- and partially-filled PDEs, respectively. Further, they assumed that the thermal efficiency of a fully- and partially-filled PDE are approximately equal, and then deduced a relation for the ratio of characteristic exhaust velocities of the partially- and fully-filled PDE, namely, $v_p/v_f \approx \sqrt{Z}$, where the subscripts p and f correspond to partially- and fully-filled, respectively. From

this relation, they were able to show that the normalized specific impulse ratio can simply be written as

$$\frac{I_{sp}}{I_{sp,full}} = \frac{1}{\sqrt{Z}} = \eta \tag{6.3}$$

Further, for the purposes of this study, it is convenient to write η in terms of α and the inert-to-detonable density ratio, ρ_i/ρ_d, as

$$\eta = \left[1 + \left(\frac{1}{\alpha} - 1\right)\frac{\rho_i}{\rho_d}\right]^{1/2} \tag{6.4}$$

Additionally, for comparison purposes, it is convenient to re-write the normalized specific impulse from the Gurney model using the mass fraction parameter Z as

$$\frac{I_{sp}}{I_{sp,full}} = \sqrt{\frac{4}{3}}\left(\frac{1}{Z} - \frac{1}{2}\right)\left(\frac{1}{Z} - \frac{1}{3}\right)^{-1/2} \tag{6.5}$$

A few comments can be made about these models. As the mass and fill fractions approach zero, the normalized specific impulse tends towards infinity. Unfortunately, both the Sato and Cooper models suffer from this singularity in the limit of zero α. Additionally, this behavior is inconsistent with experimental and numerical observations [98, 110]. Although not the target of the current parametric study, it is noted that the magnitude of $I_{sp}/I_{sp,full}$ as α approaches zero can be estimated using the models developed by Cooper [110] and Endo et al. [112].

The normalized specific impulse ratio for partially-filled PDEs operating with H_2–O_2 and C_2H_4–O_2 detonable propellants are shown in Fig. 6.10. Note, the mass fraction Z is varied in accordance with the previously discussed parametric study of sweeping the fill fraction ($0.2 \leq \alpha \leq 1$), helium mole fraction ($0 \leq X_{He} \leq 1$), inert mixture temperature ($150 \leq T_i \leq 800$), and blowdown pressure ratio ($1 \leq \psi \leq 100$). It is noted that for the cases of varying blowdown pressure ratio, the partially-filled specific impulse is normalized by the specific impulse of a fully-filled PDE that is operating at the same blowdown pressure ratio. It is evident from Fig. 6.10 that the normalized specific impulse ratio predicted by the MOC model is best modeled using the scaling law proposed by Sato et al. [98], with an average error of 2 percent for Z ranging from 0.1–1. Moreover, an average error of 4

percent is obtained between the results of the present MOC model and the Gurney model proposed by Cooper [110]; however, the Gurney model mostly over-predicts the MOC results for $Z < 0.5$. Therefore, the model proposed by Sato et al. [98] is used in the subsequent analysis to further normalize the total impulse and average thrust of partially-filled PDEs. It is worth mentioning that despite the simplicity of the Sato model, it still manages to capture the effects of sweeping ψ for partially- and fully-filled PDEs operating at the same blowdown pressure ratio. This is a result that has not yet been reported for partially-filled PDEs operating in sub-atmospheric environments, which increases the applicability of the model proposed by Sato et al. [98].

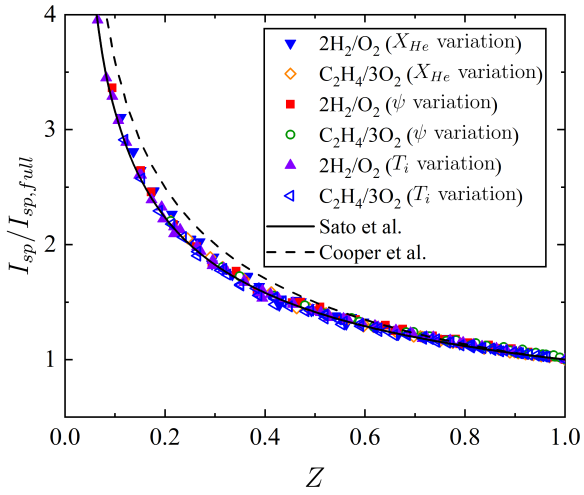

Figure 6.10. Comparison of normalized MOC specific impulse $I_{sp}/I_{sp,full}$ with the scaling laws of [98, 110] in Eqs. (6.3) and (6.5) for fill fractions ranging from 0.2–1.0 while varying the helium mole fraction for the helium–air inert mixture, inert mixture temperature, and blowdown pressure ratio.

It is of interest to investigate how the combination of fill fraction and density ratio of detonable-to-inert gas mixture influences the behavior of $\eta = I_{sp}/I_{sp,full}$. By inspection of Eq. (6.4), it is clear that η increases with decreasing fill fraction, for any combination of detonable and inert mixtures. This is consistent with all of the previous analysis and discussion on partial filling. Similarly, as the fill fraction increases, the effects of the inert

mixture becomes less significant as the density ratio ρ_i/ρ_d is scaled by $1/\alpha - 1$. Hence, when the fill fraction equals unity, i.e., a fully-filled PDE thrust chamber with no inert mixture, η becomes independent of the inert mixture or ambient condition and equals unity. In a similar manner, holding the fill fraction constant at a value less than unity, it is clear from (6.4) that η will increase with increasing ρ_i/ρ_d. Effectively, this is equivalent to raising the density of the inert mixture ρ_i, which is analogous to increasing the acoustic impedance of the inert mixture. This is an alternative way of viewing the effects of partial filling that provides better insights into the dependency and sensitivity of the partial-fill effect to fill fraction and density ratio of the inert-to-detonable mixture. Figure 6.11 is a contour plot of how the reduced normalized specific impulse $(\eta - 1)$ varies with fill fraction and detonable-to-inert density ratio. Such a contour plot is useful for visualizing the performance map of partially-filled PDEs. For instance, if it were desired to obtain a specific impulse ratio of $\eta = 1.5$, then identifying the curve with a magnitude of 0.5 reveals all the combinations of α and ρ_d/ρ_i required to achieve this level of propulsive performance. Hence, for a fixed fill fraction, varying either the propellant equivalence ratio or inert temperature could tune the desired propulsive performance. Additionally, for fixed detonable and inert mixture densities, varying the fill fraction could tune the desired propulsive performance. Lastly, in the case of sub-atmospheric operation, the density of the ambient is dropping with altitude; hence, varying both the fill fraction and equivalence ratio of the detonable propellant can be used to obtain the desired propulsive performance. Note that the fill fraction varies from 0–1 in Fig. 6.11; however, the model proposed by Sato et al. [98] fails in the limit of zero fill fraction. Hence, the results in the range of $\alpha < 0.2$ should be taken with caution.

The total impulse defined by Eq. (4.14) is an important propulsive performance parameter of the PDE, for which previous researchers have tried to develop scaling relations. As previously mentioned, Cooper et al. [108] provided a piecewise correlation for $I_t/I_{t,full}$ in terms of the volumetric fill fraction ranging from 0–1 for experimental and numerical hydrocarbon data of [87, 89, 90, 107, 109]. However, given the previous discussion, it is evident

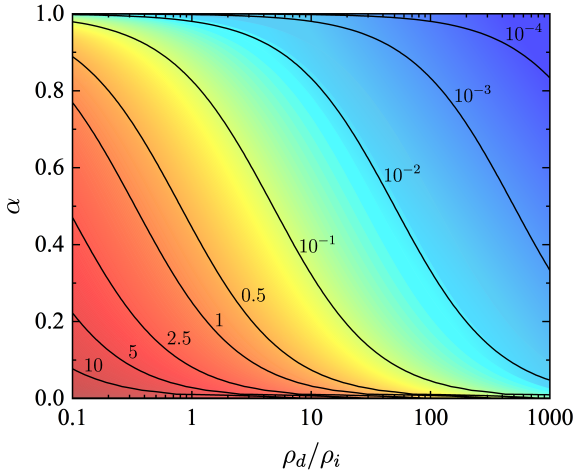

Figure 6.11. Contour plot of reduced normalized specific impulse, $\eta - 1$, vs. fill fraction and detonable-to-inert mixture density ratio.

that any correlation based solely on fill fraction is not general, but specific to the respective detonable and inert mixture combination. Therefore, in the remainder of the section, the scaling law of Sato et al. [98] is extended to the total impulse ratio and compared with the results of the MOC model and existing numerical and experimental data.

From the definition of specific impulse in Eq. (4.15), it can be shown that the total impulse ratio of a partially- to fully-filled PDE takes the form $I_t/I_{t,full} = \alpha I_{sp}/I_{sp,full}$; hence, in terms of η,

$$\frac{I_t}{I_{t,full}} = \alpha\eta = \Omega \tag{6.6}$$

where Ω can be expressed in terms of Z, ρ_d, ρ_i and α as,

$$\Omega = Z^{1/2}\left[\frac{\rho_d}{\rho_i} + \left(1 - \frac{\rho_d}{\rho_i}\right)Z\right]^{-1} = \left[\frac{\rho_i}{\rho_d}\alpha + \left(1 - \frac{\rho_i}{\rho_d}\right)\alpha^2\right]^{1/2} \tag{6.7}$$

Inspection of Eq. (6.7) reveals the dependency of the total impulse ratio on the partially-filled PDE operating parameters. For instance, using the expression for Ω in terms of α and ρ_i/ρ_d, it is clear that Ω^2 is quadratic in α with coefficients proportional to the ratio of densities of the detonable and inert mixtures. In this form, it is clear that the total impulse ratio $I_t/I_{t,full} = \Omega$ vanishes as the fill fraction approaches zero, which is consistent with experimental observations and physical intuition. Additionally, as the fill fraction

approaches unity, much like the expression for η, the influence of the inert mixture vanishes, and Ω subsequently approaches unity. It is interesting to note that Eq. (6.7) implies Ω does not have to be bounded between 0–1 for a fill fraction less than unity. For instance, for a fill fraction of less than unity, it is possible to have a combination of detonable and inert densities such that $\Omega > 1$. This is in contrast to the conclusions presented in [108]. However, as will be shown in the subsequent analysis, heavier inert gases, namely, inert mixtures with high acoustic impedance, can actually cause the total impulse ratio to exceed unity. A comparison of Eq. (6.6) with the MOC parametric sweep of fill fraction ($0.2 \leq \alpha \leq 1$), helium mole fraction ($0 \leq X_{He} \leq 1$), inert mixture temperature ($150 \leq T_i \leq 800$), and blowdown pressure ratio ($1 \leq \psi \leq 100$) for PDEs operating with H_2–O_2 and C_2H_4–O_2 detonable propellants is shown in Fig. 6.12. The scaling law in Eq. (6.6) agrees very well with the results of the MOC parametric sweep, such that an average error of 2 percent is obtained over the range $0.2 < \Omega \lesssim 1$. This implies that the extended scaling law of Sato et al. [98] also accurately represents the total impulse ratio, including PDEs operating in sub-atmospheric environments.

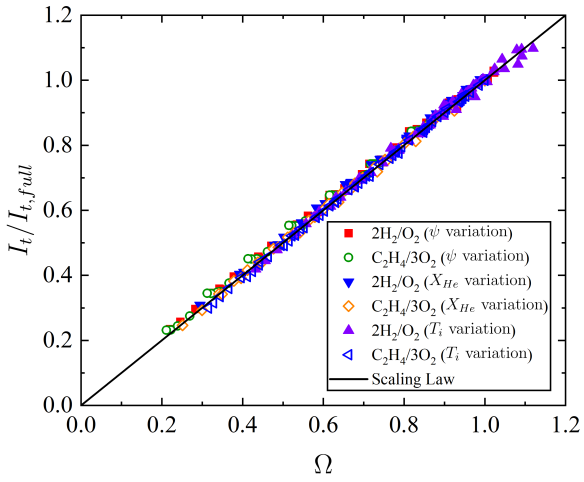

Figure 6.12. Comparison of the normalized MOC total impulse $I_t/I_{t,full}$ with the scaling law in Eq. (6.6) for fill fractions ranging from 0.2–1.0 while varying the helium mole fraction for the helium–air inert mixture, inert mixture temperature, and blowdown pressure ratio.

It is of interest to compare the generalized expression for $I_t/I_{t,full} = \Omega$ with existing partially-filled PDE numerical and experimental data. For this, the numerical results of [76, 83, 98, 107] and experimental results of [89, 95, 97, 101, 102] are used, which were previously discussed in Ch. 4. In addition to the previously discussed results, the numerical results of [71] and experimental results of [87, 90, 103, 106] are also used. In the MOC study carried out by Guzik et al. [71], the detonable propellant is a gaseous propane–oxygen mixture with ambient air as the inert mixture, and the fill fraction is varied from 0.2-1 by adding straight constant-area extensions to the PDE. In the experimental study carried out by Zhdan et al. [87], single-shot (SS) experiments were conducted with a detonation tube and the impulse was directly measured using a ballistic pendulum arrangement. The detonation tube was evacuated by a vacuum pump prior to operation and then filled with a stoichiometric acetylene–oxygen mixture, where a thin diaphragm was used to separate the detonable propellant from the ambient air. Further, detonation was achieved by direct initiation using an initiating tube, and the fill fraction was varied from 0.14–1 by adding straight-tube extensions with the same area. Similarly, in the experimental study conducted by Cooper et al. [90], single-shot (SS) experiments were conducted with a detonation tube and the impulse was directly measured using a ballistic pendulum setup. No internal obstacles were used to enhance the DDT length. The detonation tube was evacuated with a vacuum pump and then filled with a nitrogen diluted ethylene–oxygen mixture that was separated from the ambient air using a thin Mylar diaphragm. The nitrogen dilution was varied from 0–40 percent and a fill fraction was changed from 1 to 0.63 by adding a straight-tube extension with the same area. In the experiments conducted by Kasahara et al. [103], a partially-filled multi-cycle PDE was operated at frequencies ranging from 2.5–8.3 Hz, and the thrust was directly measured using a spring-damper mechanism and a dynamic load cell. An ethylene–oxygen detonable mixture was injected using solenoid valves, and the PDE was purged with helium after each cycle. Further, the fill fraction was varied from 0.075–0.26 by precision timing of the solenoid valves. A value for the fully-filled specific impulse was not

reported, thus the data was normalized using the theory of Endo et al. [65]. For this case, the inert mixture was taken as helium since the PDE was purged with helium. However, it was noted in [103] that the unfilled portion of the tube contained a mixture of helium, burned products from the previous cycle, and suctioned air from the ambient. Additionally, for the lowest fill fractions of 0.075–0.087, it was concluded that proper detonation was not achieved due to diffusion between the helium and fresh propellant interface. Lastly, in the experiments conducted by Wang et al. [106], a valveless partially-filled multi-cycle PDE was operated at frequencies ranging from 50–96 Hz, and the thrust was determined using the arithmetic mean of dynamic thrust loading measured with a load cell. An oxygen-enriched gasoline propellant was used as the detonable mixture, which required no purge during the PDE operation, and a combination of burned products and ambient air acted as the inert mixture in the unfilled portion of the PDE. The fill fraction was varied from roughly 0.5–1 by tuning the operating frequency, and a Shchelkin spiral was used to aid the DDT process. As noted in [106], the detonable-to-inert density ratio was determined to be equal to unity, which provided the best agreement with the specific impulse model of Sato et al. [98].

In each of these studies, if the total impulse was not reported, then it is calculated based on the reported specific impulse, geometry of the PDE thrust chamber, detonable propellant and inert mixture, and fill fraction. Further, if the fill fraction was varied by adding straight-tube extensions to the PDE, the normalized total impulse is adjusted for an equivalent fully-filled PDE. Lastly, the fill fraction and densities of the reported detonable and inert mixtures are used to calculate the equivalent numerical or experimental value of Ω. Figure 6.13 provides a comparison of the scaling law in Eq. (6.6) with the partially-filled PDE results of [71, 76, 83, 87, 89, 90, 95, 97, 98, 101–104, 106, 107]. Astonishingly, remarkable agreement is obtained with existing published performance data, which encompasses partially-filled PDEs operating over a very wide range of conditions. An average error of 6 percent is obtained between Eq. (6.6) and the numerical and experimental data shown in Fig. 6.13 over a range $0.1 < \Omega \lesssim 1.0$. In contrast to the specific impulse ratio, η, good

agreement with experimental data is maintained at very low fill fractions. This is primarily caused by the scaling for Ω vanishing at a fill fraction of zero, which is consistent with the physical operating aspects of partially-filled PDEs.

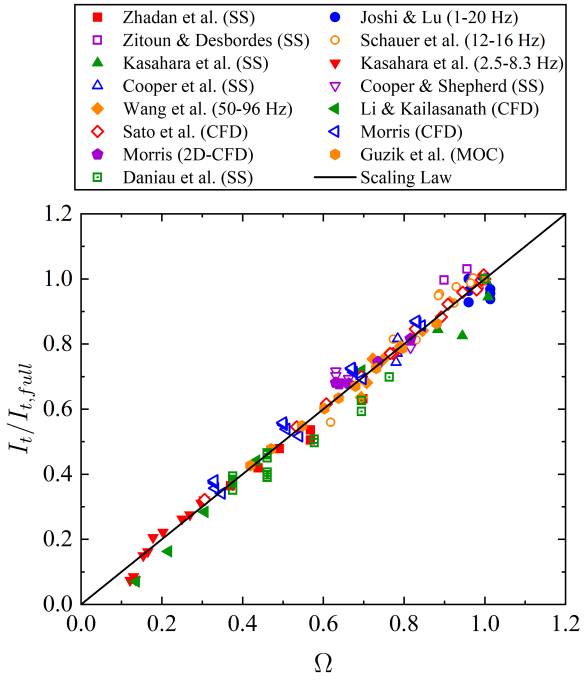

Figure 6.13. Comparison of normalized total impulse $I_t/I_{t,full}$ scaling law in Eq. (6.6) with experimental and numerical results of [71, 76, 83, 87, 89, 90, 95, 97, 98, 101–104, 106, 107].

For adequate design of PDEs employing the partial-filling method, it is of interest to visualize the performance map of $I_t/I_{t,full} = \Omega$, while varying the operating parameters for a partially-filled PDE. Figure 6.14 is a contour plot demonstrating how Ω varies with fill fraction and density ratio of the detonable-to-inert mixtures. As previously mentioned, there is no restriction on Eq. (6.7) which limits $\Omega \leq 1$. This is shown in Fig. 6.14 for combinations of α and ρ_d/ρ_i that are less than unity. For instance, for a fill fraction of 0.5, a density ratio of $\rho_d/\rho_i < 0.33$ is required to achieve an impulse ratio greater than unity. In practice, however, a density ratio of $\rho_d/\rho_i = 0.33$ would be difficult to achieve in a practical operation, as the inert mixture density would have to be 3 times that of the detonable

density. Realizable density ratios of approximately 0.4 for the case of stoichiometric H_2–O_2 detonable propellant and ambient air as the inert mixture can be achieved, which results in a maximum total impulse ratio of $I_t/I_{t,full} = 1.014$ at a fill fraction of $\alpha = 0.88$. This condition was experimentally studied by Joshi and Lu [97], with the PDE operating at 10 Hz, where they obtained an impulse ratio of $I_t/I_{t,full} = 0.97$ at a fill fraction of 0.88. Although the experimentally obtained total impulse ratio does not actually exceed unity, it is very close to the value predicted by Eq. (6.7) and within the range of experimental error. Given these results, this is an area of partially-filled PDEs that warrants further experimental investigation in order to verify the degree to which the impulse ratio can practically be held at or above unity. In the case of sub-atmospheric PDE operation, the benefit of partial filling becomes drastically diminished as ρ_d/ρ_i, or blowdown pressure ratio, increases. In fact, as demonstrated in Eq. (6.7) and Fig. 6.14, the normalized total impulse equals the fill fraction in the limit where $\rho_d/\rho_i \to \infty$. This is a characteristic result that is obtained when the acoustic impedance of the inert mixture is effectively zero and has no influence on the thrust chamber gasdynamics of the PDE. Conversely, as ρ_d/ρ_i decreases, the acoustic impedance of the inert mixture begins to influence the thrust chamber gasdynamics of the PDE for $\alpha < 1$, and the resulting impulse ratio varies as shown in Fig. 6.14.

The final propulsive performance metric of interest in the design of partially-filled PDEs is the time-averaged thrust over a single-cycle. Therefore, it is of interest to normalize the single-cycle time-averaged thrust of a partially-filled PDE to that of a fully-filled PDE. From the definition of total impulse in Eq. (4.14), the normalized time-averaged thrust ratio, $\bar{F}/\bar{F}_{full}$, is related to the ratio of gasdynamic blowdown time, τ, by

$$\frac{\bar{F}}{\bar{F}_{full}} = \frac{I_t}{I_{t,full}} \left(\frac{t_f}{t_{f,full}} \right)^{-1} = \frac{\Omega}{\tau} \tag{6.8}$$

A comparison of Eq. (6.8) with the MOC parametric sweep of fill fraction ($0.2 \leq \alpha \leq 1$), helium mole fraction ($0 \leq X_{He} \leq 1$), inert mixture temperature ($150 \leq T_i \leq 800$), and blowdown pressure ratio ($1 \leq \psi \leq 100$) for PDEs operating with H_2–O_2 and C_2H_4–O_2 detonable propellants is shown in Fig. 6.15. The scaling law in Eq. (6.8) agrees very well

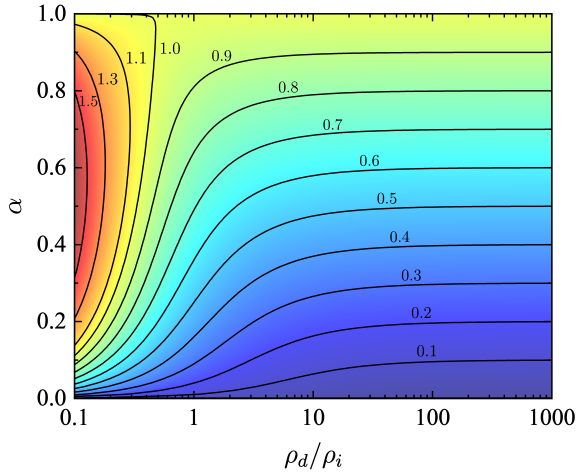

Figure 6.14. Contour plot of normalized total impulse $I_t/I_{t,full}$ in Eq. (6.6) vs. fill fraction and detonable-to-inert mixture density ratio.

with the results of the MOC parametric sweep, such that an average error of roughly 3% is obtained over the range $0.3 < \Omega/\tau < 1$. This further signifies that the extended scaling law of Sato et al. [98] also accurately represents the time-averaged thrust ratio of partially-filled PDEs.

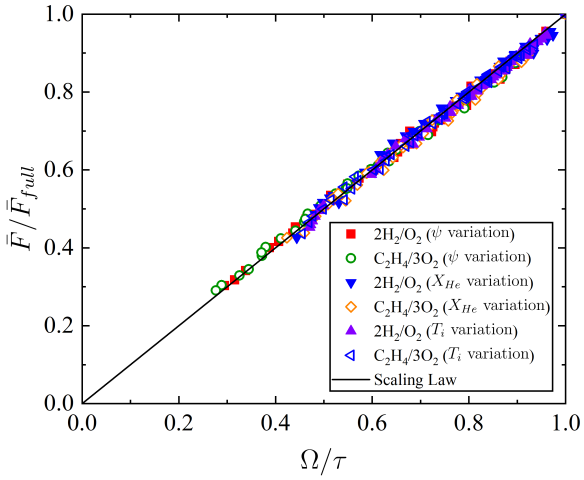

Figure 6.15. Comparison of the normalized MOC time-averaged thrust $\bar{F}/\bar{F}_{full}$ with the scaling law in Eq. (6.8) for fill fractions ranging from 0.2–1.0 while varying the helium mole fraction for the helium–air inert mixture, inert mixture temperature, and blowdown pressure ratio.

Although the scaling relationship in Eq. (6.8) captures the time-averaged thrust characteristics, the accurate determination of τ in practice is quite difficult, and usually requires numerical analysis of the PDE thrust chamber gasdynamics. Hence, it is of interest to obtain a reduced-order expression for τ in terms of the partial filling parameters that approximately models the blowdown gasdynamic behavior of fully- and partially-filled PDEs. By analysis of the behavior of τ in the parametric sweep conducted with the MOC model, an approximate scaling relation for $\rho_d/\rho_i \gtrsim 1$, in terms of the mass fraction, Z, fill fraction, α, and detonable-to-inert mixture density ratio, ρ_d/ρ_i is

$$\tau = Z^{1/7}\left[\frac{\rho_d}{\rho_i} + \left(1 - \frac{\rho_d}{\rho_i}\right) Z\right]^{-2/7} = \left[\frac{\rho_i}{\rho_d}\alpha + \left(1 - \frac{\rho_i}{\rho_d}\right)\alpha^2\right]^{1/7} \tag{6.9}$$

Substitution of this expression for τ into Eq. (6.8) yields

$$\frac{\bar{F}}{\bar{F}_{full}} = \Lambda \tag{6.10}$$

where

$$\Lambda = Z^{5/14}\left[\frac{\rho_d}{\rho_i} + \left(1 - \frac{\rho_d}{\rho_i}\right) Z\right]^{-5/7} = \left[\frac{\rho_i}{\rho_d}\alpha + \left(1 - \frac{\rho_i}{\rho_d}\right)\alpha^2\right]^{5/14} \tag{6.11}$$

A comparison of Eq. (6.11) with the MOC parametric sweep is shown in Fig. 6.16. Note, in an attempt to not clutter the results in Fig. 6.16, the parametric sweep of helium mole fraction for the helium–air inert mixture was not included; however, it is noted that those results agree with the results shown. The scaling in Eq. (6.8) has very good agreement with the results of the MOC parametric sweep for $\rho_d/\rho_i \gtrsim 1$. In this case, an average error of roughly 4 percent is obtained over the range $0.3 < \Lambda < 1$. However, for $\rho_d/\rho_i < 1$, the effects of contact surface trapping becomes more evident regarding the blowdown gasdynamics at lower fill fractions, making any one general scaling law for $\tau = t_f/t_{f,full}$ difficult to obtain. This is demonstrated by the disagreement of Eq. (6.8) in Fig. 6.16 for the cases of $\rho_d/\rho_i = 0.56$ and 0.42, respectively. Despite this disagreement, in practical partially-filled PDE systems using hydrocarbon propellant, the density ratio is close to unity, which makes the scaling relationship more appropriate. This remains true for PDEs operating in

sub-atmospheric environments, as the density ratio is usually greater than unity for both hydrogen and hydrocarbon propellants.

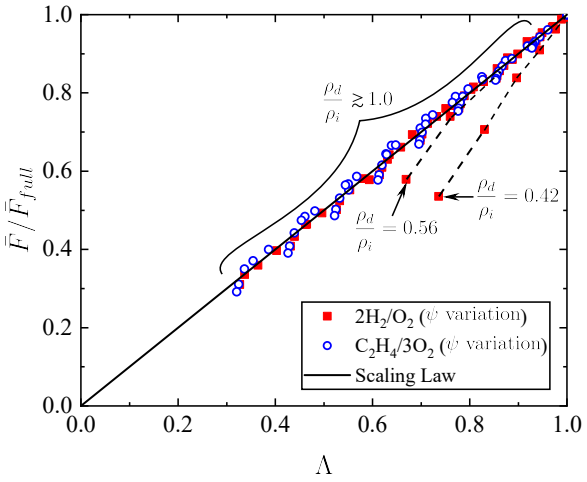

Figure 6.16. Comparison of normalized MOC time-averaged thrust $\bar{F}/\bar{F}_{full}$ with the scaling law in Eq. (6.10) for various blowdown pressure ratios.

A comparison of the scaling relation in Eq. (6.10) with the MOC results of Guzik et al. [71] and the experimental results of Schauer et al. [95] is provided in Fig. 6.17. As mentioned previously, the MOC results in [71] are associated with partially-filled PDEs operating with stoichiometric propane–oxygen detonable propellant and air as the inert mixture. Hence, this operating condition results in a detonable-to-inert density ratio of $\rho_d/\rho_i = 1.18$, which results in the very good agreement with Eq. (6.10) shown in Fig. 6.17. Conversely, the experiments of [95] are conducted with a stoichiometric hydrogen–air detonable mixture and air as the inert mixture, which results in a detonable-to-inert density ratio of $\rho_d/\rho_i = 0.72$. Hence, as expected, the agreement is not very good given the limitations on the density ratio of Eq. (6.9). Despite the disagreement with the experiments of [95], the scaling relation in Eq. (6.11) is believed to share better agreement with partially-filled PDEs operating with hydrocarbon propellants, and partially-filled PDEs operating in sub-atmospheric environments.

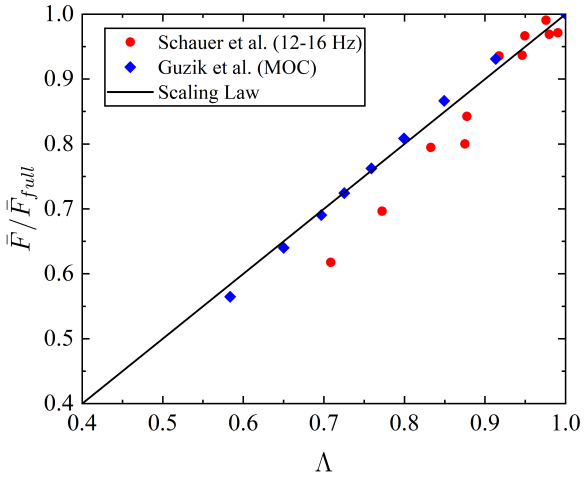

Figure 6.17. Comparison of normalized time-averaged thrust $\bar{F}/\bar{F}_{full}$ scaling law in Eq. (6.10) with previous experimental and numerical results of [71, 95].

Lastly, it is of interest to analyze the performance map of $\Lambda = \bar{F}/\bar{F}_{full}$ as a function of the partially-filled PDE operating parameters. Figure 6.18 is a contour plot showing the variation of Λ as a function of the fill fraction, α, and detonable-to-inert mixture density ratio, ρ_d/ρ_i. Because the scaling for the non-dimensional gasdynamic blowdown time, $\tau = t_f/t_{f,full}$, was used to derive the expression for Λ, the density ratio in Fig. 6.18 is limited to $\rho_d/\rho_i \geq 1$. It is evident from Fig. 6.18 that the benefits of partial filling on the normalized time-averaged thrust are more pronounced for large acoustic impedance of the inert mixture, namely, small ρ_d/ρ_i. Similar to the total impulse ratio, in the case of sub-atmospheric PDE operation, the benefit of partial filling becomes drastically diminished as ρ_d/ρ_i, or blowdown pressure ratio, increases. As demonstrated in Eq. (6.11) and Fig. 6.18, the normalized time-averaged thrust approaches $\alpha^{5/7}$ in the limit where $\rho_d/\rho_i \to \infty$. This is a characteristic of Eq. (6.11), and consistent with all previous discussion regarding the reduction in acoustic impedance of the inert mixture.

In summary, the current work provides several nondimensional scaling laws for the purposes of modeling the propulsive performance of partially-filled PDEs. In the development of these performance scaling relations, the results from Sato et al. [98] were used, and

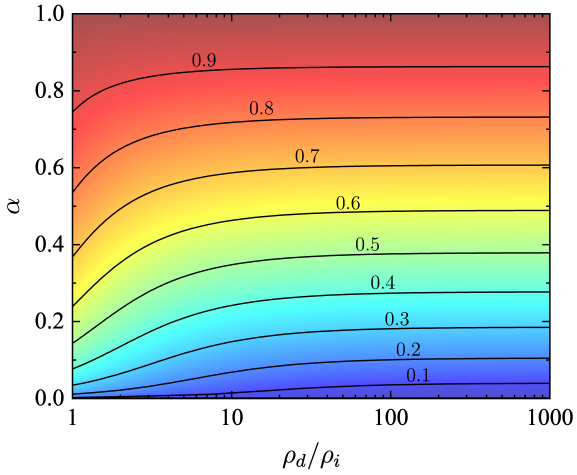

Figure 6.18. Contour plot of normalized time-averaged thrust $\bar{F}/\bar{F}_{full}$ in Eq. (6.10) vs. fill fraction and detonable-to-inert mixture density ratio.

it is therefore important that a range of applicability be mentioned for the scaling laws in Eqs. (6.7), (6.8), and (6.10). As mentioned in [98], the normalized specific impulse scaling law for η is limited to mass fractions of $0.05 < Z < 1.0$, as the model approaches infinity in the limit of zero mass fraction. However, for the normalized impulse and time-averaged thrust ratios in Eqs. (6.7) and (6.8), the mass fraction range can be extended to $0 \leq Z \leq 1$, as the scaling approaches zero in the limit of zero mass fraction, which is consistent with experimental observations. However, it is cautioned that very small values of ρ_d/ρ_i, i.e., large inert acoustic impedance, and low fill fractions may result in predictions that deviate from experiments. This is purely a consequence of the contact surface trapping becoming more severe, which changes the performance characteristics and mechanism of the partial-fill effect. Lastly, the simplified scaling for normalized time-averaged thrust in Eq. (6.11) is applicable over the mass fraction range of, $0 \leq Z \leq 1$, with the constraint that $\rho_d/\rho_i \gtrsim 1$.

For the purposes of completeness, Table 6.1 provides a comparison of the scaling laws for η, Ω, and Λ with the results of the MOC model for partially-filled PDEs with operating conditions that were not discussed in the current study. This includes partially-filled PDEs operating with H_2–O_2 and CH_4–O_2 detonable propellants at various equivalence ratios, fill

fractions, blowdown pressure ratios, and inert mixtures. The scaling laws for η and Ω are shown to accurately represent the results from the MOC model over these wide operating conditions, including the cases of krypton as the inert gas, which has a very high acoustic impedance. Further, the scaling law for Λ is only shown to accurately model the results of the MOC model for the conditions where $\rho_d/\rho_i \gtrsim 1$. Finally, it is noted that the partially-filled PDE performance can be recovered in its entirety with the scaling laws in Eqs. (6.3), (6.6), and (6.10), provided the fully-filled analytical performance model of Ch. 5 (or those of [65] and [66, 67]) is used to calculate the denominator of η, Ω, and Λ, respectively.

Table 6.1. Comparison of scaling laws for η (Eq. (6.3)), Ω (Eq. (6.6)), and Λ (Eq. (6.10)) with MOC at various operating conditions.

Propellant/Inert	ϕ	α	ψ	ρ_d/ρ_i	η	$\frac{I_{sp}}{I_{sp,full}}$	Ω	$\frac{I_t}{I_{t,full}}$	% Diff. [a]	Λ	$\frac{\bar{F}}{\bar{F}_{full}}$	% Diff.
H_2–O_2/air	0.5	0.5	1	0.589	1.642	1.657	0.821	0.829	0.9	0.869	0.812	6.6
H_2–O_2/air	1.0	0.5	1	0.416	1.845	1.833	0.922	0.916	0.6	0.944	0.862	8.7
H_2–O_2/air	2.0	0.5	1	0.278	2.145	2.096	1.072	1.048	2.3	1.051	0.913	13.1
H_2–O_2/air	1.0	0.25	1	0.416	2.865	2.975	0.716	0.744	3.8	0.788	0.623	20.9
H_2–O_2/air	1.0	0.75	1	0.416	1.342	1.360	1.006	1.020	1.4	1.005	0.953	5.1
H_2–O_2/air	1.0	0.5	10	4.163	1.114	1.146	0.557	0.573	2.9	0.658	0.624	5.2
H_2–O_2/air	1.0	0.5	100	41.63	1.012	1.095	0.506	0.547	8.2	0.615	0.593	3.5
H_2–O_2/He	1.0	0.5	1	3.000	1.155	1.164	0.577	0.528	0.8	0.675	0.660	2.3
H_2–O_2/Ar	1.0	0.5	1	0.301	2.080	2.105	1.040	1.053	1.2	1.028	0.933	9.3
H_2–O_2/Kr	1.0	0.5	1	0.143	2.824	2.763	1.412	1.381	2.2	1.280	1.094	14.5
CH_4–O_2/air	0.5	0.5	1	0.998	1.415	1.440	0.707	0.720	1.8	0.781	0.768	1.6
CH_4–O_2/air	1.0	0.5	1	0.925	1.443	1.469	0.721	0.735	1.8	0.792	0.773	2.4
CH_4–O_2/air	2.0	0.5	1	0.833	1.484	1.500	0.742	0.750	1.1	0.808	0.780	3.4
CH_4–O_2/air	1.0	0.25	1	0.925	2.060	2.133	0.515	0.533	3.5	0.623	0.617	0.9
CH_4–O_2/air	1.0	0.75	1	0.925	1.166	1.200	0.875	0.900	2.9	0.909	0.867	4.6
CH_4–O_2/air	1.0	0.5	10	9.247	1.053	1.107	0.526	0.554	5.2	0.632	0.606	4.2
CH_4–O_2/air	1.0	0.5	100	92.47	1.005	1.069	0.503	0.535	6.4	0.612	0.588	3.9
CH_4–O_2/He	1.0	0.5	1	6.665	1.072	1.068	0.536	0.534	0.4	0.641	0.638	0.4
CH_4–O_2/Ar	1.0	0.5	1	0.668	1.580	1.642	0.790	0.821	3.9	0.845	0.829	2.0
CH_4–O_2/Kr	1.0	0.5	1	0.318	2.035	2.026	1.017	1.013	0.4	1.012	0.937	7.4

[a] η and Ω share the same percent error with the MOC results.

6.2 Pulse Detonation Engines with Diverging Nozzles

In this section, the single-cycle performance characteristics of PDEs equipped with diverging nozzles are discussed, including the effects of nozzle expansion area ratio, engine blowdown pressure ratio, and inert mixture acoustic impedance. Subsequently, a parametric study is conducted to identify the general performance map of PDEs fitted with diverging nozzles, and the optimum specific impulse, nozzle expansion area ratio, and blowdown pressure ratio combinations are discussed. The effects of inert mixture are also included to highlight the influence of the partial-fill effect on blowdown pressure ratios near unity. Finally, an analytical performance model for a PDE with a quasi-steady nozzle is developed. This model is compared with the results from the MOC results at various blowdown pressure ratios in order to highlight the significant performance difference between idealized quasi-steady PDE nozzles, and those whereby the unsteady nozzle starting process of a PDE is taken into consideration.

6.2.1 Effects of Nozzle Expansion Area Ratio

It is of interest to first investigate the effects of varying the nozzle expansion area ratio, ϵ, at a fixed blowdown pressure ratio, ψ, in order to highlight the gasdynamic processes within the thrust chamber flow field that govern the observed performance of a given PDE nozzle. Additionally, this will prove to be useful for interpreting the performance results of larger parametric studies in the following subsections. For this, a PDE operating with stoichiometric H_2–O_2 detonable propellant with air as the inert mixture is utilized. Additionally, the detonable propellant is initially at 1 atm and 300 K, while the ambient air is initially held at 0.1 atm and 300 K, yielding a $\psi = 10$. The PDE is comprised of a combustion chamber of length $L_t = 0.7$ m, and a conical diverging nozzle of length $L_n = 0.3$ m, yielding a thrust chamber-to-total length ratio of $\alpha_0 = 0.7$. Moreover, the nozzle expansion area ratio is varied from $\epsilon = 1$–10, by increasing the nozzle half-angle from 0–10.2 degrees,

such that the case of a 0 degree half-angle corresponds to a straight-extension nozzle, or simply a partially-filled PDE with $\alpha = 0.7$.

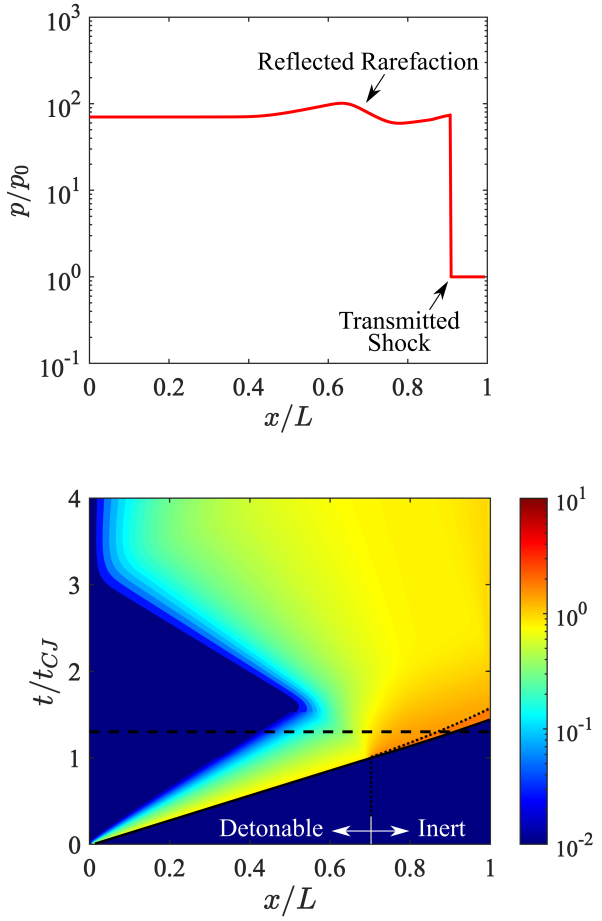

Figure 6.19. Non-dimensional x–t diagram of Mach number contour (bottom) and pressure distribution on constant dashed t–line (top) for $2H_2$–O_2 propellant and air as the inert with $\psi = 10$ and $\epsilon = 1$. Note, the detonation/transmitted shock and contact surface paths are denoted with the solid and dotted lines, respectively.

The starting flow field for $\epsilon = 1$ is shown in the form of a non-dimensional x–t diagram Mach number contour in Fig. 6.19. In this figure t_{CJ} is defined by the time required for the detonation wave to propagate from the thrust wall to the nozzle entrance, namely, $t_{CJ} =$

L_t/W_{CJ}. Similarly, the thrust chamber pressure distribution corresponds to the constant dashed t–line in the x–t diagram Mach number contour. In this case, the starting flow field is characterized by the partially-filled PDE gasdynamic processes described in the previous section, such that the flow field evolution begins with a transmitted shock and reflected rarefaction wave, since the ratio of acoustic impedance across the contact surface is $z_0/z_1 = 0.25$. Consequently, the ratio of incident transmitted shock to detonation wave velocity is $W_T/W_{CJ} = 1.03$, and the flow immediately behind the transmitted shock is initially moving supersonic with a Mach number of roughly 1.8 with respect to the laboratory frame. In fact, unsteady supersonic flow develops behind the transmitted shock and contact surface in the non-simple region where the Taylor and secondary rarefactions interact; however, the supersonic flow in this region only persists for a small fraction of the overall cycle time since the straight-extension nozzle does not feature geometric expansion to continue accelerating the gas. As a result, the flow in the straight-extension nozzle quickly returns subsonic for the remainder of the gasdynamic blowdown process. Moreover, starting at $t/t_{CJ} \approx 2$, the exhausting rarefaction wave enters the PDE thrust chamber and accelerates the gas to a sonic choking condition on the chamber exit plane. As discussed in the previous section, the exhausting rarefaction is the mechanism that eventually returns the chamber pressure back to the ambient condition.

Similarly, the starting flow field for $\epsilon = 3$ is shown in the form of a non-dimensional x–t diagram Mach number contour in Fig. 6.20, where the thrust chamber pressure distribution corresponds to the constant dashed t–line on the x–t diagram. In this case, the nozzle half-angle is 3.5 degrees, which yields a starting flow field that is drastically different from that when $\epsilon = 1$ and the nozzle half-angle is 0 degrees. In fact, a sonic choking condition is established at the inlet of the nozzle at $x/L = 0.7$ due to the geometric area change in the nozzle [118]. As mentioned in Ch. 2, this creates a condition whereby the flow field in the constant-area portion of the thrust chamber is unaffected by the nozzle flow field, and the flow field upstream of the nozzle is identical to that of a fully-filled PDE for

$\psi = 10$. Similar to the previous case, the ratio of acoustic impedance across the contact surface is $z_0/z_1 = 0.25$, which results in a reflected rarefaction that is coincident with the exhausting rarefaction that together propagate into the constant-area portion of the thrust chamber. Likewise, the ratio of incident transmitted shock to detonation wave velocity is $W_T/W_{CJ} = 1.03$, and a region of supersonic flow with a Mach number of roughly 1.8 is immediately established behind the transmitted shock. However, unlike the case of $\epsilon = 1$, supersonic flow continues to rapidly develop behinds the transmitted shock and contact surface due to the geometric expansion in the nozzle. In fact, the gas is expanded so rapidly with $\epsilon = 3$ that an unsteady secondary shock wave forms behind the contact surface in order to elevate the pressure of the expanding gas to a condition that nearly matches that at the contact surface behind the transmitted shock. Consequently, the unsteady secondary shock wave reduces the initially supersonic flow emanating from the nozzle entrance to a region consisting of nearly sonic flow, which is bounded by the secondary shock and contact surface. Eventually, the transient nozzle starting process terminates with the exit of the secondary shock from the nozzle at $t/t_{CJ} \approx 2.5$, and the nozzle flow returns entirely supersonic with an exit Mach number of roughly 2.9.

Lastly, the starting flow field for $\epsilon = 10$ is shown in the form of a non-dimensional x–t diagram Mach number contour in Fig. 6.21, where the thrust chamber pressure distribution corresponds to the constant dashed t–line on the x–t diagram. In this case, the nozzle half-angle is 10.2 degrees, which yields a starting flow field that is similar to the case of $\epsilon = 3$, although with severe over-expansion. As before, a sonic choking condition is established at the inlet of the nozzle at $x/L = 0.7$ due to the geometric area change in the nozzle, whereby the flow field in the constant-area portion of the thrust chamber is unaffected by the nozzle flow field. Similarly, for $\psi = 10$, the ratio of acoustic impedance across the contact surface is $z_0/z_1 = 0.25$, which results in a reflected rarefaction that is coincident with the exhausting rarefaction that together propagate into the constant-area portion of the thrust chamber. Likewise, the ratio of incident transmitted shock to detonation wave velocity is

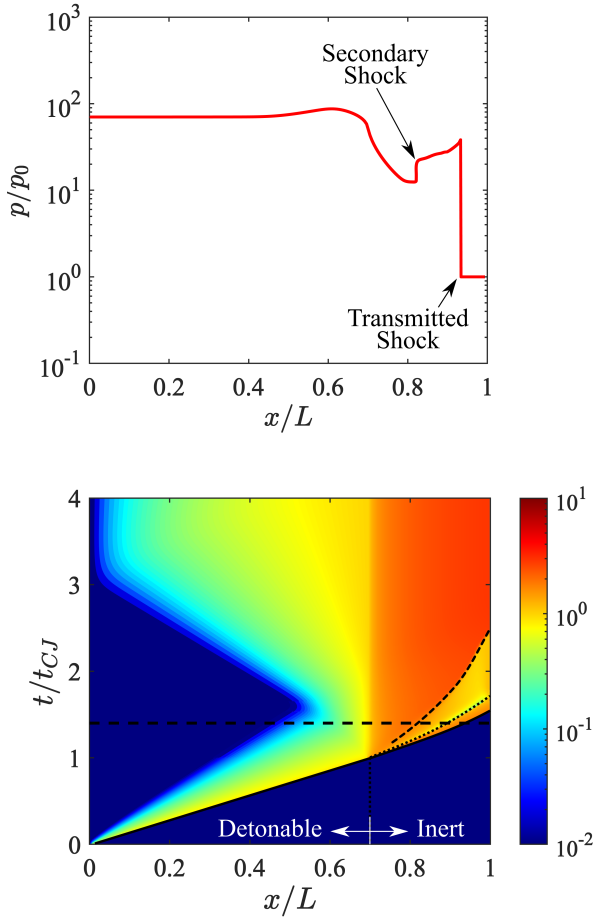

Figure 6.20. Non-dimensional x–t diagram of Mach number contour (bottom) and pressure distribution on constant dashed t–line (top) for $2H_2$–O_2 propellant and air as the inert with $\psi = 10$ and $\epsilon = 3$. Note, the detonation/transmitted shock, contact surface, and secondary shock paths are denoted with the solid, dotted, and dashed lines, respectively.

$W_T/W_{CJ} = 1.03$, and a region of supersonic flow with a Mach number of roughly 1.8 is immediately established behind the transmitted shock. Unlike the case of $\epsilon = 3$, the gas is expanded so rapidly that a relatively strong secondary shock wave forms in the nozzle in order to match the pressure condition at the contact surface behind the transmitted shock. In fact, as shown in Figs. 6.20 and 6.21, the secondary shock in this case features a pressure ratio that is roughly 6 times that of when $\epsilon = 3$ at $t/t_{CJ} \approx 1.5$. As a result, the region of

flow that is bounded by this much stronger secondary shock wave and the contact surface is entirely subsonic, a consequence of the severe nozzle over-expansion. Once the contact surface reaches the nozzle exit at $t/t_{CJ} \approx 2$, a secondary exhausting rarefaction wave enters the nozzle, which serves to accelerate the gas to a choking condition on the nozzle exit plane. Further, this secondary exhausting rarefaction eventually reaches the secondary shock and rapidly accelerates the shock towards the nozzle exit. As such, the transient nozzle starting process terminates with the exit of the secondary shock from the nozzle at $t/t_{CJ} \approx 2.8$, and the nozzle flow returns entirely supersonic with an exit Mach number of roughly 4.1.

The transient variation of thrust for the cases of $\epsilon = 1$, 2, 3, 6, and 10 at $\psi = 10$ are shown in Fig. 6.22(a), respectively. Note that the thrust force has been normalized by $A_0 p_1$, namely, the product of thrust wall area and initial propellant pressure. This transient variation in thrust is obtained by application of Eq. (4.12) at each time step, such that the contribution from all of the internal thrust surfaces are accounted for. It is noted that the thrust force is identical for each case of ϵ up until $t/t_{CJ} = 1$, namely, the moment at which the detonation wave reaches the nozzle entrance at $x/L = 0.7$. In the case of $\epsilon = 1$, the PDE thrust profile simply mimics that of a partially-filled PDE with a fill fraction of $\alpha = 0.7$. Additionally, this is the only condition where the nozzle contributes no additional thrust as the half-angle is fixed at zero, and all of the thrust comes from the pressure history at the thrust wall. In this case, it is evident that the secondary and exhausting rarefaction waves reach the thrust wall at $t/t_{CJ} \approx 3$ and $t/t_{CJ} \approx 8$, respectively. Alternatively, in the cases of $\epsilon > 1$, the thrust profiles experience a sharp rise in thrust just after $t/t_{CJ} = 1$, due to the transmitted shock wave entering the nozzle and distributing a high post-shock pressure along the nozzle wall. In fact, the maximum peak in thrust corresponds to the time at which the maximum distributed pressure is observed on the nozzle wall, which is due to the combined effects of the transmitted and secondary shock waves in the nozzle, and usually occurs before the transmitted shock reaches the nozzle exit. As such, it follows that the nozzle with the largest peak thrust corresponds to the nozzle with the largest

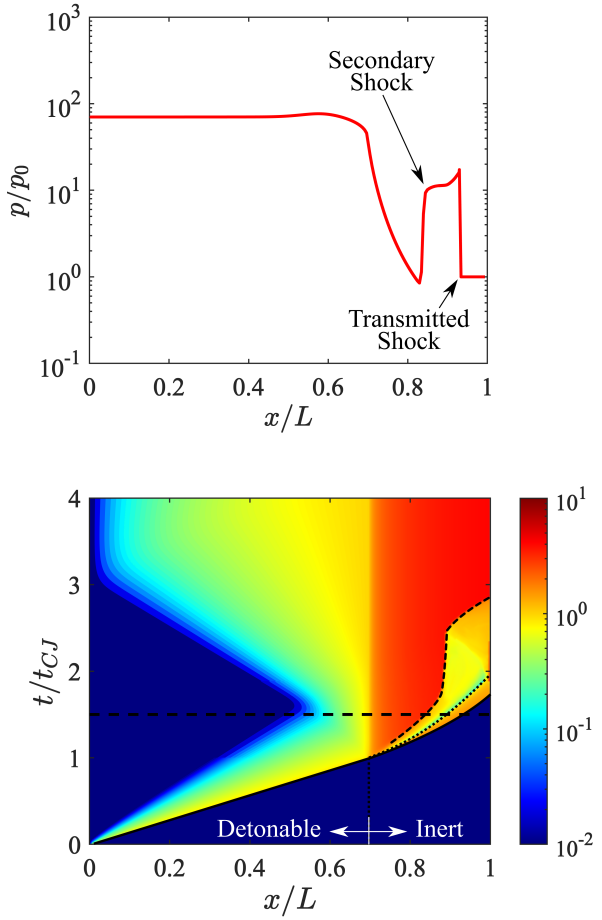

Figure 6.21. Non-dimensional x–t diagram of Mach number contour (bottom) and pressure distribution on constant dashed t–line (top) for $2H_2$–O_2 propellant and air as the inert with $\psi = 10$ and $\epsilon = 10$. Note, the detonation/transmitted shock, contact surface, and secondary shock paths are denoted with the solid, dotted, and dashed lines, respectively.

degree of over-expansion, namely, $\epsilon = 10$, whereby the strongest secondary shock is formed. Although this appears to serve as a performance benefit in the early stages of the cycle, it will be shown later that this severe over-expansion ultimately leads to a significant loss in the latter part of the cycle.

Once the transmitted and secondary shocks exit the nozzle, the pressure begins to rapidly decay in the nozzle due to the passage of the Taylor rarefaction wave. In the cases of

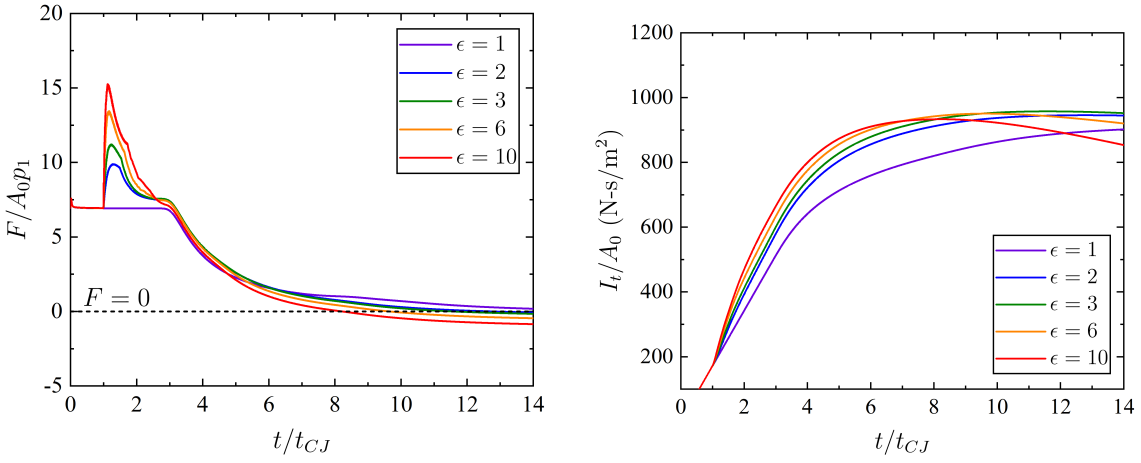

Figure 6.22. (a) Normalized thrust and (b) total impulse per unit thrust-wall area at $\psi = 10$ for a PDE operating with $2H_2$–O_2 propellant and air as the ambient at various ϵ.

$\epsilon = 2$ and 3, this rapid decay in thrust is subsequently followed by a secondary plateau, which is caused by the establishment of nearly quasi-steady flow in the nozzle. Additionally, this secondary plateau only lasts until the moment when the coincident reflected and exhausting rarefaction reach the head end of the chamber at $t/t_{CJ} \approx 3$, whereby a rapid decay in pressure at the thrust wall takes place. Note that this intermediate plateau is not entirely reached in the cases of $\epsilon = 6$ and 10, as the strong secondary shock in these cases only exits the nozzle at approximately the same time at which the coincident reflected and exhausting rarefaction reach the head end of the chamber. As such, the rapid decay in pressure in the nozzle and at the thrust wall occur at nearly the same time. For $t/t_{CJ} \gtrsim 3$, the continued decay in thrust is a result of the exhausting rarefaction wave slowly returning the pressure in the thrust chamber back to the ambient condition. Note that for some of the cases of ϵ, the net thrust drops below the zero thrust line in Fig. 6.22(a). This is a direct result of large over-expansion in the nozzle, which indicates that the resultant force on the nozzle wall from the wall pressure distribution is not able to overcome that from the ambient condition. Hence, a negative thrust is observed for a sizable portion of the cycle, as in the cases of $\epsilon = 6$ and 10, respectively.

The temporal variation in total impulse for these respective cases is shown in Fig. 6.22(b). In this case, the impulse has been scaled by the thrust wall area. As shown in Fig. 6.22(b), the maximum total impulse occurs for the case of $\epsilon = 3$, which indicates that this nozzle expansion area ratio is near the optimum for a blowdown pressure ratio of $\psi = 10$, and $\alpha_0 = 0.7$. In this case, only a slight negative thrust is obtained towards the end of the cycle, which correlates to a minor downturn in total impulse near $t/t_{CJ} \approx 12.5$. In fact, as will be shown in the coming subsections, the optimum nozzle expansion area ratio for $\psi = 10$ and $\alpha_0 = 0.7$, occurs when $\epsilon = 3.08$, whereby the thrust curve asymptotically approaches the zero thrust line in Fig. 6.22(a). Alternatively, as shown in the case of $\epsilon = 10$, the maximum total impulse occurs once the thrust curve passes through the zero thrust line at $t/t_{CJ} \approx 8$ in Fig. 6.22(a). Consequently, the remaining total impulse proceeds into a downturn, since the over-expansion in the nozzle yields a nozzle wall pressure distribution that is less than the ambient condition. As a result, the case of $\epsilon = 10$ yields a final total impulse that is 11 percent lower than the case of $\epsilon = 3$. Additionally, for the case of $\epsilon = 1$, the maximum impulse occurs once the pressure history on the thrust wall returns to the ambient condition, which results in an impulse that is roughly 4 percent lower than that of $\epsilon = 3$. Hence, it follows that at $\psi = 10$ and $\alpha_0 = 0.7$, the best performance of a PDE is achieved with a diverging nozzle that features an expansion area ratio of approximately $\epsilon = 3$. Additionally, it is worth noting that this optimum nozzle case still features a small degree of over-expansion during the unsteady nozzle starting flow process, whereby a secondary shock momentarily forms within the nozzle.

6.2.2 Effects of Blowdown Pressure Ratio

It is also of interest to investigate the effects of varying the blowdown pressure ratio, ψ, at a fixed nozzle expansion area ratio, ϵ, in order to highlight the gasdynamic processes within the thrust chamber flow field that govern the observed performance of a given PDE nozzle. As in the previous subsection, this will prove to be useful for interpreting the

performance results of larger parametric studies in the following sections. For this, a PDE operating with stoichiometric H_2–O_2 detonable propellant with air as the inert mixture is utilized. Additionally, the detonable propellant is initially at 1 atm and 300 K, while the ambient air is varied from 1–0.01 atm at 300K, yielding a blowdown pressure ratio range of $\psi = 1$–100. As before, the PDE is comprised of a combustion chamber of length $L_t = 0.7$ m, and a conical diverging nozzle of length $L_n = 0.3$ m, yielding a thrust chamber-to-total length ratio of $\alpha_0 = 0.7$. Moreover, the nozzle expansion area ratio is fixed at $\epsilon = 4$ with a half-angle of 4.8 degrees.

The starting flow field for $\psi = 4$ is shown in the form of a non-dimensional x–t diagram Mach number contour in Fig. 6.23. Note, as before, t_{CJ} is defined by the time required for the detonation wave to propagate from the thrust wall to the contact surface location at the nozzle entrance, $t_{CJ} = L_t/W_{CJ}$. Similarly, the thrust chamber pressure distribution corresponds to the constant dashed t–line in the x–t diagram Mach number contour. In this case, a weak shock reflects from the contact surface with an initial pressure ratio of 1.11 as the acoustic impedance ratio across the contact surface is $z_0/z_1 = 1.24$. As such, the ratio of incident transmitted shock to detonation wave velocity is $W_T/W_{CJ} = 0.52$, and the flow immediately behind the transmitted shock is initially moving supersonic with a Mach number of 1.6 with respect to the laboratory frame. It is noted that a nozzle with $\epsilon = 4$ at $\psi = 1$ yields a starting nozzle flow field that is severely over-expanded, in that a strong secondary shock wave forms in the nozzle. In fact, as shown in Fig. 6.23, the secondary shock features a pressure ratio of nearly 4 in the early stages of its formation in the nozzle at $t/t_{CJ} \approx 2$. Consequently, the flow field bounded by the secondary shock and contact surface is entirely subsonic until the moment when the contact surface exits the nozzle at $t/t_{CJ} \approx 3.1$, whereby a secondary exhausting rarefaction enters the nozzle and accelerates the gas to a choking condition on the nozzle exit plane. Similarly, the secondary exhausting rarefaction interacts with the secondary shock wave and accelerates the shock out of the nozzle at $t/t_{CJ} \approx 4.5$. Moreover, once the secondary shock exits the nozzle, the unsteady

nozzle starting process is terminated and the nozzle returns entirely supersonic with an exit Mach number of roughly 3.2.

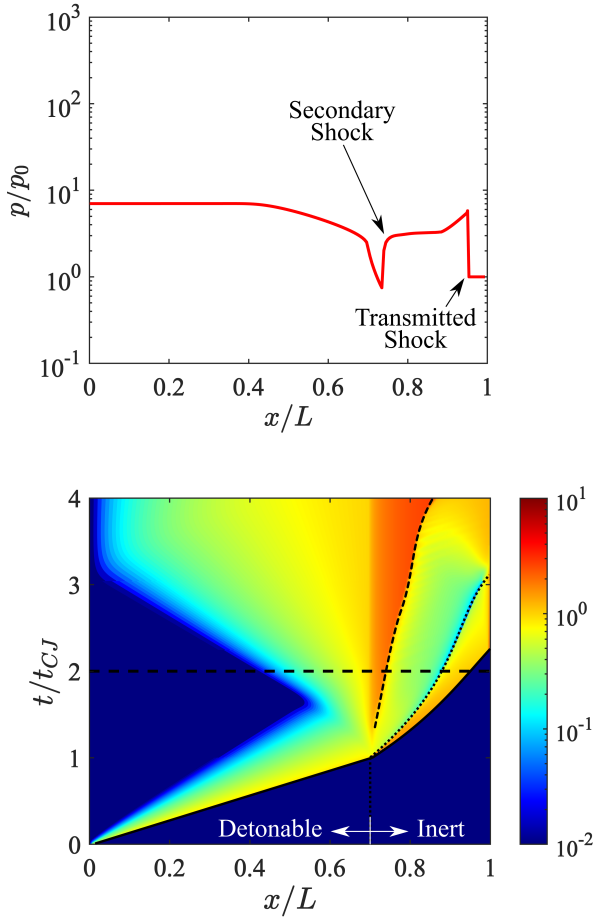

Figure 6.23. Non-dimensional x–t diagram of Mach number contour (bottom) and pressure distribution on constant dashed t–line (top) for $2H_2$–O_2 propellant and air as the inert with $\psi = 1$ and $\epsilon = 4$. Note, the detonation/transmitted shock, contact surface, and secondary shock paths are denoted with the solid, dotted, and dashed lines, respectively.

Similarly, the starting flow field for $\psi = 10$ is shown in the form of a non-dimensional x–t diagram Mach number contour in Fig. 6.24, where the thrust chamber pressure distribution corresponds to the constant dashed t–line on the x–t diagram. In this case, a

rarefaction wave reflects from the contact surface as the acoustic impedance ratio across the contact surface is $z_0/z_1 = 0.25$. As such, the ratio of incident transmitted shock to detonation wave velocity is $W_T/W_{CJ} = 1.03$, and the flow immediately behind the transmitted shock is initially moving supersonic with a Mach number of 1.8 with respect to the laboratory frame. It is noted that a nozzle with $\epsilon = 4$ at $\psi = 10$ yields a starting nozzle flow field that is slightly over-expanded compared to the results from the previous subsection. In fact, it was shown there that the optimum nozzle features an expansion area ratio of $\epsilon \approx 3$. As such a strong secondary shock wave forms in the nozzle starting flow field, where a pressure ratio of nearly 2.7 is reached during the early stages of its formation in the nozzle at $t/t_{CJ} \approx 1.5$. Consequently, the flow field bounded by the secondary shock and contact surface is slightly subsonic until the moment when the contact surface exits the nozzle at $t/t_{CJ} \approx 1.7$, whereby a secondary exhausting rarefaction enters the nozzle and accelerates the gas to a choking condition on the nozzle exit plane. As before, the secondary exhausting rarefaction interacts with the secondary shock wave and accelerates the shock out of the nozzle at $t/t_{CJ} \approx 2.5$, such that the nozzle flow field returns entirely supersonic with an exit Mach number of roughly 3.2.

Lastly, the starting flow field for $\psi = 100$ is shown in the form of a non-dimensional x–t diagram Mach number contour in Fig. 6.25, where the thrust chamber pressure distribution corresponds to the constant dashed t–line on the x–t diagram. Similar to the previous case, a rarefaction wave reflects from the contact surface as the acoustic impedance ratio across the contact surface is $z_0/z_1 = 0.041$. As such, the ratio of incident transmitted shock to detonation wave velocity is $W_T/W_{CJ} = 1.7$, and the flow immediately behind the transmitted shock is initially moving supersonic with a Mach number of nearly 1.9 with respect to the laboratory frame. It is noted that a nozzle with $\epsilon = 4$ at $\psi = 100$ yields a starting nozzle flow field that is primarily under-expanded, in that a very weak secondary shock wave briefly forms in the nozzle and exits within a small fraction of the overall cycle time. As such, the flow field bounded by the secondary shock and contact surface is only

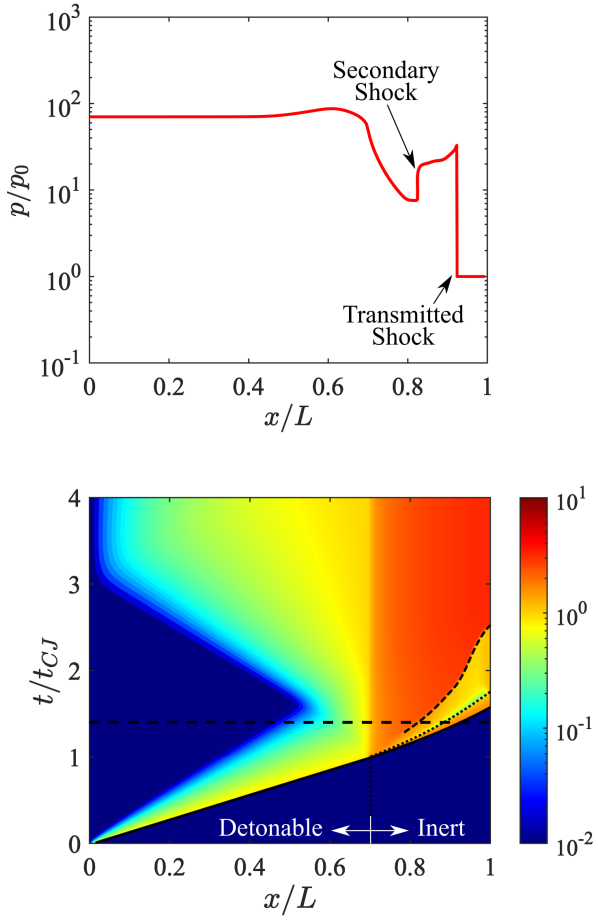

Figure 6.24. Non-dimensional x–t diagram of Mach number contour (bottom) and pressure distribution on constant dashed t–line (top) for $2H_2$–O_2 propellant and air as the inert with $\psi = 10$ and $\epsilon = 4$. Note, the detonation/transmitted shock, contact surface, and secondary shock paths are denoted with the solid, dotted, and dashed lines, respectively.

slightly supersonic until the secondary shock exits the nozzle at $t/t_{CJ} \approx 1.4$, in which case the nozzle establishes complete supersonic flow with an exit Mach number of roughly 3.2. In fact, it will be shown in the following subsection that the optimum blowdown pressure ratio for a nozzle of $\epsilon = 4$ is roughly $\psi = 17$, and the optimum nozzle expansion area ratio for $\psi = 100$ is roughly $\epsilon = 17$. Hence, it can be said that this nozzle configuration yields a

mostly under-expanded flow despite the formation of a weak secondary shock in the nozzle starting process.

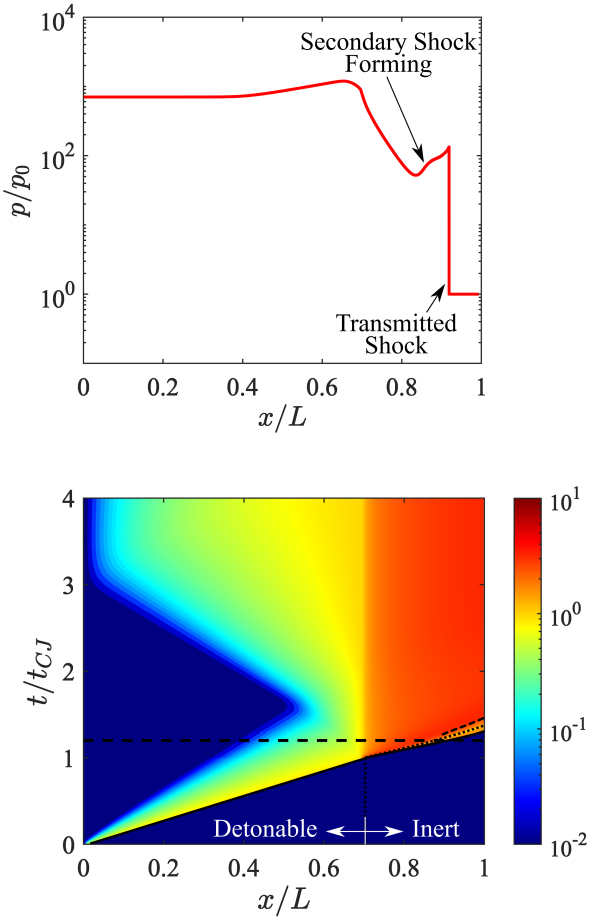

Figure 6.25. Non-dimensional x–t diagram of Mach number contour (bottom) and pressure distribution on constant dashed t–line (top) for $2H_2$–O_2 detonable propellant and air as the inert with $\psi = 100$ and $\epsilon = 4$. Note, the detonation/transmitted shock, contact surface, and secondary shock paths are denoted with the solid, dotted, and dashed lines, respectively.

The transient variation of thrust for the cases of ψ = 1, 2, 5, 10, 20, 50, and 100 for $\epsilon = 4$ are shown in Fig. 6.26(a), respectively. Note that the thrust force has been normalized by $A_0 p_1$, namely, the product of thrust wall area and initial propellant pressure.

As before, the thrust profiles experience a sharp rise in thrust just after $t/t_{CJ} = 1$, due to the transmitted shock wave entering the nozzle and distributing a high post-shock pressure along the nozzle wall. Similarly, the maximum peak in thrust corresponds to the time at which the maximum distributed pressure is observed on the nozzle wall, which is due to the combined effects of the transmitted and secondary shock waves in the nozzle, and usually occurs before the transmitted shock reaches the nozzle exit. As such, it follows that the nozzle with largest peak thrust corresponds to the nozzle with the largest degree of over-expansion, namely, $\psi = 1$. Moreover, once the transmitted and secondary shocks exit the nozzle, the pressure begins to rapidly decay in the nozzle due to the passage of the Taylor rarefaction wave. In the cases of $\psi = 10$, 20, 50, and 100, this rapid decay in thrust is subsequently followed by a secondary plateau, which is caused by the establishment of nearly quasi-steady flow in the nozzle. Additionally, this secondary plateau only lasts until the moment when the coincident reflected and exhausting rarefaction reach the head end of the chamber at $t/t_{CJ} \approx 3$, causing a rapid decay in pressure at the thrust wall. Note that this intermediate plateau is not entirely reached in the cases of $\psi = 1$, 2, and 5, as the fairly strong secondary shock in these cases only exits the nozzle at approximately the same time at which the coincident reflected and exhausting rarefaction reach the head end of the chamber. As such, the rapid decay in pressure in the nozzle and at the thrust wall occur at nearly the same time. For $t/t_{CJ} \gtrsim 3$, the continued decay in thrust is a result of the exhausting rarefaction wave slowly returning the pressure in the thrust chamber back to the ambient condition. As previously mentioned, some of the cases of ψ drop below the zero thrust line in Fig. 6.26(a). This is a direct result of large over-expansion that occurs in the nozzle, which results in a negative resultant thrust for a sizable portion of the cycle, such as in the cases of $\psi = 1$, 2, and 5, respectively.

Finally, the temporal variation in total impulse for these respective cases is shown in Fig. 6.26(b). Similar to the previous cases, the impulse has been scaled by the thrust wall area. As shown in Fig. 6.26(b), the total impulse at the end of the cycle continually

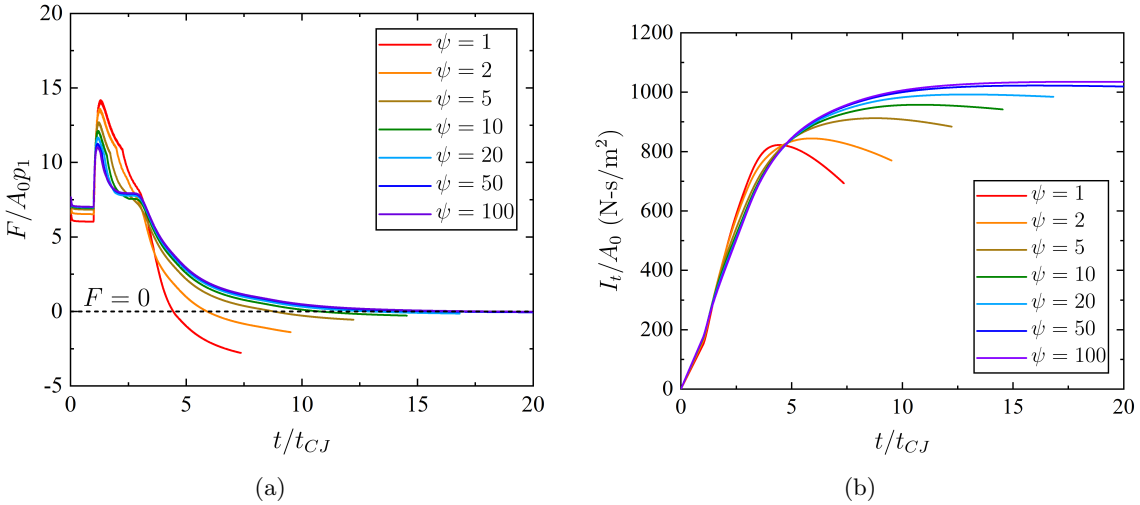

Figure 6.26. (a) Normalized thrust and (b) total impulse per unit thrust-wall area at various ψ for a PDE operating with $2H_2$–O_2 propellant and air as the ambient and with $\epsilon = 4$.

increases with increasing ψ. This is to be expected as the majority of the nozzle flow during the cycle is transitioning from over-expanded, nearly perfectly expanded, to under-expanded as ψ varies from 1–100 at a fixed nozzle expansion area ratio of $\epsilon = 4$. Despite this, it is noted that severe over-expansion is present in the case of $\psi = 1$, as the thrust curve drops well below the zero thrust line in Fig. 6.26(a), which leads to the downturn in total impulse in Fig. 6.26(b). Similarly, this occurs in the cases of $\psi = 2$, 5, and 10, although to a lesser degree. The first case to nearly terminate at the maximum total impulse occurs when $\psi = 20$. This is a direct result of the nozzle being nearly perfectly expanded for a majority of the cycle in this case, as mentioned in the previous discussion. It is noted that the severe over-expansion in the case of $\psi = 1$ yields a final total impulse that is nearly 34 percent less than that of the nearly perfectly expanded case of $\psi = 20$. Lastly, the cases of $\psi = 50$ and 100 yield mostly under-expanded nozzle flow during the gasdynamic blowdown of the PDE, such that the maximum total impulse asymptotically approaches the limiting case when $\psi \to \infty$.

6.2.3 General Nozzle Performance Characteristics

The previous subsections discussed the gasdynamic flow field and PDE performance for two separate nozzle cases, first by fixing the blowdown pressure ratio and varying the nozzle expansion area ratio, and second by fixing the nozzle expansion area ratio and varying the blowdown pressure ratio. In the current subsection, it is of interest to show the generalized performance trends of PDEs with diverging nozzles by simultaneously varying both the nozzle expansion area ratio, ϵ, and blowdown pressure ratio, ψ. For this, PDEs operating with stoichiometric H_2–O_2 and C_2H_4–O_2 detonable propellants initially at 1 atm and 300 K are utilized. Moreover, the ambient is varied between air and helium to demonstrate the effects of inert mixture acoustic impedance at lower blowdown pressure ratios. In this case, the ambient temperature is kept at 300 K and the ambient pressure is varied from 1–0.005 atm, yielding a blowdown pressure ratio range of 1–200. Similarly, the PDE is comprised of a combustion chamber of length $L_t = 0.7$ m, and a conical diverging nozzle of length $L_n = 0.3$ m, yielding a thrust chamber-to-total length ratio of $\alpha_0 = 0.7$.

The general idealized performance trends for stoichiometric H_2–O_2 detonable propellant are shown in Figs. 6.27(a) and 6.27(b) for air and helium as the ambient, respectively. One of the more important results demonstrated in Fig. 6.27(a) is that a diverging nozzle will not always yield the optimum performance solution for a PDE, especially at lower blowdown pressure ratios. For instance, when $\psi = 1$ and 2, the optimum performance is achieved when the nozzle features an expansion area ratio of $\epsilon = 1$, namely, a partially-filled PDE. In this case, the performance benefit from the partial-fill effect is superior to any performance gain that can be achieved by adding a nozzle with $\epsilon > 1$. In fact, as in the case of $\psi = 1$ and 2, the addition of a nozzle with a half-angle greater than zero results in a predominantly over-expanded nozzle flow with an associated performance loss. In the case of $\psi = 5$, the benefit from the partial-fill effect only remains superior up until $\epsilon = 2$, in which case the nozzle outperforms the partially-filled PDE; however, the performance gain is less than 1 percent. Most important, it is shown in Fig. 6.27(a) that in all other cases

where $\psi > 5$, the addition of a diverging nozzle becomes very advantageous for increasing the overall performance of the PDE. As discussed in the previous section, the performance benefit of partially filling the PDE thrust chamber becomes rapidly diminished as the ambient pressure is reduced, which causes the acoustic impedance of the inert mixture to rapidly decrease. To demonstrate this, Fig. 6.27(b) shows the same parametric sweep for nozzles, but with helium as the inert mixture. In this case, it is very evident that reducing the acoustic impedance of the inert mixture by a factor of roughly 3.4, by simply changing the inert mixture from air to helium, drastically reduces the performance gains from partial filling at small ψ. Simultaneously, reducing the acoustic impedance of the inert mixture helps demonstrate the benefit of fitting a properly designed nozzle to a PDE in situations where the acoustic impedance does not strongly influence the results. In fact, in the cases of air and helium as the inert mixture, the performance benefit of a properly designed nozzle becomes evident at only $\psi = 5$, and $\psi = 2$, respectively. Hence, at a given ψ, it is apparent that there exists an optimum nozzle expansion area ratio, ϵ, for which the specific impulse reaches a maximum. Additionally, this optimum expansion area ratio varies drastically depending on the corresponding ψ. Consequently, it can be said that there is a need for a properly designed diverging nozzle on PDE systems at higher ψ, as the straight-extension nozzle is unable to adequately convert the enthalpy of the burned products into kinetic energy, thereby enhancing the propulsive performance of the PDE. Moreover, it is also noted that as the back pressure is reduced and ψ increases, the performance difference between air and helium as the inert mixture becomes nearly indistinguishable. This is especially evident in the case of $\psi = 200$, such that the optimum specific impulse and nozzle area ratio occurs at $I_{sp} = 369.3$ seconds and $\epsilon = 40.3$, and $I_{sp} = 363.7$ seconds and $\epsilon = 36.5$, for air and helium, respectively.

Similarly, the general idealized performance trends for stoichiometric C_2H_4–O_2 detonable propellant are shown in Figs. 6.28(a) and 6.28(b) for air and helium as the ambient, respectively. As in the case of H_2–O_2 detonable propellant, it is evident that a diverging

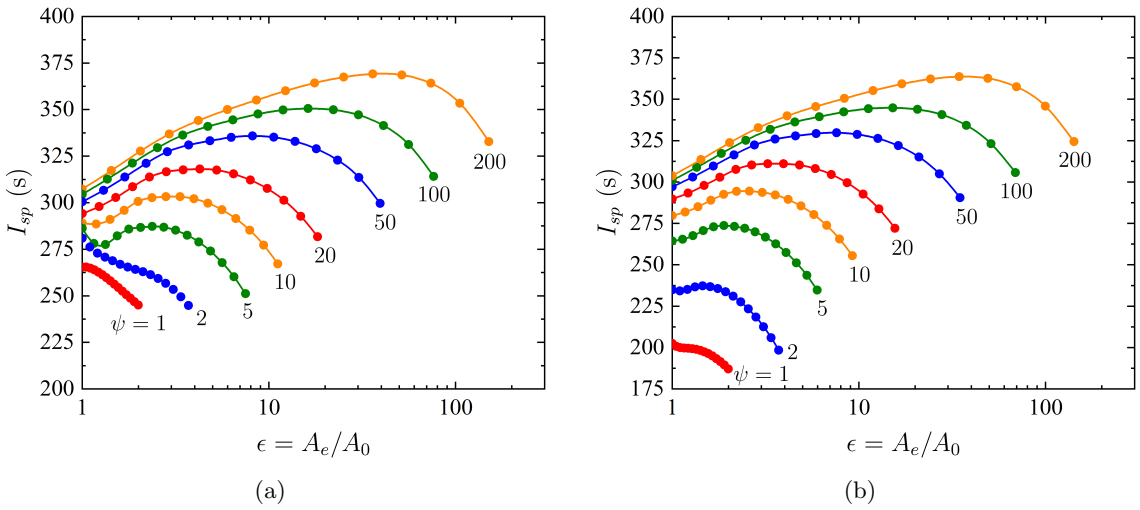

Figure 6.27. Specific impulse variation with ϵ and ψ for a PDE with $\alpha_0 = 0.7$ and operating with $2H_2$–O_2 propellant with (a) air and (b) helium as the inert mixture in the nozzle.

nozzle will not always yield the optimum performance solution for a PDE, especially at lower blowdown pressure ratios. As shown in Fig. 6.28(a), a partially-filled PDE with $\epsilon = 1$ provides the best performance for $\psi = 1$ and 2. As previously discussed, this is a direct result of the large losses associated with severe over-expansion of the burned products. However, for $\psi \gtrsim 5$, a properly designed diverging nozzle will provide the best performance for the PDE. In the case of helium as the inert mixture, it is evident from Fig. 6.28(b) that the partially-filled PDE will never provide superior performance compared to that of a PDE with a diverging nozzle. Again, this is a direct result of the reduction in acoustic impedance ratio due to the density of ethylene–oxygen mixture compared to that of a hydrogen–oxygen mixture, such that the partial-fill effect is almost entirely absent. In such a case, the optimum performance can only be achieved by adequately expanding the burned products through a diverging nozzle. Hence, it becomes of immediate importance that the PDE be equipped with a properly designed diverging nozzle in order to enhance the propulsive performance and maximize the efficiency of the system. Another important result to note is that a PDE operating with an ethylene–oxygen mixture will require a nozzle

with a expansion area ratio nearly double that of a hydrogen–oxygen mixture for the same optimum condition. This is simply due to the larger post-detonation pressures experienced in a PDE operating with hydrocarbon fuels. For instance, in the case of $\psi = 100$ and air as the inert mixture, the optimum specific impulse and nozzle area ratio occurs at $I_{sp} = 350.6$ seconds and $\epsilon = 16.7$, and $I_{sp} = 287.5$ seconds and $\epsilon = 31.2$, for stoichiometric H_2–O_2 and C_2H_4–O_2 detonable propellants, respectively.

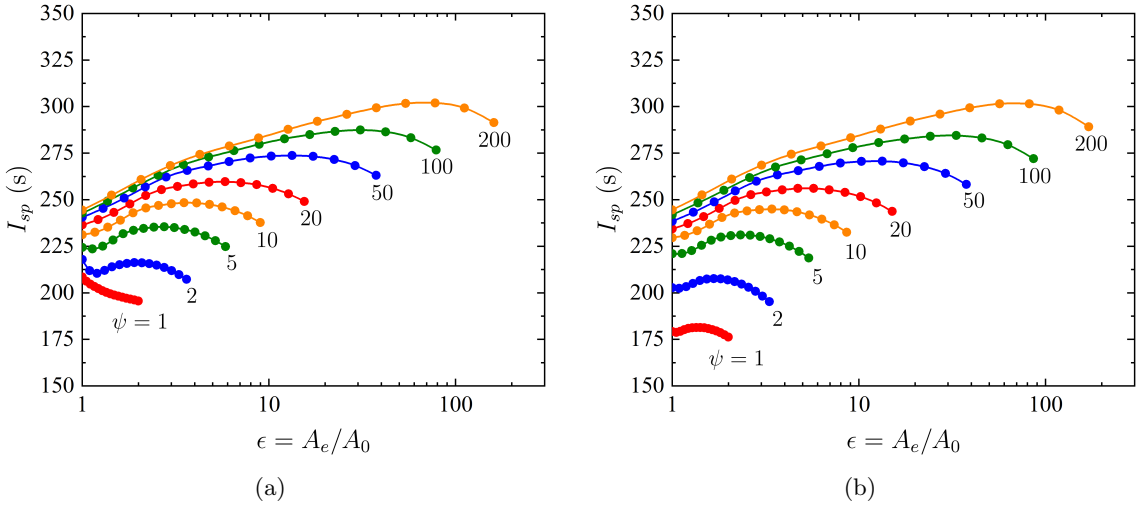

Figure 6.28. Specific impulse variation with ϵ and ψ for a PDE with $\alpha_0 = 0.7$ and operating with C_2H_4–$3O_2$ propellant with (a) air and (b) helium as the inert mixture in the nozzle.

In summary, the generalized results reported above for stoichiometric H_2–O_2 and C_2H_4–O_2 detonable mixtures demonstrate that a properly designed nozzle is crucial to the optimization of PDE performance for blowdown pressure ratios of $\psi \gg 1$. In these cases, the performance benefit due to partial filling is significantly reduced, as a result of the acoustic impedance of the inert mixture rapidly reducing with increasing ψ. Consequently, optimum performance of the PDE is achieved only through physical expansion of the burned products by means of a diverging nozzle. More important, there exist a unique optimum nozzle expansion area ratio for the PDE at a given blowdown pressure ratio, which varies

drastically as ψ increases. Hence, it is important to identify these combinations of blowdown pressure and nozzle expansion area ratio that result in the maximum specific impulse. Additionally, it is reminded that all of the results reported in this subsection are specific to the case of $\alpha_0 = 0.7$. It is noted that the PDE performance also changes given the ratio of PDE tube length-to-total length, namely, α_0, which includes the tube and nozzle lengths. As such, the optimum performance results will be reported in the final subsection of this chapter for the cases of $\alpha_0 = 0.6$, 0.7, 0.8, and 0.9, respectively.

6.2.4 Analytical Quasi-Steady Nozzle Performance Model

Before proceeding to the optimum nozzle performance results, it is of interest to develop a diverging nozzle performance model for the PDE based on a quasi-steady nozzle flow assumption. As discussed at the beginning of this section, the nozzle flow field approaches a mostly quasi-steady flow condition once the transmitted shock wave, contact surface, and secondary shock wave exit the nozzle. In fact, in the limit of $\alpha_0 \to 1$, the nozzle start up time is effectively zero and quasi-steady flow persist during the entire gasdynamic blowdown process. Moreover, in cases where $\alpha_0 \approx 1$, as $\psi \to \infty$, the nozzle start up time tends towards zero. Note, this was shown in the case of $\psi = 100$ for $\epsilon = 4$ and $\alpha_0 = 0.7$ in Fig. 6.25, where the nozzle startup time is only a small fraction of the overall cycle time. Consequently, evaluation of the PDE performance with a diverging nozzle in the limit of a quasi-steady nozzle flow assumption yields an absolute theoretical maximum performance for a PDE nozzle, such that all of the losses associated with the nozzle starting process are neglected.

Previously, Barbour and Hanson [121] developed a PDE performance model for diverging nozzles, by employing a quasi-steady assumption and extending the fully-filled models of Wintenberger et al. [66, 67] and Cooper and Shepherd [92] to PDEs with diverging nozzles in sub-atmospheric environments. The present model closely follows that of Barbour and Hanson [121]; however, the analytical model developed in Ch. 5 is utilized. Recall

that the analytical model in Ch. 5 reduced the thrust force and associated performance parameters of the fully-filled PDE to a description of the pressure history on the exit plane of the PDE. Accordingly, it follows that this pressure history can be especially useful for describing the flow condition on the exit plane of a quasi-steady diverging nozzle. For instance, it was shown that when a PDE is equipped with a diverging nozzle, the flow field within the constant-area portion of the thrust chamber is identical to that of a fully-filled PDE, due to the choking condition that develops at the nozzle inlet. Subsequently, with a quasi-steady nozzle flow assumption, the performance of a nozzle can readily be obtained by extending this pressure history at the nozzle entrance to that on the nozzle exit plane for a given expansion area ratio. Therefore, the remainder of this subsection is used to develop an expression for the thrust of a PDE that is equipped with a quasi-steady nozzle.

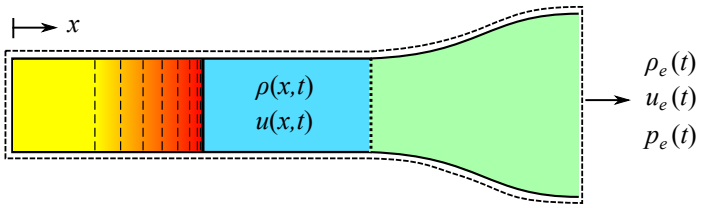

Figure 6.29. Control volume (dashed line) for simplified analytical performance model of PDE with a diverging nozzle.

For the subsequent derivation and discussion, the control volume under consideration is depicted in Fig. 6.29. For this model, it is assumed that the gasdynamics are quasi-one-dimensional, unsteady, inviscid, and absent from any heat transfer. These assumptions were shown to be in agreement with the actual gasdynamic flow field in a PDE thrust chamber during the development and validation of the MOC model in Ch. 4. Therefore, they are used here to simplify the current control volume analysis. The general linear momentum equation for the closed control volume in Fig. 6.29 is given by

$$R_x = \frac{\partial}{\partial t}\left[\int_{cv} \rho(x,t)u(x,t)\ d\mathcal{V}\right] + u_e(t)\dot{m}_e(t) + \left[p_e(t) - p_0\right] A_e \tag{6.12}$$

In this form, R_x is the resultant thrust force on the control volume, and the first, second, and third terms on the right-hand side of Eq. (6.12) represents the time rate of change of internal momentum integrated over the control volume, momentum flux at the exit control surface, and the net pressure-area force at the exit control surface, respectively. Additionally, the actual reaction thrust force on the PDE thrust chamber is obtained by application of Newton's third law, $F_x = -R_x$, namely, equal and opposite the net force on the control volume. However, without loss of generality, the negative sign can be neglected in the subsequent analysis.

Based on the analysis of Ch. 5, it was shown that over the full cycle time, t_f, the time rate of change of momentum within the constant-area portion of the control volume contributes negligibly to the overall time-averaged thrust and corresponding impulse. Moreover, for a quasi-steady nozzle, such that $\alpha_0 \to 1$, or $\psi \to \infty$, it follows that the time rate of change of momentum within the nozzle approaches zero. Hence, Eq. (6.12) reduces to the simplified form

$$F_x = u_e(t)\dot{m}_e(t) + [p_e(t) - p_0]\, A_e \tag{6.13}$$

Note, in this expression, the subscript e represents the properties on the nozzle exit plane. Further, under the assumption of a quasi-steady nozzle flow, it follows that $\dot{m}_e(t) = \dot{m}_4(t) = \rho_4(t) A_0 u_4(t)$, where it is reminded that state 4 corresponds to the condition at the exit of the constant-area portion of the thrust chamber, namely, the nozzle inlet. Similarly, due to the choking condition that develops at the nozzle inlet, it follows that

$$\dot{m}_e(t) = \frac{p_4(t) A_0}{\sqrt{T_4(t)}} \sqrt{\frac{\gamma_2}{R_2}} \tag{6.14}$$

Substituting Eq. (6.14) into Eq. (6.13), and noting that $u_2(t) = a_2 M_2$, the following expression can be obtained

$$F_x = p_4(t) A_0 \gamma_2 M_e \sqrt{\frac{T_e(t)}{T_4(t)}} + (p_e(t) - p_0)\, A_e \tag{6.15}$$

Moreover, using the isentropic relation to replace $T_e(t)/T_4(t)$ in Eq. (6.15) in terms of $p_e(t)/p_4(t)$ yields

$$F_x = p_4(t)A_0\gamma_2 M_e \left(\frac{p_e(t)}{p_4(t)}\right)^{(\gamma_2-1)/2\gamma_2} + (p_e(t) - p_0)\, A_e \tag{6.16}$$

Lastly, it can be shown [121] that the pressure ratio for a given nozzle, $p_e(t)/p_4(t)$, can be expressed in terms of the Mach number at the nozzle exit, M_e, and the nozzle expansion area ratio, $\epsilon = A_e/A_0$, as

$$\frac{p_e(t)}{p_4(t)} = (M_e\epsilon)^{-2\gamma_2/(\gamma_2+1)} \tag{6.17}$$

Hence, substitution of Eq. (6.17) into Eq. (6.16), after algebraic manipulation, yields

$$F_x = p_4(t)A_0 \left\{\gamma_2 M_e \left(M_e\epsilon\right)^{-(\gamma_2-1)/(\gamma_2+1)} + \epsilon\left[\left(M_e\epsilon\right)^{-(2\gamma_2)/(\gamma_2+1)} - \frac{p_0}{p_4(t)}\right]\right\} \tag{6.18}$$

This simple expression represents the thrust of a PDE equipped with a quasi-steady nozzle, and has been reduced to only a function of $p_4(t)$, given the nozzle expansion area ratio, ϵ, and ambient condition p_0. Additionally, it is worth noting that when $\epsilon = 1$, the Mach number at the nozzle exit is $M_e = 1$, and Eq. (6.18) reduces to that of the fully-filled case in Eq. (5.8) of Ch. 5. Hence, with Eqs. (5.41) and (5.42)–(5.45), the single-cycle variation in $F_x(t)$ can be determined for a PDE equipped with a quasi-steady diverging nozzle. Lastly, application of Eqs. (4.13)–(4.15) permits determination of the primary single-cycle performance parameters. Moreover, these expressions are used in the following subsection to identify the ideal maximum specific impulse at a given blowdown pressure ratio for a PDE with a diverging nozzle.

6.2.5 Optimum Nozzle Performance

In this section, the general optimum performance characteristics of PDEs with conical diverging nozzles are presented. These results are of great importance for the design of PDEs with diverging nozzles and for the quantification of idealized PDE performance, such that the unsteady nozzle flow field is considered. It is noted that these results are obtained by using the golden-section-search method with the current MOC model in order to locate

the optimum nozzle expansion area ratio that maximizes the specific impulse at a given blowdown pressure ratio. Similarly, the same iterative minimization scheme was used with the quasi-steady analytical performance model described in the previous subsection in order to identify the theoretical maximum PDE performance in the limit that quasi-steady nozzle flow exists in the nozzle throughout during the entire gasdynamic blowdown process. These maximum specific impulses are denoted by I^*_{sp}, which corresponds to the specific impulse obtained when the PDE nozzle is perfectly expanded for the largest fraction of the overall cycle time.

Figures 6.30(a) and 6.30(b) show the variation in I^*_{sp} for PDEs operating with stoichiometric H_2–O_2 detonable propellant and equipped with conical diverging nozzles with thrust chamber-to-total length ratios of $\alpha_0 = 0.6$, 0.7, 0.8, and 0.9 at blowdown pressure ratios ranging from 1–200, and with air and helium as the inert mixture, respectively. Note that the dashed line corresponds to the results obtained using the quasi-steady nozzle (Q-S Nozzle) model and represents the theoretical maximum performance in the limit $\alpha_0 \to 1$, while the dash-dot line represents the performance of a fully-filled PDE with no nozzle. One of the primary results demonstrated in Figs. 6.30(a) and 6.30(b) is that the optimum specific impulse increases with increasing α_0 at higher blowdown pressure ratio. For instance, in the cases of air and helium as the inert mixture, the PDE with $\alpha_0 = 0.9$ provides roughly 2.6 and 4.2 percent higher I^*_{sp} than that of the PDE with $\alpha_0 = 0.6$ at a blowdown pressure ratio of $\psi = 100$, respectively. Similarly, this increment in I^*_{sp} grows to 5.8 and 7.8 percent for air and helium inert mixture at a blowdown pressure ratio of $\psi = 200$, respectively. Alternatively, at lower blowdown pressure ratios, the PDEs with lower α_0 provide the highest I^*_{sp}. For instance, in Fig. 6.30(a) where air is the inert mixture, there is a deviation in I^*_{sp} for the $\alpha_0 = 0.6$ curve at blowdown pressure ratios of $\psi \lesssim 5$. As previously discussed, this region corresponds to the operating conditions where the optimum specific impulse is provided by a partially-filled PDE with $\epsilon = 1$ rather than a PDE with a diverging nozzle and $\epsilon > 1$. Moreover, for the case of $\alpha_0 = 0.6$, this remains true up until $\psi = 5$, whereby

a minimum in I^*_{sp} is reached. This minimum point represents the condition for which a diverging nozzle with $\epsilon > 1$ begins to provide superior performance compared to that of a partially-filled PDE. Correspondingly, for blowdown pressure ratios beyond this minimum point, namely, $\psi > 5$, a diverging nozzle with $\epsilon > 1$ provides the optimum performance. As such, the PDE with $\alpha_0 = 0.6$ provides the highest I^*_{sp} for blowdown pressure ratios of $\psi \lesssim 25$, at which point the PDE with $\alpha_0 = 0.9$ yields the optimum solution, which continues as the blowdown pressure ratio increases. Again, it is reiterated that the partial-fill effect is the mechanism that allows the PDE with $\alpha_0 = 0.6$ to provide superior performance for $\psi \lesssim 25$ when air is the inert mixture in the nozzle. Note that this is not true when the nozzle if filled with helium. For instance, in Fig. 6.30(a) where helium is the inert mixture, the partial-fill effect is almost entirely suppressed by the time the blowdown pressure ratio reaches $\psi = 2$. As such, the optimum performance is achieved from a PDE with $\alpha_0 = 0.9$ for $\psi > 2$ due to the reduced acoustic impedance.

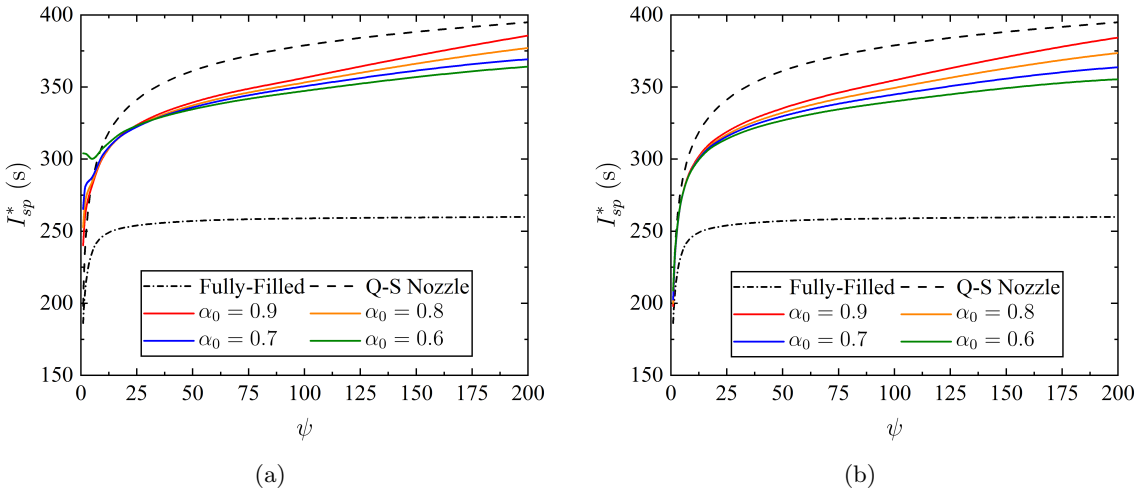

Figure 6.30. Optimum specific impulse variation with ψ for $2H_2$–O_2 propellant with (a) air and (b) helium as inert mixture in the nozzle.

Similarly, figures 6.31(a) and 6.31(b) show the variation in I^*_{sp} for PDEs operating with stoichiometric C_2H_4–O_2 detonable propellant and equipped with conical diverging noz-

zles with thrust chamber-to-total length ratios of $\alpha_0 = 0.6$, 0.7, 0.8, and 0.9 at blowdown pressure ratios ranging from 1–200, and with air and helium as the inert mixture, respectively. As before, the dashed line corresponds to the results obtained using the quasi-steady nozzle (Q-S Nozzle) model and represents the theoretical maximum performance in the limit $\alpha_0 \to 1$, while the dash-dot line represents the performance of a fully-filled PDE with no nozzle. As in the previous case, one of the primary results demonstrated in Figs. 6.31(a) and 6.31(b) is that the optimum specific impulse increases with increasing α_0 at higher blowdown pressure ratio. For instance, in the cases of air and helium as the inert mixture, the PDE with $\alpha_0 = 0.9$ provides roughly 5.5 and 6.8 percent higher I^*_{sp} than that of the PDE with $\alpha_0 = 0.6$ at a blowdown pressure ratio of $\psi = 100$, respectively. Similarly, this increment in I^*_{sp} grows to 6.6 and 7.6 percent for air and helium inert mixture at a blowdown pressure ratio of $\psi = 200$, respectively. Alternatively, unlike the case of stoichiometric H_2–O_2 detonable propellant, the partial-fill effect for the case of $\alpha_0 = 0.6$ is less pronounced at lower ψ. As discussed in the previous section, this is a direct result of the lower acoustic impedance ratio due to the increased density of a stoichiometric C_2H_4–O_2 detonable propellant. As a result, the optimum performance is achieved from a PDE with $\alpha_0 = 0.9$ for $\psi \gtrsim 8$ and $\psi \gtrsim 2$ in the cases of air and helium as the inert mixture, respectively.

A final important result demonstrated in Figs. 6.30 and 6.31 is the behavior of the quasi-steady nozzle solution, in that the solution underestimates the nozzle performance at lower ψ where the partial-fill effect is present, and over-predicts the PDE nozzle performance at higher ψ. This is to be expected as this solution simultaneously neglects the gasdynamic mechanisms that govern the partial-fill effect and the associated increase in performance, and the gasdynamic mechanisms that govern the performance losses associated with the transient nozzle startup, such as the transmitted shock, contact surface, and secondary shock motion in a diverging nozzle. Consequently, this can result in a misrepresentation of the optimum PDE nozzle performance. As such, the quasi-steady solution should be regarded as a highly idealized representation of the actual PDE nozzle performance. Al-

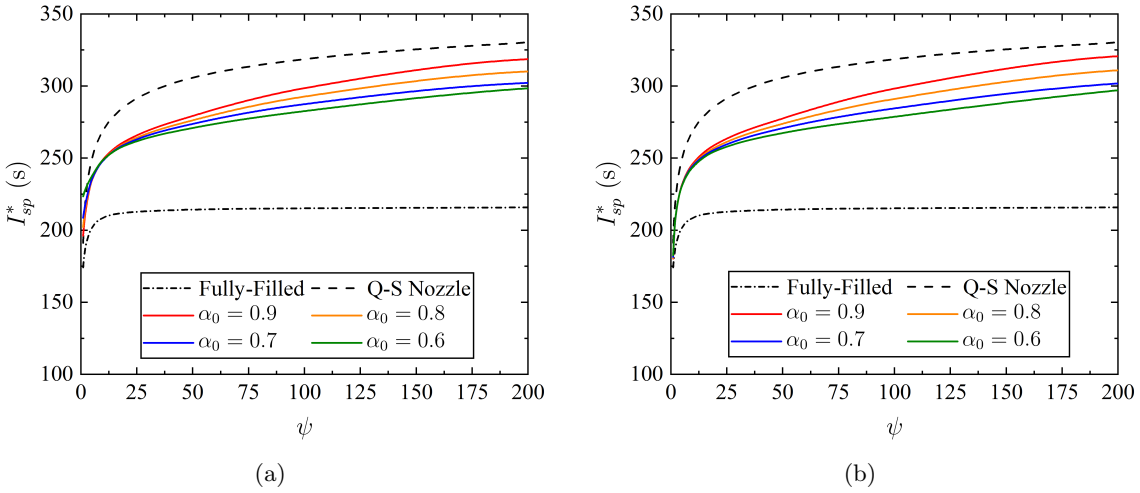

Figure 6.31. Optimum specific impulse variation with ψ for C_2H_4–$3O_2$ propellant with (a) air and (b) helium as the non-combustible mixture in the nozzle.

though, it is noted that in the limits where $\psi \to \infty$ and $\alpha_0 \to 1$, the quasi-steady nozzle solution becomes a more accurate representation of the optimum PDE nozzle performance. As mentioned previously, these cases yield a nozzle startup time that tends towards zero, and the losses associated with the unsteady nozzle startup are negligible. This is evident in Figs. 6.30 and 6.31 where the optimum I^*_{sp} from the quasi-steady nozzle model only overestimates that of the PDE with $\alpha_0 = 0.9$ by an average of 1.4 percent at $\psi = 200$. As such, only in the limit of α_0 near unity and large ψ will the quasi-steady nozzle flow assumption become an accurate depiction of the actual gasdynamic flow field in a diverging PDE nozzle.

CHAPTER 7

SHOCK DYNAMICS IN DIVERGING NOZZLES [1]

7.1 Background

One of the key aspects of the starting nozzle flow field in a PDE is the dynamic behavior of the transmitted shock wave as it traverses through the nozzle. As discussed in Chs. 2 and 6, the nozzle starting flow field is initiated once the detonation wave collides with the contact surface at the nozzle entrance, and the transmitted shock enters the nozzle. In general, the dynamics of the transmitted shock are governed by the local area change of the nozzle and the gasdynamic interaction with the flow field from behind. Moreover, as noted in the study of Wu [169], a general performance trend for PDEs with diverging nozzles is the increase in single-cycle total impulse with increasing attenuation of the transmitted shock wave strength. However, it should be noted that this trend only remains true provided severe over-expansion in the exhausting nozzle flow field is avoided during the remainder of the gasdynamic blowdown. Therefore, it is very important in the design of diverging nozzles for use in PDE propulsion systems to consider the dynamic characteristics of the transmitted shock within the nozzle. In particular, it is of great interest to identify nozzle shapes that significantly attenuate the transmitted shock wave without causing severe over-expansion in the flow field behind the shock, as in the example x–t diagram of Fig. 2.6. In the work of Wu [169], the classical Chester–Chisnell–Whitham (CCW) theory was proposed as a low-order model to determine the decay behavior of the transmitted shock. However, the classical CCW theory is really only appropriate for shock waves that are initially uniformly propagating and free of any gradients in the flow field immediately behind

[1] Parts of this chapter were published in Peace, J.T. and Lu, F.K., "On the Propagation of Decaying Planar Shock and Blast Waves Through Non-Uniform Channels," *Shock Waves*, vol. 28, no. 6, pp. 1223–1237, 2018. doi: 10.1007/s00193-018-0818-0

the shock. Additionally, given the previous discussion in Chs. 2 and 6 regarding the dynamics of the transmitted shock, the shock strength and motion is governed by both the nozzle area change, and from the interaction of the Taylor rarefaction wave from behind. Hence, the classical CCW theory is not entirely appropriate for a description of shock dynamics in PDE nozzles. It is the goal of this chapter to formulate a rigorous analytical model that can estimate the strength and motion of a transmitted shock wave through a general contour diverging nozzle. Additionally, before discussing the transmitted shock dynamics in a PDE nozzle, it is convenient to generalize the analysis to shock motion in non-uniform channels, and then apply those results to the case of a PDE.

The propagation of shock waves through non-uniform channels with varying cross-sections has been studied analytically from the 1950s. Notably, Chester [170] provided a linearized solution to the problem of a transmitted shock wave in a channel of non-uniform cross-sectional area, specifically, channels that feature monotonically increasing or decreasing sections. The solution allowed for an approximate determination of the change in shock strength over a finite length of channel of arbitrary shape. A significant result was that the shock strength, averaged at any time over the flow cross-sectional area, is proportional to the change in area of the channel. A similar theoretical treatment by Chisnell [171] yielded a closed-form approximate expression for the change in shock strength as a function of channel area by using a steady-state analysis. This was achieved by neglecting the reflected disturbances generated by the shock. The final major theoretical treatment was that of Whitham [172]. Whitham's theory allowed for the computation of the shock motion without directly determining the flow field following the shock. The shock motion was determined by integrating the Rankine–Hugoniot (RH) shock jump conditions on the forward propagating characteristic, which yielded an explicit relationship for the channel area and the local shock Mach number. The shock strength and channel area relation obtained by Whitham is exact with those of Chester and Chisnell. Whitham's theory has been widely used in analyzing the motion of shock waves in various geometries with accurate results [173–176].

Collectively, the work of Chester, Chisnell, and Whitham is known as the CCW theory. It is noted that the results of CCW theory provide the basis for formulating Whitham's theory of geometrical shock dynamics [177], which can be used to analyze shock propagation in two-dimensional geometries.

In the case of decaying shock waves, or shock motion with a non-uniform flow field following the shock, application of the classical CCW theory is not entirely appropriate. This is because the CCW theory neglects gradients in the flow field just behind a shock wave, which strictly prohibits its application to initially uniformly propagating shocks, or commonly referred to as freely propagating shocks. In regard to this aspect, Best [178] provided a theoretical framework for the generalization of CCW theory. Best reconsidered the motion of a shock through a channel of varying cross-section and described it by an infinite sequence of ordinary differential equations. Truncation was used to show the varying degree of approximation between the original CCW theory and the generalized CCW theory with the inclusion of higher-order terms for cylindrical and spherical shock motion. In this manner, a non-uniform flow field following the shock can be taken into account. Best applied the generalized theory successfully to the propagation of underwater blast waves. Moreover, the newer generalized theory was shown to have excellent agreement with the approximate Kirkwood–Bethe method [179].

The focus of this chapter is to investigate the propagation of general decaying shocks that are incident on non-uniform channels using the generalized theory of Best. This gas-dynamic process is shown schematically in Fig. 7.1 for a general diverging geometry. It is desired to analyze the case of an arbitrary strength shock that is being overtaken by an unsteady rarefaction wave, much like that of the Taylor rarefaction wave overtaking the transmitted shock in the PDE nozzle. For this particular wave process, the overtaking rarefaction wave creates a non-uniformity in the flow behind the shock that can largely influence the shock wave propagation dynamics as it traverses through a region of increasing

area. Thus, the Best generalized extension of classical CCW theory will be used to treat this gasdynamic process and is discussed in the following subsections.

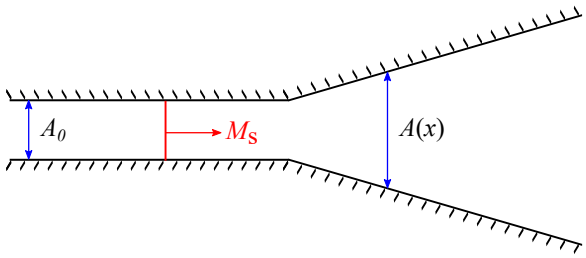

Figure 7.1. Shock wave traveling with a shock Mach number of M_s entering a diverging channel.

7.2 Generalized CCW Theory

7.2.1 Area–Mach Relation

The area–Mach (A–M) relation is a classical result obtained by Chester [170], Chisnell [171], and Whitham [172] from linearization of the governing equations of inviscid and quasi one-dimensional flow with no heat transfer or mass addition. Substituting the RH shock jump conditions on the forward propagating C_+ compatibility equation (Eq. (4.7)) yields the ordinary differential equation

$$\frac{\mathrm{d}M}{\mathrm{d}x} = -\frac{1}{g(M)}\frac{A'(x)}{A(x)} \tag{7.1}$$

where

$$g(M) = \frac{M}{M^2-1}\left(1+\frac{2}{\gamma+1}\frac{1-\mu^2}{\mu}\right)\left(1+2\mu+\frac{1}{M^2}\right) \tag{7.2}$$

and

$$\mu^2 = \frac{(\gamma-1)M^2+2}{2\gamma M^2-(\gamma-1)} \tag{7.3}$$

It is noted that through linearization, the accuracy of the above result is dependent upon the condition that [178]

$$\left|\frac{A'(x)}{A(x)}\right| \gg \frac{1}{\rho a^2 u}\left|1-\frac{a+u}{a_0 M}\right|\left|\frac{\partial p}{\partial t}+\rho a\frac{\partial u}{\partial t}\right| \tag{7.4}$$

where p, u, ρ, and a represent the post-shock state and are given by the RH shock jump conditions.

The inequality of Eq. (7.4) necessitates that the area change dominates the motion of the shock wave compared to the unsteadiness in pressure and velocity following the shock. Moreover, on the right-hand side of Eq. (7.4), the term $|1-(u+a)/(a_0 M)|$ is a measure of the coincidence between the C_+ characteristic and the shock wave in x–t space. This term is exactly equal to zero for $M=1$, and approaches 0.309, 0.274, and 0.261 as $M \to \infty$ for $\gamma = 5/3$, $7/5$, and $4/3$, respectively. The behavior of this term is shown in Fig. 7.2. Similarly, the term $|\partial p/\partial t + \rho a \partial u/\partial t|$ is a measure of the non-uniformity of the flow behind the shock and is exactly zero for a freely propagating shock, namely, uniform planar shock motion. This type of shock motion is shown schematically in Fig. 7.3(a). However, as the shock moves through an area change, the changing shock strength perturbs the immediate flow behind the shock such that $|\partial p/\partial t + \rho a \partial u/\partial t| \neq 0$. Han and Yin [180] used Chester's small perturbation theory to demonstrate that the term is usually very small along the C_+ characteristics originating from the uniform region behind the shock. Therefore, it is these conditions that justify the assumptions of Eq. (7.1), and make the A–M relation a good approximation for describing the dynamics and strength of an initially uniformly propagating shock wave as it traverses through a non-uniform area change.

7.2.2 Higher-Order Equations

For the cases of decaying shock wave propagation, such that the wave is continuously being overtaken by an unsteady rarefaction wave as shown in Fig. 7.3(b), the term $|\partial p/\partial t + \rho a \partial u/\partial t|$ can be very large, thereby violating the inequality relation in Eq. (7.4) that permits use of the A–M relation. This is especially true if the temporal and spatial decay rates of such waves are rapid. The theory of shock dynamics must therefore be extended to take into account the non-uniformity of the flow following the shock wave. This generalization was carried out by Best [178]. Best reconsidered the propagation of a shock

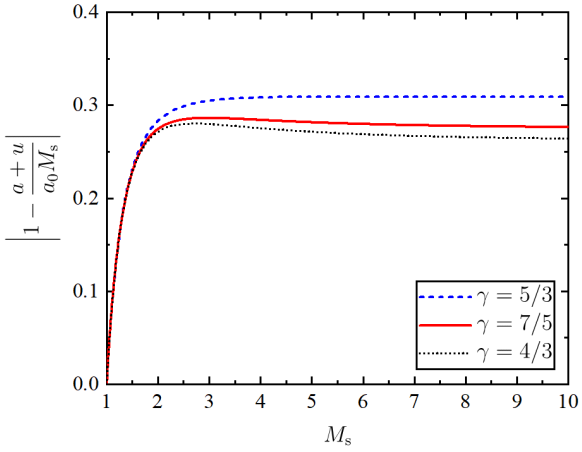

Figure 7.2. Measure of coincidence between C_+ characteristic and shock in x–t space.

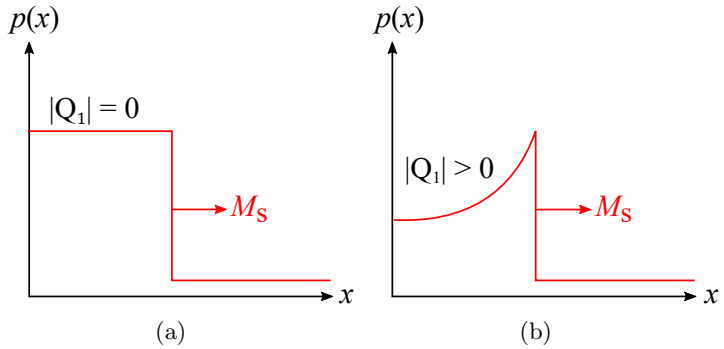

Figure 7.3. (a) Pressure profile of uniformly propagating shock wave and (b) decaying shock wave with flow non-uniformity.

wave down a channel of varying cross section and demonstrated that the motion of the shock wave is governed by an infinite sequence of ordinary differential equations given by:

$$\frac{\mathrm{d}M}{\mathrm{d}x} = -\left[\frac{1}{g\left(M\right)}\frac{A'(x)}{A(x)} + f\left(M\right)Q_1\right] \tag{7.5}$$

$$\begin{aligned}\frac{\mathrm{d}Q_n}{\mathrm{d}x} = -\Bigg[&\frac{\partial^n}{\partial t}\left(\frac{\rho a^2 u}{u+a}\right)\frac{A'(x)}{A(x)} + \sum_{i=1}^{n}\left\{\binom{n}{i}\frac{\partial^i}{\partial t}\left(\frac{1}{u+a}\right)Q_{n+1-i}\right\} \\ &+ \frac{\partial^{n-1}}{\partial t}\left(\frac{\partial(\rho a)}{\partial t}\frac{\partial u}{\partial x} - \frac{\partial(\rho a)}{\partial x}\frac{\partial u}{\partial t}\right) + \left(\frac{1}{u+a} - \frac{1}{a_0 M}\right)Q_{n+1}\Bigg]\end{aligned} \tag{7.6}$$

for $n = 1, 2, 3, ...$, where

$$Q_n = \partial_t^{n-1}\left(\partial p/\partial t + \rho a \partial u/\partial t\right) \tag{7.7}$$

$$f(M) = (\gamma+1)\left[(\gamma-1)M^2+2\right]\left[(\gamma-1)M^2-(\gamma+1)\nu M+2\right]\left[2\rho_0 a_0^3 M\left[2M^2 + (\gamma+1)\nu M-2\right]\left[(\gamma+1)\nu+2(\gamma-1)M^3+(\gamma+1)\nu M^2+4M\right]\right]^{-1}$$

and

$$\nu^2 = \frac{\left[(\gamma-1)M^2+2\right]\left[2\gamma M^2-\gamma+1\right]}{(\gamma+1)M^2} \tag{7.8}$$

Note that a derivation of Eqs. (7.5) and (7.6) is provided in section C.1 of the appendix. Moreover, the behavior of both $g(M)$ and $f(M)$ are shown in Figs. C.1 and C.2 of section C.2 of the appendix. These equations have been recast from that reported by Best for convenience to include ordinary derivatives of the spatial coordinate x, as opposed to time t. By using the general Leibniz rule combined with the characteristic form of the governing equations, Best obtained explicit formulas for the nth-order time and space partial derivatives of p, u, ρ, and a. These general formulas are not repeated here; although, the first-order time and space partial derivatives of p, u, ρ, and a are provided in section C.1 of the appendix. It is noted that these expressions are reduced to only depend on the RH shock jump conditions and channel area profile.

In order to compute a solution, truncation is required to obtain a mathematically closed set of ordinary differential equations in terms of the Mach number M and variable Q_n. As a first-order approximation for $n = 0$, Eq. (7.6) becomes null and therefore truncating Q_1 in Eq. (7.5) yields the classical CCW A–M relation. Moreover, for higher-order approximations, the term Q_{n+1} is truncated to yield a closed set of $n+1$ coupled ordinary differential equations in the variables M and Q_n, such that each additional equation is coupled to its successor. This is the same closure scheme of [178], where details regarding the convergence of such a closure scheme were discussed. For this work, only a second-order approximation is considered and the resulting equation set is used to describe the motion of decaying shock waves in non-uniform channels. Therefore, for $n = 1$, the resulting equations consists of Eq. (7.5) and

$$\frac{\mathrm{d}Q_1}{\mathrm{d}x} = -\left[\frac{\partial}{\partial t}\left(\frac{\rho a^2 u}{u+a}\right)\frac{A'(x)}{A(x)} + \frac{\partial}{\partial t}(\rho a)\frac{\partial u}{\partial x} - \frac{\partial}{\partial x}(\rho a)\frac{\partial u}{\partial t} + \frac{\partial}{\partial t}\left(\frac{1}{u+a}\right)Q_1\right] \tag{7.9}$$

where $Q_1 = \partial p/\partial t + \rho a \partial u/\partial t$, is a measure of flow non-uniformity behind the shock. Thus, with this second-order approximation, the role of flow non-uniformity on the motion of the shock, or pressure and velocity gradients behind the shock, is taken into consideration. In essence, this second-order approximation allows for an analytical description of waves in non-uniform channels where the initial value of Q_1 is non-zero. In the event that the initial condition $Q_{1,0} = 0$, namely, the gradients in the flow field following the shock are exactly zero, the shock motion is simply that of a uniformly propagating shock as shown in Fig. 7.3(a). However, if $Q_{1,0} < 0$, the shock motion is representative of one that is being overtaken by a rarefaction wave resulting in the propagation of a decaying shock as shown in Fig. 7.3(b). It is also worth noting that for decaying shock waves, the rarefaction following the shock is continuously overtaking the wave causing a decrease in the strength and velocity of the wave as it propagates. Similarly, when the shock is subjected to a non-uniform area change, the effects of the changing area alters the wave dynamics. This process is a coupling between the effects of the following rarefaction and the change in channel cross-sectional area. The current work does not exactly treat this coupling in closed form. However, the effects of the overtaking rarefaction enters the analysis through the initial condition imposed on Q_1. This aspect will be further discussed in the following sections.

Before proceeding, it is desired to investigate the nature of Eq. (7.9) and provide a formal criterion regarding its validity. Substitution of the first-order partial time and space derivatives is required to reveal the complete structure of these equations. By using the formulas obtained by Best [178] (Eqs. (C.39)–(C.46)) with the RH shock jump conditions, Eq. (7.9) can be reduced to the following ordinary differential equation

$$\frac{\mathrm{d}Q_1}{\mathrm{d}x} = \alpha_1(M)\frac{A'(x)}{A(x)}Q_1 + \alpha_2(M)\frac{\mathrm{d}M}{\mathrm{d}x}Q_1 + \alpha_3(M)\left(\frac{\mathrm{d}M}{\mathrm{d}x}\right)^2 + \alpha_4(M)\frac{\mathrm{d}M}{\mathrm{d}x} + \alpha_5(M)\left(\frac{A'(x)}{A(x)}\right)^2 \tag{7.10}$$

In this form, α_i has the functional dependence $\alpha_i = \alpha_i\left(p, u, \rho, a, \mathrm{d}p/\mathrm{d}M, \mathrm{d}u/\mathrm{d}M, \mathrm{d}\rho/\mathrm{d}M\right)$ on the shock. Note, explicit formulas were obtained within a Mathematica environment for α_i. For brevity, these relations are not reported here. However, the behavior of the α_i

coefficient functions are shown in Figs. C.3–C.7 of the appendix. It should be noted that these figures do not include real gas effects such as vibrational excitation, dissociation, or ionization; therefore, the results at higher Mach numbers in the forgoing analysis should be taken with caution. At this point, it is evident that the shock wave motion for a second-order approximation is governed by two coupled first-order, non-linear ordinary differential equations. For the purposes of establishing a formal criterion to investigate the validity of the above equations, it is convenient to define the quantity

$$\bar{\Lambda} = \alpha_1(M)\frac{A'(x)}{A(x)}Q_1 + \alpha_2(M)\frac{\mathrm{d}M}{\mathrm{d}x}Q_1 + \alpha_3(M)\left(\frac{\mathrm{d}M}{\mathrm{d}x}\right)^2 + \alpha_4(M)\frac{\mathrm{d}M}{\mathrm{d}x} + \alpha_5(M)\left(\frac{A'(x)}{A(x)}\right)^2 \tag{7.11}$$

Thus, by truncation, the accuracy of the two-equation approximation is dependent upon the condition that

$$|\bar{\Lambda}| \gg \frac{1}{u+a}\left|1 - \frac{u+a}{a_0 M}\right|\left|\frac{\partial}{\partial t}\left(\frac{\partial p}{\partial t} + \rho a\frac{\partial u}{\partial t}\right)\right| \tag{7.12}$$

It is now clear that the accuracy of Eq. (7.10) necessitates that the combined effects of area change and first-order temporal derivatives of flow properties behind the shock dominate the dynamics of the shock compared to the effects of second-order temporal derivatives of flow properties. Further, the right-hand side of Eq. (7.12) is scaled by the measure of coincidence between the C_+ characteristic and shock wave in x–t space. The behavior of this term was previously discussed in regard to the A–M inequality relation of Eq. (7.4). The second term, $|\partial/\partial t(\partial p/\partial t + \rho a \partial u/\partial t)|$, represents the first-order temporal derivative of flow non-uniformity behind the shock, which can be rewritten as $|\partial Q_1/\partial t|$. The physical interpretation of this quantity is rendered difficult given the dependence on second-order temporal derivatives of pressure and gas velocity behind the shock. Despite this complexity, the criterion remains true for the validity of a two-equation approximation for shock dynamics governed by an area change and flow non-uniformity following the shock. Further investigation regarding the behavior and estimates for the orders of magnitude of both the remaining terms and the truncated terms is provided in the following section.

7.3 Order-Of-Magnitude Analysis

It is desired to examine the conditions for which the criteria in Eqs. (7.4) and (7.12) remain true. This requires assessing the relative order of magnitude for each term contained in these criteria, namely, the channel area properties $A'(x)/A(x)$, and general flow non-uniformity properties Q_1 and Q_2. For the channel sectional area properties, a generalized relationship exists given a constant half-angle and starting channel height. This geometrical relation is given by

$$\frac{A'(x)}{A(x)} = \frac{2n\tan\theta}{h_0 + 2x\tan\theta} \tag{7.13}$$

where θ and h_0 correspond to the half-angle of the area change and starting channel height, respectively. In this expression, n represents a geometric index equaling unity for a two-dimensional finite width channel, and 2 for a conical area change in a tube. In this form, a diverging geometry corresponds to a half-angle on the range $0 < \theta < \pi/2$, with the domain $0 \leq x < \infty$. Further, the maximum of $|A'(x)/A(x)|$ occurs at the origin of the area change when $x = 0$, and is equal to $2n\tan\theta/h_0$. Moreover, as $x \to \infty$ the value of $|A'(x)/A(x)| \to 0$. A few comments can be made about the nature of diverging geometries in application to the CCW theory. For diverging geometries, the magnitude of $|A'(x)/A(x)|$ tends towards zero with increasing distance from the origin of the area change. Thus, caution must be taken in such geometries to ensure the A–M relation satisfies Eq. (7.4), as relatively minor flow non-uniformity following the shock could be enough to render the approximation invalid. For this reason, it is useful to approximate the relative order of magnitude of Q_1 and Q_2 for the sake of establishing a range of validity for the approximate shock dynamic expressions in Eqs. (7.1) and (7.9).

As previously stated, the measures of flow non-uniformity Q_1 and Q_2 are dependent on temporal partial derivatives of pressure, gas velocity, density, and sound speed behind the shock. Therefore, as a first-order approximation, the relaxation in pressure behind the shock at any point in the flow field can be characterized with the Friedlander waveform [164]

$$p(x_i, t) \approx p_\mathrm{s}\left(1 - \frac{t}{\tau}\right)\mathrm{e}^{-t/\tau} \tag{7.14}$$

In this form, τ represents the duration of the over-pressure which can be regarded as a time constant for flow non-uniformity behind the shock. In a similar manner, the transient velocity profile at a given point can be estimated with a linear decay expressed as

$$u(x_i, t) \approx u_{\mathrm{s}} \left(1 - \frac{t}{\tau}\right) \tag{7.15}$$

Further, the density profile, although not entirely similar to the pressure profile, can be estimated using an exponential decay

$$\rho(x_i, t) \approx \rho_{\mathrm{s}} \mathrm{e}^{-t/\tau} \tag{7.16}$$

In these approximate expressions, the subscript s represents the post-shock state and given by the RH shock jump conditions. Note, the above expressions merely approximate the behavior of flow properties following a decaying shock wave, and are thus used only for the sake of argument at estimating the relative order of magnitude for both Q_1 and Q_2. Assuming an ideal gas, $a^2 = \gamma p/\rho$, evaluation of the appropriate temporal derivatives of flow properties at $t = 0$ yields

$$Q_1 \approx -\frac{1}{\tau}\left(2p_{\mathrm{s}} + \rho_{\mathrm{s}} a_{\mathrm{s}} u_{\mathrm{s}}\right) \tag{7.17}$$

$$Q_2 \approx \frac{1}{\tau^2}\left(3p_{\mathrm{s}} + \gamma \frac{p_{\mathrm{s}} u_{\mathrm{s}}}{a_{\mathrm{s}}} + \frac{1}{2}\rho_s a_{\mathrm{s}} u_{\mathrm{s}}\right) \tag{7.18}$$

Thus, the estimates for flow non-uniformity scales with the properties in the post-shock state and the time constant associated with the relaxation of flow quantities behind the shock. The more important result regarding these approximations is that $Q_i \propto (-1)^i/\tau^i$, or equivalently, $|Q_i| \propto 1/\tau^i$. In most shock decay problems, the time constant of relaxation behind the shock is less than unity. Therefore, it is to be expected that $|Q_2| > |Q_1|$ under most conditions. This aspect is what motivates the investigation of the criterion in Eq. (7.12) because the term involving Q_2 is truncated for mathematical closure of the remaining coupled equations. Figures 7.4 and 7.5 show contour plots of $|Q_1|$ and $|Q_2|$ for ambient air ($\gamma = 7/5$) at standard temperature and pressure, respectively.

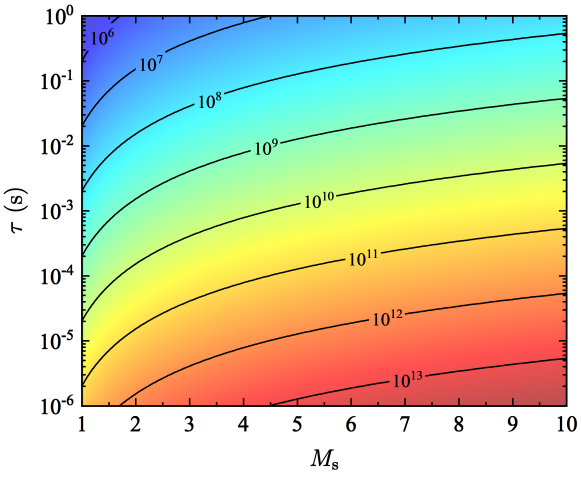

Figure 7.4. Contour plot of $|Q_1|$ (kg/m·s^3) vs. shock Mach number and time constant of flow non-uniformity τ for air at standard temperature and pressure.

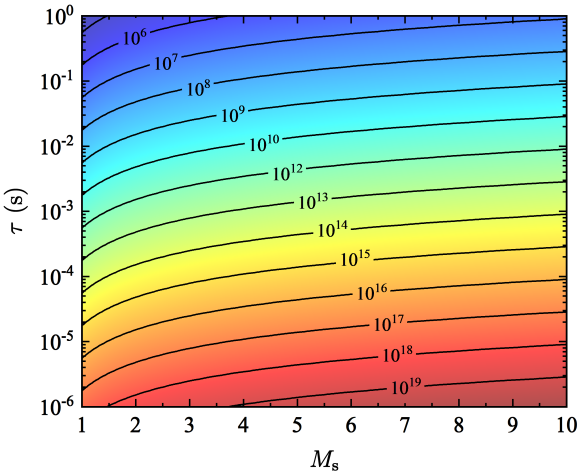

Figure 7.5. Contour plot of $|Q_2|$ (kg/m·s^4) vs. shock Mach number and time constant of flow non-uniformity τ for air at standard temperature and pressure.

7.3.1 One-Equation Approximation

It is now possible to assess the condition under which the classical A–M relation is appropriate for shock motion with a varying degree of non-uniform flow Q_1 in the immediate post-shock flow field. Defining the quantity,

$$\Psi = \frac{1}{\rho a^2 u}\left(1 - \frac{u+a}{a_0 M}\right) Q_1 \tag{7.19}$$

where ρ, u, and a correspond to the post-shock state and are given by the RH shock jump conditions, it then follows that the criterion for validity of the A–M relation can be reduced to

$$\left|\frac{A'(x)}{A(x)}\right| \gg |\Psi| \tag{7.20}$$

Fig. 7.6 is a contour plot of $|\Psi|$ with respect to the shock Mach number and time constant of relaxation for air ($\gamma = 7/5$) at standard temperature and pressure. Therefore, given the value of $|A'(x)/A(x)|$ at any location in the area change, Fig. 7.6 can be used to determine if $|A'(x)/A(x)| \gg |\Psi|$. A reasonable approximation would be the condition such that $|\Psi|/|A'(x)/A(x)| \leq 0.1$. Effectively, this would ensure the A–M relation is used under conditions where the shock motion is primarily influenced by an area change as opposed to the interaction with flow non-uniformity behind the shock. As an example, consider the case where $|A'(x)/A(x)| = 1$ and a shock Mach number of 5. Using the reasoning above, the minimum time constant of decay τ for appropriate use of the A–M relation under these conditions would be restricted to approximately 100 ms. Note that the time constant of decay is application and problem specific. However, in most laboratory conditions, a time constant on the order of 100 ms would require establishing decaying shock profiles in linear channels or tubes of impractically long length. An equivalent argument for the specified conditions in the context of flow non-uniformity can also be made. Hence, for $|A'(x)/A(x)| = 1$ and a shock Mach number of 5, the maximum magnitude of flow non-uniformity $|Q_1|$ behind the shock for appropriate use of the A–M relation would be restricted to approximately $\mathcal{O}(10^7)$ kg/m·s^3. Therefore, under most laboratory conditions, use of the A–M relation for decaying shock motion in diverging area channels would be inappropriate making higher-order approximations necessary.

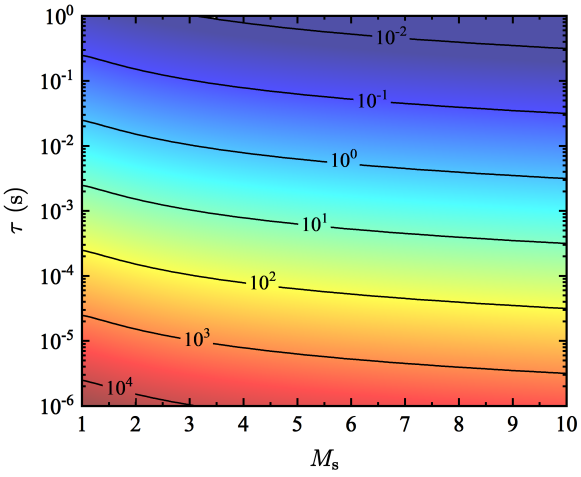

Figure 7.6. Contour plot of $|\Psi|$ (1/m) vs. shock Mach number and time constant of flow non-uniformity τ for air at standard temperature and pressure.

7.3.2 Two-Equation Approximation

In a similar manner, the two-equation approximation can be assessed to determine under which conditions Eq. (7.12) remains true. For this purpose, it is convenient to make use of Eq. (7.11) to define the ratio

$$\bar{\Omega} = \frac{1}{u+a}\left(1 - \frac{u+a}{a_0 M}\right)\left|\frac{Q_2}{\bar{\Lambda}}\right| \tag{7.21}$$

in which case the criterion for validity of the two-equation approximation reduces to

$$|\bar{\Omega}| \ll 1 \tag{7.22}$$

Note that the order of magnitude of $\bar{\Lambda}$ is dependent on $\mathrm{d}M/\mathrm{d}x$, area profile properties $A'(x)/A(x)$, coefficient functions $\alpha_i(M)$, and flow non-uniformity Q_1. The order of magnitude for $\mathrm{d}M/\mathrm{d}x$ is estimated by using (7.5) and the expressions for $g(M)$, $f(M)$, and the approximation for Q_1 in Eq. (7.17). Likewise, the order of magnitude for $\bar{\Lambda}$ is evaluated by using the expressions for $\alpha_i(M)$ and Q_1 at a specified $A'(x)/A(x)$. Figure 7.7 is a contour plot of $|\bar{\Omega}|$ with respect to shock Mach number and time constant of relaxation in air ($\gamma = 7/5$) at standard temperature and pressure for $A'(x)/A(x) = 1$. A reasonable use of the two-equation approximation is under conditions for which $|\bar{\Omega}| \leq 0.1$, namely, when the

truncated term involving Q_2 negligibly contributes to $\mathrm{d}Q_1/\mathrm{d}x$ in Eq. (7.10). Using this reasoning, and the Mach 5 example for assessing the A–M relation, the time constant of decay can be extended from 100 ms to approximately 0.1 ms with the two-equation approximation. Hence, for $|A'(x)/A(x)| = 1$ and a shock Mach number of 5, the maximum magnitude of flow non-uniformity $|Q_1|$ behind the shock for appropriate use of the two-equation approximation would be extended to approximately $\mathcal{O}(10^{10})$ kg/m·s^3. This is an important result that demonstrates the degree to which the two-equation approximation can account for non-uniform flow following the shock and still accurately represent the dynamics of a shock in a non-uniform area change. As such, it can be concluded that there exist practical problems regarding decaying shock motion for which the two-equation approximation is appropriate.

Another important feature of the two-equation approximation shown in Fig. 7.7 is the behavior in the weak shock limit. From the contour lines of $|\bar{\Omega}|$, it is clear that in the limit of weak shocks, the equations can be applied to problems with significantly smaller values of τ without exceeding $|\bar{\Omega}| \leq 0.1$. This result is to be expected as the measure in coincidence between the C_+ characteristic and shock approaches zero, which in turn cancels the effects of flow non-uniformity behind the shock. Therefore, the two-equation approximation can properly be used in the weak shock limit to describe the dynamics of decaying shocks in non-uniform area changes.

7.4 Effects of Initial Flow Non-Uniformity

It is now desired to analyze the behavior of the solutions to the coupled equations in Eqs. (7.5) and (7.10) for the case of diverging geometries and arbitrary strength shocks. For this, the conical channel ($n = 2$) under consideration consists of a tube featuring a 1 cm starting radius with a conical diverging profile characterized by a half angle of $\theta = 5$ degree.

For initially uniform planar shock motion, it follows that $Q_{1,0} \equiv 0$ and a direct comparison can be made between the A–M relation and the current second-order approx-

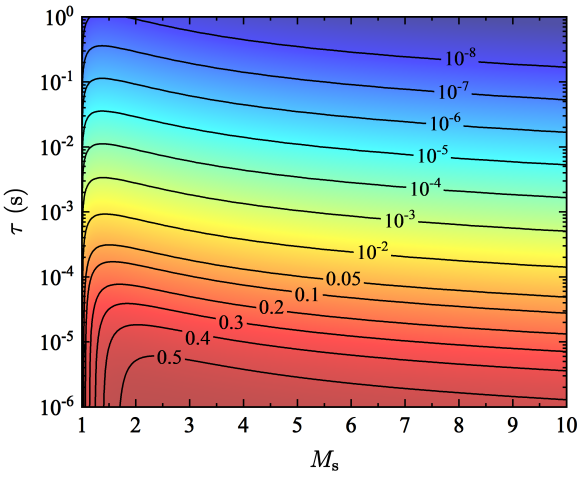

Figure 7.7. Contour plot of $|\bar{\Omega}|$ vs. shock Mach number and time constant of flow non-uniformity τ for air at standard temperature and pressure and $A'(x)/A(x) = 1$.

imation. In essence, making $Q_{1,0} = 0$ allows for isolating the effects of Q_1 on the solution behavior. Figure 7.8 shows the behavior of planar shock waves with an initial Mach number 5 in conical diverging geometries. Note that as the area ratio increases, the two-equation approximation begins to deviate from that predicted by the A–M relation. As expected, this deviation is attributed to the introduction of Q_1 into the two-equation approximation. Moreover, although the flow non-uniformity initial condition $Q_{1,0} = 0$ is being imposed, once the wave begins to propagate into the diverging area change, the value of Q_1 becomes non-zero on the shock as $\mathrm{d}Q_1/\mathrm{d}x$ is dependent on both $A'(x)/A(x)$ and $\mathrm{d}M/\mathrm{d}x$. Note that the effects of re-reflected disturbances are not accounted for in this study. As such, the degree to which these disturbances influence the shock trajectory as opposed to the changing area and $|Q_1|$ may become more significant at large distances from the start of the area change. Further analysis, similar to that carried out by Milton [181], would be required to formally assess this aspect of decaying shock propagation in non-uniform area changes.

It is also desirable to consider the influence of $Q_{1,0}$ on the behavior of the two-equation approximation in diverging geometries. This is carried out before applying the current work to PDE nozzles, as it aides to demonstrate the physical meaning and significant of the flow

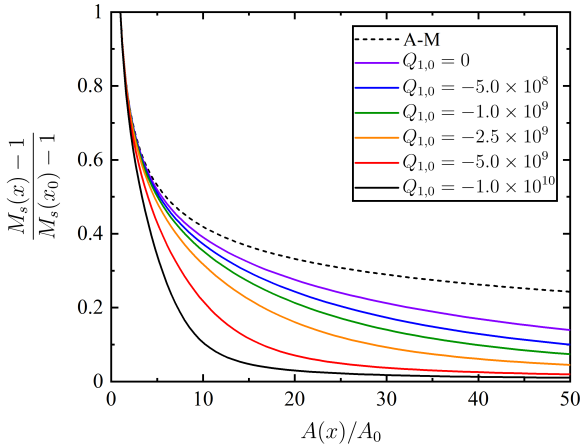

Figure 7.8. Normalized comparison of A–M relation and second-order approximation for an initial shock Mach number of 5 in conical diverging geometry with various flow non-uniformity, $Q_{1,0}$.

non-uniformity. For an initial shock wave Mach number of 5, Fig. 7.8 shows a comparison of the A–M relation and solutions to (7.5) and (7.10) for various values of flow non-uniformity $Q_{1,0} = \{0, -5.0 \times 10^8, -1.0 \times 10^9, -2.5 \times 10^9, -5.0 \times 10^9, -1.0 \times 10^{10}\}$ kg/m-s^3. Note that the initial value of $Q_{1,0}$ significantly influences the rate at which the decaying shock wave approaches an acoustic wave. For these cases, it intuitively follows that the shock wave decays faster when the initial value of $|Q_{1,0}|$ is larger because the temporal gradient of flow properties behind the shock also becomes larger. As such, it is evident that the two-equation approximation improves the versatility of an analytical model aimed at treating shock propagation problems where flow non-uniformity is present. Thus, the following section discusses the extension of the two-equation approximation to the transmitted shock in the PDE starting nozzle flow field and the associated impact on propulsive performance.

7.5 Application to Pulse Detonation Engines

In this section, it is desired to apply the two-equation approximation for shock dynamics to the transmitted shock wave in the starting flow field of PDE diverging nozzles. Additionally, the intent of this work is to identify which parameters of the PDE configura-

tion govern the magnitude of flow non-uniformity behind the incident transmitted shock, and characterize the influence of nozzle wall shape on the dynamics of the transmitted shock. Concurrently, the MOC model will be used to compare the results obtained with the current two-equation approximation in order to justify the need for a higher-order approximation of shock dynamics in PDE nozzles, and to associate a given case of transmitted shock behavior to a corresponding propulsive performance.

7.5.1 Initial Flow Non-Uniformity

In application to PDEs, the magnitude of flow non-uniformity that develops behind the incident transmitted shock is directly governed by the motion and evolution of the Taylor rarefaction wave within the constant-area portion of the thrust chamber. This creates the situation where $|Q_{1,0}|$ is inversely proportional to the PDE tube length upstream of the diverging nozzle, since the transient variation in flow properties at the nozzle throat is dependent on the time required for the Taylor rarefaction to traverse the nozzle entrance. As discussed in Ch. 5, it was shown that the head and tail of the Taylor rarefaction wave travel with the detonation wave velocity, W_{CJ}, and stagnation sound speed, a_3, respectively. Consequently, the Taylor rarefaction wave spreads out over a given length of the thrust chamber until the detonation wave reaches the contact surface at the nozzle throat. As such, the temporal gradient in flow properties behind the Taylor rarefaction wave scales inversely proportional to thrust chamber length, such that short tubes have very large magnitudes of flow non-uniformity, and long tubes have relatively low magnitudes of flow non-uniformity.

Since the PDE with a diverging nozzle chokes once the detonation wave arrives at the nozzle inlet, it follows that flow property variation at the nozzle inlet is exact to that a the exit of a fully-filled PDE. Hence, a first-order estimate for the magnitude of $Q_{1,0}$ can be obtained by considering the pressure profile at the nozzle inlet just after the transmitted shock has passed. It is noted that an expression for this pressure decay profile was derived

in Ch. 5, where the pressure profile during the Taylor wave passage was modeled using the modified Friedlander equation. In application to diverging nozzles, this profile at $x = L_t$ can be approximated by [164],

$$p_4(x = L_t, t) = p_4(t_{CJ}) \left(1 - \frac{t - t_{CJ}}{\tau}\right) \mathrm{e}^{-\alpha\left(\frac{t-t_{CJ}}{\tau}\right)} \tag{7.23}$$

where the subscript 4 corresponds to the nozzle inlet state, α is a shape parameter for the decay profile, and τ is the time constant of the decay and equal to the duration of the Taylor rarefaction wave passage given in Eq. (5.21). In this expression, the quantity $p_4(t_{CJ})$ is the incident transmitted post-shock pressure, following the interaction of the detonation wave and contact surface, which is obtained by the methods previously described in Ch. 3. Additionally, in Ch. 5 α was determined to be approximately 3 based on a least-squares fit of numerical MOC pressure profiles at the exit of a fully-filled PDE. Lastly, from the definition of Q_1 and (7.23), the initial value $Q_{1,0}$ at $t = t_{CJ}$ is estimated as

$$Q_{1,0} \approx \left(\frac{\partial p_4}{\partial t}\right)\Big|_{t=t_{CJ}} = -\frac{p_4(t_{CJ})}{\tau}\,(\alpha + 1) \tag{7.24}$$

With the expression in Eq. (7.24), the measure of initial flow non-uniformity for various detonable mixtures has been tabulated in Table 7.1 for different thrust chamber L_t/d_t. In this table, the thrust chamber diameter is held constant at 0.1 m and the various L_t/d_t correspond to different chamber lengths. It follows that the temporal gradient $|\partial p_4/\partial t|$ at the nozzle throat becomes more relaxed with longer tube lengths, namely, increasing duration of Taylor wave passage τ, such that $|Q_{1,0}|$ decreases with increasing PDE tube length. Moreover, in the limit that $L_t \to \infty$, the duration of Taylor wave passage $\tau \to \infty$ and the initial non-uniformity of the flow approaches zero. Hence, only in the limit of an infinite tube length does the incident shock dynamics at the nozzle throat become representative of a uniformly propagating shock. Additionally, it should be noted that maximum magnitude of $|Q_{1,0}|$ for realistic PDE configurations is expected to be within that deemed appropriate for use of the two-equation approximation.

Table 7.1. Typical values of incident flow non-uniformity $Q_{1,0}$ for common detonable mixtures at $\phi = 1.0$, $p_1 = 1$ atm, and $T_1 = 300$ K, in a thrust chamber tube with diameter of $d_t = 0.1$ m.

	$Q_{1,0}$ (kg/s^3)			
L_t/d_t	H_2–O_2	H_2–air	C_2H_4–O_2	C_2H_4–air
5	$-5.031 \cdot 10^{10}$	$-2.475 \cdot 10^{10}$	$-5.324 \cdot 10^{10}$	$-2.393 \cdot 10^{10}$
10	$-2.515 \cdot 10^{10}$	$-1.237 \cdot 10^{10}$	$-2.662 \cdot 10^{10}$	$-1.196 \cdot 10^{10}$
20	$-1.258 \cdot 10^{10}$	$-6.187 \cdot 10^{9}$	$-1.331 \cdot 10^{10}$	$-5.982 \cdot 10^{9}$
40	$-6.288 \cdot 10^{9}$	$-3.093 \cdot 10^{9}$	$-6.655 \cdot 10^{9}$	$-2.991 \cdot 10^{9}$
60	$-4.192 \cdot 10^{9}$	$-2.062 \cdot 10^{9}$	$-4.437 \cdot 10^{9}$	$-1.994 \cdot 10^{9}$
80	$-3.144 \cdot 10^{9}$	$-1.547 \cdot 10^{9}$	$-3.328 \cdot 10^{9}$	$-1.495 \cdot 10^{9}$
100	$-2.515 \cdot 10^{9}$	$-1.237 \cdot 10^{9}$	$-2.656 \cdot 10^{9}$	$-1.196 \cdot 10^{9}$
500	$-5.031 \cdot 10^{8}$	$-2.475 \cdot 10^{8}$	$-5.324 \cdot 10^{8}$	$-2.393 \cdot 10^{8}$
1000	$-2.515 \cdot 10^{8}$	$-1.237 \cdot 10^{8}$	$-2.662 \cdot 10^{8}$	$-1.196 \cdot 10^{8}$
∞	0	0	0	0

It is now of interest to compare the results of the current simplified two-equation approximation for the transmitted shock dynamics with that predicted by the lower-order A–M relation and the current MOC model for various thrust chamber lengths. For this, a conical diverging nozzle of fixed length $L_n = 0.5$ m is coupled to the end of a variable length thrust chamber, in order to demonstrate the effects of flow non-uniformity on the transmitted shock attenuation. Figures 7.9–7.11 show the results for a PDE filled with stoichiometric H_2–O_2 detonable mixture and air as the non-combustible at blowdown pressure ratios of $\psi = 1$, 10, and 50, and nozzle expansion area ratios of $\epsilon = 2$, 4, and 8, respectively. In these figures, the results are shown for various nozzle to thrust chamber lengths, L_n/L_t, which is related to the axial fill fraction as $L_n/L_t = (1-\alpha_0)/\alpha_0$. Similarly, the transmitted shock Mach number decrement at the exit of the nozzle is used as the basis for comparison between the various models.

In Figs. 7.9–7.11, very fundamental results are demonstrated. In these cases, it is evident that the A–M relation is unable to properly model the transmitted shock dynam-

ics in PDE nozzles, due to the relation being invariant to flow non-uniformity caused by different thrust chamber lengths. Additionally, it is only in the limit when $L_t \to \infty$ that a true uniformly propagating transmitted shock is established, and the two-equation and MOC models begin to converge towards the shock Mach number decrement predicted by the A–M relation. Secondly, it is evident that the two-equation model accurately models the transmitted shock Mach number attenuation behavior due to the variation in initial flow non-uniformity behind the shock when varying the thrust chamber length. In fact, for $L_n/L_t < 1$, or $\alpha_0 > 0.5$, the current two-equation approximation shares good agreement with the current MOC model such that an average difference of roughly 4 percent is obtained. This result indicates that under these conditions a fairly accurate description of the transmitted shock attenuation can readily be modeled with the simple two-equation approximation, which does not require direct treatment of the flow field behind the transmitted shock. Alternatively, for $L_n/L_t > 1$, or $\alpha_0 < 0.5$, the current two-equation approximation begins to deviate from the MOC results, such that an average difference of roughly 30 percent is obtained. In these cases, it is noted that the discrepancy is primarily caused by the formation of the secondary shock wave behind the transmitted shock during the nozzle starting process, which acts to delay the attenuation of the shock in the nozzle. Hence, in cases where the formation of the secondary shock significantly alters the dynamics of the transmitted shock, the transmitted shock dynamics can only accurately be described with a model similar to the MOC model. Finally, it is noted that given the optimum nozzle performance results of Ch. 6, it is not desirable to operate with $\alpha_0 < 0.5$ at high blowdown pressure ratios. Therefore, many cases of realistic PDE transmitted shock dynamics in various nozzles can be treated with a two-equation approximation, provided severe overexpansion is avoided in the nozzle starting process.

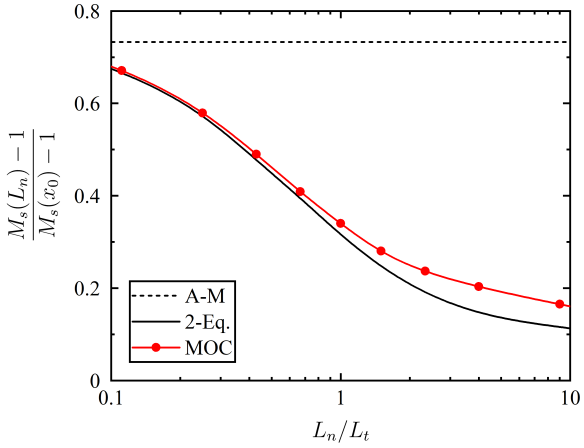

Figure 7.9. Comparison of transmitted shock Mach number decrement $[M_s(L_n) - 1]/[M_s(x_0) - 1]$ at exit of conical diverging nozzle for PDE operating with $2H_2$–O_2 propellant with air as the ambient at different thrust chamber lengths and with $L_n = 0.5$ m, $\epsilon = 2$, and $\psi = 1$.

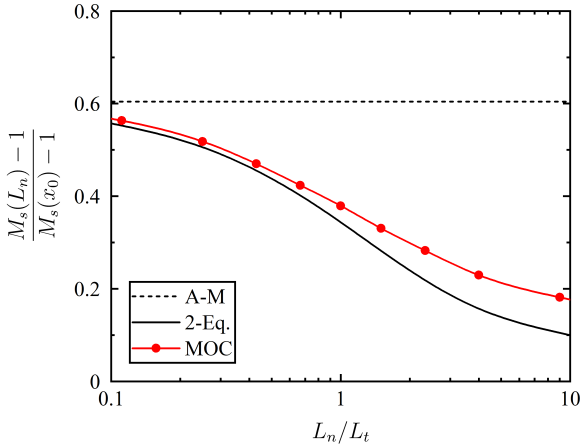

Figure 7.10. Comparison of transmitted shock Mach number decrement $[M_s(L_n) - 1]/[M_s(x_0) - 1]$ at exit of conical diverging nozzle for PDE operating with $2H_2$–O_2 propellant with air as the ambient at different thrust chamber lengths and with $L_n = 0.5$ m, $\epsilon = 4$, and $\psi = 10$.

7.5.2 Nozzle Wall Curvature

In the previous subsection, the influence of initial flow non-uniformity on the transmitted nozzle shock dynamics was investigated and discussed. However, this aspect is only one of two governing mechanisms that can influence the transmitted shock dynamics in a given nozzle. As discussed at the beginning of this chapter, it was shown that the general

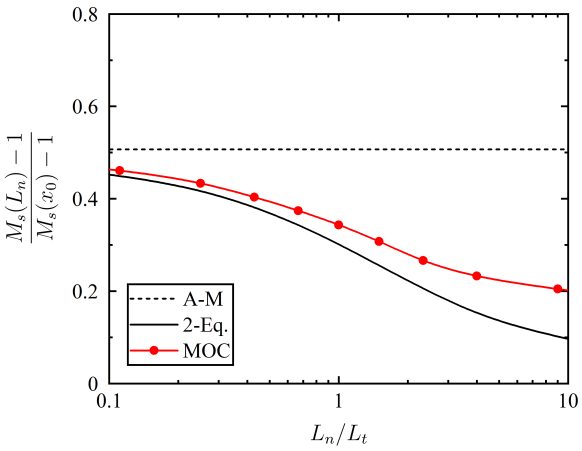

Figure 7.11. Comparison of transmitted shock Mach number decrement $[M_s(L_n) - 1]/[M_s(x_0) - 1]$ at exit of conical diverging nozzle for PDE operating with $2H_2$–O_2 propellant with air as the ambient at different thrust chamber lengths and with $L_n = 0.5$ m, $\epsilon = 8$, and $\psi = 50$.

nozzle shock dynamics is governed by a coupling of the nozzle area contour and by the magnitude of flow non-uniformity behind the transmitted shock. Therefore, it is of interest in this final subsection to investigate the effects of nozzle wall curvature on the motion of the transmitted shock. In particular, this type of study will be of most value in the design of PDE diverging nozzles, as specific nozzle geometries can be selected that most efficiently attenuate the transmitted shock and simultaneously enhance the propulsive performance. In fact, as discussed in previous numerical studies [81, 119], it was shown that bell-shaped diverging nozzles provide superior performance to conical diverging nozzles; however, those studies did not mention the importance of transmitted shock attenuation, and the underlying fundamental relation to impulse generation during the nozzle starting process. As such, a detailed study of nozzle wall curvature is provided in this subsection to highlight the connection between attenuation of the transmitted shock and the associated effects on single-cycle thrust and impulse generation.

For this study, various nozzle shapes are investigated in order to identify which nozzle shape provides the best attenuation of the transmitted shock for a given nozzle length and

expansion area ratio. A general expression for different nozzle contours can be described with an exponential relationship as [119]

$$r(x) = r_0 + (r_e - r_0)\,\frac{e^{\zeta x} - e^{\zeta x_0}}{e^{\zeta x_e} - e^{\zeta x_0}} \tag{7.25}$$

where $r(x)$, r_0, and r_e represent the general nozzle radius, initial radius at the nozzle inlet, and radius at the nozzle exit, respectively. Further, in this form, ζ corresponds to a nozzle shape parameter, such that for $\zeta < 0$, $\zeta = 0$, or $\zeta > 0$, the nozzle features negative, zero, or positive curvature, respectively. Hence, for $\zeta < 0$, the nozzle shape is representative of a classical diverging bell-shaped nozzle. In the case $\zeta = 0$, the nozzle is identical to that of a conical diverging nozzle. Lastly, for $\zeta < 0$, the nozzle shape is representative of a flare-shaped diverging nozzle. Figures 7.12(a)–7.12(c) show schematics for these general nozzle profile shapes.

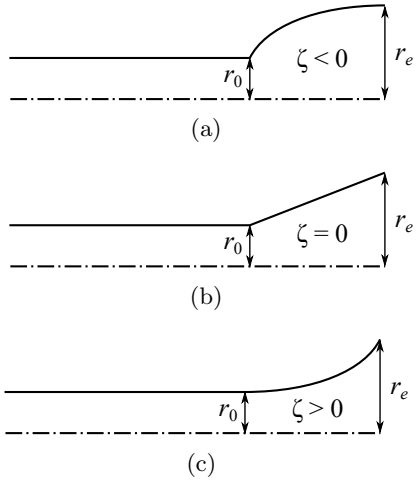

Figure 7.12. (a) Diverging bell-shaped ($\zeta < 0$), (b) conical ($\zeta = 0$), and (c) flare-shaped ($\zeta > 0$) nozzle contours.

The general transmitted shock dynamics solution from the two-equation model is shown in Fig. 7.13 for a PDE operating with stoichiometric H_2–O_2 detonable mixture and air as the ambient, with a diverging nozzle of length $L_n = 0.5$ m and characterized by various shape parameters. In this case, the nozzle consists of an axial fill fraction of $\alpha_0 = 0.7$,

with an expansion area ratio of $\epsilon = 4$ and a blowdown pressure ratio of $\psi = 10$, respectively. It is evident from Fig. 7.13 that the most rapid attenuation in transmitted shock strength is achieved with a bell-shaped diverging nozzle with negative curvature. Although not particularly surprising, this result is directly governed by the rapid expansion of area immediately downstream of the nozzle inlet, which drastically attenuates the transmitted shock. Additionally, such a result is very important and will be useful in the following discussion on impulse generation. The conical diverging nozzle solution is shown by the thick black line at $\zeta = 0$, and represents the intermediate case of transmitted shock attenuation. Lastly, the least rapid shock attenuation takes place in flare-shaped nozzles with positive curvature. Again, this result is to be expected and is directly governed by the very gradual expansion of area after the nozzle inlet, which drastically delays the attenuation of the transmitted shock.

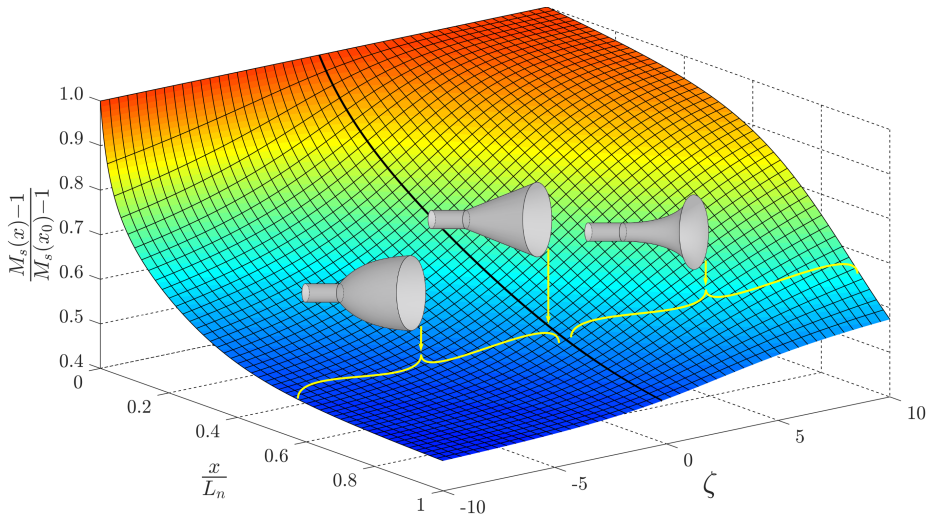

Figure 7.13. Surface plot of general transmitted shock Mach number decrement $[M_s(x) - 1]/[M_s(x_0) - 1]$ from two-equation approximation vs. nozzle location x/L_n and nozzle shape parameter ζ for PDE operating with $2H_2$–O_2 propellant and $\alpha_0 = 0.7$, $\epsilon = 4$, and $\psi = 10$.

The above analysis can be used to provide insights regarding which nozzle shape best attenuates the transmitted shock; however, without any knowledge of possible over-

expansion in the flow field behind the transmitted shock during the nozzle startup process and the resulting impact on thrust and impulse generation. Therefore, it is desired to use the MOC model and quantify the associated effects that the transmitted shock dynamics have on the overall propulsive performance. The transmitted shock dynamics solution from the MOC model is shown in Fig. 7.14 for a PDE operating with stoichiometric H_2–O_2 detonable mixture and air as the ambient, with a diverging nozzle of length $L_n = 0.5$ m and characterized by various shape parameters. As before, the nozzle consists of an axial fill fraction of $\alpha_0 = 0.7$, with an expansion area ratio of $\epsilon = 4$, and a blowdown pressure ratio of $\psi = 10$, respectively. It is noted that these results are in very good agreement with those shown in Fig. 7.13, which were computed using the two-equation approximation. Similarly, the corresponding thrust and impulse are shown in Figs. 7.15(a) and 7.15(b), respectively. In this case, the thrust force has been normalized by $A_0 p_1$, namely, the product of thrust wall area and initial propellant pressure. In these figures, the detonation wave reaches the nozzle inlet at $x/L = 0.7$ at $t/t_{CJ} = 1$, which initiates the nozzle starting process. Note that the generation of thrust from the nozzle occurs more rapidly, and with more magnitude, in the case of a bell-shaped nozzle with negative curvature when compared to that of a flare-shaped nozzle with positive curvature. Additionally, although the most rapid decay of the transmitted shock occurs in the case of $\zeta = -5$ as shown in Fig. 7.14, the location of largest transmitted post-shock pressure corresponds to the largest projected thrust area in the nozzle, which yields the thrust generation results shown in Fig. 7.15(a). Likewise, the lowest amount of thrust generation is achieved with the flare-shaped nozzle characterized with $\zeta = 5$, such that the transmitted shock rapidly attenuates due to the overtaking Taylor rarefaction from behind before encountering the portion of the nozzle that features the largest projected thrust area. Lastly, for this operating condition it follows that the bell-shaped nozzle and flare-shaped nozzle with $\zeta = -5$ and 5, yield total impulse results that are 13.4 and 8.5 percent higher than that of the fully-filled PDE at the same blowdown pressure ratio, respectively.

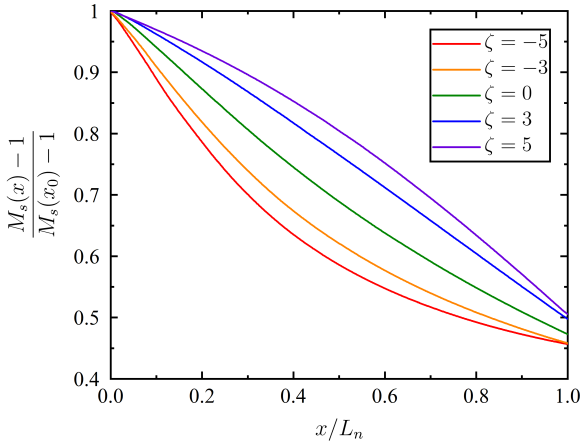

Figure 7.14. Transmitted shock Mach number decrement $[M_s(x) - 1]/[M_s(x_0) - 1]$ from MOC model vs. nozzle location x/L_n and nozzle shape parameter ζ for PDE operating with $2H_2$–O_2 detonable propellant and air as the ambient with $L_n = 0.5$ m, $\alpha_0 = 0.7$, $\epsilon = 4$, and $\psi = 10$.

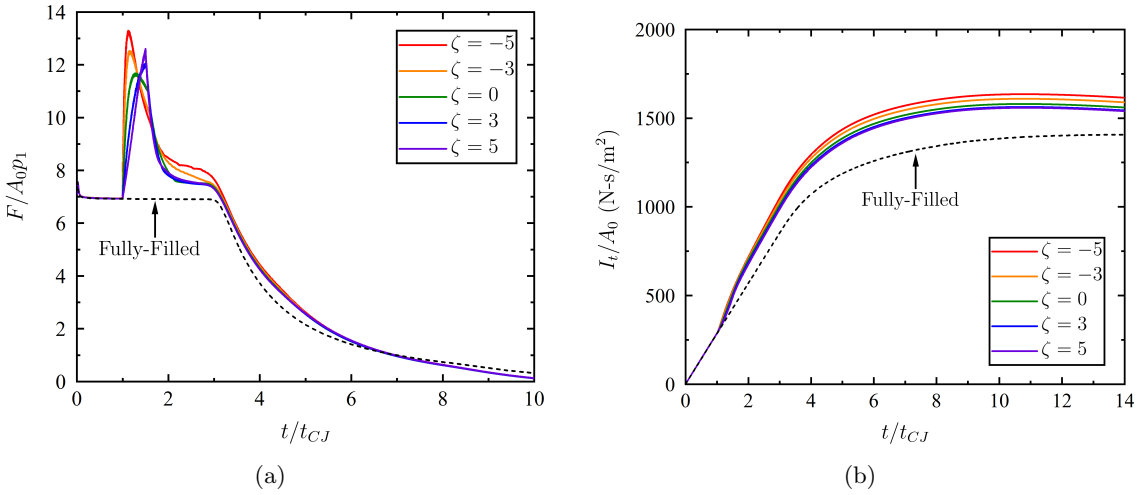

Figure 7.15. (a) Normalized thrust and (b) total impulse per unit thrust-wall area for various nozzle shape parameters ζ of a PDE operating with $2H_2$–O_2 propellant and air as the ambient with $L_n = 0.5$ m, $\alpha_0 = 0.7$, $\epsilon = 4$, and $\psi = 10$.

In a similar manner, the transmitted shock dynamics solution from the MOC model is shown in Fig. 7.16 for a PDE operating with stoichiometric H_2–O_2 detonable mixture and air as the ambient, with a diverging nozzle of length $L_n = 0.5$ m and characterized by various shape parameters. However, in this case the nozzle consists of an axial fill fraction of

$\alpha_0 = 0.7$, with an expansion area ratio of $\epsilon = 20$, and a blowdown pressure ratio of $\psi = 100$, respectively. The corresponding thrust and impulse are shown in Figs. 7.17(a) and 7.17(b), respectively. As before, the generation of thrust from the nozzle occurs more rapidly, and with more magnitude, in the case of a bell-shaped nozzle with negative curvature than that achieved with a flare-shaped nozzle and positive curvature. Similarly, although the most rapid decay of the transmitted shock occurs in the case of $\zeta = -5$ as shown in Fig. 7.16, the location of largest transmitted post-shock pressure corresponds to the largest projected thrust area in the nozzle, which yields the thrust generation results shown in Fig. 7.15(a). Moreover, as before, the lowest amount of thrust generation is achieved with the flare-shaped nozzle characterized with $\zeta = 5$. This is simply a result of the transmitted shock rapidly attenuating due to the overtaking rarefaction from behind before encountering the portion of the nozzle that features the largest projected thrust area. Lastly, for this operating condition it follows that the bell-shaped nozzle and flare-shaped nozzle with $\zeta = -5$ and 5, yield total impulse results that are 22.6 and 9.1 percent higher than that of the fully-filled PDE at the same blowdown pressure ratio.

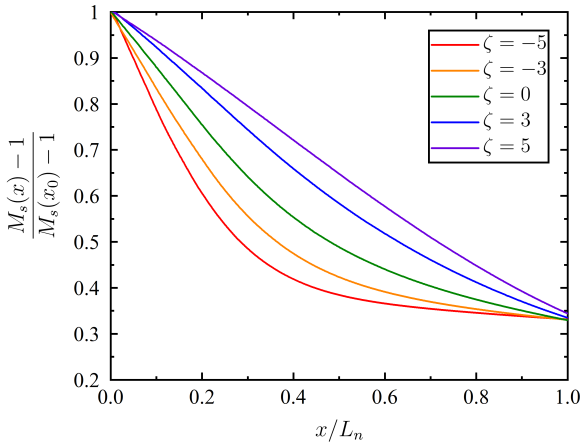

Figure 7.16. Transmitted shock Mach number decrement $[M_s(x) - 1]/[M_s(x_0) - 1]$ from MOC model vs. nozzle location x/L_n and nozzle shape parameter ζ for PDE operating with $2H_2$–O_2 propellant and air as the ambient with $L_n = 0.5$ m, $\alpha_0 = 0.7$, $\epsilon = 20$, and $\psi = 100$.

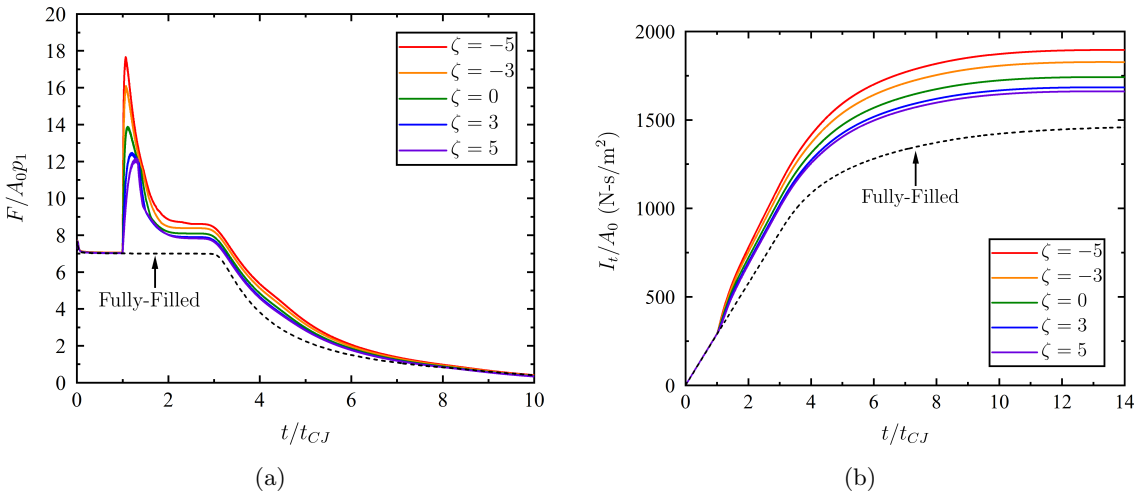

Figure 7.17. (a) Normalized thrust and (b) total impulse per unit thrust-wall area for various nozzle shape parameters ζ of a PDE operating with $2H_2$–O_2 propellant and air as the ambient with $L_n = 0.5$ m, $\alpha_0 = 0.7$, $\epsilon = 20$, and $\psi = 100$.

Finally, a parametric sweep was conducted to show the generalized performance trends of PDEs with diverging nozzles of different nozzle wall curvature by simultaneously varying both the nozzle expansion area ratio and blowdown pressure ratio. In this case, the ambient temperature is kept at 300 K and the ambient pressure is varied from 1–0.01 atm, yielding a blowdown pressure ratio range of 1–100. Similarly, the PDE is comprised of a thrust chamber-to-total length ratio of $\alpha_0 = 0.7$ m, with a diverging nozzle of length $L_n = 0.5$ m. Figure 7.18 shows these results for $\psi = 1$, 10, and 100, over a range of nozzle expansion area ratios. As mentioned previously, it is evident that the best specific impulse is achieved with a bell-shaped diverging nozzle with negative curvature. Additionally, this advantage becomes more pronounced as the nozzle expansion area ratio increases, which is caused by the rapid increase in projected thrust area coinciding with the region of strongest transmitted shock within the nozzle.

From these results, it is clear that the best performance can be achieved when the PDE is equipped with a bell-shaped nozzle over conventional conical or flare-shaped nozzles. Additionally, it appears as though this performance benefit will continue to increase

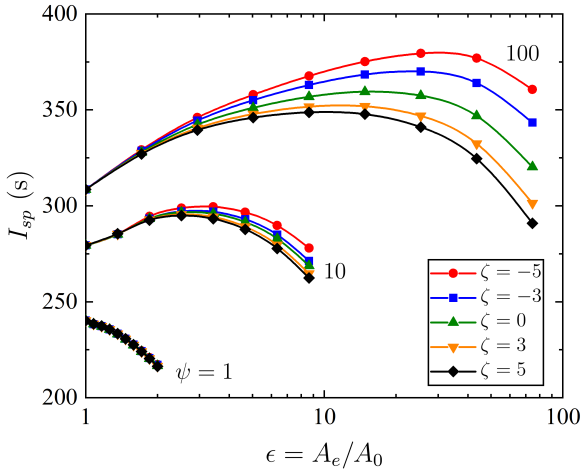

Figure 7.18. Specific impulse variation with ϵ, ψ, and ζ for a PDE with $\alpha_0 = 0.7$ and operating with $2H_2$–O_2 propellant with ambient air in the nozzle.

provided the nozzle wall curvature continually decreases. It is cautioned here that this trend will likely not continue to remain true at very large negative wall curvature. For instance, in the limit that $\zeta \to -\infty$, the bell-shaped nozzle reduces to the case of a nozzle that is characterized by an abrupt area change with a 90 degree turning angle at the nozzle entrance. Clearly, such a nozzle is not practical in PDE design and complications will arise due to the nature of transmitted shock diffraction along the convex walls. For instance, Skews [182, 183] studied shock diffraction over convex walls and noted the complex flow behavior that develops in the perturbed region behind the diffracting shock. Additionally, Skews et al. [184] later studied the shear layer behavior that develops behind a diffracting shock wave, and it was shown that flow separation can occur in the perturbed flow behind the diffracting shock for incident shock Mach numbers as low as 1.3 and deflection angles of only 20 degrees. It is noted here that this is a two-dimensional gasdynamic interaction process that is beyond the scope of the current quasi-one-dimensional analysis. Additionally, this complex gasdynamic interaction is not well studied in application to PDE diverging nozzles, and it is not entirely known to what extent the work of [182–184] is applicable in the design of PDE nozzles as the pressure profile behind the transmitted shock is more

indicative of a blast wave rather than a uniformly propagating shock. However, this complication is noted here as this gasdynamic mechanism will place a geometrical constraint on the largest negative wall curvature that can be used before severe flow separation takes place during the nozzle starting process due to shock diffraction at the nozzle inlet.

CHAPTER 8

CONCLUSIONS AND FUTURE WORK

8.1 Conclusions

The present research investigated the fundamental gasdynamic processes that govern the single-cycle propulsive performance of a pulse detonation engine (PDE). This research effort was separated into a series of related analytical, numerical, and experimental studies focused on various gasdynamic interactions within a PDE thrust chamber and nozzle flow field. The current work studied three distinct PDE operating configurations, namely, the fully- and partially-filled PDE, and PDEs equipped with diverging nozzles. The major conclusions and contributions are summarized below.

A comprehensive description of the PDE thrust chamber flow field for a fully- and partially-filled PDE, and for a PDE equipped with a diverging nozzle was provided. This discussion was used to highlight the various gasdynamic discontinuities, waves, and subsequent interactions that will arise during a single-cycle operation of a general PDE, which must be modeled appropriately in order to accurately evaluate the various propulsive performance metrics.

An analytical description for the one-dimensional interaction of a detonation wave with a contact discontinuity separating a detonable and non-combustible mixture using the Zel'dovich–von Neumann–Döring (ZND) detonation theory was provided. This particular gasdynamic interaction arises in PDEs when the detonation wave reaches the gaseous interface separating the detonable and non-combustible mixtures. Moreover, this gasdynamic interaction directly governs the incident properties of the shock that transmits into the non-combustible mixture, and the incident reflected wave type and strength that propagates upstream into the burned products, which were shown to drastically influence the evolution of the entire thrust chamber flow field. Additionally, a detonation-driven shock

tube facility was developed to experimentally investigate this particular gasdynamic interaction, whereby experiments were conducted at various detonable equivalence ratios and non-combustible inert mixture mole fractions. Finally, the experimental and analytical results were reduced in terms of the ratio of detonable and non-combustible mixture acoustic impedance.

A general quasi-one-dimensional method of characteristics (MOC) model was developed for rapidly evaluating the single-cycle evolution of gasdynamic waves and discontinuities in general PDE thrust chamber flow fields. The MOC model was developed using a simplified unit process approach with an explicit inverse time marching algorithm in order to readily construct the complex thrust chamber flow field along a predefined grid. Moreover, the model incorporated the detonation-contact surface interaction results of Ch. 3 in order to accurately treat the one-dimensional collision of a detonation wave with a contact discontinuity. A thorough validation of the model was presented over a broad range of operating conditions with existing higher-fidelity numerical and experimental performance data for fully- and partially-filled PDEs, and PDEs equipped with diverging nozzles. This included PDEs operating with a variety of detonable fuels, non-combustible inert gases, fill fractions, blowdown pressure ratios, and nozzle expansion area ratios. Further, discussion of the model limitations was provided, and particular operating conditions were addressed whereby the assumptions used in the development of the model begin to breakdown.

A simplified analytical model was developed based on control volume analysis for evaluating the primary performance metrics of a general fully-filled PDE. For this, the MOC model was used to justify and establish a simplified thrust relation based solely on the flow properties at the exit plane of a fully-filled PDE. An analytical description of the thrust chamber flow field was provided, from which an analytical piecewise expression for thrust was derived based on the exit plane pressure history. This expression was then used to evaluate the specific impulse, total impulse, and time-averaged thrust of a fully-filled PDE. Lastly, the simplified model was validated against the current MOC model

and existing higher-fidelity numerical and experimental performance data for a variety of detonable fuels, equivalence ratios, and blowdown pressure ratios.

The present MOC model was used to conduct a broad parametric study of the partially-filled PDE. For this, the method of Ch. 3 was used to tailor the acoustic impedance of the non-combustible inert gas at a fixed fill fraction in order to demonstrate the sensitivity of thrust chamber flow field and PDE performance to the non-combustible acoustic impedance. Additionally, the detonable fill fraction and non-combustible acoustic impedance were varied simultaneously in order to highlight the general role of non-combustible acoustic impedance and fill fraction on the partially-filled PDE performance. Subsequently, a parametric investigation of non-combustible mixture temperature was conducted to characterize the benefit of using moderately cold non-combustible gases at different fill fractions. Similarly, the benefit of partial filling was investigated for partially-filled PDEs operating in sub-atmospheric environments at different fill fractions. It was demonstrated that the specific impulse performance results generated with the MOC model from the various parametric investigations was successfully collapsed using the scaling law proposed by Sato et al. [98]. Additionally, this scaling law was extended to other important performance metrics, such as the total impulse and time-averaged thrust ratios.

Similarly, the single-cycle propulsive performance of PDEs with diverging nozzles was examined. A parametric investigation was conducted by simultaneously varying the nozzle expansion area and blowdown pressure ratios in order to characterize the combined effects on the resulting thrust chamber and nozzle flow fields. Detailed discussion of the transient nozzle flow field was provided in order to emphasize the influence of non-combustible acoustic impedance on the partial-fill effect in diverging nozzles, and the losses associated with severe over-expansion. Moreover, a comparative study was used to demonstrate the performance advantages of diverging nozzles in sub-atmospheric environments compared to straight-extension nozzles. Lastly, a comprehensive parametric investigation was conducted by simultaneously varying the nozzle length, expansion area ratio, and blowdown pressure

ratio in order to determine the optimum nozzle performance characteristics. These results were then compared with a PDE using an idealized quasi-steady nozzle, in order to demonstrate the importance of properly modeling the starting nozzle flow field when evaluating the propulsive performance.

Finally, a rigorous analytical description for the quasi-one-dimensional dynamics of the transmitted shock wave inside a general contour diverging nozzle was provided. This model was derived on the basis of a two-equation approximation of the generalized Chester–Chisnell–Whitham (CCW) theory for treating general shock dynamics in non-uniform channels. Additionally, unlike previous models, the present model included the effects of both area change and flow non-uniformity behind the transmitted shock, which was shown to be essential for accurate modeling of the transmitted shock dynamics in PDE nozzles. This model was also used to demonstrate how the thrust chamber length governs the magnitude of flow non-uniformity behind the transmitted shock entering the nozzle, and how drastically this can influence the nature of shock attenuation within the nozzle. Moreover, the shock dynamics model was used in conjunction with the current MOC model to demonstrate how different nozzle wall curvature influences the PDE propulsive performance, due to the changes in transmitted shock attenuation in the nozzle flow field during the nozzle starting process. It was shown that bell-shaped nozzles with negative wall curvature provide the most rapid transmitted shock attenuation and best overall propulsive performance.

8.2 Suggestions for Future Work

Based on the findings of the present research project, a few suggestions can be made to guide future research on fundamental gasdynamic interaction studies, continued development of PDE propulsion systems, and other related unsteady gasdynamic research areas. These suggestions are described below.

The analytical model developed for treating the one-dimensional interaction of a detonation wave with a contact discontinuity relied on the selection of a representative

post-detonation state to accurately model the transmitted shock and reflected wave properties. Moreover, this approach was shown to have good agreement with experimental transmitted shock velocity time-of-flight measurements in a detonation-driven shock tube. However, such an analytical model is approximate in nature, as the complete interaction of the reflected wave with the detonation induction and reaction zones are bypassed. Improvements to the present model can be made by studying this gasdynamic interaction using a high-fidelity numerical approach. For instance, a one-dimensional numerical model with a coupled finite-rate chemistry model could be used to directly compute the head-on collision of a ZND detonation wave with a contact discontinuity with high spatial and temporal resolution, including the subsequent interaction of the reflected wave with the induction and reaction zones. Such analysis could be used to provide better insights regarding the reaction zone influence on the transmitted shock properties. Additionally, improved experiments could be conducted in detonation-driven shock tubes, where the physical diaphragms are replaced with a slide gate valve and optical access is used to obtain high-speed schlieren imaging for instantaneous time-of-flight measurements.

In general, the MOC model developed in this work was shown to have very good agreement with existing higher-fidelity numerical and experimental performance data for PDEs operating with a variety of detonable fuels, non-combustible inert gases, fill fractions, blowdown pressure ratios, and nozzle expansion area ratios. However, to simplify the development of the model, the flow was assumed to be isentropic and free from any frictional and heat transfer losses. It was also demonstrated that such assumptions can lead to an underestimation of the actual PDE performance as the thrust chamber L/d increases. Therefore, improvements to the current MOC model can readily be made by incorporating the friction and heat transfer models proposed by Owens and Hanson [150] for PDEs. It is noted that incorporating these physical loss mechanisms will change the governing equations from which the characteristic and compatibility conditions used herein were based. However, details on how to extend the present MOC approach to non-isentropic flows with friction and

heat losses can be found in Zucrow and Hoffman [143,144]. Similarly, the present model can be improved by removing the frozen flow assumption for the burned products, and implementing a coupled finite-rate chemistry model with reduced chemical kinetics to treat the true chemically reacting flow field during the gasdynamic blowdown process. Although, it is noted that coupling a finite-rate chemistry model can greatly increase the computational expense of the present model.

It was shown with the proposed partially-filled PDE scaling law for $I_t/I_{t,full}$ in Eq. (6.6) that the total impulse ratio is not bounded by unity. In fact, the combination of fill fractions and detonable-to-inert mixture densities that cause $I_t/I_{t,full}$ to exceed unity were shown in Fig. 6.14. It is of interest in the future development of PDE propulsion systems to explore the operating conditions that yield $I_t/I_{t,full} \approx 1$, and verify if such performance can be realized in practical systems. At present, few experiments have explored these operating conditions, which could prove very useful for the performance enhancement of PDEs employing the partial-fill method. This is especially true for airbreathing PDEs operating with hydrogen-based fuels and ambient air as the inert gas, since the detonable-to-inert density ratio is in the appropriate region for $I_t/I_{t,full} \approx 1$. However, the present results indicate that this can also be achieved with general fuels, provided a relatively cold inert gas is used, since the inert gas acoustic impedance scales inversely with the temperature.

The parametric investigation of diverging nozzles indicated that a properly designed nozzle can be very useful at drastically enhancing the performance of a fully-filled PDE at high blowdown pressure ratios. Additionally, it was determined that bell-shaped nozzles with negative curvature provide the best diverging nozzle design for rapidly attenuating the transmitted shock and increasing the transient generation of thrust and impulse. However, these results are based on an inviscid quasi-one-dimensional analysis, such that the two-dimensional aspects of transmitted shock diffraction and subsequent shock-boundary layer interaction in the nozzle were neglected. Moreover, it is known that shock diffraction over convex walls will generally yield flow separation in the perturbed region behind the diffract-

ing shock [184]. This is a feature of PDE nozzle flows that has received minimal treatment in the literature, and is believed to be a crucial feature of proper nozzle design for PDEs. A simple inviscid reduced-order model for this problem can readily be obtained by incorporating the current two-equation approximation of shock dynamics, and the accompanying flow non-uniformity, with the classical theory of geometrical shock dynamics [177]. In this manner, the flow non-uniformity can be taken into consideration and the two-dimensional dynamics of the transmitted shock propagation through a given diverging nozzle can be studied. However, higher-fidelity numerical and experimental methods will be required to study the subsequent transmitted and secondary shock-boundary layer interactions during the nozzle starting process.

Lastly, the quasi-one-dimensional MOC model developed for this study can readily be extended to serve as a preliminary design tool for many relevant aerospace applications involving unsteady gasdynamics. For instance, the present model could be used to support the design of future shock and detonation tubes for fundamental gasdynamic studies, and the design of future high-enthalpy wind tunnel facilities such as hypersonic and detonation-driven shock tunnels.

APPENDIX A

THERMODYNAMIC CYCLE RELATIONS

A.1 Thermodynamic Cycle Derivation

As shown in Ch. 1, the general thermal efficiency for any idealized cycle can be expressed as

$$\eta_{th} = 1 - \frac{\frac{c_{p,2}T_{10}}{c_{p,1}T_0} - 1}{\bar{q}} \tag{A.1}$$

where $\bar{q} = q_{add}/c_{p,1}T_0$. Therefore, it is of interest to obtain an expression for T_{10}/T_0 for any cycle with a specified heat addition process. In general, the temperature ratio T_{10}/T_0 can be expressed as function of the upstream processes in the cycle as

$$\frac{T_{10}}{T_0} = \frac{T_{10}}{T_4}\frac{T_4}{T_3}\frac{T_3}{T_0} \tag{A.2}$$

Additionally, recall that for the idealized cycle analysis, the burned products are assumed to isentropically expand from state 4–10 through the nozzle; hence T_{10}/T_4 may be expressed as

$$\frac{T_{10}}{T_4} = \left(\frac{p_{10}}{p_4}\right)^{(\gamma_2-1)/\gamma_2} \tag{A.3}$$

Since $p_{10} = p_0$, and noting that the free stream is assumed to isentropically compress from state 0–3, Eq. (A.3) can be rewritten as

$$\frac{T_{10}}{T_4} = \left(\frac{p_3}{p_4}\right)^{(\gamma_2-1)/\gamma_2} \psi^{-\frac{\gamma_1(\gamma_2-1)}{\gamma_2(\gamma_1-1)}} \tag{A.4}$$

where $\psi = T_3/T_0$. Lastly, substituting Eq. (A.4) into (A.2), after algebraic manipulation, yields

$$\frac{T_{10}}{T_0} = \left(\frac{p_3}{p_4}\right)^{(\gamma_2-1)/\gamma_2} \left(\frac{T_4}{T_3}\right) \psi^{1-\frac{\gamma_1(\gamma_2-1)}{\gamma_2(\gamma_1-1)}} \tag{A.5}$$

Note that Eq. (A.5) is completely general for an idealized cycle and requires no knowledge of the heat addition process. As such, substituting the heat addition processes from the PDE and Brayton cycles will yield the desired temperature ratio of the rejected heat from states 10–0, and the resulting cycle thermal efficiency.

A.1.1 PDE Cycle

For the PDE cycle, the pressure and temperature ratios from state 3–4 are given by the pressure and temperature ratios across the detonation wave front. These ratios can be expressed in closed form [65] as

$$\frac{p_4}{p_3} = \frac{\gamma_1 M_{CJ}^2 + 1}{\gamma_2 + 1} \tag{A.6}$$

$$\frac{T_4}{T_3} = \frac{\gamma_1 R_1}{\gamma_2 R_2} \left(\frac{\gamma_1 M_{CJ}^2 + 1}{\gamma_1 M_{CJ}} \frac{\gamma_2}{\gamma_2 + 1} \right)^2 \tag{A.7}$$

Substituting these expressions into Eq. (A.5), after algebraic manipulation, yields

$$\frac{T_{10}}{T_0} = \frac{R_1 \gamma_1}{R_2 \gamma_2 M_{CJ}^2} \left(\frac{\gamma_1 M_{CJ}^2 + 1}{\gamma_2 + 1} \right)^{\frac{\gamma_2+1}{\gamma_2}} \psi^{1-\frac{\gamma_1(\gamma_2-1)}{\gamma_2(\gamma_1-1)}} \tag{A.8}$$

Lastly, substituting this expression into Eq. (A.1) yields the final result

$$\eta_{th,PDE} = 1 - \frac{\frac{\gamma_1 - 1}{\gamma_2 - 1} \left(\frac{\gamma_2}{\gamma_1 M_{CJ}} \right)^2 \left(\frac{\gamma_1 M_{CJ}^2 + 1}{\gamma_2 + 1} \right)^{(\gamma_2+1)/\gamma_2} \psi^{1-\frac{\gamma_1(\gamma_2-1)}{\gamma_2(\gamma_1-1)}} - 1}{\bar{q}} \tag{A.9}$$

A.1.2 Brayton Cycle

For the Brayton cycle, the constant-pressure heat addition process from state 3–4 can be expressed as,

$$q_{add} = \int_3^4 T \, ds = h_4 - h_3 = c_{p,2} T_4 - c_{p,1} T_3 \tag{A.10}$$

which makes use of the combined first and second laws for a constant-pressure process. Rearranging Eq. (A.10) yields

$$\frac{T_4}{T_3} = \frac{c_{p,1}}{c_{p,2}} \left(\frac{\bar{q}}{\psi} + 1 \right) \tag{A.11}$$

Substituting this expression into the general temperature ratio expression of Eq. (A.5), and noting that $p_4 = p_3$ for the constant-pressure heat addition process

$$\frac{T_{10}}{T_0} = \frac{c_{p,1}}{c_{p,2}} \left(\frac{\bar{q}}{\psi} + 1 \right) \psi^{1-\frac{\gamma_1(\gamma_2-1)}{\gamma_2(\gamma_1-1)}} \tag{A.12}$$

Lastly, substituting this expression into Eq. (A.1) yields the final result

$$\eta_{th,Brayton} = 1 - \frac{\left(\frac{\bar{q}}{\psi} + 1 \right) \psi^{1-\frac{\gamma_1(\gamma_2-1)}{\gamma_2(\gamma_1-1)}} - 1}{\bar{q}} \tag{A.13}$$

APPENDIX B

METHOD OF CHARACTERISTICS

In this appendix, the characteristic form of the governing equations are derived, with the accompanying characteristic and compatibility relations. This is achieved by application of the method of characteristics to the governing system of partial differential equations [143, 144]. The governing equations for an unsteady, quasi-one-dimensional flow in the absence of friction, mass addition, and heat transfer, were provided in Eqs. (4.1)-(4.3) as:

$$\frac{\partial \rho}{\partial t} + u\frac{\partial \rho}{\partial x} + \rho\frac{\partial u}{\partial x} + \rho u\frac{A'(x)}{A(x)} = 0 \tag{4.1}$$

$$\frac{\partial u}{\partial t} + u\frac{\partial u}{\partial x} + \frac{1}{\rho}\frac{\partial p}{\partial x} = 0 \tag{4.2}$$

$$\frac{\partial p}{\partial t} + u\frac{\partial p}{\partial x} - a^2\left(\frac{\partial \rho}{\partial t} + u\frac{\partial \rho}{\partial x}\right) = 0 \tag{4.3}$$

Taking a linear combination of the mass, momentum, and energy equations in the unknown parameters σ_1, σ_2, and σ_3 yields

$$\begin{aligned}\sigma_1\left[\frac{\partial \rho}{\partial t} + u\frac{\partial \rho}{\partial x} + \rho\frac{\partial u}{\partial x} + \rho u\frac{A'(x)}{A(x)}\right] + \sigma_2\left[\frac{\partial u}{\partial t} + u\frac{\partial u}{\partial x} + \frac{1}{\rho}\frac{\partial p}{\partial x}\right] \\ + \sigma_3\left[\frac{\partial p}{\partial t} + u\frac{\partial p}{\partial x} - a^2\left(\frac{\partial \rho}{\partial t} + u\frac{\partial \rho}{\partial x}\right)\right] = 0\end{aligned} \tag{B.1}$$

Factoring out the coefficients of the x derivatives in Eq. (B.1) yields

$$\begin{aligned}(\rho\sigma_1 + \rho u\sigma_2)\left[\frac{\partial u}{\partial x} + \frac{\rho\sigma_2}{\rho\sigma_1 + \rho u\sigma_2}\frac{\partial u}{\partial t}\right] + (\sigma_2 + u\sigma_3)\left[\frac{\partial p}{\partial x} + \frac{\sigma_3}{\sigma_2 + u\sigma_3}\frac{\partial p}{\partial t}\right] \\ + \left(u\sigma_1 - a^2 u\sigma_3\right)\left[\frac{\partial \rho}{\partial x} + \frac{\sigma_1 - a^2\sigma_3}{u\sigma_1 - a^2 u\sigma_3}\frac{\partial \rho}{\partial t}\right] + \sigma_1\rho u\frac{A'(x)}{A(x)} = 0\end{aligned} \tag{B.2}$$

Further, if it is assumed that $u(x,t)$, $\rho(x,t)$, and $p(x,t)$ are continuous functions, then the following exact differentials hold

$$du = \frac{\partial u}{\partial x}dx + \frac{\partial u}{\partial t}dt \tag{B.3}$$

$$d\rho = \frac{\partial \rho}{\partial x}dx + \frac{\partial \rho}{\partial t}dt \tag{B.4}$$

$$dp = \frac{\partial p}{\partial x}dx + \frac{\partial p}{\partial t}dt \tag{B.5}$$

Differentiating these expressions with respect to the spatial coordinate x yields

$$\frac{du}{dx} = \frac{\partial u}{\partial x} + \frac{\partial u}{\partial t}\frac{dt}{dx} = \frac{\partial u}{\partial x} + \lambda\frac{\partial u}{\partial t} \tag{B.6}$$

$$\frac{d\rho}{dx} = \frac{\partial \rho}{\partial x} + \frac{\partial \rho}{\partial t}\frac{dt}{dx} = \frac{\partial \rho}{\partial x} + \lambda \frac{\partial \rho}{\partial t} \tag{B.7}$$

$$\frac{dp}{dx} = \frac{\partial p}{\partial x} + \frac{\partial p}{\partial t}\frac{dt}{dx} = \frac{\partial p}{\partial x} + \lambda \frac{\partial p}{\partial t} \tag{B.8}$$

Substituting the exact differentials of Eqs. (B.6)–(B.8) into Eq. (B.2) yields,

$$(\rho\sigma_1 + \rho u\sigma_2)\frac{du}{dx} + (\sigma_2 + u\sigma_3)\frac{dp}{dx} + \left(u\sigma_1 - a^2 u\sigma_3\right)\frac{d\rho}{dx} + \sigma_1 \rho u \frac{A'(x)}{A(x)} = 0 \tag{B.9}$$

or equivalently,

$$(\rho\sigma_1 + \rho u\sigma_2)\,du + (\sigma_2 + u\sigma_3)\,dp + \left(u\sigma_1 - a^2 u\sigma_3\right)d\rho + \sigma_1 \rho u \frac{A'(x)}{A(x)}dx = 0 \tag{B.10}$$

This is the general compatibility equation and will be used to derive the compatibility relations for the C_+, C_- and C_0 characteristic in Eqs. (4.4)–(4.7).

Recognizing that the slope of the characteristic curves, $dt/dx = \lambda$, are the coefficients of the derivatives $\partial u/\partial t$, $\partial p/\partial t$, and $\partial \rho/\partial t$ in (B.2), it then follows that

$$\lambda = \frac{\sigma_2}{\sigma_1 + u\sigma_2} = \frac{\sigma_3}{\sigma_2 + u\sigma_3} = \frac{\sigma_1 - a^2\sigma_3}{u\sigma_1 - a^2 u\sigma_3} \tag{B.11}$$

Solving the system of equations in Eq. (B.11) for σ_1, σ_2, and σ_3 yields

$$\sigma_1(\lambda) + \sigma_2(u\lambda - 1) = 0 \tag{B.12}$$

$$\sigma_2(\lambda) + \sigma_3(u\lambda - 1) = 0 \tag{B.13}$$

$$\sigma_1(u\lambda - 1) + \sigma_3 a^2(1 - u\lambda) = 0 \tag{B.14}$$

Since the equation system in Eqs. (B.12)–(B.14) is homogeneous, it directly follows that the only case in which the system can have additional solutions other than the trivial solution is when the determinant of the coefficient matrix is exactly equal to zero. If this condition occurs, then there are an infinite number of solutions that satisfy the system. Thus, taking the determinant yields

$$\begin{vmatrix} \lambda & (u\lambda - 1) & 0 \\ 0 & \lambda & (u\lambda - 1) \\ (u\lambda - 1) & 0 & -a^2(u\lambda - 1) \end{vmatrix} = 0 \tag{B.15}$$

$$(u\lambda - 1)\left[(u\lambda - 1)^2 - a^2\lambda^2\right] = 0 \tag{B.16}$$

Note that Eq. (B.16) is cubic in λ and consequently has three roots. Setting the first term equal to zero and solving for the first root yields

$$\left(\frac{dt}{dx}\right)_0 = \lambda_0 = \frac{1}{u} \tag{B.17}$$

This expression represents the slope along the C_0 pathline characteristic in x–t space, as the the slope is directly equal to the local gas velocity. Similarly, letting the second term be equal to zero and solving for the two remaining roots yields

$$\left(\frac{dt}{dx}\right)_\pm = \lambda_\pm = \frac{1}{u \pm a} \tag{B.18}$$

This expressions represent the slopes along the C_+ and C_- characteristics in x–t space, respectively. Therefore, the results above indicates that the determinant of the coefficient matrix is exactly equal to zero provided $(u\lambda - 1) = 0$ along the C_0 pathline characteristic, or if $(u\lambda - 1) = a\lambda$ along the C_+ and C_- characteristics. Thus, to derive the characteristic form of the governing equations it is desired to determine the values of σ_1, σ_2, and σ_3 along the C_0, C_+, and C_- characteristics.

Along the pathline characteristic, $(u\lambda - 1) = 0$, hence:

$$\begin{aligned} \sigma_1 &= -\sigma_2\frac{(u\lambda - 1)}{\lambda} = 0 \\ \sigma_2 &= -\sigma_3\frac{(u\lambda - 1)}{\lambda} = 0 \end{aligned} \tag{B.19}$$

Consequently, σ_3 becomes arbitrary, and without loss of generality $\sigma_3 = 1$.

Along the $C_\pm$ characteristics, $(u\lambda - 1) = a\lambda$, hence:

$$\begin{aligned} \sigma_1 &= -\sigma_2\frac{(u\lambda - 1)}{\lambda} \\ \sigma_2 &= -\sigma_3\frac{(u\lambda - 1)}{\lambda} \\ \sigma_1 &= \sigma_3\frac{a^2(u\lambda - 1)}{(u\lambda - 1)} = a^2\sigma_3 \end{aligned} \tag{B.20}$$

Notice that this system is not independent since the last equation is a redundant expression in regard to the first. Therefore, there exist only two independent relations between σ_1,

σ_2, and σ_3, and one of the $\sigma's$ can be treated as arbitrary. Thus, arbitrarily letting $\sigma_3 = 1$ yields

$$\begin{aligned} \sigma_1 &= a^2 \\ \sigma_2 &= -\frac{(u\lambda - 1)}{\lambda} = \pm\frac{a\lambda}{\lambda} = \pm a \\ \sigma_3 &= 1 \end{aligned} \tag{B.21}$$

In summary it follows that:

$$\text{Along } C_0: \quad \begin{bmatrix} \sigma_1 \\ \sigma_2 \\ \sigma_3 \end{bmatrix} = \begin{bmatrix} 0 \\ 0 \\ 1 \end{bmatrix}, \quad \text{Along } C_+: \quad \begin{bmatrix} \sigma_1 \\ \sigma_2 \\ \sigma_3 \end{bmatrix} = \begin{bmatrix} a^2 \\ a \\ 1 \end{bmatrix}, \quad \text{Along } C_-: \quad \begin{bmatrix} \sigma_1 \\ \sigma_2 \\ \sigma_3 \end{bmatrix} = \begin{bmatrix} a^2 \\ -a \\ 1 \end{bmatrix} \tag{B.22}$$

Substituting the expressions for σ_1, σ_2, and σ_3 in Eq. (B.22) into the general compatibility equation in Eq. (B.10) yields, after algebraic manipulation:

$$dp_+ + \rho a du_+ = -\rho u a^2 \frac{A'(x)}{A(x)} dt \tag{B.23}$$

$$dp_- - \rho a du_- = -\rho u a^2 \frac{A'(x)}{A(x)} dt \tag{B.24}$$

$$dp_0 + a^2 \rho du_0 = 0 \tag{B.25}$$

Note that Eqs. (B.23), (B.24), and (B.25) corresponds to the differential compatibility equations along the C_+, C_-, and C_0 characteristics, respectively.

Finally, substituting the expressions for σ_1, σ_2, and σ_3 into Eq. (B.2), after algebraic manipulation, yields the characteristic form of the governing equations:

$$\frac{\partial p}{\partial t} + (u + a)\frac{\partial p}{\partial x} + \rho a \left(\frac{\partial u}{\partial t} + (u + a)\frac{\partial u}{\partial x} \right) = -\rho a^2 u \frac{A'(x)}{A(x)} \tag{B.26}$$

$$\frac{\partial p}{\partial t} + (u - a)\frac{\partial p}{\partial x} - \rho a \left(\frac{\partial u}{\partial t} + (u - a)\frac{\partial u}{\partial x} \right) = -\rho a^2 u \frac{A'(x)}{A(x)} \tag{B.27}$$

$$\frac{\partial p}{\partial t} + u\frac{\partial p}{\partial x} - a^2 \left(\frac{\partial \rho}{\partial t} + u\frac{\partial \rho}{\partial x} \right) = 0 \tag{B.28}$$

Note that Eqs. (B.26), (B.27), and (B.28) corresponds to the governing characteristic equations along the C_+, C_-, and C_0 characteristics, respectively.

In summary, Eqs. (B.17) and (B.18) represent the ordinary differential characteristic equations along the C_+, C_-, and C_0 characteristics, and Eqs. (B.23)–(B.25) represent the ordinary differential compatibility equations along the C_+, C_-, and C_0 characteristics, respectively. Hence, it has been shown that by application of the method of characteristics, the governing system of quasi-linear hyperbolic partial differential equations, namely, Eqs. (4.1)–(4.3), are transformed into a system of characteristic ordinary differential equations that can readily be solved using the simple numerical scheme detailed in Ch. 4.

APPENDIX C

GENERALIZED CCW THEORY

C.1 Generalized CCW Theory Derivation

In order to derive (7.5), it is required to apply the C_+ compatibility condition in Eq. (B.23) to the shock trajectory. Hence, differentiating (B.23) with respect to time yields,

$$\frac{dp}{dt} + \rho a \frac{du}{dt} = -\rho u a^2 \frac{A'(x)}{A(x)} \tag{C.1}$$

where the subscript + has been dropped. In this form, it is noted that dt represents a total derivative along the shock path. Therefore, expanding the left-hand side of Eq. (C.1) and noting that $dx/dt = a_0 M$ along the shock, yields,

$$\frac{dp}{dt} + \rho a \frac{du}{dt} = \frac{\partial p}{\partial t} + a_0 M \frac{\partial p}{\partial x} + \rho a \left(\frac{\partial u}{\partial t} + a_0 M \frac{\partial u}{\partial x} \right) \tag{C.2}$$

or equivalently,

$$\frac{dp}{dt} + \rho a \frac{du}{dt} = \frac{\partial p}{\partial t} + \rho a \frac{\partial u}{\partial t} + a_0 M \left(\frac{\partial p}{\partial x} + \rho a \frac{\partial u}{\partial x} \right) \tag{C.3}$$

Recall that the governing partial differential equation along the C_+ characteristic was derived in the previous section as,

$$\frac{\partial p}{\partial t} + (u+a) \frac{\partial p}{\partial x} + \rho a \left(\frac{\partial u}{\partial t} + (u+a) \frac{\partial u}{\partial x} \right) = -\rho a^2 u \frac{A'(x)}{A(x)} \tag{B.26}$$

or equivalently,

$$\frac{\partial p}{\partial x} + \rho a \frac{\partial u}{\partial x} = -\frac{1}{u+a} \left(\frac{\partial p}{\partial t} + \rho a \frac{\partial u}{\partial t} + \rho a^2 u \frac{A'(x)}{A(x)} \right) \tag{C.4}$$

Therefore, substituting Eq. (C.4) into Eq. (C.3) yields

$$\frac{dp}{dt} + \rho a \frac{du}{dt} = \frac{\partial p}{\partial t} + \rho a \frac{\partial u}{\partial t} - \frac{a_0 M}{u+a} \left(\frac{\partial p}{\partial t} + \rho a \frac{\partial u}{\partial t} + \rho a^2 u \frac{A'(x)}{A(x)} \right) \tag{C.5}$$

Grouping like terms and simplifying yields

$$\frac{dp}{dt} + \rho a \frac{du}{dt} = -\left[a_0 M \left(\frac{\rho a^2 u}{u+a} \right) \frac{A'(x)}{A(x)} + \left(\frac{a_0 M}{u+a} - 1 \right) \left(\frac{\partial p}{\partial t} + \rho a \frac{\partial u}{\partial t} \right) \right] \tag{C.6}$$

Additionally, since this expression is being applied to the shock wave, the RH shock jump conditions show that $p = p(M)$, $\rho = \rho(M)$, $u = u(M)$, and $a = a(M)$; therefore; Eq. (C.6) can be reduced to,

$$\left(\frac{dp}{dM} + \rho a \frac{du}{dM} \right) \frac{dM}{dt} = -\left[a_0 M \left(\frac{\rho a^2 u}{u+a} \right) \frac{A'(x)}{A(x)} + \left(\frac{a_0 M}{u+a} - 1 \right) \left(\frac{\partial p}{\partial t} + \rho a \frac{\partial u}{\partial t} \right) \right] \tag{C.7}$$

or equivalently,

$$\frac{dM}{dt} = -\left(\frac{dp}{dM} + \rho a \frac{du}{dM}\right)^{-1} \left[a_0 M \left(\frac{\rho a^2 u}{u+a}\right) \frac{A'(x)}{A(x)} + \left(\frac{a_0 M}{u+a} - 1\right)\left(\frac{\partial p}{\partial t} + \rho a \frac{\partial u}{\partial t}\right)\right] \quad \text{(C.8)}$$

Lastly, noting that $dx/dt = a_0 M$, it follows that

$$\begin{aligned} \frac{dM}{dx} &= -\frac{1}{a_0 M}\left(\frac{dp}{dM} + \rho a \frac{du}{dM}\right)^{-1} \\ &\times \left[a_0 M \left(\frac{\rho a^2 u}{u+a}\right) \frac{A'(x)}{A(x)} + \left(\frac{a_0 M}{u+a} - 1\right)\left(\frac{\partial p}{\partial t} + \rho a \frac{\partial u}{\partial t}\right)\right] \end{aligned} \quad \text{(C.9)}$$

Similarly, in terms of the coefficient functions $g(M)$ and $f(M)$,

$$\frac{dM}{dx} = -\left[\frac{1}{g(M)} \frac{A'(x)}{A(x)} + f(M) Q_1\right] \quad \text{(C.10)}$$

where $Q_1 = \partial p/\partial t + \rho a \partial u/\partial t$.

Similarly, in order to derive (7.6), it is required that ρ, u, and p be continuously differentiable. Hence, we can write,

$$\frac{\partial}{\partial x}\left[\frac{\partial^n}{\partial t}\left(\frac{\partial p}{\partial t} + \rho a \frac{\partial u}{\partial t}\right)\right] = \frac{\partial^{n+1}}{\partial x \partial t^n}\left(\frac{\partial p}{\partial t}\right) + \frac{\partial^{n+1}}{\partial x \partial t^n}\left(\rho a \frac{\partial u}{\partial t}\right) \quad \text{(C.11)}$$

Applying Clairaut's theorem allows reordering the partial derivatives of x and t for the second term on the right-hand side, namely,

$$\frac{\partial^{n+1}}{\partial x \partial t^n}\left(\rho a \frac{\partial u}{\partial t}\right) = \frac{\partial^{n+1}}{\partial t^n \partial x}\left(\rho a \frac{\partial u}{\partial t}\right) \quad \text{(C.12)}$$

Therefore, (C.11) can be rewritten as

$$\frac{\partial}{\partial x}\left[\frac{\partial^n}{\partial t}\left(\frac{\partial p}{\partial t} + \rho a \frac{\partial u}{\partial t}\right)\right] = \frac{\partial^{n+1}}{\partial x \partial t^n}\left(\frac{\partial p}{\partial t}\right) + \frac{\partial^{n+1}}{\partial t^n \partial x}\left(\rho a \frac{\partial u}{\partial t}\right) \quad \text{(C.13)}$$

Expanding the right-hand side of Eq. (C.13) yields,

$$\frac{\partial}{\partial x}\left[\frac{\partial^n}{\partial t}\left(\frac{\partial p}{\partial t} + \rho a \frac{\partial u}{\partial t}\right)\right] = \frac{\partial}{\partial x}\left[\frac{\partial^{n+1} p}{\partial t}\right] + \frac{\partial^n}{\partial t}\left[\rho a \frac{\partial}{\partial x}\left(\frac{\partial u}{\partial t}\right) + \frac{\partial}{\partial x}(\rho a)\frac{\partial u}{\partial t}\right] \quad \text{(C.14)}$$

or equivalently,

$$\frac{\partial}{\partial x}\left[\frac{\partial^n}{\partial t}\left(\frac{\partial p}{\partial t} + \rho a \frac{\partial u}{\partial t}\right)\right] = \frac{\partial}{\partial x}\left(\frac{\partial^{n+1} p}{\partial t}\right) + \frac{\partial^n}{\partial t}\left[\rho a \frac{\partial}{\partial x}\left(\frac{\partial u}{\partial t}\right)\right] + \frac{\partial^n}{\partial t}\left[\frac{\partial}{\partial x}(\rho a)\frac{\partial u}{\partial t}\right] \quad \text{(C.15)}$$

Similarly, we can write

$$\frac{\partial^{n+1}}{\partial t}\left(\frac{\partial p}{\partial x}+\rho a\frac{\partial u}{\partial x}\right)=\frac{\partial^{n+1}}{\partial t}\left(\frac{\partial p}{\partial x}\right)+\frac{\partial^{n+1}}{\partial t}\left(\rho a\frac{\partial u}{\partial x}\right) \tag{C.16}$$

Expanding the right-hand side Eq. (C.16) yields,

$$\frac{\partial^{n+1}}{\partial t}\left(\frac{\partial p}{\partial x}+\rho a\frac{\partial u}{\partial x}\right)=\frac{\partial^{n+1}}{\partial t}\left(\frac{\partial p}{\partial x}\right)+\frac{\partial^{n}}{\partial t}\left[\rho a\frac{\partial}{\partial t}\left(\frac{\partial u}{\partial x}\right)+\frac{\partial}{\partial t}\left(\rho a\right)\frac{\partial u}{\partial x}\right] \tag{C.17}$$

or equivalently,

$$\frac{\partial^{n+1}}{\partial t}\left(\frac{\partial p}{\partial x}+\rho a\frac{\partial u}{\partial x}\right)=\frac{\partial^{n+1}}{\partial t}\left(\frac{\partial p}{\partial x}\right)+\frac{\partial^{n}}{\partial t}\left[\rho a\frac{\partial}{\partial t}\left(\frac{\partial u}{\partial x}\right)\right]+\frac{\partial^{n}}{\partial t}\left[\frac{\partial}{\partial t}\left(\rho a\right)\frac{\partial u}{\partial x}\right] \tag{C.18}$$

Rearranging Eq. (C.18) yields

$$\frac{\partial^{n}}{\partial t}\left[\rho a\frac{\partial}{\partial t}\left(\frac{\partial u}{\partial x}\right)\right]=\frac{\partial^{n+1}}{\partial t}\left(\frac{\partial p}{\partial x}+\rho a\frac{\partial u}{\partial x}\right)-\frac{\partial^{n+1}}{\partial t}\left(\frac{\partial p}{\partial x}\right)-\frac{\partial^{n}}{\partial t}\left[\frac{\partial}{\partial t}\left(\rho a\right)\frac{\partial u}{\partial x}\right] \tag{C.19}$$

Once again, from the Clairaut theorem, it follows that

$$\frac{\partial}{\partial x}\left(\frac{\partial u}{\partial t}\right)=\frac{\partial}{\partial t}\left(\frac{\partial u}{\partial x}\right) \tag{C.20}$$

Therefore substituting (C.20) into (C.19) yields

$$\frac{\partial^{n}}{\partial t}\left[\rho a\frac{\partial}{\partial x}\left(\frac{\partial u}{\partial t}\right)\right]=\frac{\partial^{n+1}}{\partial t}\left(\frac{\partial p}{\partial x}+\rho a\frac{\partial u}{\partial x}\right)-\frac{\partial^{n+1}}{\partial t}\left(\frac{\partial p}{\partial x}\right)-\frac{\partial^{n}}{\partial t}\left[\frac{\partial}{\partial t}\left(\rho a\right)\frac{\partial u}{\partial x}\right] \tag{C.21}$$

Now substituting (C.21) into (C.15) yields

$$\begin{aligned}\frac{\partial}{\partial x}\left[\frac{\partial^{n}}{\partial t}\left(\frac{\partial p}{\partial t}+\rho a\frac{\partial u}{\partial t}\right)\right]=&\frac{\partial}{\partial x}\left(\frac{\partial^{n+1}p}{\partial t}\right)+\frac{\partial^{n+1}}{\partial t}\left(\frac{\partial p}{\partial x}+\rho a\frac{\partial u}{\partial x}\right)-\frac{\partial^{n+1}}{\partial t}\left(\frac{\partial p}{\partial x}\right)\\&-\frac{\partial^{n}}{\partial t}\left[\frac{\partial}{\partial t}\left(\rho a\right)\frac{\partial u}{\partial x}\right]+\frac{\partial^{n}}{\partial t}\left[\frac{\partial}{\partial x}\left(\rho a\right)\frac{\partial u}{\partial t}\right]\end{aligned} \tag{C.22}$$

Once again, from the Clairaut theorem, it follows that

$$\frac{\partial}{\partial x}\left(\frac{\partial^{n+1}p}{\partial t}\right)=\frac{\partial^{n+1}}{\partial t}\left(\frac{\partial p}{\partial x}\right) \tag{C.23}$$

Thus, (C.22) can be reduced to

$$\begin{aligned}\frac{\partial}{\partial x}\left[\frac{\partial^{n}}{\partial t}\left(\frac{\partial p}{\partial t}+\rho a\frac{\partial u}{\partial t}\right)\right]=&\frac{\partial^{n+1}}{\partial t}\left(\frac{\partial p}{\partial x}+\rho a\frac{\partial u}{\partial x}\right)\\&-\frac{\partial^{n}}{\partial t}\left[\frac{\partial}{\partial t}\left(\rho a\right)\frac{\partial u}{\partial x}\right]+\frac{\partial^{n}}{\partial t}\left[\frac{\partial}{\partial x}\left(\rho a\right)\frac{\partial u}{\partial t}\right]\end{aligned} \tag{C.24}$$

or equivalently,

$$\frac{\partial}{\partial x}\left[\frac{\partial^n}{\partial t}\left(\frac{\partial p}{\partial t}+\rho a\frac{\partial u}{\partial t}\right)\right]=\frac{\partial^{n+1}}{\partial t}\left(\frac{\partial p}{\partial x}+\rho a\frac{\partial u}{\partial x}\right)+\frac{\partial^n}{\partial t}\left[\frac{\partial}{\partial x}\left(\rho a\right)\frac{\partial u}{\partial t}-\frac{\partial}{\partial t}\left(\rho a\right)\frac{\partial u}{\partial x}\right] \quad \text{(C.25)}$$

Now to set up the desired expression in Eq. (7.6), it is required to evaluate the total derivative on the shock for the quantity $\partial^n/\partial t(\partial p/\partial t+\rho a\partial u/\partial t)$. Note, this represents the effects of flow non-uniformity behind the shock, and will set up the closure scheme for the final result. Hence,

$$\frac{d}{dt}\left[\frac{\partial^n}{\partial t}\left(\frac{\partial p}{\partial t}+\rho a\frac{\partial u}{\partial t}\right)\right]=\frac{\partial^{n+1}}{\partial t}\left(\frac{\partial p}{\partial t}+\rho a\frac{\partial u}{\partial t}\right)+a_0M\frac{\partial}{\partial x}\left[\frac{\partial^n}{\partial t}\left(\frac{\partial p}{\partial t}+\rho a\frac{\partial u}{\partial t}\right)\right] \quad \text{(C.26)}$$

Substituting (C.25) into (C.26) yields

$$\begin{aligned}\frac{d}{dt}\left[\frac{\partial^n}{\partial t}\left(\frac{\partial p}{\partial t}+\rho a\frac{\partial u}{\partial t}\right)\right]=\frac{\partial^{n+1}}{\partial t}\left(\frac{\partial p}{\partial t}+\rho a\frac{\partial u}{\partial t}\right)+a_0M\Bigg\{&\frac{\partial^{n+1}}{\partial t}\left(\frac{\partial p}{\partial x}+\rho a\frac{\partial u}{\partial x}\right)\\&+\frac{\partial^n}{\partial t}\left[\frac{\partial}{\partial x}\left(\rho a\right)\frac{\partial u}{\partial t}-\frac{\partial}{\partial t}\left(\rho a\right)\frac{\partial u}{\partial x}\right]\Bigg\}\end{aligned} \quad \text{(C.27)}$$

Further, expanding the right-hand side of (C.27) yields

$$\begin{aligned}\frac{d}{dt}\left[\frac{\partial^n}{\partial t}\left(\frac{\partial p}{\partial t}+\rho a\frac{\partial u}{\partial t}\right)\right]=&\frac{\partial^{n+1}}{\partial t}\left(\frac{\partial p}{\partial t}+\rho a\frac{\partial u}{\partial t}\right)+a_0M\frac{\partial^{n+1}}{\partial t}\left(\frac{\partial p}{\partial x}+\rho a\frac{\partial u}{\partial x}\right)\\&+a_0M\frac{\partial^n}{\partial t}\left[\frac{\partial}{\partial x}\left(\rho a\right)\frac{\partial u}{\partial t}-\frac{\partial}{\partial t}\left(\rho a\right)\frac{\partial u}{\partial x}\right]\end{aligned} \quad \text{(C.28)}$$

Substituting (C.4) yields

$$\begin{aligned}\frac{d}{dt}\left[\frac{\partial^n}{\partial t}\left(\frac{\partial p}{\partial t}+\rho a\frac{\partial u}{\partial t}\right)\right]=&\frac{\partial^{n+1}}{\partial t}\left(\frac{\partial p}{\partial t}+\rho a\frac{\partial u}{\partial t}\right)\\&+a_0M\frac{\partial^{n+1}}{\partial t}\left[-\frac{1}{u+a}\left(\frac{\partial p}{\partial t}+\rho a\frac{\partial u}{\partial t}+\rho a^2u\frac{A'(x)}{A(x)}\right)\right]\\&+a_0M\frac{\partial^n}{\partial t}\left[\frac{\partial}{\partial x}\left(\rho a\right)\frac{\partial u}{\partial t}-\frac{\partial}{\partial t}\left(\rho a\right)\frac{\partial u}{\partial x}\right]\end{aligned} \quad \text{(C.29)}$$

Lastly, rearranging yields

$$\begin{aligned}\frac{d}{dt}\left[\frac{\partial^n}{\partial t}\left(\frac{\partial p}{\partial t}+\rho a\frac{\partial u}{\partial t}\right)\right]=&-a_0M\frac{\partial^{n+1}}{\partial t}\left(\frac{\rho a^2u}{u+a}\right)\frac{A'(x)}{A(x)}\\-a_0M\frac{\partial^{n+1}}{\partial t}&\left[\frac{1}{u+a}\left(\frac{\partial p}{\partial t}+\rho a\frac{\partial u}{\partial t}\right)\right]-a_0M\frac{\partial^n}{\partial t}\left[\frac{\partial}{\partial t}\left(\rho a\right)\frac{\partial u}{\partial x}-\frac{\partial}{\partial x}\left(\rho a\right)\frac{\partial u}{\partial t}\right]\\&+\frac{\partial^{n+1}}{\partial t}\left(\frac{\partial p}{\partial t}+\rho a\frac{\partial u}{\partial t}\right)\end{aligned} \quad \text{(C.30)}$$

Applying the general Leibniz formula to the term $-a_0M\partial^{n+1}/\partial t[1/(u+a)(\partial p/\partial + \rho a \partial u/\partial t)]$ of Eq. (C.30) yields

$$\begin{aligned} -a_0M\frac{\partial^{n+1}}{\partial t}\left[\frac{1}{u+a}\left(\frac{\partial p}{\partial t}+\rho a\frac{\partial u}{\partial t}\right)\right] = \\ -a_0M\sum_{i=0}^{n+1}\left\{\binom{n+1}{i}\frac{\partial^i}{\partial t}\left(\frac{1}{u+a}\right)\frac{\partial^{n+1-i}}{\partial t}\left(\frac{\partial p}{\partial t}+\rho a\frac{\partial u}{\partial t}\right)\right\} \end{aligned} \tag{C.31}$$

Expanding the first term of the summation in Eq. (C.31) yields

$$\begin{aligned} -a_0M\frac{\partial^{n+1}}{\partial t}\left[\frac{1}{u+a}\left(\frac{\partial p}{\partial t}+\rho a\frac{\partial u}{\partial t}\right)\right] = -\frac{a_0M}{u+a}\frac{\partial^{n+1}}{\partial t}\left(\frac{\partial p}{\partial t}+\rho a\frac{\partial u}{\partial t}\right) \\ -a_0M\sum_{i=1}^{n+1}\left\{\binom{n+1}{i}\frac{\partial^i}{\partial t}\left(\frac{1}{u+a}\right)\frac{\partial^{n+1-i}}{\partial t}\left(\frac{\partial p}{\partial t}+\rho a\frac{\partial u}{\partial t}\right)\right\} \end{aligned} \tag{C.32}$$

Similarly, substituting (C.32) into (C.30) yields

$$\begin{aligned} \frac{d}{dt}\left[\frac{\partial^n}{\partial t}\left(\frac{\partial p}{\partial t}+\rho a\frac{\partial u}{\partial t}\right)\right] = -a_0M\frac{\partial^{n+1}}{\partial t}\left(\frac{\rho a^2u}{u+a}\right)\frac{A'(x)}{A(x)} - \frac{a_0M}{u+a}\frac{\partial^{n+1}}{\partial t}\left(\frac{\partial p}{\partial t}+\rho a\frac{\partial u}{\partial t}\right) \\ -a_0M\sum_{i=1}^{n+1}\left\{\binom{n+1}{i}\frac{\partial^i}{\partial t}\left(\frac{1}{u+a}\right)\frac{\partial^{n+1-i}}{\partial t}\left(\frac{\partial p}{\partial t}+\rho a\frac{\partial u}{\partial t}\right)\right\} \\ -a_0M\frac{\partial^n}{\partial t}\left[\frac{\partial}{\partial t}(\rho a)\frac{\partial u}{\partial x}-\frac{\partial}{\partial x}(\rho a)\frac{\partial u}{\partial t}\right]+\frac{\partial^{n+1}}{\partial t}\left(\frac{\partial p}{\partial t}+\rho a\frac{\partial u}{\partial t}\right) \end{aligned} \tag{C.33}$$

Regrouping terms,

$$\begin{aligned} \frac{d}{dt}\left[\frac{\partial^n}{\partial t}\left(\frac{\partial p}{\partial t}+\rho a\frac{\partial u}{\partial t}\right)\right] = -a_0M\frac{\partial^{n+1}}{\partial t}\left(\frac{\rho a^2u}{u+a}\right)\frac{A'(x)}{A(x)} \\ -a_0M\sum_{i=1}^{n+1}\left\{\binom{n+1}{i}\frac{\partial^i}{\partial t}\left(\frac{1}{u+a}\right)\frac{\partial^{n+1-i}}{\partial t}\left(\frac{\partial p}{\partial t}+\rho a\frac{\partial u}{\partial t}\right)\right\} \\ -a_0M\frac{\partial^n}{\partial t}\left[\frac{\partial}{\partial t}(\rho a)\frac{\partial u}{\partial x}-\frac{\partial}{\partial x}(\rho a)\frac{\partial u}{\partial t}\right]+\left(1-\frac{a_0M}{u+a}\right)\frac{\partial^{n+1}}{\partial t}\left(\frac{\partial p}{\partial t}+\rho a\frac{\partial u}{\partial t}\right) \end{aligned} \tag{C.34}$$

or equivalently,

$$\begin{aligned} \frac{d}{dt}\left[\frac{\partial^n}{\partial t}\left(\frac{\partial p}{\partial t}+\rho a\frac{\partial u}{\partial t}\right)\right] = -\Bigg[a_0M\frac{\partial^{n+1}}{\partial t}\left(\frac{\rho a^2u}{u+a}\right)\frac{A'(x)}{A(x)} \\ +a_0M\sum_{i=1}^{n+1}\left\{\binom{n+1}{i}\frac{\partial^i}{\partial t}\left(\frac{1}{u+a}\right)\frac{\partial^{n+1-i}}{\partial t}\left(\frac{\partial p}{\partial t}+\rho a\frac{\partial u}{\partial t}\right)\right\} \\ +a_0M\frac{\partial^n}{\partial t}\left(\frac{\partial(\rho a)}{\partial t}\frac{\partial u}{\partial x}-\frac{\partial(\rho a)}{\partial x}\frac{\partial u}{\partial t}\right)+\left(\frac{a_0M}{u+a}-1\right)\frac{\partial^{n+1}}{\partial t}\left(\frac{\partial p}{\partial t}+\rho a\frac{\partial u}{\partial t}\right)\Bigg] \end{aligned} \tag{C.35}$$

Similarly, noting that $dx/dt = a_0 M$ on the shock, it then follows that Eq. (C.35) can be recast as

$$\begin{aligned}\frac{d}{dx}\left[\frac{\partial^n}{\partial t}\left(\frac{\partial p}{\partial t}+\rho a\frac{\partial u}{\partial t}\right)\right] &= -\left[\frac{\partial^{n+1}}{\partial t}\left(\frac{\rho a^2 u}{u+a}\right)\frac{A'(x)}{A(x)}\right.\\ &+\sum_{i=1}^{n+1}\left\{\binom{n+1}{i}\frac{\partial^i}{\partial t}\left(\frac{1}{u+a}\right)\frac{\partial^{n+1-i}}{\partial t}\left(\frac{\partial p}{\partial t}+\rho a\frac{\partial u}{\partial t}\right)\right\}\\ &\left.+\frac{\partial^n}{\partial t}\left(\frac{\partial(\rho a)}{\partial t}\frac{\partial u}{\partial x}-\frac{\partial(\rho a)}{\partial x}\frac{\partial u}{\partial t}\right)+\left(\frac{1}{u+a}-\frac{1}{a_0 M}\right)\frac{\partial^{n+1}}{\partial t}\left(\frac{\partial p}{\partial t}+\rho a\frac{\partial u}{\partial t}\right)\right]\end{aligned} \tag{C.36}$$

Lastly, in terms of the non-uniformity parameter $Q_n = \partial_t^{n-1}\left(\partial p/\partial t + \rho a \partial u/\partial t\right)$, Eq. (C.36) can be simplified to

$$\begin{aligned}\frac{\mathrm{d}Q_n}{\mathrm{d}x} &= -\left[\frac{\partial^n}{\partial t}\left(\frac{\rho a^2 u}{u+a}\right)\frac{A'(x)}{A(x)}+\sum_{i=1}^{n}\left\{\binom{n}{i}\frac{\partial^i}{\partial t}\left(\frac{1}{u+a}\right)Q_{n+1-i}\right\}\right.\\ &\left.+\frac{\partial^{n-1}}{\partial t}\left(\frac{\partial(\rho a)}{\partial t}\frac{\partial u}{\partial x}-\frac{\partial(\rho a)}{\partial x}\frac{\partial u}{\partial t}\right)+\left(\frac{1}{u+a}-\frac{1}{a_0 M}\right)Q_{n+1}\right]\end{aligned} \tag{C.37}$$

In summary equations (C.10) and (C.37) are the generalized governing conditions on the shock. Moreover, for $n = 1$, Eq. (C.37) simplifies to:

$$\frac{\mathrm{d}Q_1}{\mathrm{d}x} = -\left[\frac{\partial}{\partial t}\left(\frac{\rho a^2 u}{u+a}\right)\frac{A'(x)}{A(x)}+\frac{\partial}{\partial t}\left(\rho a\right)\frac{\partial u}{\partial x}-\frac{\partial}{\partial x}\left(\rho a\right)\frac{\partial u}{\partial t}+\frac{\partial}{\partial t}\left(\frac{1}{u+a}\right)Q_1\right] \tag{C.38}$$

where the term involving Q_2 has been truncated.

Finally, in order to obtain the simplified expression in Eq. (7.10), it is required to replace the partial time and space derivatives of p, u, ρ and a in Eq. (C.38) with the formulas derived by Best [178]. Note, these formulas were obtained in [178] by manipulating the characteristic form of the governing equations on the C_+, C_-, and C_0 characteristics, namely, Eqs. (B.26)–(B.28). Hence, the first-order partial time and space derivative of p, u, ρ and a in terms of the shock properties are listed as follows:

$$\frac{\partial p}{\partial t} = \frac{\left\{\begin{array}{r} a_0 M\frac{dM}{dx}\left[\left(a^2+u\left(a_0 M-u\right)\right)\frac{dp}{dM}+a_0 M\rho a^2\frac{du}{dM}\right] \\ +\,a_0 M\rho a^2 u\left(a_0 M-u\right)\frac{A'(x)}{A(x)}\end{array}\right\}}{\left(a^2-\left(a_0 M-u\right)^2\right)} \tag{C.39}$$

$$\frac{\partial p}{\partial x} = -\frac{\left\{a_0 M\frac{dM}{dx}\left[\left(a_0 M-u\right)\frac{dp}{dM}+\rho a^2\frac{du}{dM}\right]+\rho a^2 u\left(a_0 M-u\right)\frac{A'(x)}{A(x)}\right\}}{\left(a^2-\left(a_0 M-u\right)^2\right)} \tag{C.40}$$

$$\frac{\partial u}{\partial t} = \frac{\left\{ a_0 M \frac{dM}{dx} \left[\frac{a_0 M}{\rho} \frac{dp}{dM} + \left(a^2 + u \left(a_0 M - u \right) \right) \frac{du}{dM} \right] + a_0 M a^2 u \frac{A'(x)}{A(x)} \right\}}{\left(a^2 - \left(a_0 M - u \right)^2 \right)} \tag{C.41}$$

$$\frac{\partial u}{\partial x} = -\frac{\left\{ a_0 M \frac{dM}{dx} \left[\frac{1}{\rho} \frac{dp}{dM} + \left(a_0 M - u \right) \frac{du}{dM} \right] + a^2 u \frac{A'(x)}{A(x)} \right\}}{\left(a^2 - \left(a_0 M - u \right)^2 \right)} \tag{C.42}$$

$$\frac{\partial \rho}{\partial t} = \frac{\left\{ \begin{array}{l} a_0 M \frac{dM}{dx} \left[a_0 M \frac{dp}{dM} + a_0 M \left(a_0 M - u \right) \frac{du}{dM} \right. \\ \quad \left. - u \left(a^2 - \left(a_0 M - u \right)^2 \frac{d\rho}{dM} \right) \right] + a_0 M \rho u \left(a_0 M - u \right)^2 \frac{A'(x)}{A(x)} \end{array} \right\}}{\left(a_0 M - u \right) \left(a^2 - \left(a_0 M - u \right)^2 \right)} \tag{C.43}$$

$$\frac{\partial \rho}{\partial x} = -\frac{\left\{ \begin{array}{l} a_0 M \frac{dM}{dx} \left[\frac{dp}{dM} + a_0 M \rho \left(a_0 M - u \right) \frac{du}{dM} \right. \\ \quad \left. - \left(a^2 - \left(a_0 M - u \right)^2 \frac{d\rho}{dM} \right) \right] + \rho u \left(a_0 M - u \right)^2 \frac{A'(x)}{A(x)} \end{array} \right\}}{\left(a_0 M - u \right) \left(a^2 - \left(a_0 M - u \right)^2 \right)} \tag{C.44}$$

Lastly, with the speed of sound defined by $a^2 = \gamma p / \rho$:

$$\frac{\partial a}{\partial t} = \frac{\gamma}{2a} \left(\frac{1}{\rho} \frac{\partial p}{\partial t} - \frac{p}{\rho^2} \frac{\partial \rho}{\partial t} \right) \tag{C.45}$$

$$\frac{\partial a}{\partial x} = \frac{\gamma}{2a} \left(\frac{1}{\rho} \frac{\partial p}{\partial x} - \frac{p}{\rho^2} \frac{\partial \rho}{\partial x} \right) \tag{C.46}$$

Note, substitution of Eqs. (C.39)–(C.46) into Eq. (C.38) yields the result shown in (7.10), which is reduced in terms of the coefficient functions $\alpha_i(M)$.

C.2 CCW Coefficient Functions

This section provides plots to show the behavior of the $\alpha_i(M)$ coefficient functions in Eq. (7.10).

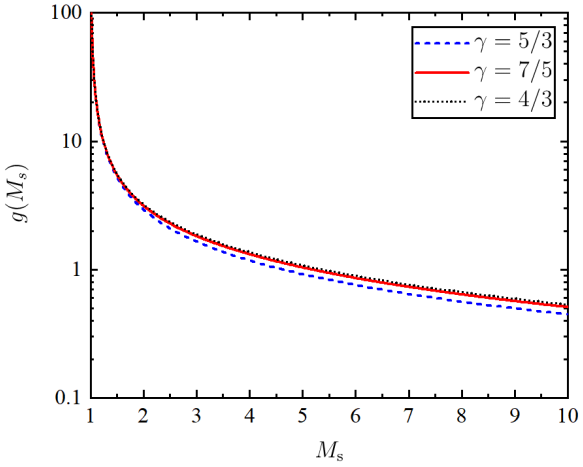

Figure C.1. $g(M_s)$ vs. shock Mach number.

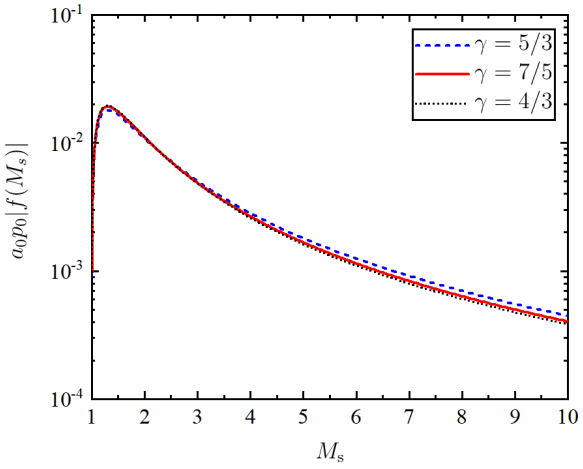

Figure C.2. $a_0 p_0 |f(M_s)|$ vs. shock Mach number.

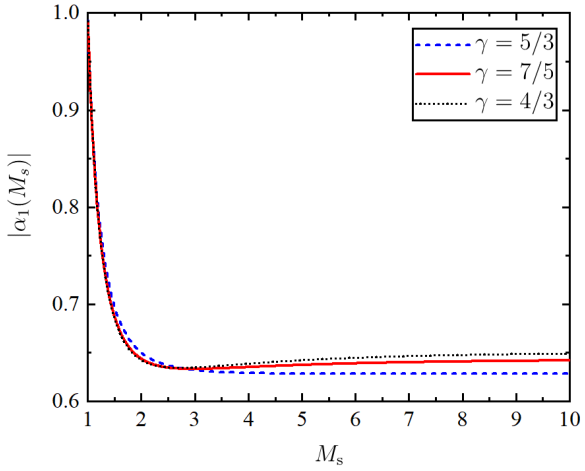

Figure C.3. $|\alpha_1(M_s)|$ vs. shock Mach number.

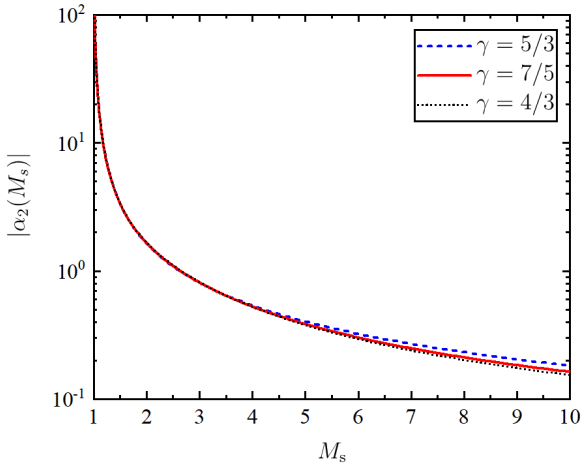

Figure C.4. $|\alpha_2(M_s)|$ vs. shock Mach number.

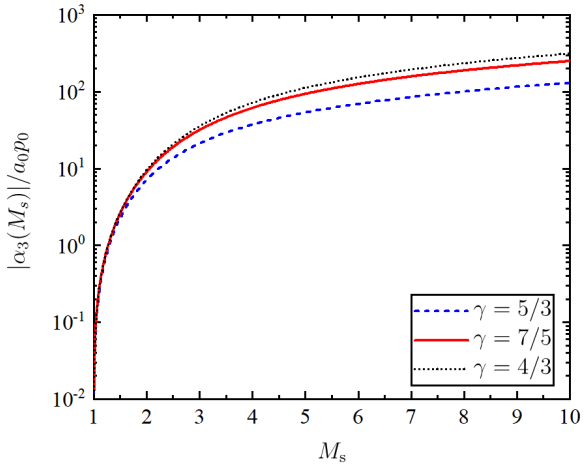

Figure C.5. $|\alpha_3(M_\mathrm{s})|/a_0p_0$ vs. shock Mach number.

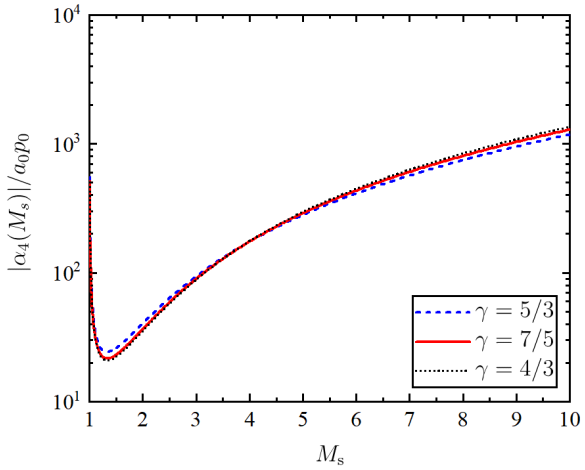

Figure C.6. $|\alpha_4(M_\mathrm{s})|/a_0p_0$ vs. shock Mach number.

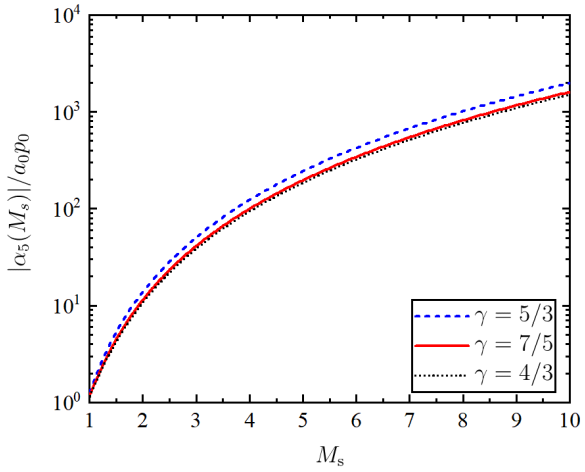

Figure C.7. $|\alpha_5(M_\mathrm{s})|/a_0p_0$ vs. shock Mach number.

REFERENCES

[1] Glassman, I. and Yetter, R. A., *Combustion*, 4th ed., Elsevier Academic Press, Burlington, MA, 2008.

[2] Lee, J. H. S., *The Detonation Phenomenon*, Cambridge University Press, New York, NY, 2008.

[3] Mallard, E. and Le Chatelier, H., *Recherches expérimentales et théoriques sur la combustion des mélanges gazeux explosives*, H. Dunod et E. Pinat, Paris, 1883.

[4] Lewis, B. and von Elbe, G., "On the Theory of Flame Propagation," *The Journal of Chemical Physics*, vol. 2, no. 8, pp. 537–546, 1934. doi: 10.1063/1.1749523

[5] Zel'dovich, Y. B. and Frank-Kamenetsky, D. A., "Theory of Thermal Flame Propagation," *Zhurnal Fizicheskoy Khimii*, vol. 12, no. 1, pp. 100–105, 1938.

[6] Oran, E. S. and Gamezo, V. N., "Origins of the Deflagration-to-Detonation Transition in Gas-Phase Combustion," *Combustion and Flame*, vol. 148, no. 1, pp. 4–47, 2007. doi: 10.1016/j.combustflame.2006.07.010

[7] Ivanov, M., Kiverin, A., Yakovenko, I., and Liberman, M., "Hydrogen–Oxygen Flame Acceleration and Deflagration-to-Detonation Transition in Three-Dimensional Rectangular Channels with No-Slip Walls," *International Journal of Hydrogen Energy*, vol. 38, no. 36, pp. 16 427–16 440, 2013. doi: 10.1016/j.ijhydene.2013.08.124

[8] Shepherd, J. E. and Lee, J. H. S., *On The Transition from Deflagration to Detonation*, Springer New York, New York, NY, 1992, pp. 439–487.

[9] Urtiew, P. and Oppenheim, A., "Experimental observations of the transition to detonation in an explosive gas," *Proceedings of the Royal Society of London A: Mathematical, Physical and Engineering Sciences*, vol. 295, no. 1440, pp. 13–28, 1966. doi: 10.1098/rspa.1966.0223

[10] Kuo, K., *Principles of Combustion*, 2nd ed., John Wiley & Sons, Hoboken, NJ, 2005.

[11] Strehlow, R. A. and Cohen, A., "Initiation of Detonation," *The Physics of Fluids*, vol. 5, no. 1, pp. 97–101, 1962. doi: 10.1063/1.1706497

[12] Bdzil, J. B. and Kapila, A. K., "Shock-to-Detonation Transition: A Model Problem," *Physics of Fluids A: Fluid Dynamics*, vol. 4, no. 2, pp. 409–418, 1992. doi: 10.1063/1.858312

[13] Chan, C. K., Lau, D., Thibault, P. A., and Penrose, J. D., "Ignition and Detonation Initiation by Shock Focussing," *AIP Conference Proceedings*, vol. 208, no. 1, pp. 161–166, 1990. doi: 10.1063/1.39434

[14] Lee, J. H. S., "Initiation of Gaseous Detonation," *Annual Review of Physical Chemistry*, vol. 28, no. 1, pp. 75–104, 1977. doi: 10.1146/annurev.pc.28.100177.000451

[15] Berthelot, M. and Vielle, P., "Sur la vitesse de propagation des phénomènes explosifs dans les gaz," *Comptes Rendus Hebdomadaires des Séances de l'Académie des Sciences*, vol. 93, pp. 18–21, 1881.

[16] Berthelot, M., "Détonation de l'acétylène, du cyanogène et des combinaisons endothermiques en général," *Comptes Rendus Hebdomadaires des Séances de l'Académie des Sciences*, vol. 93, pp. 613–619, 1881.

[17] Berthelot, M. and Vieille, P., "Sur la période d'état variable qui précède le régime de détonation et sur les conditions d'établissement de l'onde explosifs," *Comptes Rendus de l'Académie de Paris*, vol. 95, pp. 199–205, 1882.

[18] Berthelot, M. and Vielle, P., "Sur les vagues explosifs," *Comptes Rendus Hebdomadaires des Séances de l'Académie des Sciences*, vol. 94, pp. 149–152, 1882.

[19] Rankine, W. J. M., "On the Thermodynamic Theory of Waves of Finite Longitudinal Disturbance," *Philosophical Transactions of the Royal Society of London*, vol. 160, pp. 277–288, 1870. doi: 10.1098/rstl.1870.0015

[20] Hugoniot, H., *Mémoire sur la propagation du mouvement dans les corps et spécialement dans les gaz parfaits*, Gauthier-Villars, Paris, 1887–1889.

[21] Chapman, D. L., "On the Rate of Explosion in Gases," *The London, Edinburgh, and Dublin Philosophical Magazine and Journal of Science*, vol. 47, no. 284, pp. 90–104, 1899. doi: 10.1080/14786449908621243

[22] Jouguet, E., "Sur la propagation des réactions chimiques dans les gaz," *The Journal de Mathématiques Pures et Appliquées*, vol. 1, pp. 347–425, 1905.

[23] Jouguet, E., "Sur la propagation des réactions chimiques dans les gaz," *The Journal de Mathématiques Pures et Appliquées*, vol. 2, pp. 5–86, 1906.

[24] Goodwin, D. G., Moffat, H. K., and Speth, R. L., "Cantera: An Object-Oriented Software Toolkit for Chemical Kinetics, Thermodynamics, and Transport Processes," http://www.cantera.org, 2016. version 2.2.1.

[25] Rayleigh, L., "Aerial Plane Waves of Finite Amplitude," *Proceedings of the Royal Society of London A: Mathematical, Physical and Engineering Sciences*, vol. 84, no. 570, pp. 247–284, 1910. doi: 10.1098/rspa.1910.0075

[26] Taylor, G. I., "The Conditions Necessary for Discontinuous Motion in Gases," *Proceedings of the Royal Society of London A: Mathematical Physical, and Engineering Sciences*, vol. 84, no. 571, pp. 371–377, 1910. doi: 10.1098/rspa.1910.0081

[27] Crussard, L., "Sur quelques propriétés de l'onde explosifs," *Comptes Rendus de l'Académie des Sciences*, vol. 144, pp. 417–420, 1907.

[28] Gordon, S. and McBride, B. J., "Computer Program for Calculation of Complex Chemical Equilibrium Compositions, Rocket Performance, Incident and Reflected Shocks, and Chapman-Jouguet Detonations," NASA, Tech. Rep. SP-273, 1971.

[29] Browne, S., Ziegler, J., and Shepherd, J. E., "Numerical Solution Methods for Shock and Detonation Jump Conditions," GALCIT, Tech. Rep. FM2006.006, 2008.

[30] Kao, S. and Shepherd, J. E., "Numerical Solution Methods for Constant Volume Explosions and ZND Detonation Structure," GALCIT, Tech. Rep. FM2006.007, 2008.

[31] Zel'dovich, Y. B., "On the Theory of the Propagation of Detonation in Gaseous Systems," *Zhurnal Experimental'noi i Teoreticheskoi Fiziki*, vol. 10, no. 5, pp. 542–568, 1940.

[32] von Neumann, J., "Theory of Detonation Waves," O.S.R.D., Tech. Rep. 549, 1942.

[33] Döring, W., "On Detonation Process in Gases," *Annalen der Physik*, vol. 435, no. 6-7, pp. 421–436, 1943. doi: 10.1002/andp.19434350605

[34] Denisov, Y. N. and Troshin, Y. K., "Structure of Gaseous Detonation in Tubes," *Soviet Physics–Technical Physics*, vol. 5, no. 4, pp. 419–431, 1960.

[35] White, D., "Turbulent Structure of Gaseous Detonation," *Physics of Fluids*, vol. 4, no. 4, pp. 465–480, 1961. doi: 10.1063/1.1706350

[36] Lee, J. and Radulescu, M. I., "On the Hydrodynamic Thickness of Cellular Detonations," *Combustion, Explosion and Shock Waves*, vol. 41, no. 6, pp. 745–765, 2005. doi: 10.1007/s10573-005-0084-1

[37] Oppenheim, A. and Soloukhin, R., "Experiments in Gasdynamics of Explosions," *Annual Review of Fluid Mechanics*, vol. 5, no. 1, pp. 31–58, 1973.

[38] Wintenberger, E. and Shepherd, J. E. (2004, January) Detonation Waves and Pulse Detonation Engines. California Institute of Technology, Pasadena, CA. [Online]. URL: http://shepherd.caltech.edu/EDL/projects/pde/Ae103-012704.pdf

[39] Strehlow, R. and Crooker, A., "The Structure of Marginal Detonation Waves," *Acta Astronautica*, vol. 1, no. 3, pp. 303–315, 1974. doi: 10.1016/0094-5765(74)90100-3

[40] Lee, J. H. S., "Dynamic Parameters of Gaseous Detonations," *Annual Review of Fluid Mechanics*, vol. 16, no. 1, pp. 311–336, 1984. doi: 10.1146/annurev.fl.16.010184.001523

[41] Knystautas, R., Lee, J., and Guirao, C., "The Critical Tube Diameter for Detonation Failure in Hydrocarbon-Air Mixtures," *Combustion and Flame*, vol. 48, pp. 63–83, 1982. doi: 10.1016/0010-2180(82)90116-X

[42] Ciccarelli, G., Ginsberg, T., Boccio, J., Finfrock, C., Gerlach, L. *et al.*, "Detonation Cell Size Measurements in High-Temperature Hydrogen-Air-Steam Mixtures at

the BNL High-Temperature Combustion Facility," Brookhaven National Laboratory, Tech. Rep. NUREG/CR-6391, BNL-NUREG-52482, 1997.

[43] Tieszen, S., Stamps, D., Westbrook, C., and Pitz, W., "Gaseous Hydrocarbon–Air Detonations," *Combustion and Flame*, vol. 84, no. 3, pp. 376–390, 1991. doi: 10.1016/0010-2180(91)90013-2

[44] Manzhalei, V., Mitrofanov, V., and Subbotin, V., "Measurement of Inhomogeneities of a Detonation Front in Gas Mixtures at Elevated Pressures," *Combustion, Explosion, and Shock Waves*, vol. 10, no. 1, pp. 89–95, 1974. doi: 10.1007/BF01463793

[45] Bauer, P. A., Presles, H. N., Heuze, O., and Brochet, C., "Measurement of Cell Lengths in the Detonation Front of Hydrocarbon Oxygen and Nitrogen Mixtures at Elevated Initial Pressures," *Combustion and Flame*, vol. 64, no. 1, pp. 113–123, 1986. doi: 10.1016/0010-2180(86)90102-1

[46] Guirao, C., Knystautas, R., Lee, J. H., Benedick, W., and Berman, M., "Hydrogen-Air Detonations," in *Symposium (International) on Combustion*, vol. 19, no. 1, 1982. doi: 10.1016/S0082-0784(82)80232-4 pp. 583–590.

[47] Beeson, H. D., McClenagan, R. D., Bishop, C. V., Benz, F. J., Pitz, W. J. *et al.*, "Detonability of Hydrocarbon Fuels in Air," in *Dynamics of Detonations and Explosions: Detonations*, Kuhl, A., Leyer, J., Borisov, A., and Sirignano, W., Eds., vol. 133, Progress in Astronautics and Aeronautics, 1991. doi: 10.2514/5.9781600866067.0019.0036 pp. 19–36.

[48] Knystautas, R., Guirao, C., Lee, J., and Sulmistras, A., "Measurement of Cell Size in Hydrocarbon-Air Mixtures and Predictions of Critical Tube Diameter, Critical Initiation Energy and Detonability Limits," in *Dynamics of Shock Waves, Explosions, and Detonations*, Soloukhin, R. I., Oppenheim, A. K., Manson, N., and Bowen, J. R., Eds., vol. 94, Progress in Astronautics and Aeronautics, 1984. doi: 10.2514/5.9781600865695.0023.0037 pp. 23–37.

[49] Zipf Jr., R., Gamezo, V., Sapko, M., Marchewka, W., Mohamed, K. *et al.*, "Methane–Air Detonation Experiments at NIOSH Lake Lynn Laboratory," *Journal of Loss Prevention in the Process Industries*, vol. 26, no. 2, pp. 295–301, 2013. doi: 10.1016/j.jlp.2011.05.003

[50] Bussing, T. R. A. and Pappus, G., "Pulse Detonation Engine Theory and Concepts," in *Developments in High-Speed Vehicle Propulsion Systems*, vol. 165, 1996. doi: 10.2514/5.9781600866401.0421.0472 pp. 421–472.

[51] Heiser, W. H. and Pratt, D. T., "Thermodynamic Cycle Analysis of Pulse Detonation Engines," *Journal of Propulsion and Power*, vol. 18, no. 1, pp. 68–76, 2002. doi: 10.2514/2.5899

[52] Roy, G. D., Frolov, S. M., Borisov, A. A., and Netzer, D. W., "Pulse Detonation Propulsion: Challenges, Current Status, and Future Perspective," *Progress in Energy and Combustion Science*, vol. 30, no. 6, pp. 545–672, 2004. doi: 10.1016/j.pecs.2004.05.001

[53] Kailasanath, K., "Review of Propulsion Applications of Detonation Waves," *AIAA Journal*, vol. 38, no. 9, pp. 1698–1708, 2000. doi: 10.2514/2.1156

[54] Wolański, P., "Detonative Propulsion," *Proceedings of the Combustion Institute*, vol. 34, no. 1, pp. 125–158, 2013. doi: 10.1016/j.proci.2012.10.005

[55] Lu, F. K. and Braun, E. M., "Rotating Detonation Wave Propulsion: eExperimental Challenges, Modeling, and Engine Concepts," *Journal of Propulsion and Power*, vol. 30, no. 5, pp. 1125–1142, 2014. doi: 10.2514/1.B34802

[56] Doychak, J., "Vulcan: Powering the Future of Hypersonics," 2008. Defense Advanced Research Projects Agency.

[57] Eidelman, S. and Grossmann, W., "Pulsed Detonation Engine Experimental and Theoretical Review," 28th Joint Propulsion Conference & Exhibit, Nashville, TN, AIAA Paper 1992-3168, 1992. doi: 10.2514/6.1992-3168

[58] Kailasanath, K., "Recent Developments in the Research on Pulse Detonation Engines," *AIAA Journal*, vol. 41, no. 2, pp. 145–159, 2003. doi: 10.2514/2.1933

[59] Kailasanath, K., "Research on Pulse Detonation Combustion Systems: A Status Report," 47th AIAA Aerospace Sciences Meeting Including the New Horizons Forum and Aerospace Exposition, Orlando, FL, AIAA Paper 2009-631, 2009. doi: 10.2514/6.2009-631

[60] Hoffman, H., "Reaction Propulsion by Intermittent Detonative Combustion," *Ministry of Supply, Volkenrode Translation*, 1940.

[61] Nicholls, H. R., Wilkinson, R. B., and Morrison, J. A., "Intermittent Detonation as a Thrust-Producing Mechanism," *Journal of Jet Propulsion*, vol. 27, no. 5, pp. 534–541, 1957.

[62] Krzycki, L. J., "Performance Characteristics of an Intermittent-Detonation Device," Naval Ordnance Test Station China Lake Calif., Tech. Rep. 7655, 1962.

[63] Moen, I. O., Funk, J. W., Ward, S. A., Rude, G. M., and Thibault, P. A., "Detonation Length Scales for Fuel-Air Explosives," in *Dynamics of Shock Waves, Explosions, and Detonations*, Soloukhin, R. I., Oppenheim, A. K., Manson, N., and Bowen, J. R., Eds., vol. 94, Progress in Astronautics and Aeronautics, 1984, pp. 55–79.

[64] Helman, D., Shreeve, R., and Eidelman, S., "Detonation Pulse Engine," 22nd Joint Propulsion Conference, Huntsville, AL, AIAA Paper 1986-1683, 1986. doi: 10.2514/6.1986-1683

[65] Endo, T., Kasahara, A., J.and Matsuo, Sato, S., Inaba, K., and Fujiwara, T., "Pressure History at the Thrust Wall of a Simplified Pulse Detonation Engine," *AIAA Journal*, vol. 42, no. 9, pp. 1921–1930, 2004. doi: 10.2514/1.976

[66] Wintenberger, E., Austin, J. M., Cooper, M., Jackson, S., and Shepherd, J. E., "Analytical Model for the Impulse of Single-Cycle Pulse Detonation Tube," *Journal of Propulsion and Power*, vol. 19, no. 1, pp. 22–38, 2003. doi: 10.2514/2.6099

[67] Wintenberger, E., Austin, J. M., Cooper, M., Jackson, S., and Shepherd, J. E., "Erratum for "Analytical Model for the Impulse of Single-Cycle Pulse Detonation Tube"," *Journal of Propulsion and Power*, vol. 20, no. 4, pp. 765–767, 2004. doi: 10.2514/1.9442

[68] Sterling, J., Ghorbanian, K., Humphrey, J., Sobota, T., and Pratt, D., "Numerical Investigations of Pulse Detonation Wave Engines," 31st Joint Propulsion Conference & Exhibit, San Diego, CA, AIAA Paper 1995-2479, 1995. doi: 10.2514/6.1995-2479

[69] Kailasanath, K., Patnaik, G., and Li, C., "Computational Studies of Pulse Detonation Engines - A Status Report," 35th Joint Propulsion Conference & Exhibit, Los Angeles, CA, AIAA Paper 1999-2634, 1999. doi: 10.2514/6.1999-2634

[70] Morris, C. I., "Simplified Analysis of Pulse Detonation Rocket Engine Performance," 38th AIAA/ASME/SAE/ASEE Joint Propulsion Conference & Exhibit, Indianapolis, IN, AIAA Paper 2002-3715, 2002. doi: 10.2514/6.2002-3715

[71] Guzik, S., Harris, P. G., and De Champlain, A., "An Investigation of Pulse Detonation Engine Configurations Using the Method of Characteristics," 38th AIAA/ASME/SAE/ASEE Joint Propulsion Conference & Exhibit, Indianapolis, IN, AIAA Paper 2002-4066, 2002. doi: 10.2514/6.2002-4066

[72] Ebrahimi, H. B. and Merkle, C. L., "Numerical Simulation of a Pulse Detonation Engine with Hydrogen Fuels," *Journal of Propulsion and Power*, vol. 18, no. 5, pp. 1041–1048, 2002. doi: 10.2514/2.6053

[73] Ebrahimi, H. B., Mohanraj, R., and Merkle, C. L., "Multilevel Analysis of Pulsed Detonation Engines," *Journal of Propulsion and Power*, vol. 18, no. 2, pp. 225–232, 2002. doi: 10.2514/2.5932

[74] He, X. and Karagozian, A. R., "Numerical Simulation of a Pulse Detonation Engine Phenomena," *Journal of Scientific Computing*, vol. 19, no. 1–3, pp. 201–224, 2003. doi: 10.1023/A:102535192

[75] Wu, Y., Ma, F., and Yang, V., "System Performance and Thermodynamic Cycle Analysis of Airbreathing Pulse Detonation Engines," *Journal of Propulsion and Power*, vol. 19, no. 4, pp. 556–567, 2003. doi: 10.2514/2.6166

[76] Morris, C. I., "Numerical Modeling of Single-Pulse Gasdynamics and Performance of Pulse Detonation Rocket Engines," *Journal of Propulsion and Power*, vol. 21, no. 3, pp. 527–538, 2005. doi: 10.2514/1.7875

[77] Eidelman, S., Grossmann, W., and Lottati, I., "Air-breathing Pulsed Detonation Engine Concept - A Numerical Study," 26th Joint Propulsion Conference, Orlando, FL, AIAA Paper 1990-2420, 1990. doi: 10.2514/6.1990-2420

[78] Lynch, E. D. and Edelman, R. B., "Analysis of the Pulse Detonation Wave Engine," in *Developments In High-Speed Vehicle Propulsion Systems*, Murthy, S. N. B. and Curran, E. T., Eds., vol. 165, Progress in Astronautics and Aeronautics, 1996, pp. 473–516.

[79] Li, C., Kailasanath, K., and Patnaik, G., "A Numerical Study of Flow Field Evolution in a Pulsed Detonation Engine," 38th Aerospace Sciences Meeting & Exhibit, Reno, NV, AIAA Paper 2000-314, 2000. doi: 10.2514/6.2000-314

[80] Kailasanath, K., Patnaik, G., and Li, C., "The Flowfield and Performance of Pulse Detonation Engines," *Proceedings of the Combustion Institute*, vol. 29, no. 2, pp. 2855–2862, 2002. doi: 10.1016/S1540-7489(02)80349-2

[81] Yungster, S., "Analysis of Nozzle Effects on Pulse Detonation Engine Performance," 41st Aerospace Sciences Meeting & Exhibit, Reno, NV, AIAA Paper 2003-1316, 2003. doi: 10.2514/6.2003-1316

[82] Ma, F., Choi, J.-Y., and Yang, V., "Thrust Chamber Dynamics and Propulsive Performance of Single-Tube Pulse Detonation Engines," *Journal of Propulsion and Power*, vol. 21, no. 3, pp. 512–526, 2005. doi: 10.2514/1.8182

[83] Morris, C. I., "Axisymmetric Modeling of Pulse Detonation Rocket Engines," 41st AIAA/ASME/SAE/ASEE Joint Propulsion Conference & Exhibit, Tucson, AZ, AIAA Paper 2005-3508, 2005. doi: 10.2514/6.2005-3508

[84] Harris, P. G., Stowe, R. A., Ripley, R. C., and Guzik, S., "Pulse Detonation Engine as a Ramjet Replacement," *Journal of Propulsion and Power*, vol. 22, no. 2, pp. 462–473, 2006. doi: 10.2514/1.15414

[85] Ma, F., Choi, J.-Y., and Yang, V., "Propulsive Performance of Airbreathing Pulse Detonation Engines," *Journal of Propulsion and Power*, vol. 22, no. 6, pp. 1188–1203, 2006. doi: 10.2514/1.8182

[86] Ivanov, V. S. and Frolov, S. M., "Numerical Simulation of the Operation Process and Thrust Performance of an Air-Breathing Pulse Detonation Engine in Supersonic Flight Conditions," *Russian Journal of Physical Chemistry B*, vol. 5, no. 4, pp. 597–609, 2011. doi: 10.1134/S1990793111040075

[87] Zhdan, S. A., Mitrofanov, V. V., and Sychev, A. I., "Reactive Impulse from the Explosion of a Gas Mixture in a Semiinfinite Space," *Combustion, Explosion, and Shock Waves*, vol. 30, no. 5, pp. 657–663, 1994. doi: 10.1007/BF00755833

[88] Hinkey, J., Bussing, T., and Kaye, L., "Shock Tube Experiments for the Development of a Hydrogen-Fueled Pulse Detonation Engine," 31st Joint Propulsion Conference & Exhibit, San Diego, CA, AIAA Paper 1995-2578, 1995. doi: 10.2514/6.1995-2578

[89] Zitoun, R. and Desbordes, D., "Propulsive Performances of Pulsed Detonations," *Combustion Science and Technology*, vol. 144, no. 1-6, pp. 93–144, 1999. doi: 10.1080/00102209908924199

[90] Cooper, M. A., Jackson, S., Austin, J., Wintenberger, E., and Shepherd, J. E., "Direct Experimental Impulse Measurements for Detonations and Deflagrations," *Journal of Propulsion and Power*, vol. 18, no. 5, pp. 1033–1041, 2002. doi: 10.2514/2.6052

[91] Lieberman, D., Parkin, K., and Shepherd, J. E., "Detonation Initiation by a Hot Turbulent Jet for use in Pulse Detonation Engines," 38th AIAA/ASME/SAE/ASEE

Joint Propulsion Conference & Exhibit, Indianapolis, IN, AIAA Paper 2002-3909, 2002. doi: 10.2514/6.2002-3909

[92] Cooper, M. A. and Shepherd, J. E., "Detonation Tube Impulse in Subatmospheric Environments," *Journal of Propulsion and Power*, vol. 22, no. 4, pp. 845–851, 2006. doi: 10.2514/1.16979

[93] Aarnio, M., Hinkey, J., and Bussing, T., "Multiple Cycle Detonation Experiments During the Development of a Pulse Detonation Engine," 32nd Joint Propulsion Conference & Exhibit, Lake Buena Vista, FL, AIAA Paper 1996-3263, 1996. doi: 10.2514/6.1996-3263

[94] Hinkey, J., Williams, J., Henderson, S., and Bussing, T., "Rotary-Valved, Multiple-Cycle, Pulse Detonation Engine Experimental Demonstration," 33rd Joint Propulsion Conference & Exhibit, Seattle, WA, AIAA Paper 1997-2746, 1997. doi: 10.2514/6.1997-2746

[95] Schauer, F., Stutrud, J., and Bradley, R., "Detonation Initiation Studies and Performance Results for Pulsed Detonation Engine Applications," 39th AIAA Aerospace Science Meeting & Exhibit, Reno, NV, AIAA Paper 2001-1129, 2001. doi: 10.2514/6.2001-1129

[96] Kasahara, J., Hasegawa, A., Nemoto, T., Yamaguchi, H., Yajima, T. *et al.*, "Performance Validation of a Single-Tube Pulse Detonation Rocket System," *Journal of Propulsion and Power*, vol. 25, no. 1, pp. 173–180, 2009. doi: 10.2514/1.37924

[97] Joshi, D. D. and Lu, F. K., "Unsteady Thrust Measurement for Pulse Detonation Engines," *Journal of Propulsion and Power*, vol. 32, no. 1, pp. 225–236, 2015. doi: 10.2514/1.B35520

[98] Sato, S., Matsuo, A., Endo, T., and Kasahara, J., "Numerical Studies on Specific Impulse of Partially Filled Pulse Detonation Rocket Engines," *Journal of Propulsion and Power*, vol. 22, no. 1, pp. 64–69, 2006. doi: 10.1159/000092938

[99] Heiser, W. H. and Pratt, D. T., *Hypersonic Airbreathing Propulsion*, American Institue of Aeronautics and Astronautics, Washington, DC, 1994.

[100] Mattingly, J. D., *Elements of Propulsion: Gas Turbines and Rockets*, American Institute of Aeronautics and Astronautics, Reston, VA, 2006.

[101] Kasahara, J., Arai, T., and Matsuo, A., "Experimental Analysis of Pulse Detonation Engine Performance by Pressure and Momentum Measurements," 41st Aerospace Sciences Meeting & Exhibit, Reno, NV, AIAA Paper 2003-893, 2003. doi: 10.2514/6.2003-893

[102] Cooper, M. A. and Shepherd, J. E., "Single-Cycle Impulse from Detonation Tubes with Nozzles," *Journal of Propulsion and Power*, vol. 24, no. 1, pp. 81–87, 2008. doi: 10.2514/1.30192

[103] Kasahara, J., Hirano, M., Matsuo, A., Daimon, Y., and Endo, T., "Thrust Measurement of a Multicycle Partially Filled Pulse Detonation Rocket Engine," *Journal of Propulsion and Power*, vol. 25, no. 6, pp. 1281–1290, 2009. doi: 10.2514/1.42224

[104] Daniau, E., Zitoun, R., Couquet, C., and Desbordes, D., "Effects of Nozzles of Different Length and Shape on the Propulsion Performance of Pulsed Detonation Engines," in *High-Speed Deflagration and Detonation: Fundamentals and Control*, Roy, G., Frolov, S. M., Netzer, D. W., and Borisov, A. A., Eds., 2001, pp. 251–262.

[105] Li, J.-L., Fan, W., Chen, W., Wang, K., and Yan, C.-J., "Propulsive Performance of a Liquid Kerosene/Oxygen Pulse Detonation Rocket Engine," *Experimental Thermal and Fluid Science*, vol. 35, no. 1, pp. 265–271, 2011. doi: 10.1016/j.expthermflusci.2010.09.014

[106] Wang, K., Fan, W., Lu, W., Zhang, Q., Chen, F. *et al.*, "Propulsive Performance of a Pulse Detonation Engine Rocket Engine Without the Purge Process," *Energy*, vol. 79, no. 1, pp. 228–234, 2015. doi: 10.1016/j.energy.2014.11.017

[107] Li, C. and Kailasanath, K., "Partial Fuel Filling in Pulse Detonation Engines," *Journal of Propulsion and Power*, vol. 19, no. 5, pp. 908–916, 2003. doi: 10.2514/2.6183

[108] Cooper, M. A., Shepherd, J. E., and Schauer, F., "Impulse Correlation for Partially Filled Detonation Tubes," *Journal of Propulsion and Power*, vol. 20, no. 5, pp. 947–950, 2004. doi: 10.2514/1.4997

[109] Falempin, F., Bouchaud, D., Forrat, B., Desbordes, D., and Daniau, E., "Pulse Detonation Engine Possible Applications to Low Cost Tactical Missile and Space Launcher," 37th Joint Propulsion Conference & Exhibit, Salt Lake City, UT, AIAA Paper 2001-3815, 2001. doi: 10.2514/6.2001-3815

[110] Cooper, M. A., "Impulse Generation by Detonation Tubes," Ph.D. dissertation, California Institute of Technology, 2004.

[111] Gurney, R. W., "The Initial Velocities of Fragments from Bombs, Shells, and Grenades," Army Ballistic Research Laboratory, Tech. Rep. BRL 405, 1943.

[112] Endo, T., Yatsufusa, T., Taki, S., Matsuo, A., Inaba, K. *et al.*, "Homogeneous-Dilution Model of Partially Fueled Simplified Pulse Detonation Engines," *Journal of Propulsion and Power*, vol. 23, no. 5, pp. 1033–1041, 2007. doi: 10.2514/1.21223

[113] Kasahara, J., Liang, Z., Browne, S. T., and Shepherd, J. E., "Impulse Generation by an Open Shock Tube," *AIAA Journal*, vol. 46, no. 7, pp. 1593–1603, 2008. doi: 10.2514/1.27467

[114] Eidelman, S. and Yang, X., "Analysis of Pulse Detonation Engine Efficiency," 34th AIAA/ASME/SAE/ASEE Joint Propulsion Conference & Exhibit, Cleveland, OH, AIAA Paper 1998-3877, 1998. doi: 10.2514/6.1998-3877

[115] He, X. and Karagozian, A. R., "Pulse-Detonation-Engine Simulations with Alternative Geometries and Reaction Kinetics," *Journal of Propulsion and Power*, vol. 22, no. 4, pp. 852–861, 2006. doi: 10.2514/1.17847

[116] Kailasanath, K., "A Review of Research on Pulse Detonation Engine Nozzles," 37th Joint Propulsion Conference & Exhibit, Salt Lake City, UT, AIAA Paper 2001-3932, 2001. doi: 10.2514/6.2001-3932

[117] Zhang, Q., Fan, W., Wang, K., Lu, W., Chi, Y. *et al.*, "Impact of Nozzles on a Valveless Pulse Detonation Rocket Engine Without the Purge Process," *Applied Thermal Engineering*, vol. 100, pp. 1161–1168, 2016. doi: 10.1016/j.applthermaleng.2016.02.135

[118] Owens, Z. C. and Hanson, R. K., "Single-Cycle Unsteady Nozzle Phenomena in Pulse Detonation Engines," *Journal of Propulsion and Power*, vol. 23, no. 2, pp. 325–337, 2007. doi: 10.2514/1.22415

[119] Cambier, J. L. and Tegnér, J. K., "Strategies for Pulsed Detonation Engine Performance Optimization," *Journal of Propulsion and Power*, vol. 14, no. 4, pp. 489–498, 1998. doi: 10.2514/2.5305

[120] Allgood, D., Gutmark, E., Hoke, J., Bradley, R., and Schauer, F., "Performance Measurements of Multicycle Pulse-Detonation-Engine Exhaust Nozzles," *Journal of Propulsion and Power*, vol. 22, no. 1, pp. 70–779, 2006. doi: 10.2514/1.11499

[121] Barbour, E. A. and Hanson, R. K., "Analytic Model for Single-Cycle Detonation Tube with Diverging Nozzles," *Journal of Propulsion and Power*, vol. 25, no. 1, pp. 162–172, 2009. doi: 10.2514/1.35420

[122] Taylor, G. I., "The Dynamics of the Combustion Products behind Plane and Spherical Detonation Fronts in Explosives," *Proceedings of the Royal Society of London A: Mathematical Physical, and Engineering Sciences*, vol. 200, no. 1061, pp. 235–247, 1950. doi: 10.1098/rspa.1950.0014

[123] Smith, C. E., "The Starting Process in a Hypersonic Nozzle," *Journal of Fluid Mechanics*, vol. 24, no. 4, pp. 625—640, 1966. doi: 10.1017/S0022112066000880

[124] Amann, H. O., "Experimental Study of the Starting Process in a Reflection Nozzle," *The Physics of Fluids*, vol. 12, no. 5, pp. I–150–I–153, 1969. doi: 10.1063/1.1692597

[125] Saito, T. and Takayama, K., "Numerical Simulations of Nozzle Starting Process," *Shock Waves*, vol. 9, no. 2, pp. 73–79, 1999. doi: 10.1007/s001930050141

[126] Paterson, S., "The Reflection of a Plane Shock Wave at a Gaseous Interface," *Proceedings of the Physical Society*, vol. 61, no. 2, pp. 119–121, 1948. doi: 10.1088/0959-5309/61/2/302

[127] Bitondo, D., Glass, I., and Paterson, G., "One-Dimensional Theory of Absorption and Amplification of a Plane Shock Wave by a Gaseous Layer," University of Toronto Institute of Aerophysics, Tech. Rep. 5, 1950.

[128] Bitondo, D., "Experiments on the Amplification of a Plane Shock Wave," University of Toronto Institute of Aerophysics, Tech. Rep. 7, 1950.

[129] Glass, I. I., "Shock Tubes, Handbook of Supersonic Aerodynamics," NAVORD, Tech. Rep. 1488, vol. 6, section 18, 1959.

[130] Ablow, C. M., "Wave Refraction at an Interface," *Quarterly of Applied Mathematics*, vol. 18, no. 1, pp. 15–29, 1960. doi: 10.1090/qam/135022

[131] Glass, I. I., "Over Forty Years of Continuous Research at UTIAS on Nonstationary Flows and Shock Waves," *Shock Waves*, vol. 1, no. 1, pp. 75–86, 1991. doi: 10.1007/BF01414870

[132] Brouillette, M., "The Richtmyer–Meshkov Instability," *Annual Review of Fluid Mechanics*, vol. 34, no. 1, pp. 445–468, 2002. doi: 10.1146/annurev.fluid.34.090101.162238

[133] Morrison, R. R., "A Shock Tube Investigation of Detonative Combustion," University of Michigan, Engineering Research Institute, Ann Arbor, Michigan, Tech. Rep. UMM-97, 1952.

[134] Paterson, S., "Contact Transmission of Detonation," *Symposium (International) on Combustion*, vol. 4, no. 1, pp. 468–471, 1953. doi: 10.1016/S0082-0784(53)80065-2

[135] Pack, D. C., "The Reflection and Transmission of Shock Waves I: The Reflection of a Detonation Wave at a Boundary," *The Philosophical Magazine: A Journal of Theoretical Experimental and Applied Physics*, vol. 2, no. 14, pp. 182–188, 1957. doi: 10.1080/14786435708243807

[136] Fickett, W., "Motion of an Explosive-Induced Plane Shock Wave," *Quarterly of Applied Mathematics*, vol. 32, no. 1, pp. 71–84, 1974. doi: 10.1090/qam/99688

[137] Thomas, G., Sutton, P., and Edwards, D., "The Behavior of Detonation Waves at Concentration Gradients," *Combustion and Flame*, vol. 84, no. 3, pp. 312–322, 1991. doi: 10.1016/0010-2180(91)90008-Y

[138] Glass, I. and Sislian, J., "One-Dimensional Flow in a Simple Shock Tube," in *Nonstationary Flows and Shock Waves*, Cullen, A., Woods, L., Brady, J., Brennen, C., Eatock Taylor, W. *et al.*, Eds., Clarendon Press, Oxford, 1994.

[139] Anderson, J. D., *Hypersonic and High Temperature Gas Dynamics*, American Institue of Aeronautics and Astronautics, Reston, VA, 2006.

[140] Millikan, R. C. and White, D. R., "Systematics of Vibrational Relaxation," *The Journal of Chemical Physics*, vol. 39, no. 12, pp. 3209–3213, 1963. doi: 10.1063/1.1734182

[141] Li, J., Chung, K., and Hsu, Y., "Diaphragm Effect on the Detonation Wave Transmission Across the Interface Between Two Mixtures," *Combustion, Explosion, and Shock Waves*, vol. 51, no. 6, pp. 717–721, 2015. doi: 10.1134/S0010508215060131

[142] Henderson, L., *The Refraction of Shock Waves*, Academic Press, San Diego, 2001.

[143] Zucrow, M. J. and Hoffman, D. J., *Gas Dynamics*, John Wiley & Sons, New York, NY, 1976, vol. 1.

[144] Zucrow, M. J. and Hoffman, D. J., *Gas Dynamics, Multidimensional Flow*, John Wiley & Sons, New York, NY, 1977, vol. 2.

[145] Guzik, S., "Venting Optimization of a Pulse Detonation Engine," Master's thesis, Université Laval, Département de génie mécanique, 2003.

[146] Povinelli, L. A. and Yungster, S., "Airbreathing Pulse Detonation Engine Performance," NASA, Tech. Rep. TM-2002-211575, 2002.

[147] Povinelli, L. A. and Yungster, S., "Real Gas Effects on the Performance of Hydrocarbon-Fueled Pulse Detonation Engines," NASA, Tech. Rep. TM-2003-212211, 2003.

[148] Kiyanda, C., Tanguay, V., Higgins, A., and Lee, J., "Effect of Transient Gasdynamic Processes on the Impulse of Pulse Detonation Engines," *Journal of Propulsion and Power*, vol. 18, pp. 1124–1126, 2002. doi: 10.2514/2.6045

[149] Radulescu, M. I. and Hanson, R. K., "Effect of Heat Loss on Pulse-Detonation-Engine Flow Fields and Performance," *Journal of Propulsion and Power*, vol. 21, no. 2, pp. 274–285, 2005. doi: 10.2514/1.10286

[150] Owens, Z. C. and Hanson, R. K., "The Influence of Wall Heat Transfer, Friction, and Condensation on Detonation Tube Performance," *Combustion Science and Technology*, vol. 182, no. 8, pp. 1104–1140, 2010. doi: 10.1080/00102200903485202

[151] Kawane, K., Shimada, S., Kasahara, J., and Matsuo, A., "The Influence of Heat Transfer and Friction on the Impulse of a Detonation Tube," *Combustion and Flame*, vol. 158, no. 10, pp. 2023–2036, 2011. doi: 10.1016/j.combustflame.2011.02.017

[152] Harris, P. O., Farinaccio, R., Stowe, R. A., Higgins, A. J., Thibault, P. A. *et al.*, "The Effect of DDT Distance on Impulse in a Detonation Tube," 37th Joint Propulsion Conference & Exhibit, Salt Lake City, UT, AIAA Paper 2001-3467, 2001. doi: 10.2514/6.2001-3467

[153] Laviolette, J. P., Kiyanda, C. B., and Higgins, A. J., "The Effect of Friction and Heat Transfer on Impulse in a Detonation Tube," Canadian Section of Combustion Institute, 2002.

[154] Vincenti, W. G. and Kruger, C., *Introduction to Physical Gas Dynamics*, John Wiley & Sons, New York, NY, 1965.

[155] Zel'dovich, Y. B. and Raizer, Y. P., *Physics of Shock Waves and High-Temperature Hydrodynamic Phenomena*, Dover Publications, Inc., Mineola, NY, 1966.

[156] Bray, K., *Nonequilibrium Nozzle Flows*, Marcel Dekker, Inc., New York, NY, 1970, pp. 59–157.

[157] Kung, R. T. V. and Center, R. E., "High Temperature Vibrational Relaxation of H_2O by H_2O, He, Ar, and N_2," *The Journal of Chemical Physics*, vol. 62, no. 6, pp. 2187–2194, 1975. doi: 10.1063/1.430786

[158] Center, R. E. and Newton, J. F., "Vibrational Relaxation of N_2 by H_2O," *The Journal of Chemical Physics*, vol. 68, no. 8, pp. 3327–3333, 1978. doi: 10.1063/1.436237

[159] Gou, X., Sun, W., Chen, Z., and Ju, Y., "A Dynamic Multi-Timescale Method for Combustion Modeling with Detailed and Reduced Chemical Kinetic Mechanisms," *Combustion and Flame*, vol. 157, no. 6, pp. 1111–1121, 2010. doi: 10.1016/j.combustflame.2010.02.020

[160] Kailasanath, K., Li, C., and Cheatham, S., "Computational Studies of Pulse Detonation Engines," in *Combustion Processes in Propulsion: Control, Noise, and Pulse Detonation*, Roy, G., Ed., Elsevier Inc., Burlington, MA, 2006, pp. 377–388.

[161] Barbour, E. A. and Hanson, R. K., "Chemical Nonequilibrium, Heat Transfer, and Friction in a Detonation Tube with Nozzles," *Journal of Propulsion and Power*, vol. 26, no. 2, pp. 230–239, 2010. doi: 10.2514/1.44814

[162] Summerfield, M., Forster, C., and Swan, W., "Flow Separation in Overexpanded Supersonic Exhaust Nozzle," *Jet Propulsion*, vol. 24, no. 9, pp. 319–321, 1954.

[163] Anderson, J. D., *Modern Compressible Flow: With Historical Perspective*, 3rd ed., McGraw Hill, New York, NY, 2003.

[164] Friedlander, F. G., "The Diffraction of Sound Pulses I. Diffraction by a Semi-Infinite Plane," *Proceedings of the Royal Society of London A: Mathematical, Physical and Engineering Sciences*, vol. 186, no. 1006, pp. 322–344, 1946. doi: 10.1098/rspa.1946.0046

[165] Ma, F., Choi, J.-Y., and Yang, V., "Thrust Chamber Dynamics and Propulsive Performance of MultiTube Pulse Detonation Engines," *Journal of Propulsion and Power*, vol. 21, no. 4, pp. 681–691, 2005. doi: 10.2514/1.8182

[166] Rasheed, A., Furman, A. H., and Dean, A. J., "Pressure Measurements and Attenuation in a Hybrid Multitube Pulse Detonation Turbine System," *Journal of Propulsion and Power*, vol. 25, no. 1, pp. 148–161, 2009. doi: 10.2514/1.31893

[167] Rasheed, A., Furman, A. H., and Dean, A. J., "Experimental Investigations of the Performance of a Multitube Pulse Detonation Turbine System," *Journal of Propulsion and Power*, vol. 27, no. 3, pp. 586–596, 2011. doi: 10.2514/1.B34013

[168] Kennedy, J. E., *The Gurney Model of Explosive Output for Driving Metal*, Springer, New York, NY, 1998, pp. 221–257.

[169] Wu, Y., "System Performance and Thermodynamic Cycle Analysis of Air-Breathing Pulse Detonation Engines," Ph.D. dissertation, Pennsylvania State University, 2002.

[170] Chester, W., "CXLV. The Quasi-Cylindrical Shock Tube," *The London, Edinburgh, and Dublin Philosophical Magazine and Journal of Science*, vol. 45, no. 371, pp. 1293–1301, 1954. doi: 10.1080/14786441208561138

[171] Chisnell, R. F., "The Motion of a Shock Wave in a Channel, with Applications to Cylindrical and Spherical Shock Waves," *Journal of Fluid Mechanics*, vol. 2, no. 3, pp. 286–298, 1957. doi: 10.1017/S0022112057000130

[172] Whitham, G., "On the Propagation of Shock Waves Through Regions of Non-uniform Area or Flow," *Journal of Fluid Mechanics*, vol. 4, no. 4, pp. 337–360, 1958. doi: 10.1017/S0022112058000495

[173] Russell, D. A., "Shock-Wave Strengthening by Area Convergence," *Journal of Fluid Mechanics*, vol. 27, no. 2, pp. 305–314, 1967. doi: 10.1017/S0022112067000333

[174] Setchell, R. E., Storm, E., and Sturtevant, B., "An Investigation of Shock Strengthening in a Conical Convergent Channel," *Journal of Fluid Mechanics*, vol. 56, no. 3, pp. 505–522, 1972. doi: 10.1017/S0022112072002484

[175] Nettleton, M. A., "Shock Attenuation in a 'Gradual' Area Expansion," *Journal of Fluid Mechanics*, vol. 60, no. 2, pp. 209–223, 1973. doi: 10.1017/S0022112073000121

[176] Igra, O., Elperin, T., Falcovitz, J., and Zmiri, B., "Shock Wave Interaction with Area Changes in Ducts," *Shock Waves*, vol. 3, no. 3, pp. 233–238, 1994. doi: 10.1007/BF01414717

[177] Whitham, G., "A New Approach to Problems of Shock Dynamics Part I Two-Dimensional Problems," *Journal of Fluid Mechanics*, vol. 2, no. 2, pp. 145–171, 1957. doi: 10.1017/S002211205700004X

[178] Best, J. P., "A Generalisation of the Theory of Geometrical Shock Dynamics," *Shock Waves*, vol. 1, no. 4, pp. 251–273, 1991. doi: 10.1007/BF01418882

[179] Kirkwood, J. G. and Bethe, H. A., "The Pressure Wave Produced by an Underwater Explosion III," National Defense Research Committee of the Office of Scientific Research and Development, Tech. Rep. 588, 1942.

[180] Han, Z. and Yin, X., "Relation Between M and A for a Uniform Quiescent Gas Ahead of a Shock Wave," in *Shock Dynamics*, Springer, Beijing, 1993.

[181] Milton, B. E., "Mach Reflection Using Ray-Shock Theory," *AIAA Journal*, vol. 13, no. 11, pp. 1531–1533, 1975. doi: 10.2514/3.60566

[182] Skews, B. W., "The Shape of a Diffracting Shock Wave," *Journal of Fluid Mechanics*, vol. 29, no. 2, pp. 297–304, 1967. doi: 10.1017/S0022112067000825

[183] Skews, B. W., "The Perturbed Region Behind a Diffracting Shock Wave," *Journal of Fluid Mechanics*, vol. 29, no. 4, pp. 705–719, 1967. doi: 10.1017/S0022112067001132

[184] Skews, B. W., Law, C., Muritala, A., and Bode, S., "Shear Layer Behavior Resulting from Shock Wave Diffraction," *Experiments in Fluids*, vol. 52, no. 2, pp. 417–424, 2012. doi: 10.1007/s00348-011-1233-9

BIOGRAPHICAL STATEMENT

James T. Peace was born in Denison, Texas, in 1992. He joined the University of Texas at Arlington (UTA) in 2011 and received a B.S. degree in Aerospace Engineering in 2014. After the completion of his undergraduate degree, he continued his graduate studies as a B.S. to Ph.D. student at UTA. He joined the Aerodynamics Research Center (ARC) in 2012 as an undergraduate research assistant due to his interests in aerodynamics, gasdynamics, and propulsion. He was a recipient of an Enhanced Graduate Teaching Assistantship at UTA. During his doctoral studies, he continued conducting research at the ARC with a focus on gasdynamic phenomena in pulse detonation engines and published his findings in numerous conference papers and journal articles.